Dipartimento di Scienze
Biologiche, Geologiche e Ambientali

UNIVERSITÁ DEGLI STUDI DI CATANIA
DIPARTIMENTO DI SCIENZE BIOLOGICHE, GEOLOGICHE E AMBIENTALI

Ph.D course in “Earth and Environmental Science”
Dottorato di Ricerca in “Scienze della Terra e dell’ambiente”
Curriculum in “Geoscience”
(XXXIII Cycle)

EVALUATION OF NEW USES OF VOLCANIC ASHES AND PALEO-SOILS COMING FROM MT. ETNA VOLCANO IN THE GEOPOLYMER PRODUCTION

Doctor Europaeus candidate

CLAUDIO FINOCCHIARO

Advisor:
Prof. Paolo Mazzoleni

Co-Advisor:
Prof.ssa Germana Barone

Coordinator:
Prof.ssa Agata Di Stefano

Ph.D attended during 2017/2020

Index

1. Introduction ... 1
  1.1 Geological setting ... 1
  1.2 Effects of volcanic explosive activity ... 5
  1.3 Legislation ... 6
  1.4 What is geopolymer? ... 8
    1.4.1 Precursors and activators ... 10
    1.4.2 Geopolymers Vs OPC ... 12
  1.5 State of art on geopolymers based on volcanic materials ... 13
  1.6 Historical uses of volcanic rocks and particles ... 15
2. Materials ... 20
  2.1 Volcanic precursors: sampling ... 20
  2.2 Metakaolin ... 22
  2.3 Activators ... 22
  2.4 Characterization methods for volcanic raw materials ... 23
    2.4.1 X-ray power diffraction (XRD) ... 23
    2.4.2 X-ray fluorescence (XRF) ... 23
    2.4.3 Fourier-transform infrared spectroscopy (FT-IR) ... 24
    2.4.4 Thermogravimetric analysis (TGA) ... 24
    2.4.5 Raman spectroscopy ... 24
    2.4.6 Scanning electron microscope (SEM) ... 25
  2.5 Results ... 25
    2.5.1 XRF: chemical composition ... 25
    2.5.2 XRD: mineralogical composition ... 27
    2.5.3 FTIR (KBr method) ... 28
    2.5.4 Raman spectroscopy ... 30
    2.5.5 TGA: thermal analysis ... 33
    2.5.6 SEM-EDX: morphological and EDX analysis ... 34
3. Geopolymerization process ... 37
  3.1 Thermal treatments of the slurry ... 39
    3.1.1 Integrity test results ... 41
  3.2 Addition of metakaolin on total weight of the matrix ... 41
    3.2.1 Integrity test results ... 44
    3.2.2 Macroscopic observations on carbonatation phenomena ... 45
  3.3 Thermal treatments on volcanic precursors ... 47
  3.4 Mechanosynthesis ... 47

4. Characterization approaches and results ... 48
4.1 Methods details ... 48
4.1.1 OM: optical microscope ... 48
4.1.2 XRD: X-ray powder diffraction ... 48
4.1.3 FTIR: Fourier transform infrared ... 48
4.1.4 Raman spectroscopy ... 49
4.1.5 Mechanical performance: compressive test ... 49
4.1.6 SEM-EDX: Scanning electron microscope – energy dispersive x-ray ... 50
4.1.7 Permeable porosity test for total absorption ... 50
4.1.8 Hg porosimetry ... 51
4.2 Results on geopolymers thermically treated ... 51
4.2.1 OM: petrographic analysis ... 51
4.2.2 XRD analysis ... 53
4.2.3 FTIR analysis (KBr method) ... 55
4.3 Results of VM1 and GM1 series ... 57
4.3.1 OM: petrographic analysis ... 57
4.3.2 XRD analysis ... 59
4.3.3 FTIR analysis (KBr method) ... 62
4.3.4 Raman Spectroscopy ... 64
4.3.5 SEM: microstructural analysis ... 69
4.3.6 Mechanical compressive strength ... 74
4.3.7 Water absorption and porosity ... 76
4.4 Conclusions ... 79
5. I insight: comparison between two samples set activated by Na and K solutions ... 80
5.1 Materials: precursors, activators and geopolymers ... 80
5.2 Methods ... 82
5.3 Results ... 86
5.3.1 In situ ATR-FTIR spectroscopy on fresh slurries ... 86
5.3.2 FTIR on consolidated samples after 21 days (KBr method) ... 93
5.3.3 XRD: mineralogical analysis ... 94
5.3.4 Thermal analysis ... 95
5.3.5 Mechanical properties ... 98
5.3.6 Porosimetric properties ... 101
5.3.7 Physical properties correlations ... 103
5.3.8 RAMAN spectroscopy ... 104

5.3.9 SEM-EDX analysis 111
5.4 Conclusions 119
6. II insight: neural network approach and comparison with conventional approach (MLR) 120
6.1 Materials and sample preparation 120
6.2 Experimental methods 122
6.3 Analysis approaches: ANN and MLR 122
6.3.1 ANN principles 122
6.3.2 ANN design 124
6.3.3 MLR principles 126
6.3.4 MLR design 127
6.4 Experimental results 127
6.5 ANNs results 132
6.5.1 V-ANNs 132
6.5.2 G-ANNs 134
6.6 MLR results 137
6.6.1 V-MLR 137
6.6.2 G-MLR 138
6.7 Conclusion 140
7. Applications: tiles, quick-setting binders and mortars 142
7.1 Tiles: synthesis approach 142
7.1.1 Tests on tiles 143
7.2 Quick-setting geopolymeric binders: synthesis approach 143
7.3 Geopolymeric mortars: synthesis approach 145
7.4 Characterization methods 148
7.5 Results 148
7.6 Conclusion 153
8. Conclusions and final remarks 154
9. Bibliography 156

List of figures

Fig. 1.1 - Map of volcanoes around the world : volcanoes in red triangles (Smithsonian Institute Global Volcano Program. Global Volcanism Program, 2013. Volcanoes of the World, v. 4.8.2. Venzke, E (ed.). Smithsonian Institution. Downloaded 29 Aug 2019. https://doi.org/10.5479/si.GVP.VOTW4-20)..1

Fig. 1.2 - Sketch map of eastern Sicily showing location of Etna and other important structural elements of the geology of the region. Faults are shown in black; the volcanic areas of the Hyblean Plateau (Monti Iblei) are shown in pink colour (Monaco et al., 1997). 2

Fig. 1.3 - Basic tectonic and geologic map of Mount Etna (1:250.000 scale) (Branca et al., 2011). Symbols: PF, Pernicana fault; SLF, S. Leonardello fault; STF, S. Tecla fault; AF, Acireale fault; TCF, Trecastagni fault; TMF, Tremestieri fault. Legend: 1, Present and recent covers; 2, Il Piano Synthem (Mongibello volcano) (a, sedimentary deposits); 3, Concazze Synthem (Ellittico volcano) (a, sedimentary deposits); 4, Zappini Synthem (Cuvigghiuni, Salifizio, Giannicola and Monte Cerasa volcanoes); 5, Croce Menza Synthem (Trifoglietto, Rocche and Tarderia volcanoes); 6, S. Alfio Synthem; 7, Acireale Synthem (a, sedimentary deposits); 8, Adrano Synthem; 9, Aci Trezza Synthem (a, sedimentary deposits); 10, sedimentary and metamorphic basement..............................4

Fig. 1.4 - Sampling in the storage area of Santa Venerina town....................................7

Fig. 1.5 - Geopolymer terminology proposed by Davidovits (Davidovits, 1991)............9

Fig. 1.6 - Semi-schematic structure for Na-polysialate polymer (Barbosa et al., 2000)..9

Fig. 1.7 - Sketch of geopolymer process considering the three main steps: dissolution, condensation and polycondensation (Duxson et al., 2007). 10

Fig. 1.8 - CaO-Al_2O_3-SiO_2 ternary diagram of cementitious materials. Abbreviation: OPC- Ordinary Portland Cement..11

Fig. 1.9 - Detailed sketch of Model proposed for N-A-S-H gel formation (Duxson et al., 2007; Palomo et al., 2014)..12

Fig. 1.10 – Global distribution of natural pozzolana deposits (grey areas) (Snellings et al., 2012). 16

Fig. 1.11 – Etna map showing the main lava fields erupted from 1669 to 2002, focusing on 1669's eruption at Mts. Rossi. The dashed segments indicate the position of the S Rift and the NE Rift (Bonaccorso et al., 2016). 17

Fig. 1.12 – a) example of ghiara quarry (Mt. Etna, Italy): the white dashed line divides the ancient volcanic soil with the 1408 lava flow; b) ghiara particles with different grain size...18

Fig. 1.13 – Example of ancient applications: a) Detachment of historical mortar based on ghiara; b) Original plaster application in San Salvatore church in Viagrande, Catania, Italy. 19

Fig. 2.1 – Digital elevation model (DEM) map of Mt. Etna volcano (Sicily, Italy): volcanic building in red...21

Fig. 2.2– Sampling and treatments of raw materials: a) sampling of volcanic ash in Santa Venerina landfill; b) cleaning step with distilled water; c) drying step into oven; d) press machine for milling; e) sieves used: 250 µm, 125 µm, 75 µm; f) final powder < 75 µm to be used for alkaline process...21

Fig. 2.3 - Histogram graph of major elements (including standard deviation).............26

Fig. 2.4– Diffractometric patterns of volcanic raw materials (VLA raw, GHI raw) and metakaolin (MK). Legenda: An: anorthite; Ano: anorthoclase; Aug: Augite; Fo: forsterite; Mag: magnetite; Hem: hematite; Gt: goethite; Qtz: quartz; Ms: muscovite; Ant: anatase; Crn: corundum. 28

Fig. 2.5 – a) tubular furnace used for thermically treated the volcanic precursors; b) entrance of furnace; c) little ceramic rectangular bowl with volcanic ash after treatment; d) little ceramic rectangular bowl with ghiara after treatment. 29

Fig. 2.6 – Overlapping absorbance FTIR spectra of volcanic raw materials (room temperature and thermically treated at 200, 300 and 400°C) in the range 4000-400 cm^{-1}. (a) volcanic ash (V) and (b) ghiara (G) raw materials..30

Fig. 2.7 - Overlapping of Raman spectra of volcanic ash samples (V) and standard mineral (downloaded by rruff database). Legenda: pyroclastite (pr); powder (pw); anorthite (An); augite (Au); forsterite (Fo); hematite (He); magnetite (Mg)................31

Fig. 2.8 - Micrographs of Raman spot analyses for the following samples: a) V_pw2 (powder); b) V_pw3 (powder); c) V_pr3 (pyroclastite)...31

Fig. 2.9 - Overlapping of Raman spectra of ghiara samples (G) and standard mineral (downloaded by rruff database). Legenda: pyroclastite (pr); powder (pw); anorthite (An); augite (Au); forsterite (Fo); hematite (He); magnetite (Mg).......................................32

Fig. 2.10 - Micrographs of Raman spot analyses for the following samples: a) G_pw1 (powder); b) G_pr2 (pyroclastite); c) G_pr1 (pyroclastite)...33

Fig. 2.11 – Thermal analysis curves of weight loss (—) and heat flow (---) for (a) volcanic ash and (b) ghiara raw materials. 34

Fig. 2.12 – Morphological photos of volcanic ash: a) porous structure (magnification 300x); b) general preview of structure particle with magnification 145x and spot analysis (a) with corresponding histogram of EDX analysis..35

Fig. 2.13 – Morphological photos of ghiara particles at different magnifications: a) porous structure (500x); b) 1Kx and spot analysis (a) with corresponding histogram of EDX analysis...36

Fig. 3.1 – Reactants mixing step: a) precursor: volcanic ash powder; b) reactants properly weighted before to be mixed; c) manually mixing with spatula; d) mechanically mixing with electrical mixer; e) filling of moulds; f) covering of samples through thin polymer film. 38

Fig. 3.2 – Integrity test observations and consequently thermal treatments: a) example of good stability in water; b) example of partial dissolving; c) example of interaction between sample and water, changing colour of water; d) thermal treatments at 400°C into oven; e) samples treated at 400°C once removed by oven; f) samples treated at 100°C once removed by oven. 41

Fig. 3.3 – Summary of the main steps for AAMs production with MK addition. A) mixing of ghiara and metakaolin and use of a sieve to homogenise; B) result after the sieving step; C) mixing with alkaline solution and mechanical mixer; D) fill of cubic moulds with the fresh slurry; E) after 24/36h of consolidation and before to unmould. *42*

Fig. 3.4 - Carbonates crystallization micro-pictures (approximately each photo represents 1 cm^2 *of sample) with a short description of AAMs based on volcanic ash and metakaolin with different percentage of NaOH (x-axis) and metakaolin (y-axis). Map results evidenced by different colours (green: positive and without carbonates crystallization; yellow: passed the integrity test but crystallization occurred; red failed test).* *45*

Fig. 3.5 - Carbonates crystallization micro-pictures (approximately each photo represents 1 cm^2 *of sample) with a short description of AAMs based on ghiara and metakaolin with different percentage of NaOH (x-axis) and metakaolin (y-axis). Map results evidenced by different colours (green: positive and whiteout carbonates crystallization; yellow: passed the test but crystallization occurred; red failed test).* ... *46*

Fig. 4.1 - Representative photographs of cubic samples regarding the series GM1 (a) and VM1 (b) after polishing surfaces step. *50*

Fig. 4.2 – OM micrographs (left: parallel nicols; right: crossed nicols) of the following geopolymers with volcanic ash: A) geopolymer treated at 100 ° C (VLA1_100); B) geopolymer treated at 400 ° C (VLA1_400). *52*

Fig. 4.3 – OM micrographs (left: parallel nicols; right: crossed nicols) of the following geopolymers with ghiara: A) geopolymer treated at 100 ° C (GHI4_100); B) geopolymer treated at 400 ° C (GHI4_400). *53*

Fig. 4.4 – Representative pattern of volcanic ash for following typology: raw material, treated at 100/400°C and one with metakaolin addition (20%) (An: anorthite; Aug: Augite; Fo: forsterite; Mag: magnetite; Crn: corundum). *54*

Fig. 4.5 – Representative pattern of ghiara for following typology: raw material, treated at 100/400°C and one with metakaolin addition (20%) (An: anorthite; Ano: anorthoclase; Aug: augite; Fo: forsterite; Hem: hematite; Gt: goethite Mag: magnetite; Crn: corundum). *55*

Fig. 4.6 – FT-IR spectra obtained by KBr method. a) AAMs based on volcanic ash thermically treated at 100° (black) and 400°C (red); b) AAMs based on ghiara thermically treated at 100° (black) and 400°C (red). The dashed lines indicate the main contributions. Spectra resolution 4 cm^{-1}*.* *56*

Fig. 4.7 – OM micrographs (left: parallel nicols; right: crossed nicols) of the following geopolymers with volcanic ash: A) geopol. volcanic ash and 15 wt. % of MK (VM1-15); B) geopol. volcanic ash and 25 wt. % of MK (VM1-25); C) geopol. volcanic ash and 20 wt. % of MK with low L/S ratio (VM1-20LS). *58*

Fig. 4.8 – OM micrographs (left: parallel nicols; right: crossed nicols) of the following geopolymers with ghiara: A) geopol. ghiara and 15 wt. % of MK (GM1-15); B) geopol. ghiara and 25 wt. % of MK (GM1-25); C) geopol. ghiara and 20 wt. % of MK with low L/S ratio (GM1-20LS). *59*

Fig. 4.9 – XRD pattern of VM1 series and precursors: volcanic ash (VLA raw) and metakaolin (MK). Legenda: An: anorthite; Aug: augite; Fo: forsterite; Hem: hematite; Mag: magnetite; Gis: gismondine; Qtz: quartz; Ms: muscovite; Ant: anatase; Crn: corundum. *61*

Fig. 4.10 – XRD pattern of GM1 series and precursors: ghiara (GHI raw) and metakaolin (MK). Legenda: An: anorthite; Ano: anorthoclase; Aug: augite; Fo: forsterite; Hem: hematite; Gt: goethite; Qtz: quartz; Ms: muscovite; Ant: anatase; Crn: corundum. *61*

Fig. 4.11 – FT-IR spectra obtained by KBr method on samples belonging to VM1 and GM1 series. a) complete spectra of geopolymers with 10 wt % MK; b) spectra of geopolymers with 15 (a), 20 (b) and 25 (c) wt % of MK in the range 1800-400 cm^{-1}*; c) complete spectra of geopolymers labelled "green formulations" with 20 wt % MK and lowest L/S ratio. The dashed lines indicate the main contributions. Spectra resolution 4* cm^{-1}*.* *63*

Fig. 4.12 - Overlapping of Raman spectra regarding the sample VM1-10 and some mineralogical phases downloaded by rruff database (An: anorthite, Au: augite, Fo: forsterite, He: hematite) and micrograph of spot analyses corresponding to the spectrum. *65*

Fig. 4.13 - Overlapping of Raman spectra regarding the sample VM-20 and some mineralogical phases downloaded by rruff database (An: anorthite, Au: augite, Fo: forsterite, He: hematite) and micrograph of spot analyses corresponding to the spectrum. *66*

Fig. 4.14 - Overlapping of Raman spectra regarding the sample VM1-20LS and some mineralogical phases downloaded by rruff database (An: anorthite, Au: augite, Fo: forsterite, He: hematite; At: anatase) and micrograph of spot analyses corresponding to each spectrum. The peak indicated with "" corresponds to trona phase according to rruff catalogue (R050499).* *66*

Fig. 4.15 - Overlapping of Raman spectrum regarding the sample GM1-10 and some mineralogical phases downloaded by rruff database (An: anorthite, Au: augite, Fo: forsterite, He: hematite) and micrograph of spot analyses corresponding to the spectrum. *67*

Fig. 4.16 - Overlapping of Raman spectra regarding the sample GM1-20 and some mineralogical phases downloaded by rruff database (An: anorthite, Au: augite, Fo: forsterite, He: hematite; At: anatase) and micrographs of spot analyses corresponding to each spectrum. *68*

Fig. 4.17 - Overlapping of Raman spectra regarding the sample GM1-20LS and some mineralogical phases downloaded by rruff database (An: anorthite, Au: augite, Fo: forsterite, He: hematite; Qt: quartz; At: anatase) and micrographs of spot analyses corresponding to each spectrum. *69*

Fig. 4.18 (a-d) – SEM images at high magnifications. Legenda: a) sample VM1-10; b) sample VM1-20; c) sample GM1-10; d) sample GM1-20. Images acquired respectively in fisheye, 53x, 124x and 228x (magnifications). Crack deflection mechanism indicated by yellow arrows. *71*

Fig. 4.19 (a-d) – SEM micro-images of thin sections with high magnifications with spot analysis expressed in red dots, EDS spectra of representative point analyses and tables with histograms where weight of the oxides (% wt.) are listed. Legenda: A) sample VM1-10 (magnifications 498x and 2.38 kx); B) sample VM1-20 (magnification 3.67 kx); C) sample GM1-10 (magnification 2.58 kx); D) sample GM1-20 (magnification 3.23 kx). Crack deflection mechanism indicated by yellow arrows...72

Fig. 4.20 (a-i) - Elements maps of VM1-10 sample: a) backscattered electron (BSE) map; b) SiK; c) AlK; d) Ca; e) FeK; f) NaK; g) KK; h) MgK; i) TiK....................................74

Fig. 4.21 – Correlation between compressive strengths and metakaolin (wt.%) (including standard deviation). 75

Fig. 4.22 (a-b) – Cumulative pore volume vs pore size graphs: a) representative samples of VM1 set and the corresponding aged one year (dashed lines); b) representative samples of GM1 set and the corresponding aged one year (dashed lines).....................77

Fig. 4.23 – Chromatic comparison between the volcanic raw materials and the respective AAMs with the colour classification (RAL). Legenda: A) ghiara raw material and representative sample belonging to GM1 series; B) Colour card (RAL 8002) corresponding to signal brown; C) volcanic ash raw material and representative sample belonging to VM1 series; B) Colour card (RAL 8019) corresponding to grey brown...79

Fig. 5.1 – Milling and granulometric analysis of raw materials: a) sediment quartering; b) mechanical milling using porcelain jars; c) sieve to easily remove the alumina balls from the powder; d) final powder; e) laser particle sizer used to evaluate the granulometric curve of the volcanic precursors...81

Fig. 5.2 – Values of particle size distribution after dry milling....................................81

Fig. 5.3 – Photos of FT-IR equipment and sample preparation: a) little plastic pot with powder to be analysed; b) small agata mortar with alumina spatula for sample preparation; c) matrix "Specac" for pressure step; d) Thermo Fisher Scientific 380 infrared spectrometer (Nicolet) programmed for KBr measurements; e) press used to pellet preparation; f) analysis on fresh slurry of geopolymer in ATR mode. 83

Fig. 5.4 – XRD analysis: a) XRD equipment of IRCER (Limoges University): Brucker-D8 Advance with a Bragg-Brentano geometry; b) geopolymer specimens in powder ready to be analysed....84

Fig. 5.5 – a) TGA equipment; b) detail of sample measuring; c) sample of geopolymer based on volcanic ash after TGA; d) sample of geopolymer based on ghiara after TGA. 84

Fig. 5.6 – Photos of mechanical compressive test: a) panoramic of samples prepared and cured in plastic pots; b) filling of accommodations to polish both surfaces of samples; c) polishing phase through abrasion mechanism; d) volcanic ash samples after surfaces rectification; e) ghiara samples after surfaces rectification; f) breaking moment of ghiara sample after compressive test; g) breaking moment of volcanic ash sample after compressive test. 85

Fig. 5.7 – Demonstrative example of a polycondensation reaction occurrence through the progressive shift of in situ FTIR spectra over time (a spectrum represents the acquisition each 10 minutes). 87

Fig. 5.8 – Trends of in situ FTIR regarding the progressive shift of Si-O-M positions in 8 hour (spectra resolution: 4 cm^{-1}). Legenda: (—) Na-VM/GM, (—) K-VM/GM; a) Na/K-VM-20; b) Na/K-VM-10; c) Na/K-GM-20; d) Na/K-GM-10. 88

Fig. 5.9 – Demonstrative example of no polycondensation reaction............................. 88

Fig. 5.10 – Comparison of effects caused by the activation with both alkaline solutions. A) Na/K-VM-20; B) Na/K-GM-20 (spectra resolution: 4 cm^{-1})..................................... 89

Fig. 5.11 – Trends of the progressive shift of Si-O-M positions over 30 hours obtained by in situ FT-IR analysis. Legenda: a) Na/K-VM-10; b) Na/K-VM-20; c) Na/K-GM-10; d) Na/K-GM-20. 90

Fig. 5.12 (a-b) – a) FT-IR spectra obtained using KBr method collected in the range of 4000-400 cm-1 for (---) K-VM and (—) Na-VM; b) in the range of 1800-800 cm-1. The dashed arrows indicate the carbonate contributions... 94

*Fig. 5.13 – XRD patterns of raw precursors and consolidated materials. Pdf files : Q : quartz (04-016-2085) ; An : anorthite (04-05-4988) ; Au : augite (04-017-4396) ; Fo : forsterite (04-017-0663) ; M : Magnetite (00-900-5814) Mu: muscovite (00-060-1516) ; He :hematite (00024-0072) ; A : anatase (00-021-1272), * corundum......................... 95*

Fig. 5.14 - Thermal curves of weight loss (—) and (---) heat flow for (a) Na-GM-10, (b) K-GM-10, (c) Na-GM-20, (d) K-GM-20, (e) Na-VM-10, (f) K-VM-10, (g) Na-VM-20 and (h) K-VM-20. 98

Fig. 5.15 – Average of compressive strength in function of time after (—)7 and (---) 21 days for samples based on (a) VM and (b) GM activated with (A) sodium and (B) potassium solution and with (—)10 and (—)20% of metakaolin. 100

Fig. 5.16 – Value of specific mechanical compressive in function of Al concentration for (■)VM, (★) GM, (—) Na-samples, (—)K-samples, (■) after 7 days, (□) after 21 days. 101

Fig. 5.17 (a-c) – Cumulative pore volume vs pore size graphs: a) Na/K-VM-10/20; b) Na/K-GM-10/20; (—) Na-solution, (---) K-solution, (—) 10% wt. M, (—) 20% wt. M; c) plot bulk density vs porosity: (■)VM, (★) GM, (—) Na-samples, (—) K-samples, (□) 10% wt. M, (■)20% wt. M. 103

Fig. 5.18 - Matrix scatter plot of density, mechanical strengths after 7 days, weight loss in the range 200-500°C and accessible porosity; (□) Na and (x) K solutions; Sequences: I-IV for columns; a-d for rows. The boxplots of each variable are reported in the matrix are formed by scatter plots of the variable defined by the intersection with the diagonal. 104

Fig. 5.19 - Overlapping of Raman spectra regarding the sample Na-VM-10 and some mineralogical phases downloaded by rruff database (An: anorthite, Au: augite, Fo: forsterite, He: hematite) and micrographs of spot analyses corresponding to each spectrum. 106

Fig. 5.20 - Overlapping of Raman spectra regarding the sample Na-VM-20 and some mineralogical phases downloaded by rruff database (An: anorthite, Au: augite, Fo: forsterite, He: hematite) and micrograph of spot analysis corresponding to the spectrum. 106

Fig. 5.21 - Overlapping of Raman spectra regarding the sample Na-GM-10 and some mineralogical phases downloaded by rruff database (An: anorthite, Au: augite, Fo: forsterite, He: hematite) and micrographs of spot analyses corresponding to each spectrum. *107*

Fig. 5.22 - Overlapping of Raman spectra regarding the sample Na-GM-20 and some mineralogical phases downloaded by rruff database (An: anorthite, Au: augite, Fo: forsterite, He: hematite) and micrographs of spot analyses corresponding to each spectrum. *108*

Fig. 5.23 - Overlapping of Raman spectra regarding the sample K-VM-10 and some mineralogical phases downloaded by rruff database (An: anorthite, Au: augite, Fo: forsterite, He: hematite) and micrograph of spot analyses corresponding to the spectrum. *109*

Fig. 5.24 - Overlapping of Raman spectra regarding the sample K-VM-20 and some mineralogical phases downloaded by rruff database (An: anorthite, Au: augite, Fo: forsterite, He: hematite) and micrograph of spot analyses corresponding to the spectrum. *109*

Fig. 5.25 - Overlapping of Raman spectra regarding the sample K-GM-10 and some mineralogical phases downloaded by rruff database (An: anorthite, Au: augite, Fo: forsterite, He: hematite) and micrograph of spot analyses corresponding to the spectrum performed using a 20x objective. The peak indicates with "" corresponding to magnetite phase according to rruff catalogue (R061111).* *110*

Fig. 5.26 - Overlapping of Raman spectra regarding the sample K-GM-20 and some mineralogical phases downloaded by rruff database (An: anorthite, Au: augite, Fo: forsterite, He: hematite) and micrographs of spot analyses corresponding to each spectrum. The peaks indicated with "" correspond to diopside (R040028), while Pl (plagioclase) indicates bytownite (R070598) phases according to rruff catalogue.* *111*

Fig. 5.27 – SEM micrographs of Na-VM-10 sample: a) Mag. 500x; b) Mag. 1.5Kx; c) Mag. 4 Kx and EDX analysis whose spot analysis is indicated in red dot (a). *112*

Fig. 5.28 – SEM micrographs of Na-VM-20 sample: a) Mag. 500x; b) Mag. 1.5Kx; c) Mag. 4 Kx and EDX analysis whose spot analysis are indicated in red dots (a and b). *113*

Fig. 5.29 – SEM micrographs of Na-GM-10 sample: Mag. 150x; b) Mag. 1Kx; c) Mag. 5 Kx., and EDX analysis whose spot analysis are indicated in red dots (a-c) *114*

Fig. 5.30 – SEM micrographs of Na-GM-20 sample: Mag. 150x; b) Mag. 1Kx; c) Mag. 5 Kx., and EDX analysis whose spot analysis is indicated in red dot (a). *114*

Fig. 5.31 – SEM micrographs of K-VM-10 sample: Mag. 150x; b) Mag. 500x; c) Mag. 1Kx and EDX analysis whose spot analysis are indicated in red dots (a-c) *116*

Fig. 5.32 – SEM micrographs of K-VM-20 sample: Mag. 500x; b) Mag. 1.5Kx; c) Mag. 1Kx and EDX analysis whose spot analysis are indicated in red dots (a-c) *117*

Fig. 5.33 – SEM micrographs of K-GM-10 sample: Mag. 150x; b) Mag. 1Kx; c) Mag. 5Kx and EDX analysis whose spot analysis are indicated in red dots (a and b) *117*

Fig. 5.34 – SEM micrographs of K-GM-20 sample: Mag. 150x; b) Mag. 1Kx; c) Mag. 5Kx and EDX analysis whose spot analysis are indicated in red dots (a-c)................118

Fig. 6.1 – ANN model used: neuron (circle) and weight (arrow). Input layer: volcanic ash/ghiara (V/G); metakaolin (MK); sodium hydroxide (H); sodium silicate with SiO2/Na2O = 2 (S2); sodium silicate with SiO2/Na2O = 3 (S3); water (W). Hidden layer (H01-10); Output layer (O1-4): weight loss, conductivity, pH and compressive strengths. 125

Fig. 6.2 - Conductivity trends over time for each series: a) VM_2; b) GM_2; c) VM_3; d) GM_3. 129

Fig. 6.3 - Trends of weight loss Vs metakaolin amount. The samples "LS" are set as 19% wt. MK...130

Fig. 6.4 - Histograms of compressive strengths of all series. The samples "LS" are set as 30% wt. MK...131

Fig. 6.5 (a-d) – V-ANNs plots for each ANN created: a) weight loss; b) conductivity; c) pH; d) average compressive strengths. In x axis experimental results, while in y axis calculated one. The dashed line indicates the trendline passing for the origin. Legends: ● VM_2 series ○ VM_3 series..133

Fig. 6.6 (a-d) – G-ANNs plots using VM-training: a) weight loss; b) conductivity; c) pH; d) average compressive strengths. In x axis experimental results, while in y axis calculated one. The dashed line indicates the trendline passing for the origin. Legends: ● GM_2 series ○ GM_3 series. 134

Fig. 6.7 (a-d) – G-ANNs plots for each ANN created: a) weight loss; b) conductivity; c) pH; d) average compressive strengths. In x axis experimental results, while in y axis calculated one. The dashed line indicates the trendline passing for the origin. Legends: ● GM_2 series ○ GM_3 series. 135

Fig. 6.8 (a-d) – V-ANNs plots using GM-training: a) weight loss; b) conductivity; c) pH; d) average compressive strengths. In x axis experimental results, while in y axis calculated one. The dashed line indicates the trendline passing for the origin. Legends: ● VM_2 series ○ VM_3 series. 136

Fig. 6.9 (a-d) – V-MLR plots for each MLR created: a) weight loss; b) conductivity; c) pH; d) average compressive strengths. In x axis experimental results, while in y axis calculated one. The dashed line indicates the trendline passing for the origin. Legends: ● VM_2 series ○ VM_3 series. 138

Fig. 6.10 (a-d) – G-MLR plots for each MLR created: a) weight loss; b) conductivity; c) pH; d) average compressive strengths. In x axis experimental results, while in y axis calculated one. The dashed line indicates the trendline passing for the origin. Legends: ● GM_2 series ○ GM_3 series. 139

Fig. 7.1 – Tiles just removed from the mould. 143

Fig. 7.2 - Samples prepared to estimate the curing time at increasing prompt amount. 145

Fig. 7.3 – Photographs of geopolymeric mortars prepared with 30 % wt. aggregates of two grain size ranges: (a-b-e-f) 500µm-1mm; (c-d-g-h) 1-2 mm. Legenda: a)

2_VM2_a30; b) 4_VM1_a30; c) 3_VM2_A30; d) 5_VM1_A30; e) 2_GM2_a30; f) 4_GM1_a30; g) 3_GM2_A30; h) 5_GM1_A30. .... *146*

Fig. 7.4 – SEM photographs of VM-10-a30 sample: a) Mag. 500x; b) Mag. 1,5Kx; c) Mag. 4Kx. *149*

Fig. 7.5 – SEM photographs of VM-10-A30 sample: a) Mag. 500x; b) Mag. 1,5Kx; c) Mag. 4Kx. *149*

Fig. 7.6 – SEM photographs of VM-20-a30 sample: a) Mag. 500x; b) Mag. 1Kx; c) Mag. 4Kx. *150*

Fig. 7.7 – SEM photographs of VM-20-A30 sample: a) Mag. 500x; b) Mag. 1Kx; c) Mag. 4Kx. *150*

Fig. 7.8 – SEM photographs of GM-10-a30 sample: a) Mag. 150x; b) Mag. 150x; c) Mag. 1Kx. *151*

Fig. 7.9 – SEM photographs of GM-10-A30 sample: a) Mag. 150x; b) Mag. 1Kx; c) Mag. 5Kx. *152*

Fig. 7.10 – SEM photographs of GM-20-a30 sample: a) Mag. 150x; b) Mag. 150x; c) Mag. 1Kx. *152*

Fig. 7.11 – SEM photographs of GM-20-A30 sample: a) Mag. 150x; b) Mag. 150x; c) Mag. 1Kx. *153*

List of tables

Table 2.1 - Major elements of volcanic raw materials (XRF) and volcanic glass (SEM-EDS), this latter analysed by Barone et al., 2016. The abundances are expressed as weight % of oxides. *26*

Table 2.2 – Chemical molar ratio of raw materials (volcanic ash, ghiara raw and metakaolin) used as precursors in alkaline activation. *26*

Table 2.3 – Mineralogical results obtained by XRD analysis with Rietveld Method. *28*

Table 2.4 - Summary of main IR attributions in the range 1200-400 cm^{-1} of volcanic ash's samples (V) and ghiara's samples (G). *30*

Table 3.1 – Labels, ratios among activators and curing setting. Legenda: volcanic ash (V); ghiara (G). The horizontal straight-line divides above the samples activated using the Na_2SiO_3 with SiO_2/Na_2O ratio=3, and below those with SiO_2/Na_2O ratio=2. .... *40*

Table 3.2 – Labels, ratios among activators and curing setting. Legenda: volcanic ash (V); ghiara (G) and metakaolin (M). *43*

Table 4.1 - Mineralogical results obtained by XRD analysis with Rietveld Method. *55*

Table 4.2 - Summary of main IR attributions in the range 1500-400 cm^{-1} for geopolymers based on volcanic ash and ghiara thermically treated at 100°C and 400°C. *56*

Table 4.3 - Mineralogical results obtained by XRD analysis with Rietveld Method. *62*

Table 4.4 - Summary of IR attributions in the range 4000-400 cm^{-1} for geopolymers belonging to VM1 and GM1 series (expect green formulations). *64*

Table 4.5 – Summary table with the average values regarding the density after 24/36 h and mechanical strength after 28 curing days with its relative standard deviation (S.d.). *75*

Table 4.6 - Results of permeable porosity test for total absorption (W_a) and average density of cubes prepared for mechanical compressive test. *76*

Table 4.7 – Density, porosity and pore information obtained by Hg porosimetry analysis. For each pore size ranges the total incremental volumes (%) were calculated. The prefix x indicates samples aged one year. *78*

Table 5.1 – List of formulations, detailing labels, precursors and activating solutions. *82*

Table 5.2 – Summary of all Si-O-M positions and values obtained by the differences between the starting and ending points (except for the sample K-VM-20 where the value of 17 hours was considered as ending point). *92*

Table 5.3 – Summary of all intensity ratios over time (t0, t5, t18 and t30 hours) considering the absorbance intensity of positions: 1642 and 920 cm^{-1}. *92*

Table 5.4 – Weight's loss values in the two temperature regions (25-200°C and 200-500°C) for all the AAMs considered. *98*

Table 5.5 – Values of density and mechanical compressive strengths (MPa) of all samples after 7 and 21 of aging days. *100*

Table 5.6 – Density, porosity and pore information obtained by Hg porosimetry analysis for each AAMs samples and summary results. For each pore size ranges the total incremental volumes were calculated. *103*

Table 6.1 – Labels and formulation details (in % wt.) of the experimentally prepared AAMs. *121*

Table 6.2 – Parameters used in ANNs. *125*

Table 6.3 – Summary with input data (% wt. reactants) and output data (experimental results). These latter include the results of chemical stability test (weight loss, ionic conductivity and pH) and compressive strengths after 28 curing days. The errors of each equipment are: 0.01g referred to balance sensitivity for weight loss; ±1% full scale accuracy for ionic conductivity; ±0.1 pH; standard deviation was calculated for compressive strength. The double line divides the samples according to V/G-ANNs. The results of VM/GM$_2$ *are reported from (Barone et al., 2020).* *125*

Table 6.4 - Conductivity results over time (t0-t24) for each series. *129*

Table 6.5 - Summary results of all experimental test after 28 curing days: weight loss, conductivity, pH and compressive strengths. *131*

Table 6.6 – Correlation between experimental and calculated data using V-training. *134*

Table 6.7 – Correlation between experimental and calculated data using G-training. *136*

Table 6.8 – MLR correlations of VM and GM samples for each physical property. *139*

Table 6.9 – Experimental and calculated results for each physical property. MLR formula was applied to calculate the data. *139*

Table 7.1 – Formulation details of geopolymeric mortars of testes for tiles production. The values were calculated considering the total weight among binders, aggregates and water. *143*

Table 7.2 - Details of ratio sources and curing time estimation. *144*

Table 7.3 – Formulation details of geopolymeric mortars express in wt %. Mortars with ID 1 represent test with maximum possible (in terms of workability) aggregate contents for each binder without water addition, differently for the other ID mortars which indicate test with a fixed aggregate content (30 wt %) and small water additions to allow the mixing. *147*

ACKNOWLEDGEMENTS

My 3-years PhD program was certainly stimulating, intense and strongly formative for my personal and professional enrichments thanks the many activities and experiences carried out. From these latter, I could meet many wonderful people both within and outside the Catania University which have contributed with own time and knowledge to support my project. For this reason, I would like to thank, firstly, my kind Supervisors, Prof. Paolo Mazzoleni and Prof. Germana Barone, whose I am very grateful to give me precious teachings and to have transmitted to me their passion to make research. My Ph.D. project benefited also of several contributions from other Universities. Indeed, I'm honoured and very thankful to have collaborated with the head of the Italian Geopolymer group, Prof.ssa Cristina Leonelli of Modena and Reggio Emilia University, which has transferred me the fundamental principles of chemistry linked to alkaline synthesis following my short stays in "Enzo Ferrari" Department (UNIMORE) and some of her research colleagues: Prof.ssa Isabella Lancellotti and Dr. Caterina Sgarlata which have followed me during the experiments in laboratory and have contributed in some results of my research, as well as the Prof. Marcello Romagnoli to have helped me in the implementation of mathematical previsional models. Thanks to the formative experiences carried out at UNIMORE, a strong synergy among both research teams was born. The abroad experience at the Institut de Recherche sur les Céramiques (IRCER) of Limoges University (France) was certainly positive and highly educational. At this purpose, I want to intensely thank the Supervisor, Professor Sylvie Rossignol, for her availability and perseverance, from which I have learnt her scientific approach and new analytical methods, as well as all her research team and in particular: the Dr. Ameni Gharzouni, Remì Farges, Lila Ouamara and Dr. Anas El Khomsi.

I wish to thank all the "Crew" (i.e. my colleagues team) to have supported and tolerated me: Antonio, which shared with me some experiences from the beginning of my path; Cristina and Alessia which have helped to clarify some of my doubts on setting measurements and interpretations of Raman spectra as well as friendly advice, Maura and Roberta for the oral comparisons on laboratory tasks and data processing; and Gabriele for some precious suggestions on researcher's life. Moreover, I wish to thank the Doctorate Coordinator, Prof.ssa Agata Di Stefano, for her constant support in administrative items linked to national and international missions.

I wish to thank the foreign reviewers, Prof. Giuseppe Cultrone of Granada University (Spain) and Prof. Jan Jehlička of Charles University (Czech Republic), who positively evaluated my PhD thesis for the expositive clarity, good organization of the work and the abundance of obtained results by different analytical methodologies, as well as to give me some improvement suggestions as a graphical summary for the project contents;

The companies Bal-Co s.p.a.. for supplying the metakaolin “ARGICAL 1000” and Ingessil s.r.l., for supplying the sodium silicate; further Mr. Filippo Musarra and Mr. Alfio Grassi for kindly supplying ghiara paleo-soils. The period abroad has been supported by Catania University and partially by the grant of Erasmus traineeship.

Finally, but not least, my family to whom I owe the teachings of life and the moral support, as well as my wonderful girlfriend, Anna, who was a strong shoulder of solace and continuous support, as well as my best friends who have been near physically and/or morally.

THANKS ALL!!

ITALIAN SUMMARY

Titolo: Valutazione di nuovi utilizzi delle ceneri vulcaniche e paleosuoli etnei nella produzione di geopolimeri

Com’è ampiamente noto, il patrimonio artistico culturale è fortemente influenzato dalla geologia locale. In quest’ottica, il percorso di ricerca ha previsto di valorizzare, mediamente il processo di attivazione alcalina, due materiali vulcanici: da un lato, i depositi di cenere vulcanica, diffusi nell’area Etnea e considerati dalle normative vigenti un materiale di scarto naturale, e dall’altro, i paleo-suoli di ghiara, ampiamente utilizzati nel XVII e XVIII secolo come aggregati per la produzione di malte da impiegare nell'architettura del centro storico di Catania e dintorni. I materiali derivanti dal processo di attivazione alcalina (AAMs: alkali activated materials), anche noti come geopolimeri, sono prodotti dalla combinazione di un precursore alluminosilicatico polverizzato e da una soluzione alcalina. L’interesse per questi materiali sta crescendo esponenzialmente nel tempo grazie alle alte performance fisico-meccaniche riscontrate in letteratura, in aggiunta alle basse emissioni di CO_2, se confrontate alle emissioni derivanti dalla produzione dei tradizionali cementi Portland, e al buon rapporto qualità-prezzo, se come precursori sono impiegati scarti naturali o industriali. I risultati di caratterizzazione chimica-mineralogica delle materie prime vulcaniche Etnee hanno confermato l'idoneità ad essere utilizzate come precursori nel processo di sintesi alcalina grazie all’elevato contenuto di Si e Al e alla prevalente struttura amorfa che favorisce la sintesi in ambiente alcalino.

Inizialmente, il primo approccio di sintesi aveva come obiettivo la produzione di geopolimeri 100% vulcanici a temperatura ambiente, quindi utilizzando solo i depositi vulcanici come precursori e una soluzione attivante sodica come attivatore. Tuttavia, tale approccio è stato necessariamente modificato con l’aggiunta di trattamenti termici al fine di ridurre i lunghi tempi di presa della pasta geopolimerica per via della bassa reattività della polvere vulcanica. Quest’ultimo approccio è stato subito abbandonato poiché poco sostenibile dal punto di vista del consumo energetico e delle emissioni, così come, precludeva la possibilità di produrre leganti e/o malte da applicare in interventi di restauro. In quest’ottica, sono stati testati ulteriori approcci che hanno previsto da un lato il trattamento termico a 400°C del solo precursore vulcanico prima di essere aggiunto alla soluzione attivante, dall’altro un processo di attivazione chimico-meccanica mediante

l’uso di giarette. Tuttavia, questi approcci non sono stati all’altezza delle aspettative tali da essere immediatamente abbandonati.

Diversamente, l’approccio di sintesi, che ha previsto l’utilizzo di piccole quantità di metacaolino per la produzione di miscele binarie a temperatura ambiente, è risultato adeguato allo scopo. La caratterizzazione di questi materiali è stata eseguita con un approccio multidisciplinare. I risultati XRD hanno mostrato una composizione prevalentemente amorfa (confermata anche dall'analisi SEM-EDX che ha evidenziato un gel *N-A-S-H: sodium aluminosilicate hydrate*) combinata alle fasi mineralogiche dei precursori vulcanici, nonché una piccola quantità di fasi appartenenti al gruppo delle zeoliti (es. Serie VM1 e GM1), a testimonianza di una parziale organizzazione della struttura. La combinazione delle tecniche spettroscopiche utilizzate (Raman e FTIR) ha permesso di confermare le strutture alluminosilicatiche con un contributo più o meno marcato di carbonati, che decresce all'aumentare del contenuto di metacaolino nella miscela (es. Na/K-V/GM-10/20) o dovuto al prolungato tempo d’esposizione all'aria che genera fenomeni di efflorescenza (es. serie VM1 e GM1; abbastanza comune nei sistemi alcalini). Inoltre, le analisi FTIR in situ sono state utili per evidenziare le reazioni di policondensazione immediatamente dopo la miscelazione con le soluzioni alcaline (es. Na/K-V/GM-10/20). In base ai risultati ottenuti, è stato possibile affermare che i geopolimeri a base di depositi piroclastici necessitano di un basso rapporto liquido/solido (L/S) al fine di evitare fenomeni di efflorescenza e per ottenere resistenze a compressione maggiori, a differenza del metacaolino che richiede un L/S più elevato per favorire la lavorabilità della miscela.

Inoltre, è stato ampiamente confermato come il metacaolino, utilizzato come componente additivo, abbia un'influenza positiva sulle prestazioni meccaniche nonché su una migliore organizzazione del network. Le resistenze a compressione hanno registrato, anche dopo una settimana, un valore elevato (es. 17 MPa per Na-V/GM-10 mentre 45 MPa per Na-V/GM-20) con un aumento del 15% dopo 21 giorni di invecchiamento. A tale scopo sono state prodotte malte con inerti della stessa natura del precursore vulcanico utilizzato per i leganti (es. Na-V/GM-10/20) con lo scopo di simulare le malte storiche dell'architettura catanese. Microscopicamente, questi materiali sono microporosi con pori medi di 0,04 µm concentrati principalmente nell'intervallo 0,1-0,01 µm. Tuttavia, queste dimensioni aumentano nelle malte (SEM) a causa della porosità intrinseca degli inerti utilizzati. Dall’approfondimento condotto nel periodo all’estero è stato dimostrato come la tipologia di soluzione attivante influenzi le prestazioni fisico-meccaniche del prodotto finale. Infatti, i campioni K-V/GM-10/20 hanno evidenziato una resistenza a compressione maggiore e una minore porosità a differenza di quelli attivati con la soluzione sodica. Inoltre, è stato condotto un approfondimento sulle potenzialità delle reti neurali nel valutare la stabilità chimica del dataset considerato, evidenziando i punti di forza dei reagenti utilizzati sulla reticolazione del prodotto finale, così da definire un mix design ottimale di partenza per formulazioni future. I risultati ottenuti da tale percorso di ricerca lasciano ben sperare sulla fattibile applicazione delle malte/leganti nell'ambito del restauro o come materiali da costruzione prefabbricati da immettere sul mercato così da incentivare la *circular economy* locale.

PREFASE

Mt. Etna volcano (Sicily, Italy), following its intense activities, offers large quantity of pyroclastic deposits around its flanks, which contribute to make them fertile and unique in all the world over the centuries. Moreover, the historical architecture of Etnean area has been strongly influenced by the local geological setting, which provided stone materials and aggregates to apply in building field. However, the volcanic activities have, also, negative effects on the ecosystem, causing pollution, logistic problems to society and influencing the clime. Despite the abundance of pyroclastic materials, they are, unfortunately, considered a waste material according to the current legislation due to the possible interactions with other matrices (e.g. smog caused by engines of cars, modifying so their natural origin), Therefore, they are stocked in disposal areas with a high cost management, instead of to be treated and used. Moreover, worth of note is that the use of pyroclastic rocks in the mortars is limited to the old leached deposits since the fresh volcanic products have an excessively high chlorides and sulphates content due to their interaction with the volcanic gasses (Barone et al., 2016). Therefore, the thick pyroclastic deposits produced by the recent frequent explosive activity of Mt. Etna and stocked in dedicated disposal areas, cannot be used in the traditional cement industry. In the last decades, a new class of innovative material was proposed as alternative to traditional Ordinary Portland Cement (OPC), whose general name is geopolymer, belonging to alkali activated material class. Geopolymers have several advantages: high physical properties and wide selection of application fields.

In this scenario, this thesis aims to investigate the potential use of pyroclastic products and ancient pyroclastic soils, locally named ghiara, come from Mt. Etna volcano, as raw materials for geopolymers production with the following aims: i) to make pyroclastic deposits an important resource for Etnean population through a sustainable management and a recycling at km0, supporting an economic development of this territory through a *circular economy*; ii) contributing to environmental policy, proposing eco-friendly materials with low emission impact, valorising local natural waste; iii) to reproduce ancient binders and mortars for the restoration interventions, using local raw materials, maintaining so unaltered the lithological and chromatic aspects of historical monuments and buildings of Catania's Cultural Heritage.

This work is articulated in different steps according to the experience acquired during this educational path. After accurate chemical and mineralogical studies of the volcanic raw materials, aforementioned above, several kinds of alkaline formulations were tested using different methodological approaches. Firstly, each raw material has undergone a manually dry grinding, using press and sieving, with the aim to obtain a grain size < 75 micron, considered suitable for alkaline synthesis (Lancellotti et al., 2013). Then, mechanical grinding approach with jars and laser for grain size detection (this latter performed in the abroad experience) were used with the aim to use the finer particles, suitable to enhance the reactivity. Different mixing in alkaline environment were performed using only volcanic precursors with the aim to obtain the sol-gel formation at room temperature, but without to achieve the aim. Therefore, thermal treatments were necessary to complete the reaction and so to reach a good stiffness in few days. However, to limit the energy consume link to the treatments and to allow the complete reaction at room temperature, a small amount of commercially metakaolin was added in the volcanic matrix. In this scenario, two set of formulations were considered suitable for binders' production. Contextually, mineralogical, structural and molecular investigations were carried out to characterize the geopolymer binders. However, only one set was developed for mortar's production because better physical properties were recorded. Finally, production of composites materials was performed using volcanic aggregates with the aim to simulate the original historical mortars of Catania's Cultural Heritage, thus maintaining the original colours, morphologies, expansion, and vapour permeability of the old buildings.

In this work, two insights were performed in collaboration with two different Institutions:

- Evaluation of polycondensation reaction considering two set of geopolymers activated using respectively two different alkaline solution: one based on sodium, while the second one based on potassium and consequently compare them in terms of structure, mechanical resistance and porosity. This study was performed in collaboration with IRCER (Institut de Recherche sur les Céramiques) of Limoges University, following my abroad period of four months.
- Implementation of unconventional and conventional previsional approaches: Artificial Neural Networks (ANNs) and Multiple linear regressions (MLR) using as dataset, information linked to physical features of analysed geopolymer specimens. These approaches were made

in collaboration with the Department of Engineering “Enzo Ferrari” of Modena and Reggio Emilia University.

RESEARCH HIGHLIGHTS

- Complete characterization of pyroclastic deposits of Mt. Etna volcano to evaluate the feasibility for alkaline activation.
- Evaluation of the most suitable synthesis approaches to overcome the critical issues encountered and allow the transfer to companies for industrial scale-up.
- Test the physical-mechanical performances of different sets of geopolymers produced.
- Consideration on the results obtained in order to optimize the formulations produced.
- Integration of the experimental results with those calculated by traditional (MLR: multiple linear regression) and non-traditional (ANNs: artificial neural networks) statistical approaches aimed to the evaluation of the chemical stability of some sets of samples.
- Research and develop of formulations to be used as building materials: mortars, pre-casting tiles and quick-setting binders.

Parole chiavi: *attivazione alcalina; riciclo; valorizzazione; cenere vulcanica; scarto naturale*

Keywords: *alkaline activation; recycling; valorisation; volcanic ash; natural waste*

GRAPHICAL CONTENTS

Reactants

Precursors:
Volcanic raw materials:
- Volcanic ash
- Ghiara

Activators:
Sodium hydroxide and Na-silicate

Characterization Methods of raw materials:

- XRF: X-ray fluorescence
- XRD: X-ray diffraction (Rietveld method)
- SEM-EDX
- RAMAN Spectroscopy
- FTIR: Fourier Transform Infrared Spectroscopy (KBr)
- TGA: Thermal gravimetric analysis

General synthesis approach:

- Mixing of volcanic precursors (powder < 75 µm) and alkaline solution at room temperature.
- Slip casting and vibration to remove air bubbles.
- Covering with thin polymer film for 24h to maintain constant the level of moisture.
- Curing at air exposition.

Synthesis approaches used:

- 100% volcanic binders at room temperature.
- ***Thermal treatments at different temperatures to reduce the long setting time.***
- ***Use of small metakaolin amount as additive component.***
- Thermal treatments on volcanic powders before to be mixed with the sodium activating solution.
- Mechanosynthesis: mechanical mixing during activation among precursors and activators (without the use of metakaolin).

Characterization Methods of AAMs thermically treated:

- OM: Optical microscope
- XRD: X-ray diffraction (Rietveld method)
- FTIR: Fourier Transform Infrared Spectroscopy (KBr)

Characterization Methods of AAMs with 5-25%wt metakaolin addition (VM1 and GM1 series):

- OM: Optical microscope
- XRD: X-ray diffraction (Rietveld method)
- RAMAN Spectroscopy
- MIP: Mercury Intrusion Porosimetry
- Porosimetry for total absorption
- SEM-EDX
- Compressive test
- FTIR: Fourier Transform Infrared Spectroscopy (KBr)

I Insight: Comparison between Na and K alkaline activation

Characterization Methods:
- In situ FTIR (ATR) on fresh binders
- XRD: X-ray diffraction
- FTIR (Kbr method) on consolidated samples
- TGA: Thermal gravimetric analysis
- Compressive test

- MIP: Mercury Intrusion Porosimetry
- RAMAN Spectroscopy
- SEM-EDX

II Insight: Comparison between (artificial neural networks) ANNs and (multiple linear regression) MLR approaches

General approach:
- Sample set: 18
- Chemical-physical properties: weight loss, ph, conductivity and compressive strength
- V-ANNs, G-ANNs, V-MLRs and G-MLRs

Applications:
- Tiles
- Quick-setting binders
- Mortars

Characterization Methods on mortars:
- SEM: Scanning electron microscope

1. INTRODUCTION

This first chapter focus on general topics of different nature, starting from the geological setting of Mt. Etna volcano, from which volcanic ash is generated, to the new technological frontier of alkali activated materials in comparison to the traditional ones and their historical uses in Catania's architecture. Particular attention was aimed at legislation of natural volcanic waste. Moreover, a general preview on geopolymers was discussed, focusing on their advantages, application fields, synthesis process and the comparison of physical properties with the ordinary Portland cement. Finally, the tight link between volcanic rocks and particles and the ancient uses as building materials in Etnean area was analysed.

1.1 GEOLOGICAL SETTING

Volcanoes are a key part of the Earth system and an open window into the inner of the planet. About thousands of active volcanoes are located in plate boundaries around the world (Fig. 1.1), and, obviously, their activity influences the whole eco-system.

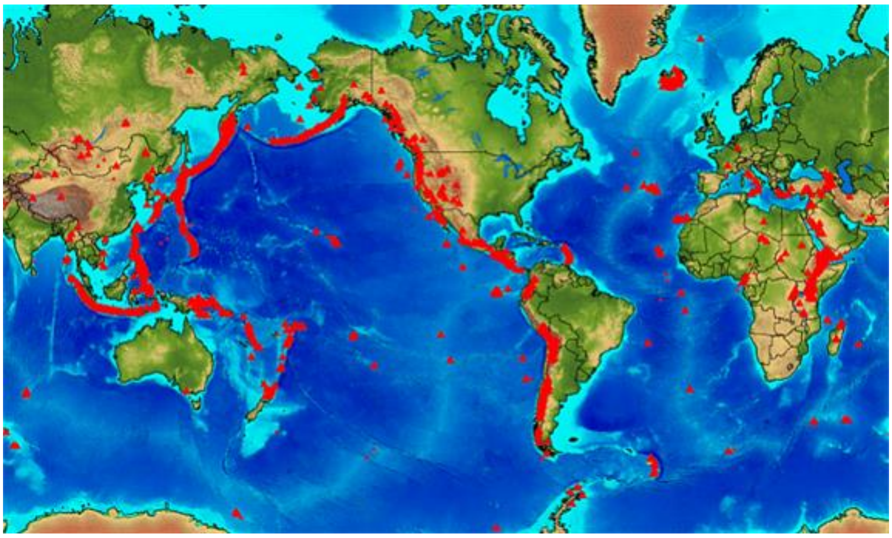

Fig. 1.1 - Map of volcanoes around the world : volcanoes in red triangles (Smithsonian Institute Global Volcano Program. Global Volcanism Program, 2013. Volcanoes of the World, v. 4.8.2. Venzke, E (ed.). Smithsonian Institution. Downloaded 29 Aug 2019. https://doi.org/10.5479/si.GVP.VOTW4-20)

Mt. Etna volcano, located in Sicily island (Italy), is the Europe’s highest volcano and the second most active volcano in the world, following the Kilauea volcano on Hawaii

(USA) and preceding the Piton de la Fournaise on La Réunion island (France). Since 2013, it holds the recognition of Cultural Heritage UNESCO site. The morphology of this volcano is typical of stratovolcano, whose high reaches 3340 m and its area extends over 1250 km^2 in the eastern coast of Sicily, in a complex geodynamic setting, resulting from the Neogene convergence between the European and African plates. Mt. Etna volcano is located at the intersection of two major faults-oriented NNW-SSE (Tindari-Letojanni-Malta faults system) and NNESSW (Messina-Giardini faults) (Azzaro et al., 2012; Bonforte et al., 2011; Branca et al., 2011). Geologically, it covers three structural domains: i) Peloritani mountain chain to the north, corresponding to the Apennine–Maghrebian overthrust belt; ii) the little deformed northern margin of African plate, constituted by the Hyblean Plateau, to the south, which plunges under the Catania–Gela foredeep; iii) thin sedimentary cover overlying the oceanic Ionian lithosphere, considered to be a remnant of the Mesozoic Tethys (Cristofolini et al., 1985; Monaco et al., 1997; Scribano et al., 2009) (Fig. 1.2).

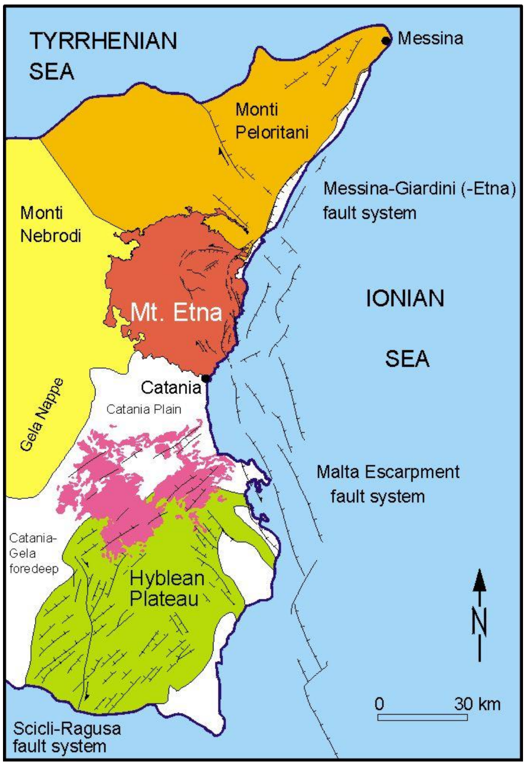

Fig. 1.2 - Sketch map of eastern Sicily showing location of Etna and other important structural elements of the geology of the region. Faults are shown in black; the volcanic areas of the Hyblean Plateau (Monti Iblei) are shown in pink colour (Monaco et al., 1997).

The Etnean area shows a complex interaction between regional tectonics, flank instability processes and basement morphology (Bousquet & Lanzafame, 2004; Giudice & Rasà, 1992; Monaco et al., 1997; Neri et al., 2004; Rust & Neri, 1996). The main structural lineaments (Fig. 1.3), reported from Branca et al., 2011 and Azzaro et al., 2012 can be listed as follow:

- *Pernicana* transtensive fault system, E–W oriented, extending from the upper northeast flank to the Ionian coast, characterised by a left strike-slip displacement (Rasà et al., 1996).
- *Tremestieri–Trecastagni* fault system (NNW–SSE to NW–SE), formed by two normal faults with right-lateral component representing the southern boundary of the unstable eastern flank (Giudice & Rasà, 1992; Solaro et al., 2010).
- *Timpe* normal fault system with a right-lateral component dissecting the lower eastern flank. It is formed by several main segments (e.g. Acireale, S. Tecla, Moscarello and S. Leonardello faults).

Moreover, the eastern flank of Etna is influenced by a seaward gravitational sliding (Borgia et al., 1992; Giudice & Rasà, 1992; Mc Guire et al., 1996; Rust & Neri, 1996) resulting from the interaction between gravity, regional tectonics and recurrent dike intrusions (Azzaro et al., 2013; Rasà et al., 1996). The geochemistry of volcanic gasses (CO_2, SO_2, HCl and HF) strongly influences the atmosphere (10-15 % of global volcanogenic budget, Allard et al., 1991).

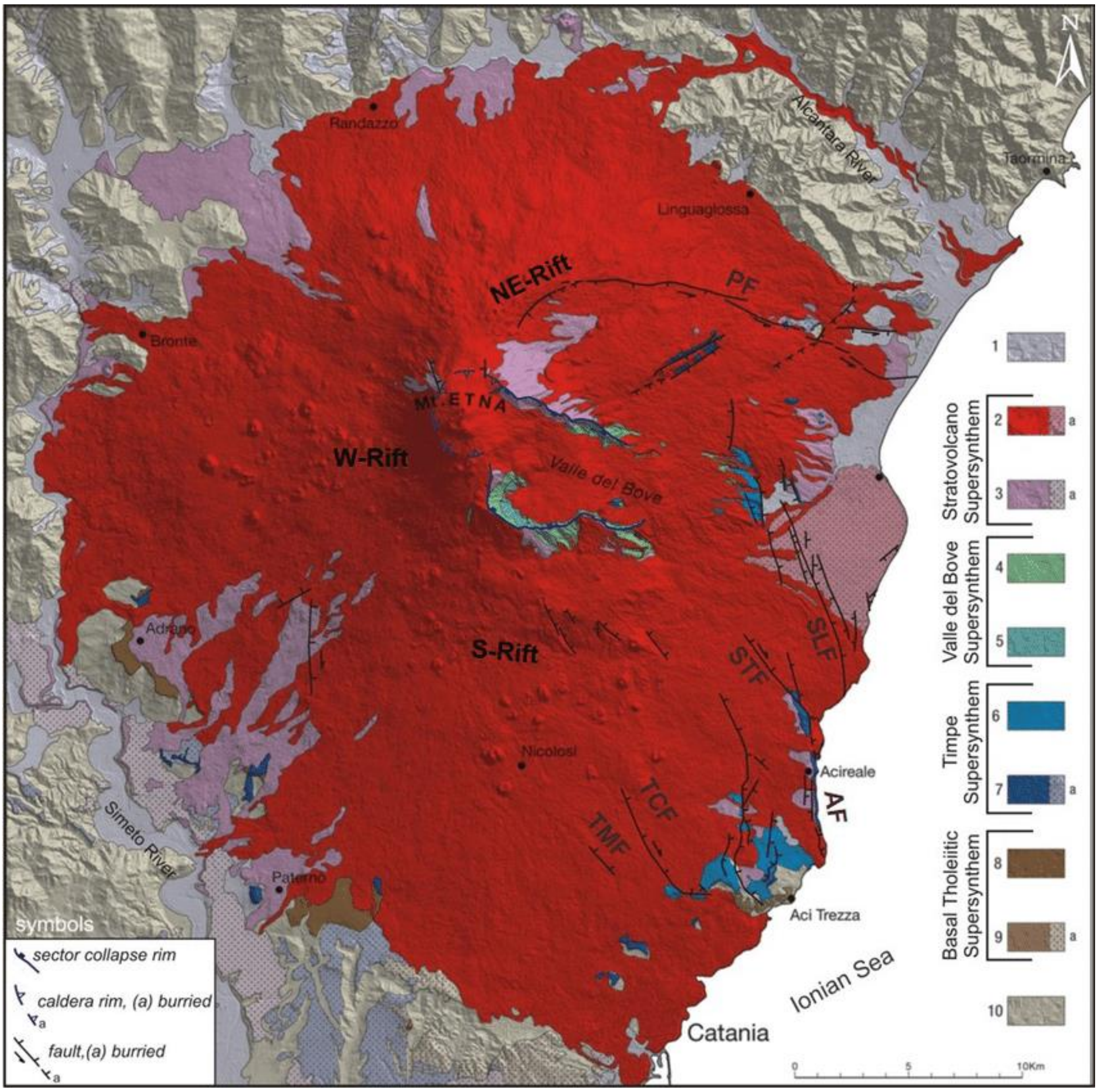

Fig. 1.3 - Basic tectonic and geologic map of Mount Etna (1:250.000 scale) (Branca et al., 2011). Symbols: PF, Pernicana fault; SLF, S. Leonardello fault; STF, S. Tecla fault; AF, Acireale fault; TCF, Trecastagni fault; TMF, Tremestieri fault. Legend: 1, Present and recent covers; 2, Il Piano Synthem (Mongibello volcano) (a, sedimentary deposits); 3, Concazze Synthem (Ellittico volcano) (a, sedimentary deposits); 4, Zappini Synthem (Cuvigghiuni, Salifizio, Giannicola and Monte Cerasa volcanoes); 5, Croce Menza Synthem (Trifoglietto, Rocche and Tarderia volcanoes); 6, S. Alfio Synthem; 7, Acireale Synthem (a, sedimentary deposits); 8, Adrano Synthem; 9, Aci Trezza Synthem (a, sedimentary deposits); 10, sedimentary and metamorphic basement.

Etnean activity can be simplified in four periods:

- I phase *"Pre-Etnean"* began about 0.5 Ma (million years) ago with emissions of sub-marine tholeiitic lavas on the Catania north coast (Aci Castello, Acitrezza) and followed, at~ 0.3 Ma, by sub-aerial tholeiitic lavas in the SW sector of Etna (Romano, 1982; Branca et al., 2008; Clocchiatti et al.,1998).

- II phase *"Ancient Etna"* began about 170 ka (thousand years) ago: mafic alkaline magmas were emitted to form several eruptive centers (Romano, 1982) and possibly the first major Etnean edifice was Calanna eruptive center (Gillot et al., 1994).
- III phase *"Trifoglietto II"* showed the construction of a succession of volcanic edifices with alternating pyroclastic and effusive products, whose major eruptive centers were Trifoglietto II, Vavalaci and Cuvigghiuni (Gillot et al., 1994).
- IV phase *"Mongibello"* evidenced different activities: during the earlier stage, which includes Ellittico and Leone volcanic centers and formation of the homonymous calderas. The erupted magmas were the most chemically evolved (trachytic) in Etna history. Differently for the latter period, which contributed to the construction of the modern summit cone which was interrupted at least once by caldera collapse (Piano caldera, about 2 ka). The result of this evolution produced a high complex edifice made of a strato-cone and whose eastern flank hosts the Valle del Bove, a vast caldera depression formed during successive collapse events beginning during the late Trifoglietto stage and continuing through the Holocene (Behncket, 2001).

1.2 EFFECTS OF VOLCANIC EXPLOSIVE ACTIVITY

Mt. Etna lies on the densely inhabited Ionian coast and it is a classic example interaction between a volcano and its population. Among all negative effects, the volcanic ash emission represents one of the most important risks of Italy, influencing about 2 million of people, due to the high concentration of active volcanoes on territory. The explosive activity produces different volcanic products, named *pyroclastic rocks* and classified according to own grain size. In detail, three main categories can be distinguished: bomb (>64 mm), lapilli (64-2 mm) and ash (< 2 mm) (Schmid, 1981). However, the volcanic ash follows an additional division, distinguishing the fine volcanic ash (or also known as volcanic dust) with a grain size under 63 μm, regarded as the most dangerous for human health and for engine failure in jet aircraft. The grain size of pyroclastic particles strongly depends on the explosive power, translating in gas amount.

Pyroclastic particles are formed through bubble fragmentation when exsolution overpressures are generated in vesicles as magma rises rapidly to the surface (Sparks, 1978). The effects of a volcanic eruption can appear even at long distances (thousands of kilometres) thanks to wind action (Pyle et al., 2006). One of the most recent and impressive volcanic eruption in aviation history, causing widespread airport closures due to emissions dispersing through European airspace was the eruption of the Eyjafjallajökull volcano in April 2010 (Iceland). The ash dispersion is directly proportional with the particles grain size: decreasing the grain size increases the particles position into the plume, the time to reach that position and the distance from the eruptive centre. Indeed, particles less than 63 μm in diameter are transported in the dispersing cloud and remain suspended in the atmosphere for hours to days, or longer, until different km far away (Durant et al., 2010). Ash fallout can have several negative effects on population: to cause building collapse due to rapid accumulation and the high density of individual volcanic ash particles (Spence et al., 2005); aviation travels; water contamination (Stewart et al., 2006); human respiratory health hazards due to airborne ash and toxic gases (e.g. SO_2) in high concentrations or due to the presence of crystalline silica (e.g. cristobalite) and transition metals such as iron (Bardelli et al., 2020; Fubini & Fenoglio, 2007; Horwell & Baxter, 2006). In this scenario, a multidisciplinary research strategy, involving different fields (field and physical volcanology, atmospheric science, remote sensing, physics, chemistry, biology, and epidemiology) is needed to have a complete understanding of the impacts of pyroclastic particulates, especially derived by the finer ones.

1.3 LEGISLATION

Unfortunately, pyroclastic particles, once erupted, negativity effects the population. Therefore, following an eruption, clean-up measures in the urban environment are constantly adopted, firstly focusing on road system and the public areas for safety reasons (Hayes et al., 2015). Afterwards, in Italy, they are stocked in landfill, with huge areas occupation and costs, because considered waste materials. Indeed, they are classified as waste with code 200303 (Municipal waste) in the List of Wastes (LOW) Regulations, that transpose the European Waste Catalogue (EWC) into domestic legislation and provide codes for all hazardous and non–hazardous wastes (Contrafatto, 2017). However, in March 2014 following a significant eruption occurred in March 2013 in Mt. Etna, the waste code was temporarily modified in 17 05 04 (Soil and Rock – excavated), but, as a transitory and special measure in the territory. In this scenario, the reuse of this resource is still in discussion due to the absence of a clear and official normative reference and, especially, due to the lack of information about its applications as cement replacement or recycled aggregates in mortar and concrete production (Contrafatto, 2017). Moreover, the use of natural recycled aggregate is neglected also in the Italian standard, starting from NTC2008 to NTC2018 (Infrastrutture, 2008), mentioning only references for the use of construction and demolition wastes (CDW). The cleaning of public infrastructures is a delicate procedure because, inevitably, the cleaning machines influence the original particles. Therefore, they can be contaminated by the presence of other elements, including paper, rubber, metals, mud and oils, which are previously on the soil. Afterwards, they were stockpiled in disposal areas. Some of the foothill towns, such as Santa Venerina, have a civil protection plan for volcanic risk, which provides the collection and storage of waste in public spaces in temporary storage areas, which unfortunately remain definitive (Fig. 1.4).

Fig. 1.4 - Sampling in the storage area of Santa Venerina town.

1.4 WHAT IS GEOPOLYMER?

Until now, concrete industry is moving forward the developing of the world population, contributing for nearly 8% of the world's total carbon dioxide discharge into the environment. Most of CO_2 pollution is linked to the carbonation of calcium carbonate and clinker production (Provis & Bernal, 2014). Besides the increasing of environmental impact, the resistances at high temperatures and corrosion of the Portland cement has been questioned. Therefore, the interest to develop a new class of construction materials which are environmentally friendly, low-energy-consuming and cost-efficient, as well as the attention to a sustainable management of waste materials, increased exponentially in the last decades. In this scenario, alkali activated materials (AAMs) and geopolymers (GP) are good alternatives, enclosing all features requested by industrial community (Provis & Bernal, 2014). This class of solid materials is synthesised by the reaction of a finely milled aluminosilicate powder with alkaline solution. The alkaline process is dated back to a first patent awarded to Kühl in 1908 (Kühl, 1908), the research conducted by Purdon in the 1930s-1940s (Purdon, 1940), and the extensive program of research, development and commercial-scale promoted by Glukhovsky from the 1950s onwards (Glukhovsky, 1959) and continued by Krivenko from 1990s (Krivenko, 1994). In detail, the term "geopolymer", coined in the 1970s by Prof. Davidovits and patented in 1982 (Davidovits, 1982), represents a sub-part of AAMs class, limited to the use of aluminosilicate powder having low calcium content (e.g. fly ash type F or metakaolin) which look like an artificial rock, having better properties (mechanical properties, resistance against temperature, acid or external sulphate attack) than the traditional Portland cement (Duxson et al., 2007). Moreover, some authors define geopolymers as "ceramics" consolidated for alkaline reaction, thus "alkali bonded ceramics" and not for a sintering process (Gordon et al., 2006), obtaining chemical and physical properties similar to those of ceramic materials. These materials are based on an amorphous alumino-silicate network, made of tetrahedral units alternately linked by sharing oxygen atoms, whose chemical nomenclature, proposed by Davidovits has been established under the term poly(sialate), considering sialate an abbreviation of silico-oxo-aluminate (Davidovits, 1991) (Fig. 1.5). To balance the negative charge of tetrahedra, cations come from alkaline solutions, such as Na^+ or K^+, are present in framework cages (Davidovits, 1994; Duxson et al., 2007), leading to a final structure as that one proposed by Barbosa et al., (2000) (Fig. 1.6), corresponding to the following chemical formula:

$$M_n[-(SiO_2)_z - AlO_2]_n \cdot wH_2O$$

Where *z* is the Si/Al molar ratio, *M* the monovalent cation (i.e. alkaline element), *n* the degree of polymerisation and *w* the amount of bound water.

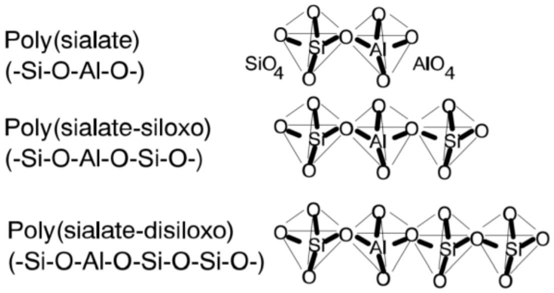

Fig. 1.5 - Geopolymer terminology proposed by Davidovits (Davidovits, 1991).

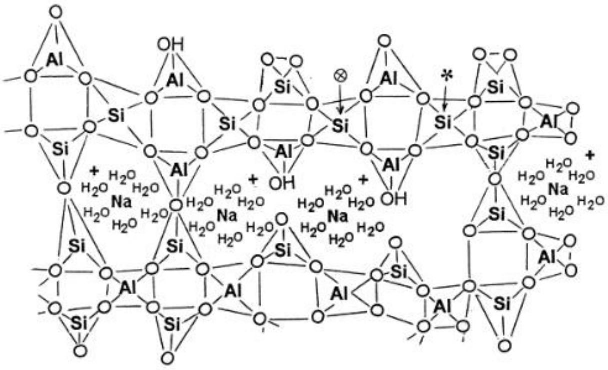

Fig. 1.6 - Semi-schematic structure for Na-polysialate polymer (Barbosa et al., 2000).

However, the geopolymerization process are not fully understood until now. This latter, proposed by Glukhovsky (1959) for the first time, was further developed by other scientists, outlining the transformation of aluminosilicate precursors into a synthetic gel. This model can be divided into three main reaction stages which occur rapidly making them of difficult distinguish (Palomo et al., 1999; Xu & Van Deventer, 2000):

- *Dissolution* of aluminosilicate source in high pH solution to form reactive precursor of silica and alumina hydroxyl group. However, the dissolution rate of the aluminium and silicon species depends on the amorphous nature of the precursor materials as well as the fineness of powder particles. Moreover, it increases linearly to the pH of the solution.

- Rearrangement of aluminosilicate structure to more stable states through *condensation*. In the early period of the process, the faster dissolution capability of aluminum, due to the weaker Al-O bonds than silicon produces a higher concentration of Al^{3+} ions forming the so called Gel 1 (Fernández-Jiménez et al. 2006; Provis et al., 2005). Afterwards, starting the dissolution of silica from the solid source, the development of new gel Si-rich, known as Gel 2, is induced (Fig. 1.7).
- *Polycondensation*: polymerisation in 3D polymeric chain and ring structure consisting of Si-O-Al-O bonds.

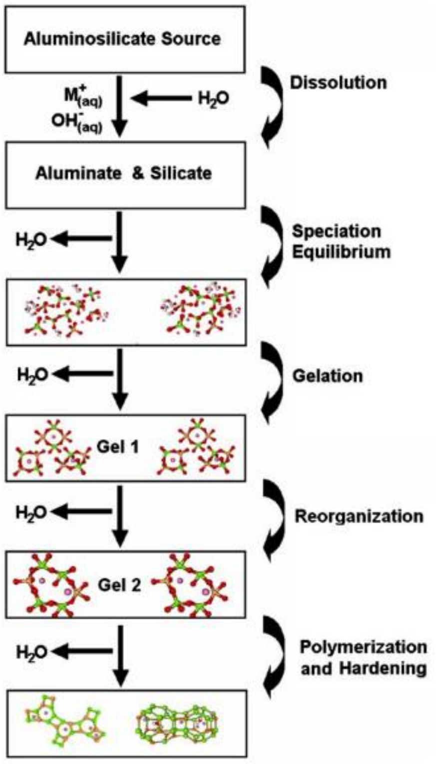

Fig. 1.7 - Sketch of geopolymer process considering the three main steps: dissolution, condensation and polycondensation (Duxson et al., 2007).

1.4.1 PRECURSORS AND ACTIVATORS

Different raw materials are considered suitable for geopolymer process, as long as they have an aluminosilicate composition (preferably the sum of silica and alumina higher 80%) which can be dissolved in alkaline environment (Fig. 1.8). Different typologies of sources were proposed in literature: volcanic ash, coal slag ash, granulated blast furnace slag, palm oil fuel ash, rice husk ash, fly ash and metakaolin. The latter is the most used for its high reactivity (Romisuhani et al., 2017), but, contemporary the most expensive due to the thermal treatment undergone. Therefore, scientists started to focus on natural (e.g. volcanic ash etc.) and industrial (e.g. ashes or slag etc.) waste materials to use as secondary raw materials with the aim to limit the environmental impact. However, considering the differences among all the precursors, a classification according own reactivity was proposed, as following: metakaolin > zeolite > slag > fly ash > pozzolanic material > kaolin (Panagiotopoulou et al., 2007).

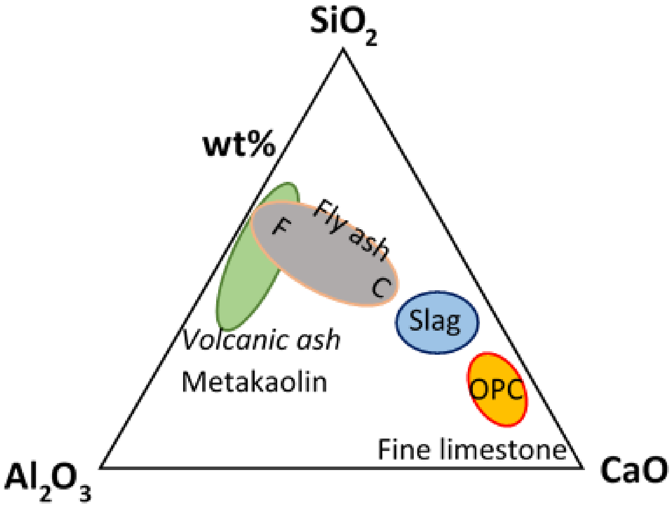

Fig. 1.8 - CaO-Al_2O_3-SiO_2 ternary diagram of cementitious materials. Abbreviation: OPC-Ordinary Portland Cement.

Generally, sodium and potassium hydroxides with/without silicates are the most used as activators in an alkali activation system. The combination between solution and raw material produces an exothermic reaction. Since the sodium cation (Na^+) is smaller than potassium one, the sodium solution promotes a better alkaline reaction because the cations can easily move in the network. Moreover, NaOH concentration is directly proportional to mechanical strength, increasing the concentration, the strength improves (Memon et al., 2013). Potassium hydroxide (KOH) has high reactivity with the aluminosilicate material and it influence the compressive strength and porosity. Rarely, sodium silicate (Na_2SO_3) is used as single activator because in combination with NaOH the activation power increases. Differently, potassium silicate can be used alone. However, alkaline hydroxides are more environmentally friendly and cheaper than silicates, especially for Na_2SiO_3, in terms of CO_2 emissions and cost production (Speight, 2002). The choice of reactants for the geopolymer process is a fundamental step because it influences the final properties of material. Indeed, their properties are highly depending of: Si/Al ratio, activator and its concentration, nature source and its grain size, water amount, mix design, hardening/curing time, synthesis temperature and calcium amount (Burduhos Nergis et al., 2018; Khan et al., 2014; Strydom & Swanepoel, 2002). According to this latter, two categories can be defined: high-calcium and low-calcium AAMs. In the first case, C-A-S-H (calcium aluminate silicate hydrate) gel, similar to C-S-H (calcium silicate hydrate) one, obtained during Portland cement hydration, is the main reaction product following of Ca-silicate source dissolution, whose Al contribution is taken in structure thanks to few alumina available released by precursor (Garcia-Lodeiro et al., 2011). Contrary, in the second system, N-A-S-H (or alkaline aluminosilicate hydrate) gel is produced by the dissolution of aluminosilicate precursors (e.g. metakaolin or type F fly ash), whose alkaline contributions are given by activation solution (Palomo et al., 1999) (Fig. 1.9). The amorphous structure and its chemical compositions make it comparable with synthetic zeolites (Duxson et al. 2007; Palomo et al. 1999; Provis et al., 2005).

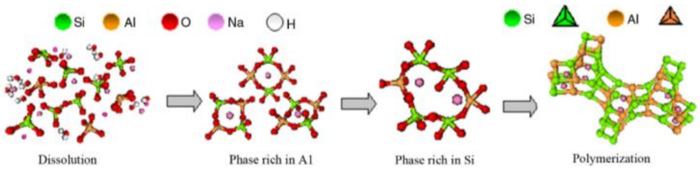

Fig. 1.9 - Detailed sketch of Model proposed for N-A-S-H gel formation (Duxson et al., 2007; Palomo et al., 2014)

1.4.2 GEOPOLYMERS VS OPC

Geopolymers have many advantages and better properties than ordinary Portland Cement (OPC). Firstly, the emission of CO_2 and energy consumption are very low, offering a strong reduction of the global warming by releasing just 169 kg CO_2/m^3 Vs 306 kg CO_2/m^3 of OPC for the same mechanical properties, representing a decrease of emission by 45% (Habert et al., 2011). Moreover, the possibility to use natural and industrial wastes represents a strong economic advantage. Indeed, huge fly ash deposits, generated by coal based thermal power plants, are widespread in the world and are considered a sustainable precursor for geopolymer synthesis. AAMs achieve good mechanical strengths already after one day of curing, comparable to those of OPC after 28 days of hardening (Hawa et al., 2013). Moreover, differently to OPC materials, they can be applied in different application fields, such as building materials (high-tech ceramics, thermal insulating foams, protective coatings, fireproof building materials and refractory materials (Barbosa & MacKenzie, 2003; Fernández-Jiménez et al., 2010; Kong et al., 2007; Rickard et al., 2013) and hazardous waste encapsulation (Shi & Fernández-Jiménez, 2006), guaranteeing high strength, low shrinkage, low carbon emission, acid resistance (Duxson et al., 2007; Komnitsas & Zaharaki, 2007), sulphates resistance (Bakharev, 2005b, 2005a); chloride resistance (e.g. sea water) (Zhang et al., 2010b, 2010a). Finally, the good performance and the high versatility are motivating the community to invest on these materials. However, the implementation of an industrial plant is not so easy due to the corrosive chemical substances involved in the process.

1.5 STATE OF ART ON GEOPOLYMERS BASED ON VOLCANIC MATERIALS

The high content of silica and alumina makes volcanic ash a suitable geo-resource for alkaline activation. However, the chemical-mineralogical heterogeneity strongly affects their reactivity, positively influenced by the amorphous phase, the fineness of the ashes and depending on the SiO_2/Al_2O_3 molar ratio of the amorphous fraction (Djon Li Ndjock et al., 2017; Lemougna et al., 2014). Different approaches were proposed in literature to overcome this limit of some volcanic ashes:

- *Heat treatment for calcination*: a calcination temperature range suitable for altering the reactivity was defined at 700 - 900 °C (Bondar et al., 2011b, 2011a). Indeed, the final properties of volcanic ash-based geopolymer pastes were positively influenced. This study demonstrated that the effectiveness of calcination depends on the LOI content and the amount of altered minerals (clay minerals), as well as this approach increases the compressive strength from 22.5 to 42.5 MPa after calcining at 700 °C (Bondar et al., 2011b).
- *Alkali fusion by calcination*: this approach was tested in presence of NaOH after 2 h and with a calcination temperature ranging at 550°C (Tchakoute et al., 2013).

In this scenario, the excess of sodium hydroxide, which has not taken part in the reaction, needs to be consumed by adding another aluminosilicate such as metakaolin with consequently increase of the cost. Other study demonstrates the influence of mixture volcanic ash/NaOH ratio varying Al_2O_3/Na_2O molar ratio from 0.77 to 0.06. Already at 550 °C for 1 h, the compressive strength significantly increases: the highest compressive strength of 41.5 MPa and lowest initial setting time of 15 min at 27 °C were achieved for molar ratio Al_2O_3/Na_2O of 0.13 (Tchakoute et al., 2013).

- *Mechanical activation* of volcanic ash, for different time up to 120 min using vibratory mill, has considerably changed the physico-mechanical properties of resulting geopolymer pastes. The initial setting time was reduced from more than 600 min for samples milled for 30 min to 15 min after 90 min of milling, corresponding to 95% of reduction. Moreover, also the compressive strength benefited of this treatments: for 0-30 min of milling was negligible reaching 29-54 MPa after 60-120 min of milling time (Djobo et al., 2016).
- *Mineral additives:* metakaolin represents one of the most natural additive used in binary mixture to consume the excess of alkali presented in the system once activated the precursors and to enhance setting time, linear shrinkage, and compressive strength (Barone et al., 2020; Djobo et al., 2014; Finocchiaro et al., 2020; Robayo-salazar et al., 2016; Tchakoute et al., 2013). Bauxite and calcined oyster shell, respectively, as source of Al and Ca were used in combination to volcanic ash evidencing: a decrease of linear shrinkage for any percentage of addition and the initial setting time with addition of calcined oyster shell or up to 20% mass of bauxite; trivial increase of 28-day compressive due to the higher crystallinity of mineral additives, which, for a certain amount, became detrimental for the reaction (Djobo et al. 2016a). Instead, the GGBF (Ground-granulated blast-furnace) slag, tested as industrial additive by some authors, could be used only in the range 5-25% of weight to appreciate slight increase of 28-day compressive strength (Allahverdi et al., 2011).

To sum-up, the calcination mostly affects the clay mineral contents, while the mechanical activation produces structural changes to all minerals (Balczár et al., 2016). Therefore, this latter could be more advisable to enhance powder’s reactivity as well as the setting time to allow the application also in masonry works. Moreover, the reactivity is not depending on the type and dosage of alkaline activators (Djobo et al., 2017). However, this limitation can be easily overcame using natural additive as metakaolin in few quantities, benefiting of high physical performance. Among the peculiar features of volcanic ash-based geopolymer products, the stability at heating represents one of the most appreciated, retaining about 60% of their initial compressive strength with low firing shrinking up to 900 °C (Djobo et al., 2017).

1.6 HISTORICAL USES OF VOLCANIC ROCKS AND PARTICLES

Since ancient times, pyroclastic materials (pumice, scoria, and ashes) have been widely used in architecture and ceramic field: i) production of highly durable cements with pozzolanic features during the imperial roman age (27 BC–AD 476), whose heritage are still well conserved still now (e.g. Villa San Marco in Naples bay) (Belfiore et al., 2015; Izzo et al., 2016); ii) use of volcanic ash in the production of ancient ceramic materials (Cabadas-Báez et al., 2017; Morra et al., 2013). The main advantages to use volcanic rocks or ashes in cement and concreate production are linked to an improvement of resistance to sulphate/chlorides and alkali silica reaction due to pore refinement (ACI Committee, 2001) and a reduction of clinker production and associated CO_2 emissions (Scrivener et al., 2018).

Even now, volcanic particles represent the major natural pozzolanic materials in use, thanks to widespread availability of volcanic rocks worldwide (Fig. 1.10). Most of these deposits are in areas of Cenozoic volcanic activity. However, not all volcanic rocks are suitable as pozzolanic material. This latter is defined according to the reaction ability with calcium hydroxide to form hydraulic compounds in the presence of water (i.e. C-S-H product). Pyroclastic materials, generated by the rapid quenching during a volcanic explosion, such as ashes or pumices show higher pozzolanic activity due to their higher glass content and highly porous structure (Walker & Pavía, 2011). The eruption type largely depends on the magma viscosity which is related to the “acidity”, provided for example by SiO_2 content of the magma. Generally, more siliceous magma produces more explosive activities and products with better pozzolanic properties (Snellings et al., 2012).

Fig. 1.10 – Global distribution of natural pozzolana deposits (grey areas) (Snellings et al., 2012).

The mineralogy of unaltered pyroclastic rocks is mainly influenced by the presence of phenocrystals and volcanic aluminosilicate glass usually present in quantities ranging between 45 and 75% wt., whose chemical composition can differ slightly from the bulk composition of origin magma. Generally, a basaltic glass has a lower pozzolanic activity then the more acid glasses (Akman et al., 1992; Mielenz et al., 1950).

The close relationship between architecture and raw materials provided by geology of a territory is well-known (Prentice, 1990). This is particularly evident in the area of Catania, where since prehistoric times the rocks coming from Mt. Etna eruptive activity have been used in building (Andreozzi, 2003; Mazzoleni, 2007; Barone and Mazzoleni, 2012). The most important activities of the last centuries, which strongly devastated the Cultural-historical Heritage, was the 1669's eruption, that produced between 0.5 to 1 km^3 of lava, covering a surface of 37 km^2, and about 0.25 km^3 of pyroclastic deposits (Branca et al., 2013) (Fig. 1.11). Few years later, the disastrous 1693 earthquake affecting eastern Sicily, produced over 60.000 victims and total destruction of several villages and towns in the districts of Siracusa, Ragusa, and Catania (Piatanesi and Tinti, 1998). The combination of these catastrophic events caused the beginning of the rebuilding of Catania old town with volcanic local materials as aggregates to produce mortars and building elements, such as eruptive rock blocks. The use of these materials represents a common feature typical of Baroque Sicilian architecture that for its importance is included in the list of UNESCO World Heritage Sites.

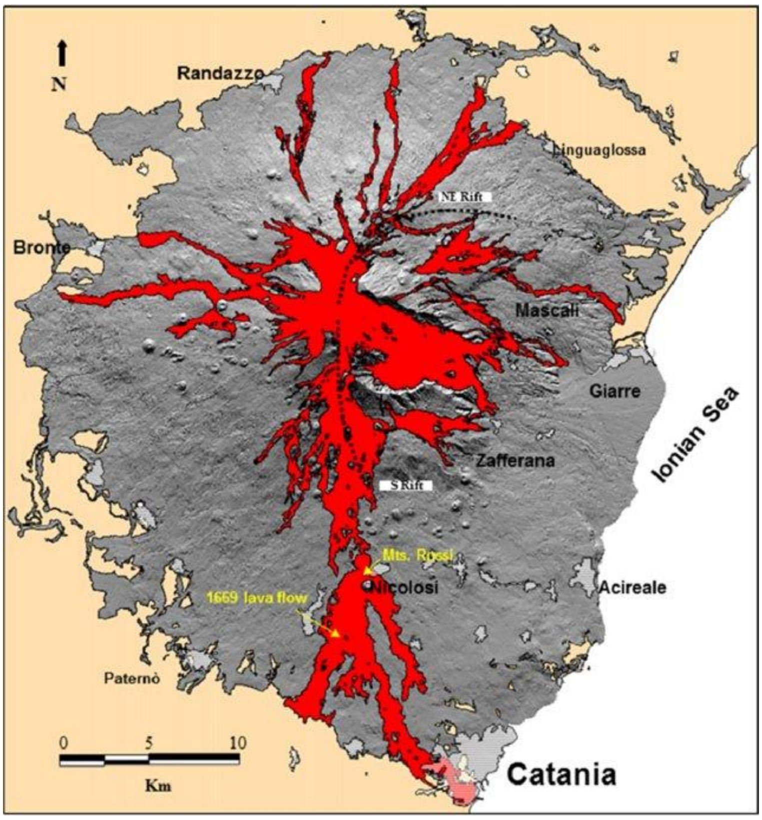

Fig. 1.11 – Etna map showing the main lava fields erupted from 1669 to 2002, focusing on 1669's eruption at Mts. Rossi. The dashed segments indicate the position of the S Rift and the NE Rift (Bonaccorso et al., 2016).

In particular, mortars and plasters, used in many important monuments, are characterized by a peculiar dark grey colour but, especially in the nearby of Catania town, it is common the use of mortars with brick-red colour. These latter are produced with the use of the so-called "*ghiara*". This material is a paleo-soils characterized by a reddish hue due its high iron content combined with the high temperatures (800-900°C) and oxidising conditions reached in contact with the overlying lava flow (Fig. 1.12a). Generally, layer of "ghiara'' paleo-soils has thickness ranging from few centimetres to about 1 m, and are macroscopically heterogeneous, since its aspect reproduces the origin of the sediments involved by the overflowing lava, deriving from epiclastic or pyroclastic deposits (Belfiore et al., 2010). The grain size of these paleo-soils is variable, but the ghiara deposits used as mortars aggregates are formed by prevailing sandy-silty granulometric fraction (Fig. 1.12b). Its volcanic origin is a peculiar feature of the Etnean area and it is found nowhere else in the world. Indeed, this material was extracted for long time in different anthropic cavities (tunnels also several kilometres long), located in Etnean territory, so taking advantages of the several lava field around the volcanic flanks, to be used as aggregate in Catania architecture in XVII-XVIII centuries in the mortars and plasters production thanks to is high pozzolanic behaviour (Fig. 1.13). However, ghiara genesis is still in discussion, even if it seems to be influenced by the brittle behaviour of lava flow, the presence of gas and meteoric water. In detail, during the cooling down of lava flow, fractures take place and the meteoric water penetrates inside the lava flow and soil, bringing in depth gas elements kept by the fresh rocks through a leaching process. Exclusively this model can explain the considerable thick of soil involved in this transformation process. On the other hand, the firing temperature can "cook" only few centimetres and not meters, as well as in the quarries were found.

Historically, mortar based on ghiara are mixtures of lime and ghiara in the ratio from 1:4 to 1:3 with water content enough to reach the optimal plasticity and workability. In the second half of XIX century, due to the minor amount of lime, it replaced the dark grey mortar based on lime and old Mt. Etna pyroclastic products or crushed basalts locally named *"azolo"* (Sciuto Patti, 1896; Battiato, 1988; Mazzoleni, 2007). Furthermore, the results of uniaxial test obtained on samples of mortar based on lime with both volcanic materials used as aggregate, showed that one with ghiara have a strength 30-50% higher than that with azolo (Battiato, 1988). However, at the beginning of the twentieth century, the ghiara-based mortars were no longer produced due to the difficulties in finding the raw materials and the development of new industrial productions.

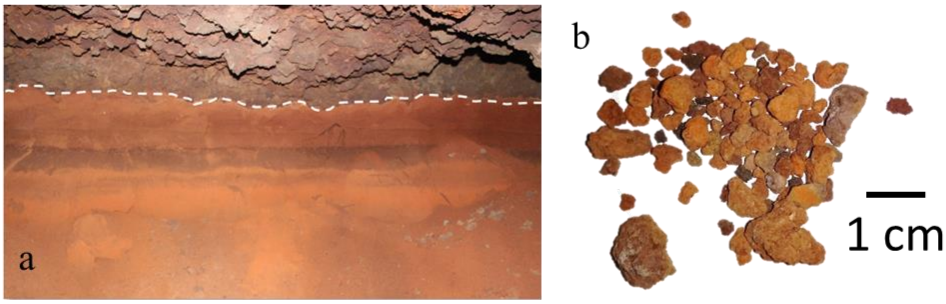

Fig. 1.12 – a) example of ghiara quarry (Mt. Etna, Italy): the white dashed line divides the ancient volcanic soil with the 1408 lava flow; b) ghiara particles with different grain size.

Fig. 1.13 – Example of ancient applications: a) Detachment of historical mortar based on ghiara; b) Original plaster application in San Salvatore church in Viagrande, Catania, Italy.

Different type of mortars are used in architecture and each one needs specific conservation and recovery requirements fund on: good durability, adequate aesthetic aspect and less invasivity towards the recovery subject (ISCARSAH, 2003). Therefore, the development of a recovery mortar has to consider, firstly, the compatibility with contact materials, satisfying compositional, physical and mechanical aspects. Indeed, a recovery mortar should have a good adhesion with the substrate, high resistance to acid attacks (e.g. acid rains), similar total porosity to the original material with micro pores able to support the micro circulation of water and a lower mechanical strength than the recovery material. A wide classification of mortars, depending on the type of recovery to perform, exists, for: masonry, plasters, application of flooring, decorations, pointing and sealing works. Geopolymers represent a valid alternative as sustainable recovery mortar thanks to own high-tech features. Until now, few test regarding recovery interventions with alkaline activated binders are reported in literature: fixing of detached parts both in stone and terracotta materials and substitutions of deteriorating parts (Clausi, et al., 2016a; Clausi et al., 2016b; Geraldes et al., 2016; Hanzlíček et al., 2009).

Therefore, this thesis aims to test for the first time pyroclastic deposits came from Mt. Etna volcano through alkaline synthesis to produce alkaline binders and mortars to apply in recovery interventions of local Cultural Heritage, maintaining thus the recovery requirements according to recovery recommendations (ISCARSAH, 2003), in addition to a sustainable management of a waste natural material (i.e. volcanic ash).

2. MATERIALS

In this chapter, we focus our attention on reactants used for alkaline activation process: on one hand volcanic raw materials of Mt. Etna as precursors and on the other hand the alkaline solutions used as activators. In detail, the sampling phase of pyroclastic deposits, chemical-mineralogical characterization and morphologies results were discussed in addition to the release of heavy metals and their thermal behaviour.

2.1 VOLCANIC PRECURSORS: SAMPLING

Taken into account pyroclastic particles classification of Schmid (1981), in this thesis, we indicate with the term volcanic ash both categories of lapilli and ashes. The volcanic ashes were sampled in a landfill near the Santa Venerina town (in the south-east slope of Mt. Etna volcano; Fig. 2.1) after the 16/03/2013 eruption (Fig. 2.2a), which produced huge amount of pyroclastic materials. Moreover, they are considered as recent and not influenced by important chemical-mineralogical modifications and thus usable for our aims. The dimensional sorting of the particles of the pyroclastic deposits was low ranging from 2 cm to 0.1 mm. Special care was taken to prevent the contamination of the volcanic material with other natural (e.g., dust or ash from previous eruptions) or anthropic particulates. Anyway, a cleaning step was performed to easily remove organic particles (Fig. 2.2b)

Ghiara samples were collected in the “Orcio” quarry, located in the district of Trecastagni village (in the south slope of Mt. Etna). It is one of the largest anthropic cavities of Etnean area, mainly used in ancient time for the extraction of this red paleo-soils. The deposit has a variable thick (1.20 -1.60 m) and is characterized by a grain size between 2 mm and 0.5 mm. Ghiara colour changes from yellowish hue near the contact with the lava roof, to brick-reddish hue in deposit core. Once the moisture has dried and removed after a drying at 105°C into the oven (Fig. 2.2c), both materials were dry milled (Fig. 2.2d) and sieved to obtain a grain size < 75 μm (Fig. 2.2e-f), considered suitable for the alkali activation process (Lancellotti et al., 2013).

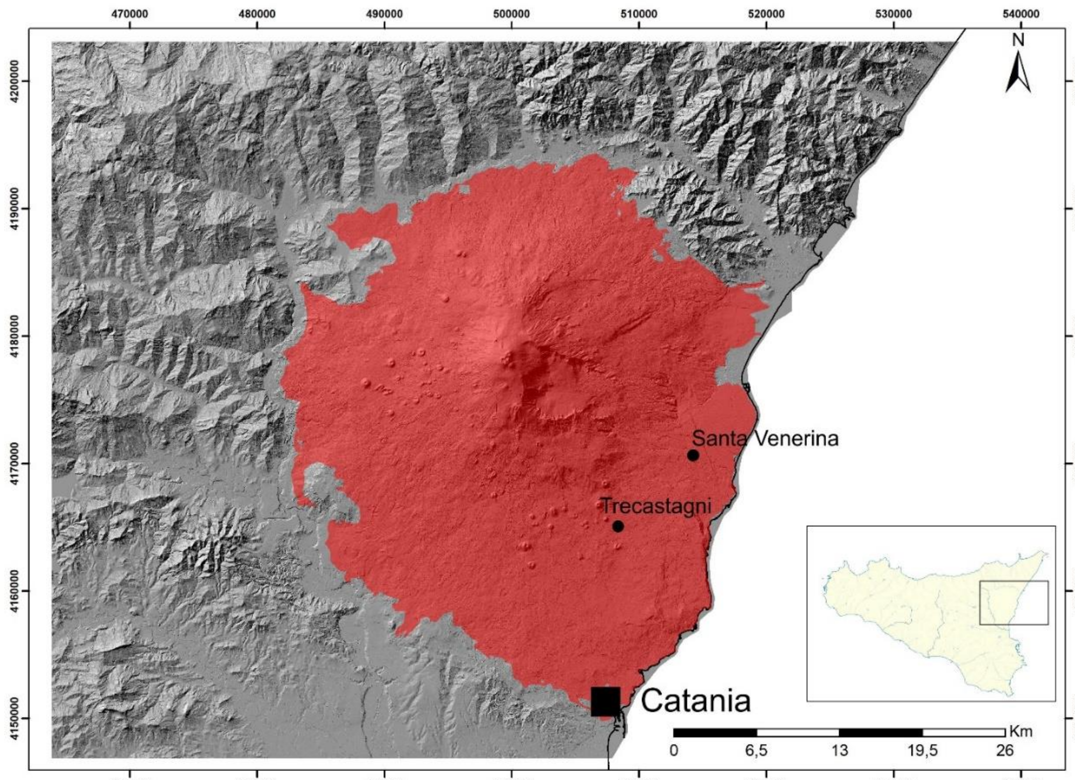

Fig. 2.1 – Digital elevation model (DEM) map of Mt. Etna volcano (Sicily, Italy): volcanic building in red.

Fig. 2.2– Sampling and treatments of raw materials: a) sampling of volcanic ash in Santa Venerina landfill; b) cleaning step with distilled water; c) drying step into oven; d) press machine

for milling; e) sieves used: 250 μm, 125 μm, 75 μm; f) final powder < 75 μm to be used for alkaline process.

2.2 METAKAOLIN

Metakaolin is a de-hydroxylated form of the clay mineral kaolinite with 4-, 5-, and 6-coordinated aluminium ions in alumina polyhedron sheet structures (i.e. metakaolinite), produced by the calcination of kaolin, normally, at a temperature range of 600-800 °C (Duxson et al., 2007). It is considered the most suitable precursor for geopolymer production due to its reactivity and the excellent properties of the final geopolymer pastes (Clausi et al., 2016; Duxson et al., 2007; Siddique & Klaus, 2009). It is characterized by: high specific area, good absorbability and strong coordinative bonds when stimulated (Cheng et al., 2012). These features make the MK-based geopolymer a material with high level of resistance to different acids and salt solutions ranges, low shrinkage and low thermal conductivity (Duxson et al., 2007; Palomo et al., 1999). In my project, a metakaolin, provided by IMERYS company (France) already milled, was used as additive component in small amount in addition to the volcanic mixture. Its commercially name is ARGICAL™ M1000, whose chemical composition provided by producer is: SiO_2 =55%; Al_2O_3 = 40%, Fe_2O_3 = 1.4%; TiO_2 = 1.5%; Na_2O + K_2O = 0.8%; CaO + MgO = 0.3%; LOI =1%.

2.3 ACTIVATORS

For each formulation, activated using Na-solution, a mix of sodium hydroxide and sodium silicate was used. Generally, sodium hydroxide with a concentration of 8M (mol/L) was used for almost all tests and sometimes that one with 12M was tested but with bad results, excluding so additional test. Regarding silicates, two types of sodium silicates were used in this thesis with different SiO_2/Na_2O ratio: a pure sodium silicate, provided by Carlo Erba company (code: 373908), with ratio SiO_2/Na_2O = 2 and a liquid sodium silicate, provided by Ingessil s.r.l. with a molar ratio SiO_2/Na_2O = 3. The pure sodium silicate in solid state was opportunely dissolved in distillate water and mixed in a hotplate at a temperature of 100°C until to reach a transparent solution, meaning the totally dissolving of silicate.

2.4 CHARACTERIZATION METHODS FOR VOLCANIC RAW MATERIALS

Pyroclastic particles of volcanic ash and ghiara, once reduced to fine powders, were analysed from different point of views: chemical and mineralogical investigations using respectively, XRD with Rietveld method and XRF analysis at the Department of Biological, Geological and Environmental Sciences of Catania University; FT-IR spectroscopy by KBr method on the natural samples at room temperature and those thermically treated respectively at 200°, 300° and 400°C with the aim to determine structural modifications at increasing temperature, as well as TGA-DTA analysis to evaluate the thermal behaviour of the raw materials, both performed at Limoges University, during my abroad period; Raman spectroscopy as complementary technique to FTIR; morphological and structural analysis using SEM of Physics and Astronomy Department of Catania University. All measurement setting of each equipment used are listed below.

2.4.1 X-RAY POWER DIFFRACTION (XRD)

Siemens D5000 diffractometer was used for diffractometric analysis, with Cu Kα radiation and Ni filter, in the 2θ range 3-70°, using a step size of 0.02°, a counting time of 5s for step, divergence and anti-scatter slit of 1° and receiving slit of 0.2 mm. The quantitative data were obtained with Rietveld method using GSASII software (Toby and Von Dreele, 2013). The amorphous abundance was calculated by means of internal corundum standard addition (Gualtieri and Zanni, 1998).

2.4.2 X-RAY FLUORESCENCE (XRF)

X ray fluorescence spectroscopy (XRF) analyses were carried out using a PHILIPS PW2404 spectrometer on powder-pressed pellets; total loss on ignition (LOI) was gravimetrically estimated after overnight heating at 950°C. The quantitative analysis was carried out using a calibration line based on 45 international rocks standards. The limits of detection (LOD) were: SiO_2 = 1 wt%, TiO_2 = 0.01 wt%, Al_2O_3 = 0.1 wt%, Fe_2O_3 = 0.05 wt%, MnO = 0.01 wt%, MgO = 0.02 wt%, CaO = 0.05 wt%, Na_2O = 0.01 wt%, K_2O = 0.05 wt%, P_2O_5 = 0.01. The precision was monitored by routinely running a well-investigated in-house standard (obsidian). The average relative standard deviations (RSD) were less than 5%. Finally, the accuracy was evaluated using an international standard that is compositionally similar to the analysed samples. The accuracy was good for major elements (<3%), except MnO. In detail, five XRF measurements for major and trace elements on both volcanic powders were performed, whose final results were obtained from their average.

2.4.3 FOURIER-TRANSFORM INFRARED SPECTROSCOPY (FT-IR)

Infrared analyses were performed using a Thermo Fisher Scientific 380 infrared spectrometer (Nicolet) of IRCER lab (Limoges-France). Briefly, pellets were prepared by mixing 1 mg of powdered sample with 150 mg of KBr. The mixture was then compressed with a manual press applying 6 metric-tons of force. For each sample three pellets were prepared to have a good statistical redundancy. All spectra were recorded between 4000 and 400 cm^{-1} with a spectra resolution of 4 cm^{-1}. For comparison reasons, the spectra were baseline-corrected and normalized (Gharzouni et al., 2016) and treated in absorbance. The OMNIC software was used for data acquisition and spectral analysis.

2.4.4 THERMOGRAVIMETRIC ANALYSIS (TGA)

Thermogravimetric analysis (TGA) analyses were performed using an SDT-Q600 apparatus of Thermal Analyzer of IRCER lab (Limoges-France) in an atmosphere of flowing dry air (100mL/min). The signal was measured with Pt/Pt-10% Rh thermocouples. The volcanic powders were heated at 1350°C with a rate of 5°C/min in alumina crucibles under air.

2.4.5 RAMAN SPECTROSCOPY

Raman spectroscopy was executed using a Raman Jasco NRS-3100 apparatus equipped by a microscope with x5, x10, x20, x50 and x100 objectives. Spectra were collected using as setting measurement a green laser with excitation source at 532 nm, 6 cycles of accumulation of 5 minutes and the x50 objective. Laser power was controlled by means of a series of density filter, to avoid heating effects. In detail, for ghiara measurements no filter was used due to the high presence of hematite, differently for volcanic ash samples whose iron oxides could be strongly influenced, risking thus to modify the real mineralogical phases (Faria, 1997). For this latter, an optical density (OD) filter was set to 1 with the aim to keep the laser power below 1 mW and to allow a fair signal/noise ratio. The depth resolution was set to a few micrometers by means of a confocal hole. The spectroscopic techniques (i.e. FTIR and Raman) were used to analyse both raw materials and geopolymers in order to evidence structural modifications after geopolymerization process. However, these latter were better evidenced with FTIR method than RAMAN one.

2.4.6 SCANNING ELECTRON MICROSCOPE (SEM)

Morphological investigations were carried out on both volcanic particles, characterized by original irregular shape, using a Gemini Field Emission SEM (FE-SEM) Carl Zeiss SUPRA 25, equipped with an EDAX EDX detector. Data were collected using a voltage of 20 kV and different magnification according the interest of spot analysis. The analysis surfaces were covered with a thin layer of gold to prevent charging of the specimen and to increase signal to noise ratio.

2.5 RESULTS

2.5.1 XRF: CHEMICAL COMPOSITION

The averages of five measurements regarding the major elements of volcanic materials are plotted in Fig. 2.3 and listed in in Table 2.1, whose values are expressed in weight percentage. Moreover, considering the importance of the amorphous content (volcanic glass) of precursors for the alkaline activation process, its chemical composition was reported as by literature (Barone et al., 2016) in Table 2.1 and Fig. 2.3. The chemical compositions of both raw materials are quite similar but ghiara has a higher Al_2O_3 abundance and a lower CaO than volcanic ashes. The molar ratios of the major elements, regarding volcanic materials and metakaolin used as precursors in alkaline activation, were calculated and presented in Table 2.2. Volcanic precursors show higher Si/Al molar ratio than metakaolin (2.54, 2.17 and 1.17 for volcanic ash, ghiara and metakaolin respectively). Volcanic materials are also richer in iron, magnesium and calcium elements compared to metakaolin.

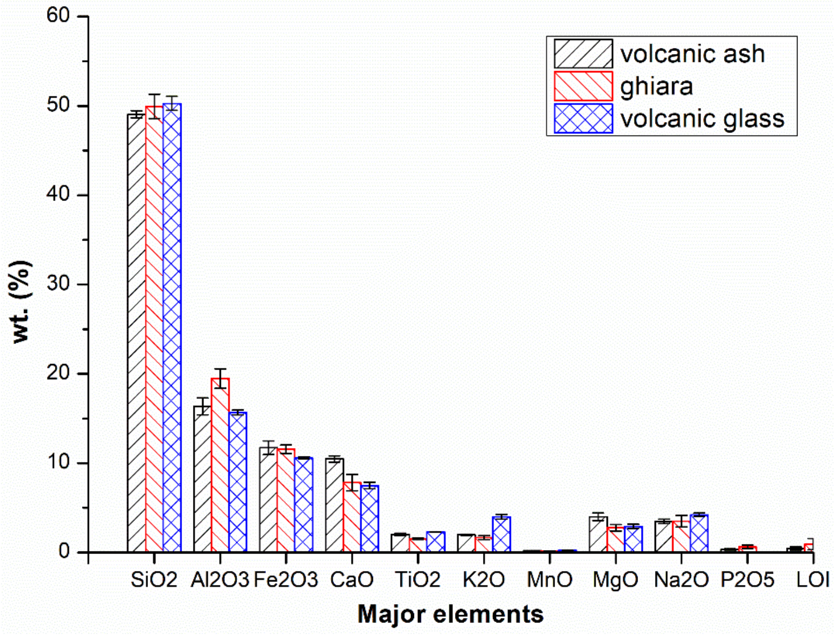

Fig. 2.3 - Histogram graph of major elements (including standard deviation).

Table 2.1 - Major elements of volcanic raw materials (XRF) and volcanic glass (SEM-EDS), this latter analysed by Barone et al., 2016. The abundances are expressed as weight % of oxides.

	Volcanic ash		**Ghiara**		**Volcanic glass**	
	Average	*Sd.*	*Average*	*Sd.*	*Average*	*Sd.*
SiO_2	49.05	0.4	49.95	1.36	50.27	0.79
Al_2O_3	16.36	0.95	19.47	1.11	15.67	0.25
Fe_2O_3	11.73	0.76	11.58	0.47	10.59	0.13
CaO	10.47	0.35	7.82	0.91	7.49	0.37
TiO_2	2	0.14	1.54	0.1	2.28	0.04
K2O	1.96	0.1	1.66	0.22	4.01	0.28
MnO	0.2	0.01	0.16	0.01	0.23	0.02
MgO	3.98	0.42	2.76	0.38	2.93	0.24
Na_2O	3.48	0.24	3.49	0.66	4.22	0.19
P_2O_5	0.35	0.07	0.63	0.2	-	-
LOI	0.44	0.17	0.93	0.64	-	-
SiO_2/Al_2O_3 (molar ratio)	5.11	0.31	4.37	0.29	5.44	0.05
$SiO_2+Al_2O_3$	65.4	0.58	69.42	1.67	65.94	0.95

Table 2.2 – Chemical molar ratio of raw materials (volcanic ash, ghiara raw and metakaolin) used as precursors in alkaline activation.

Ratios	***Volcanic ash raw***	***Ghiara raw***	***Metakaolin***
Si/Al	2.54	2.17	1.17
Si/Fe	5.56	5.50	52.21

Si/Mg	8.27	11.90	-
Si/Ca	4.37	5.90	-
Fe/Al	0.46	0.40	0.02
Mg/Al	0.31	0.18	-
Ca/Al	0.31	0.37	-
LOI	0.44	0.49	1

2.5.2 XRD: MINERALOGICAL COMPOSITION

The mineral phases were also determined, as well as quantitative analysis using Rietveld method, whose results are reported in Table 2.3, while the references/labels are anorthite (An), amcsd 0001287 (Angel, Carpenter, & Finger, 1990); anorthoclase (Ano), code 9000855 (Harlow, 1982); augite (Aug), code 1000035 (Clark & Appleman, 1969); forsterite (Fo), amcsd 0000886 (Nord, Annersten, & Filippidis, 1982); hematite (Hem), amcsd 0002228 (Gualtieri & Venturelli, 1999); goethite (Gt), amcsd 0002226 (Gualtieri & Venturelli, 1999); amorphous (Amorp). In general, they showed more than 50% of amorphous phase (volcanic glass), in particular in volcanic ash, value reached almost 75%, so perfectly suitable to be used in alkali synthesis. Moreover, volcanic ash evidenced the typical mineralogical phases of Mt. Etna basaltic rocks, such as calcium plagioclase, pyroxene and olivine (± magnetite) (Fig. 2.4), as also reported by Barone et al., 2016; Corsaro and Métrich, 2016, while ghiara paleo-soil highlighted, in addition to the aforementioned phases, iron oxides and hydroxides (goethite and hematite) and, in some cases, calcite (Fig. 2.4). Instead, quartz, anatase and muscovite were recorded in metakaolin (Fig. 2.4). Therefore, chemical and mineralogical composition of Mt. Etna lavas are similar to other volcanic rocks used in literature for geopolymer productions, make them suitable for alkaline activation (Djobo et al., 2017; Tchakoute Kouamo et al., 2013).

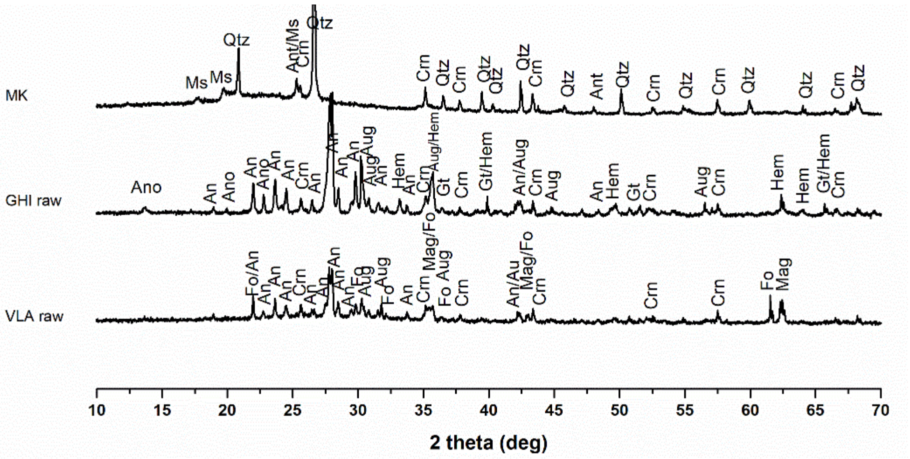

Fig. 2.4– Diffractometric patterns of volcanic raw materials (VLA raw, GHI raw) and metakaolin (MK). Legenda: An: anorthite; Ano: anorthoclase; Aug: Augite; Fo: forsterite; Mag: magnetite; Hem: hematite; Gt: goethite; Qtz: quartz; Ms: muscovite; Ant: anatase; Crn: corundum.

Table 2.3 – Mineralogical results obtained by XRD analysis with Rietveld Method.

% Weight	**An**	**Ano**	**Aug**	**Fo**	**Hem**	**Gt**	**Amorp**
Volcanic ash	*12.4*	–	*12.5*	*0.7*	–	–	*74.5*
Ghiara	*23.3*	*11.8*	*9.1*	–	*1.9*	*0.1*	*53.8*

2.5.3 FTIR (KBR METHOD)

Infrared analyses were performed on volcanic ash and ghiara samples at IRCER lab of Limoges. Furthermore, the same materials were analysed after thermal treatments at 200, 300 and 400°C using a tubular furnace (Fig. 2.5) to evaluate the reactivity of the powder at temperature increasing in terms of structural modifications. In general, volcanic ash's samples showed affinities (Fig. 2.6a): presence of water content at ~ 3450 and 1625 cm^{-1} respectively due to ν O-H and δ H-O-H features and aluminosilicate contributions at ~755 cm^{-1} (ν Si-O), ~620 cm^{-1} (νs Si-O-Si), ~570 cm^{-1} (ν SiO4), ~540 cm^{-1} (δ Si-O-Al), ~465 cm^{-1} (ρ Si-O-Si). However, a slight shift from 1000 cm^{-1} to 975 cm^{-1} in the sample treated at 400°C, corresponding to νs Si-O-Si (Al), and an increase of water content were recorded, evidencing, thus, a structural modification occurred after 400°C. Contrary, in ghiara's samples, no changes were evidenced: the main band centred at ~1000 cm^{-1} evidences a further contribution at ~1130 cm^{-1} position, corresponding to ν Al-O or Si-O; in addition to others peaks located at: ~760 cm^{-1} (ν Si-O), ~620 cm^{-1} (νs Si-O-Si), ~580 cm^{-1} (ν SiO_4), ~540 cm^{-1} (δ Si-O-Al) and ~465 cm^{-1} (ρ Si-O-Si), corresponding to aluminosilicate structure. Therefore, infrared results have evidenced affinities between both volcanic materials, whose contributions are linked to the presence of aluminosilicates species in the range of 1200-400 cm^{-1} as reported in Table 2.4. In detail, this range can be sum-up in: 757, 580, and 545 cm^{-1} related to the ring vibrations of Si–O bonds of silicate network (Tchadjié et al., 2016); the peak at 472 cm^{-1} corresponding to the vibration of Si–O–Fe bond (Tchakouté et al., 2015); while the main band relating to the vibration of SiO/Al–O bond of aluminosilicate framework.

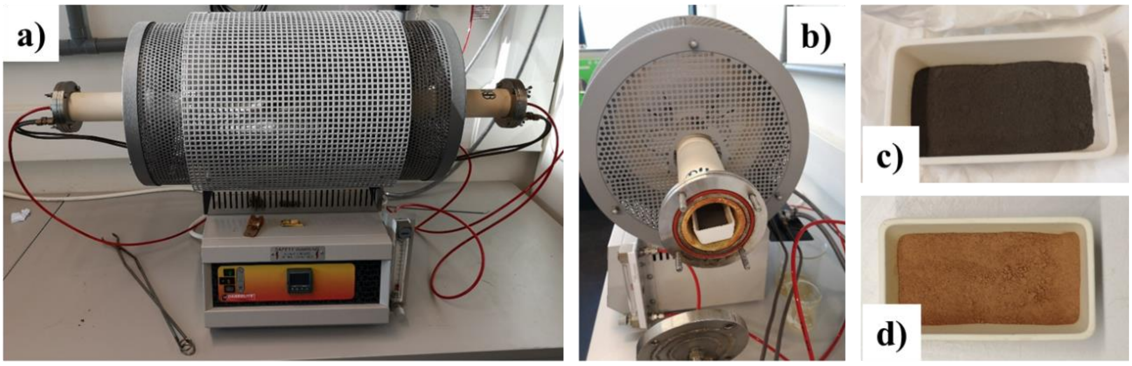

Fig. 2.5 – a) tubular furnace used for thermically treated the volcanic precursors; b) entrance of furnace; c) little ceramic rectangular bowl with volcanic ash after treatment; d) little ceramic rectangular bowl with ghiara after treatment.

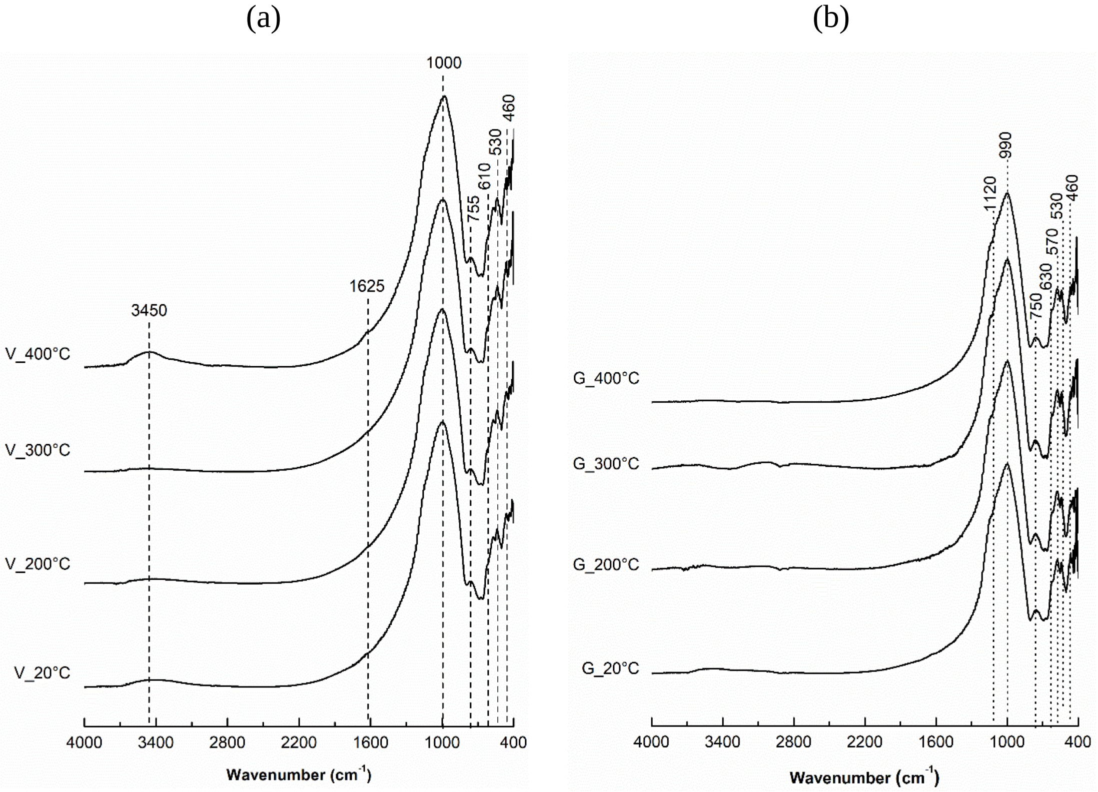
(a) (b)

Fig. 2.6 – Overlapping absorbance FTIR spectra of volcanic raw materials (room temperature and thermically treated at 200, 300 and 400°C) in the range 4000-400 cm^{-1}. (a) volcanic ash (V) and (b) ghiara (G) raw materials.

Table 2.4 - Summary of main IR attributions in the range 1200-400 cm^{-1} of volcanic ash's samples (V) and ghiara's samples (G).

	Samples:				
	V_20°C	*V_200°C*	*V_300°C*	*V_400°C*	**Assignments:**
Aluminosilicate: wavenumber range (400-1200 cm^{-1})	464	466	469	465	*ρ Si-O-Si or ν Si-O or Si–O–Fe*
	540	539	540	542	*δ Si-O-Al or ν Si-O*
	572	572	571	574	*ν SiO4*
	620	620	619	624	*νs Si-O-Si*
	762	764	757	757	*ν Si-O or ν Al^4-O-Si*
	998	1005	1002	975	*νs Si-O-Si (Al) or ν Si-O*
	G_20°C	*G_200°C*	*G_300°C*	*G_400°C*	**Assignments:**
Aluminosilicate: wavenumber range (400-1200 cm^{-1})	464	471	468	469	*ρ Si-O-Si or ν Si-O or Si–O–Fe*
	541	542	541	539	*δ Si-O-Al or ν Si-O*
	582	579	579	580	*ν SiO4*
	618	619	624	621	*νs Si-O-Si*
	756	760	761	761	*ν Si-O or ν Al^4-O-Si*
	999	1000	1001	1003	*νs Si-O-Si (Al) or ν Si-O*
	1133	1134	1133	1135	*ν Al-O as Si (TO4)*

2.5.4 RAMAN SPECTROSCOPY

Raman analysis were carried out on pyroclastic samples and on powders with a x50 objective. For each typology, ten measurements were performed in order to analyse different sample's areas, to obtain a complete characterization and a redundancy of results. Indeed, in each figure, only three Raman spectra are considered representative of all measurements. The spectra were compared with those of some standard minerals, detected by XRD analysis, and downloaded by rruff dataset: anorthite, augite, forsterite, hematite and magnetite. The results of volcanic ash evidenced a rather intense fluorescence (especially the measurements on pyroclastic sample "pr"), but with the overlapping of all representative spectra, different peaks has been observed (Fig. 2.7). Indeed, two mineralogical phases were well detected: augite (325, 388, 660, 815, 928 and

1002 cm^{-1}) and anorthite in the region 400-600 cm^{-1}. Fig. 2.8 shows the micrographs of spot analyses for each spectrum selected.

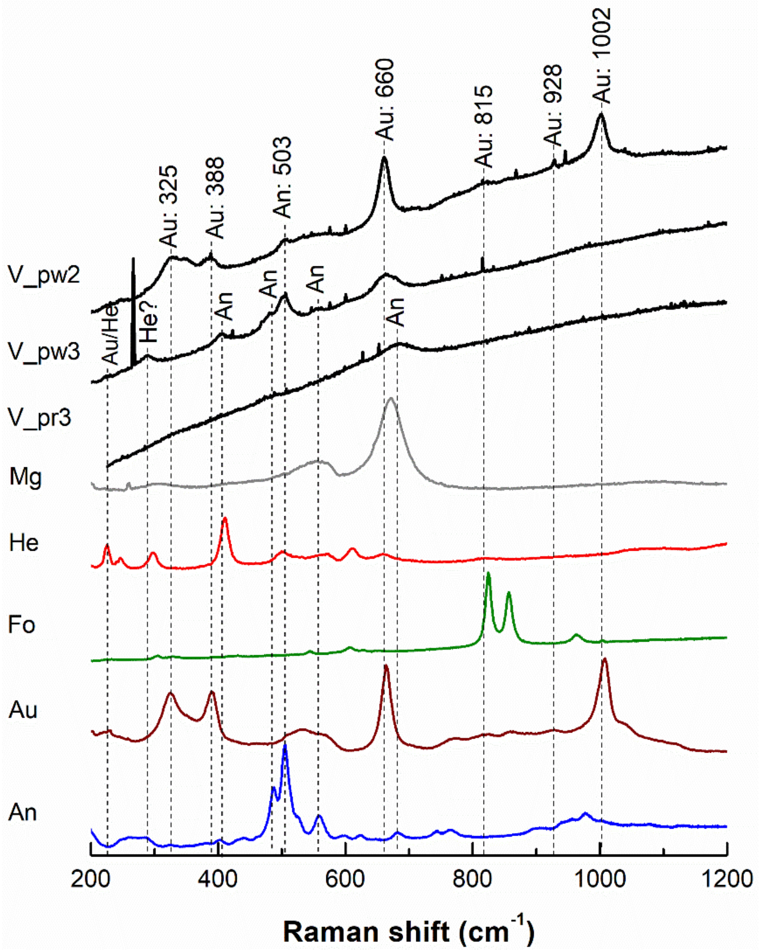

Fig. 2.7 - Overlapping of Raman spectra of volcanic ash samples (V) and standard mineral (downloaded by rruff database). Legenda: pyroclastite (pr); powder (pw); anorthite (An); augite (Au); forsterite (Fo); hematite (He); magnetite (Mg).

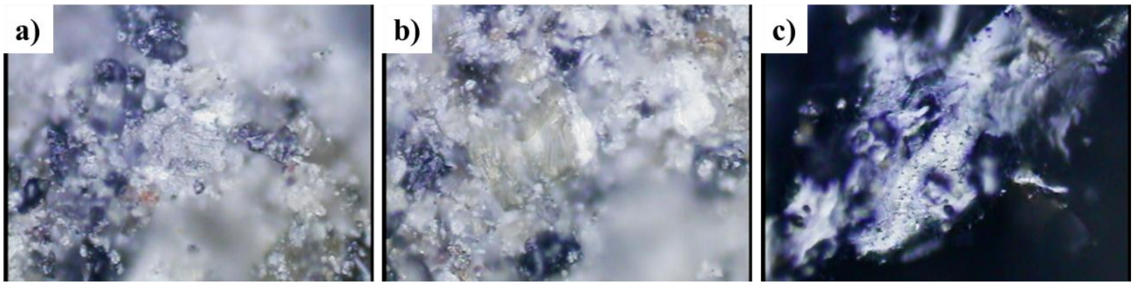

Fig. 2.8 - Micrographs of Raman spot analyses for the following samples: a) V_pw2 (powder); b) V_pw3 (powder); c) V_pr3 (pyroclastite).

Instead, ghiara samples have evidenced a lower fluorescence phenomenon then volcanic ash in favour to more complex spectra with many peaks. Indeed, anorthite, augite, forsterite (825 and 858 cm^{-1}) and hematite (223, 245, 290, 408 and 609 cm^{-1}) with different contributions were mainly observed (Fig. 2.9). Therefore, the measurement setting chosen for both specimens was able to define the main mineralogical compositions, which are generally of difficult detection due to the high fluorescence typical of amorphous with few crystalline amount materials. Fig. 2.10 shows the micrographs of spot analyses for each spectrum selected.

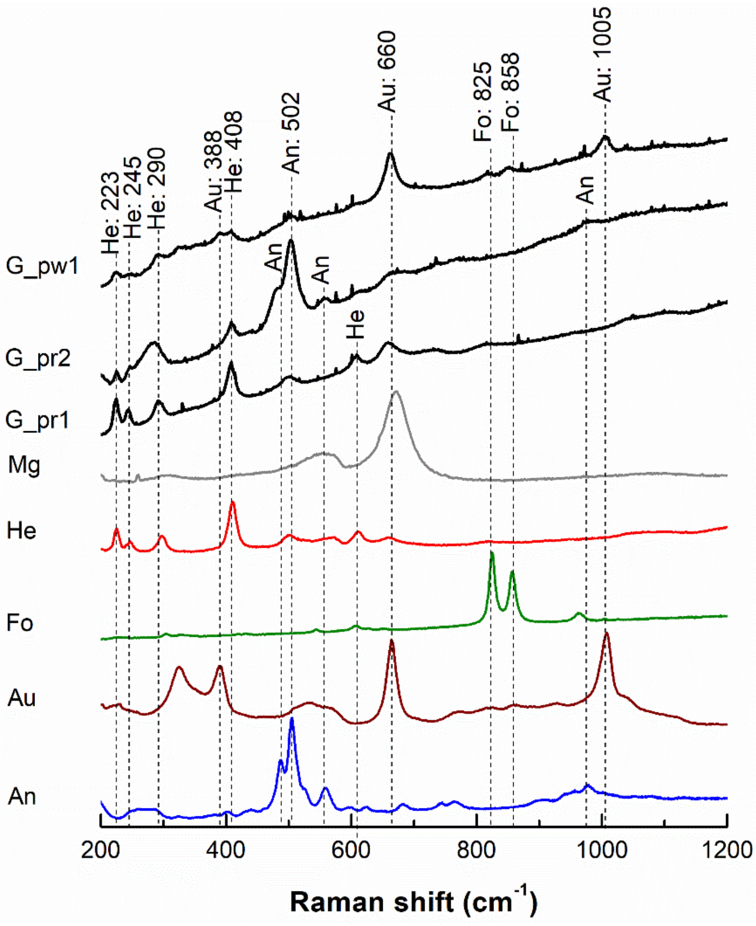

Fig. 2.9 - Overlapping of Raman spectra of ghiara samples (G) and standard mineral (downloaded by rruff database). Legenda: pyroclastite (pr); powder (pw); anorthite (An); augite (Au); forsterite (Fo); hematite (He); magnetite (Mg).

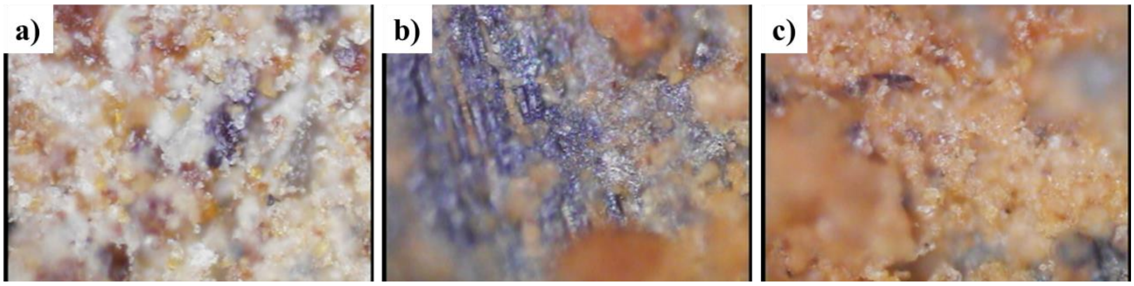

Fig. 2.10 - Micrographs of Raman spot analyses for the following samples: a) G_pw1 (powder); b) G_pr2 (pyroclastite); c) G_pr1 (pyroclastite).

2.5.5 TGA: THERMAL ANALYSIS

Thermal analysis (DTA -TGA) were carried out on raw materials, at IRCER lab of Limoges, with the aim to know their behaviour under high temperature. The obtained thermal curves of volcanic precursors are showed in Fig. 2.11. Both volcanic materials showed a very low weight loss about 0.5% until 200°C corresponding to the elimination of physically adsorbed water. Afterwards, the main weight loss was recorded at 500°C (1%) for volcanic ash (Fig. 2.11a), whereas at 1100°C (1%), ending point of analysis, for ghiara (Fig. 2.11b) following a possible release of silica hydroxyl groups (Si (OH_4))(Gharzouni et al., 2015). These low values are in accordance with literature for volcanic materials (Alraddadi, 2020; Djobo et al., 2016). The ghiara's behaviour can be explained by the natural phenomena of oxidation undergone during its formation at high temperature, for which ghiara shows a *"temperature memory"* such as to require higher temperature before structural modifications occurrence. However, the volcanic ash showed an increase of weight at 550°, 800° and 1200°C (this latter very evident) due to the oxidation phenomenon of iron being in iron oxide phases (e.g. magnetite) according to the measurement setting in air flow (Chen, 2013) or it might include allotropic transformation of iron oxides (Leonelli et al., 2007).

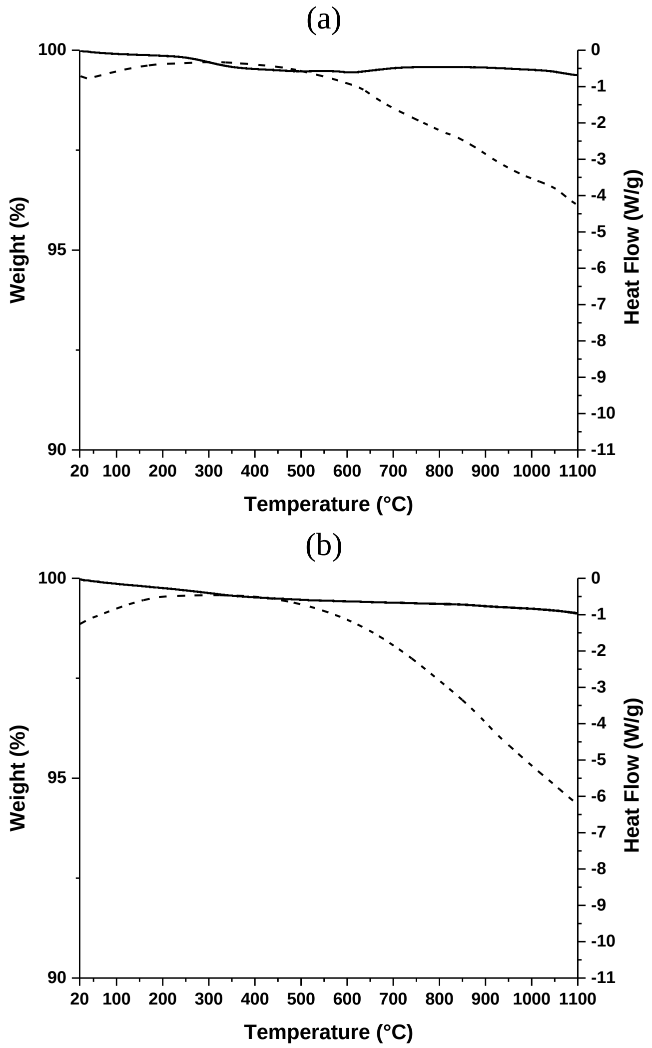

Fig. 2.11 – Thermal analysis curves of weight loss (—) and heat flow (---) for (a) volcanic ash and (b) ghiara raw materials.

2.5.6 SEM-EDX: MORPHOLOGICAL AND EDX ANALYSIS

Morphological analyses were performed on some pyroclastic particles of both raw materials. For volcanic ash, particles sampled at Santa Venerina area after the 16/03/2016 eruption was chosen. Vesicular structure with macro-porous and also pores of hundreds of microns size with sub spherical shape were evidenced (Fig. 2.12a-b), demonstrating the gas exsolution inside the lava sherds during the ascent into the plume. The semi quantitative analysis, performed by means EDX, showed the typical chemical composition of a volcanic particle (i.e. glass), corresponding mainly in an aluminosilicate composition with contributions of other elements: Na, Mg, Ca and Fe (spot analysis “a” in Fig. 2.12b). The particles of ghiara have evidenced a clear porous structure with sub spherical pores of micrometric order size (Fig. 2.13a-b). The EDX analyses confirmed the high iron content typical of this paleo-soil (spot analysis “a” in Fig. 2.13b) differently to the “fresh” volcanic deposits which have not undergone physical modifications due to oxidating conditions. However, an aluminosilicate composition with contributions of other elements have been observed.

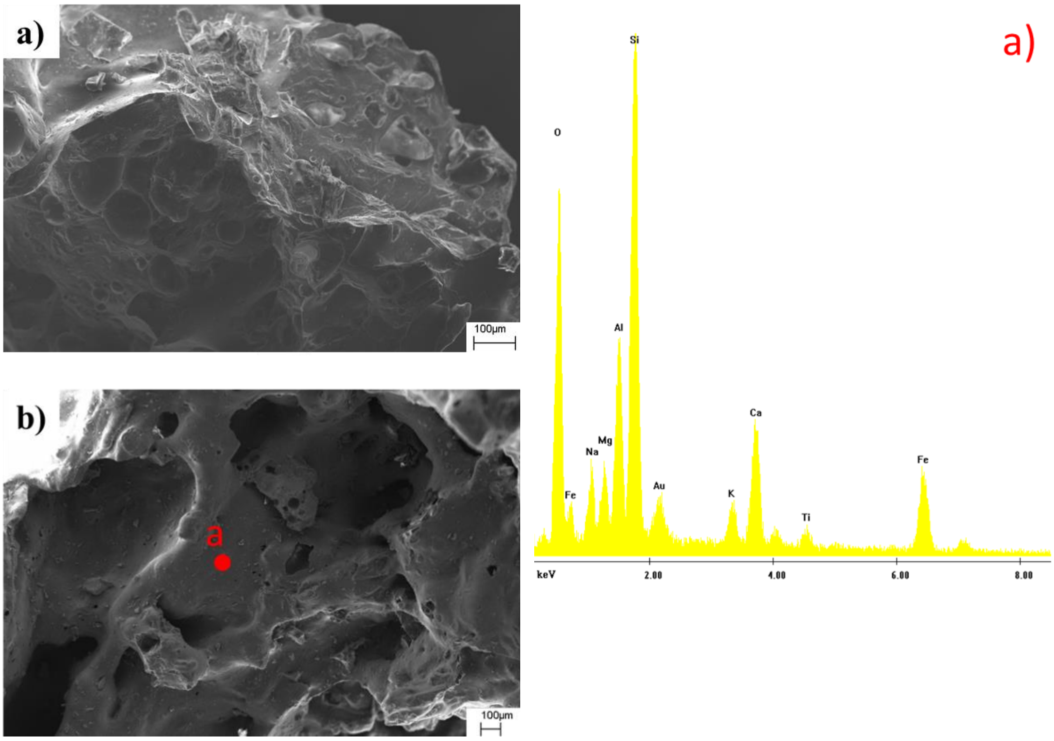

Fig. 2.12 – Morphological photos of volcanic ash: a) porous structure (magnification 300x); b) general preview of structure particle with magnification 145x and spot analysis (a) with corresponding histogram of EDX analysis.

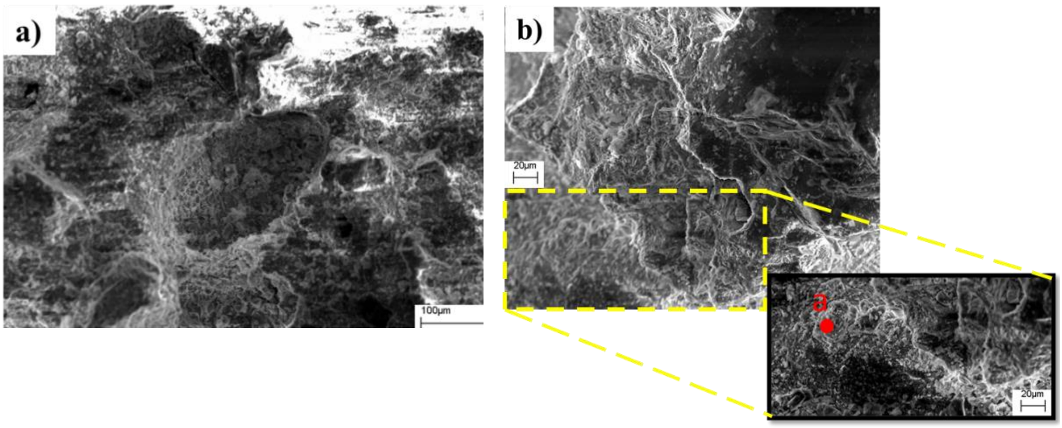

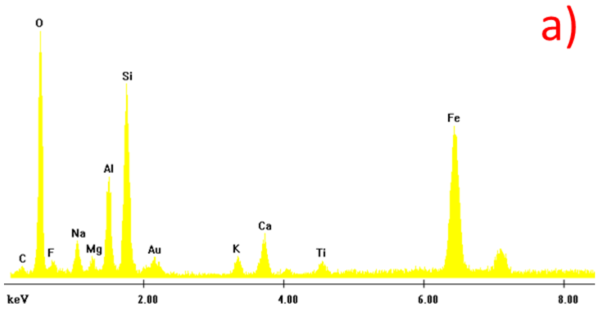

Fig. 2.13 – Morphological photos of ghiara particles at different magnifications: a) porous structure (500x); b) 1Kx and spot analysis (a) with corresponding histogram of EDX analysis.

3. GEOPOLYMERIZATION PROCESS

This chapter wants to explain the development of alkaline activation approaches used during the educational path, not forgetting the will to valorise pyroclastic deposits of Mt. Etna volcano, limiting at minimum the environmental impact in terms of energy and emissions and to scale up the optimum geopolymeric process found at industrial scale. Volcanic precursor is one of the most suitable aluminosilicate source for AAMs production thanks to high amorphous content generated by the rapid quenching during a volcanic explosion which prevail on crystallinity grade, as well as different oxides contents compared to SiO_2/Al_2O_3 (Djobo et al., 2017b; Lemougna et al., 2018; Tchakoute et al., 2013a). However, its reactivity is strongly depending on mineralogical and chemical composition, particle size distribution and especially the amount of amorphous phase. Indeed, it is direct proportional to amorphous content, the fineness of powder and SiO_2/Al_2O_3 molar ratio of the amorphous fraction, which should be below 4 (Djon Li Ndjock et al., 2017; Lemougna et al., 2014). However, the volcanic materials considered in this thesis have an higher SiO_2/Al_2O_3 molar ratio, reaching 5.11 and 4.37 for volcanic ash and ghiara respectively (Table 2.1).

The general approach has foreseen the use of twenty-five grams of the volcanic materials powders with < 75 µm grain size (Fig. 3.1a), which were mixed, manually with spatula or mechanically with a mixer, with different alkali solutions to obtain a highly viscous paste (Fig. 3.1b-d), which was slip cast in a cylinder plastic moulds and vibrated for 1 minute to remove air bubbles (Fig. 3.1e). The specimens were covered for 24h with a thin polymer film to maintain a constant level of moisture (Fig. 3.1f), then, they were air exposed to complete alkali synthesis at room temperature (25±3°C). Initially, the main aim is to activate exclusively the pyroclastic powders as precursors to produce 100% volcanic binders, using a sodium solution made of sodium hydroxide (8M) and sodium silicate, but not achieving at room temperature the expected results in a prefixed time window (i.e. within a week).

In detail, the test known as known as *integrity test* failed. Generally, the good success of each formulation was evaluated on the basis of the results of this test performed after 7 and/or 28 days of curing with the aim to obtain an immediate feedback on the chemical stability in water and preliminary strengths to manually stress (Lancellotti et al., 2013). The test consisted in the immersion in water of a sample shard with a solid/liquid ratio of 1/10. After 24h, the integrity of sample was evaluated in terms of dimension and surface conditions as well as change of color water. The defining characteristic of a geopolymer is that the alkali aluminosilicate gel is extremely resistant to dissolution in water (Mackenzie, 2003; Rees et al., 2007).

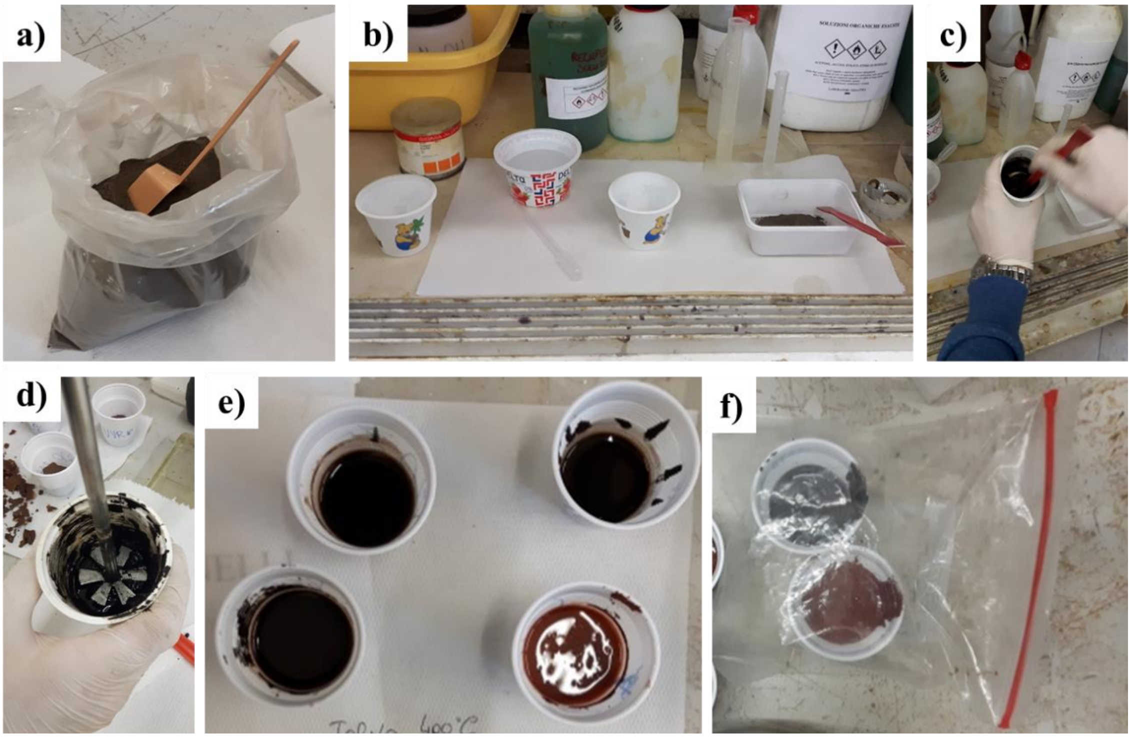

Fig. 3.1 – Reactants mixing step: a) precursor: volcanic ash powder; b) reactants properly weighted before to be mixed; c) manually mixing with spatula; d) mechanically mixing with electrical mixer; e) filling of moulds; f) covering of samples through thin polymer film.

Considering the outcomes of these test and the development of my educational path, different approaches were tested with the aim to find the best formulation approach for geopolymeric binders:

1. Thermal treatments at different temperatures on geopolymeric pastes after few activation days were performed to reduce the long setting time.
2. Use of small metakaolin amount as additive component (whose chemical molar ratio were reported in Table 2.2) in order to limit the energy use and the environmental impact. In detail, two series for each volcanic precursor were created mixing two different sodium silicates characterized by different SiO_2/Na_2O molar ratios and used in different proportions in combination with NaOH.
3. Thermal treatments on volcanic powders before to be mixed with the sodium activating solution.

4. *Mechanosynthesis* (i.e. mechanical mixing during activation among precursors and activators) with the aim to enhance the reactivity of these volcanic materials in alkaline environment without the use of metakaolin.

In this scenario, hundreds of formulation's tests were carried out.

3.1 THERMAL TREATMENTS OF THE SLURRY

The curing time of geopolymeric slurry, obtained by the mixing of only volcanic precursors with the alkaline solution, was very long and slow. The setting time is strongly influenced by SiO_2/Al_2O_3 and liquid/solid ratios (Ling et al., 2019). The high stability of volcanic glass in alkaline environment is the reason of this behaviour, contrary to those of the more reactive precursors such as metakaolin and fly ashes. Indeed, the consistency of some samples, prepared with 100 wt. % of volcanic precursor, was not enough after 48 hours to perform and/or to pass the integrity test, supposing an incomplete alkali activation. Indeed, the integrity test, performed on geopolymers based on only volcanic precursors, showed partial or total dissolution of sample and consequently water turbidity, suggesting an incomplete reaction. (Fig. 3.2a-c). Thermal treatments represent an interesting solution for low reactivity materials, such as volcanic ones (Bondar et al., 2011; Kamseu et al., 2009; Kani & Allahverdi, 2009; Robayo-salazar & Gutiérrez, 2018). Moreover, their effects were directly correlated to the mechanical behaviour (Kamseu et al., 2009). Therefore, thermal curing into oven, at 100°C for 48 hours and 400°C for 12 hours (using pots respectively in Teflon and ceramic), were performed on slurries based on volcanic precursors to complete the reaction and to achieve a good hardness in few time (Fig. 3.2d-f). In detail, one formulation using volcanic ash (VLA1) and four formulations of ghiara (GHI1-4) were produced due to the numerous results reported in literature for thermal treatment of AAMs based on volcanic ash (e.g. Kamseu et al., 2009), contrary to totally lack of data on alkali synthesis with ghiara. All details of these formulations are reported in Table 3.1. Therefore, the volcanic deposits, used as activators, require thermal treatments to complete the alkaline activation in low setting time and to influence positively the properties of final products, as evidenced also by literature (e.g. Kamseu et al., 2009; Leonelli et al., 2010).

Table 3.1 – Labels, ratios among activators and curing setting. Legenda: volcanic ash (V); ghiara (G). The horizontal straight-line divides above the samples activated using the Na_2SiO_3 with SiO_2/Na_2O ratio=3, and below those with SiO_2/Na_2O ratio=2.

	NaOH wt. %	**Na_2SiO_3 wt. %**	**Water (ml)**	**Curing Temp./Time**
VLA1_100	*30*	*70*	−	*100°C (48h)*
VLA1_400	*30*	*70*	−	*400 °C (12h)*
GHI4_100	*50*	*50*	−	*100°C (48h)*
GHI4_400	*50*	*50*	−	*400 °C (12h)*
GHI1_100	*23*	*77*	*2*	*100°C (24h)*
GHI1_400	*23*	*77*	*2*	*400 °C (8h)*
GHI2_100	*50*	*50*	*1.5*	*100°C (24h)*
GHI2_400	*50*	*50*	*1.5*	*400 °C (8h)*
GHI3_100	*50*	*50*	−	*100°C (24h)*
GHI3_400	*50*	*50*	−	*400 °C (8h)*

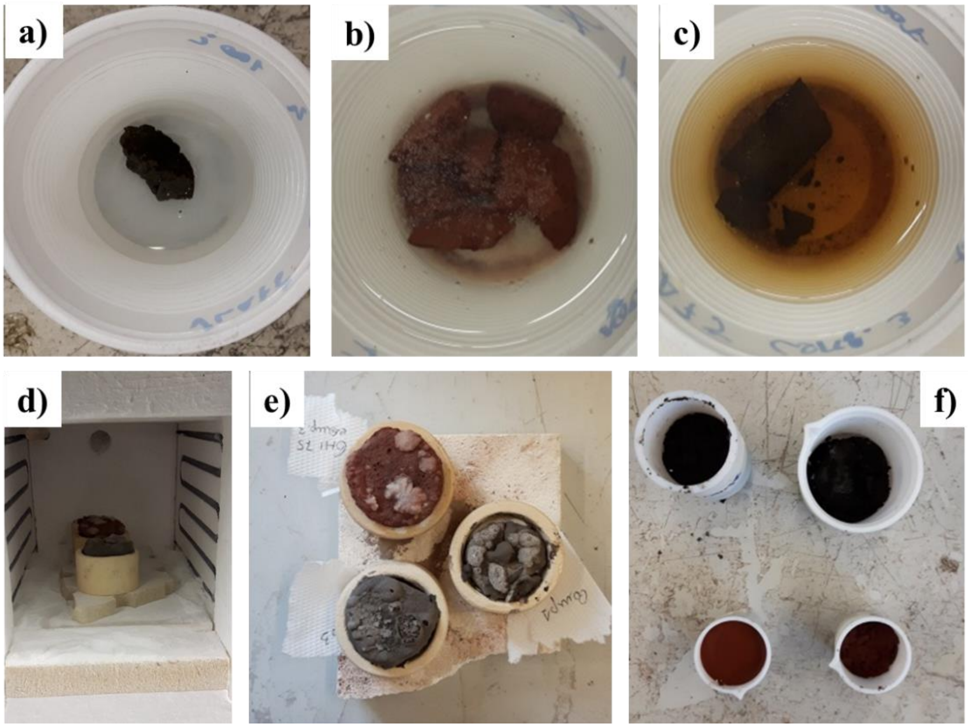

Fig. 3.2 – Integrity test observations and consequently thermal treatments: a) example of good stability in water; b) example of partial dissolving; c) example of interaction between sample and water, changing colour of water; d) thermal treatments at 400°C into oven; e) samples treated at 400°C once removed by oven; f) samples treated at 100°C once removed by oven.

3.1.1 INTEGRITY TEST RESULTS

VLA1 sample treated at 400°C was chemically stable, while the sample at 100°C did not pass the integrity test. Instead, all ghiara samples have already reached a good stability and stiffness at 100°C (after 48 h), even though impurities observed in water suggest a not complete activation. This demonstrates the efficiency of thermal treatment in enhancing the reactivity of the precursors powder and the potentiality of alkali activation of volcanic deposits, even if the treatment at 100-400°C is not a realistic solution to be used in-situ applications, so they weren't further performed in my experiments.

3.2 ADDITION OF METAKAOLIN ON TOTAL WEIGHT OF THE MATRIX

With the aim to avoid thermal treatments and thus to reduce environmental impact in terms of energy and emission, geopolymers with small amount (% wt.) of metakaolin addition to the total volcanic powder were prepared. In this scenario, the reactivity of the system has increased, while the setting time has decreased, allowing an alkaline activation at room temperature thanks to the additive function provided by metakaolin. Regarding to these formulations, a methodological approach, slight different to the general one, was considered: preparation of the precursors, sieving step of the powders to well homogenise the matrix and avoid the formation of metakaolin clumps (Fig. 3.3a-b) (or mixing of the powders in porcelain mortar), addition of alkaline solution and mixing with mechanical mixer (Fig. 3.3c), filling in moulds (Fig. 3.3d) and vibration to remove micro air bubbles; covering with plastic films for 24h to maintain the humidity and following exposition to air; removal of specimens once obtained consolidation after 24/36 hours from the moulds (Fig. 3.3e); rectification surfaces.

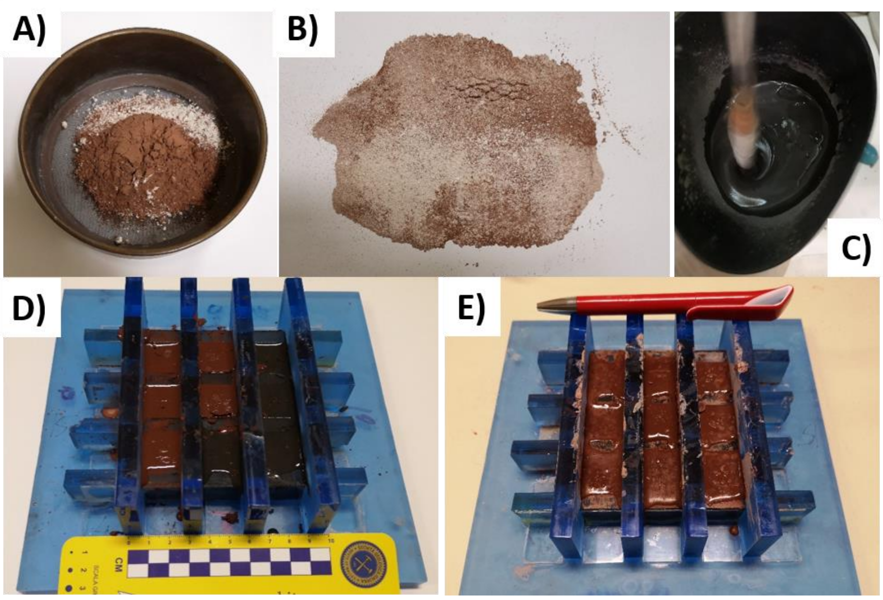

Fig. 3.3 – Summary of the main steps for AAMs production with MK addition. A) mixing of ghiara and metakaolin and use of a sieve to homogenise; B) result after the sieving step; C) mixing with alkaline solution and mechanical mixer; D) fill of cubic moulds with the fresh slurry; E) after 24/36h of consolidation and before to unmould.

In detail, for each volcanic precursor, two series with a progressive increase of metakaolin from 5% to 25% on total weight of the volcanic powder were produced: on one hand, a pure sodium silicate, provided by Carlo Erba company (code: 373908) with ratio $SiO_2/Na_2O = 2$ was used, whose samples are labelled *VM1-5/25%* and *GM1-5/25%*, while, on the other hand, a liquid sodium silicate, provided by Ingessil s.r.l. with a molar ratio $SiO_2/Na_2O = 3$, was used, whose details are presented in Chapters 5.1 and 6.1. The reason of use these different silicates is entirely due to the development of my project and the availability of reactants: at the beginning, I used the pure sodium silicate with SiO_2/Na_2O = 2 molar ratio, while, after half of my path (including the abroad experience), that one with SiO_2/Na_2O = 3. However, in this chapter and following ones (excluding the chapters regarding the insights), the samples belong to the series VM1-5/25% and GM1-5/25%, where sodium silicate with SiO_2/Na_2O = 2 was used. In detail, different $NaOH/Na_2SiO_3$% ratios were used (Table 3.2) in order to investigate the best conditions to avoid efflorescence on samples' surface after air exposition, as well as "green formulations" with 20% wt. of metakaolin (labelled VM1-20LS and GM1-20LS) were produced with the aim to reduce at minimum the use of silicate, reaching low setting time but higher viscosity.

Table 3.2 – Labels, ratios among activators and curing setting. Legenda: volcanic ash (V); ghiara (G) and metakaolin (M).

	***NaOH* wt. %**	***Na_2SiO_3* wt. %**	***Water* (ml)**	***Metakaolin* wt. %**	***Curing* Temp./Time**
VM 1 -05	*23*	*77*	–	*5*	*25°C*
VM 1 -10	*23*	*77*	–	*10*	*25°C*
VM 1 -15	*23*	*77*	–	*15*	*25°C*
VM 1 -20	*23*	*77*	–	*20*	*25°C*
VM 1 -25	*23*	*77*	–	*25*	*25°C*
VM1-20LS	*30*	*70*	–	*20*	*25°C*
VM5-20	*10*	*90*	*4*	*20*	*25°C*
VMT2-10	*10*	*90*	–	*10*	*25°C*
VMT1-20	*40*	*60*	–	*20*	*25°C*
VMT3-15	*40*	*60*	–	*15*	*25°C*
VMX-20	*50*	*50*	–	*20*	*25°C*
VMT4-25	*60*	*40*	–	*25*	*25°C*
VM4-20LS	*60*	*40*	–	*20*	*25°C*
GM 1 -05	*27*	*73*	–	*5*	*25°C*
GM 1 -10	*27*	*73*	–	*10*	*25°C*

GM 1 -15	*27*	*73*	–	*15*	*25°C*
GM 1 -20	*27*	*73*	–	*20*	*25°C*
GM 1 -25	*27*	*73*	–	*25*	*25°C*
GHIT3-15	*10*	*90*	–	*15*	*25°C*
GM1-20 LS	*30*	*70*	–	*20*	*25°C*
GHIT1-20	*40*	*60*	–	*20*	*25°C*
GHI5-20	*50*	*50*	–	*20*	*25°C*
GHIT2-20	*60*	*40*	–	*20*	*25°C*

3.2.1 INTEGRITY TEST RESULTS

The results of geopolymers based on volcanic precursors and the addition of 5-25 wt. % of metakaolin are interesting. In this case (VM1 and GM1series), the use of activation solution (formed by NaOH = 23% and pure water glass = 77% for VM1 while 27/73 for GM1) produced AAMs with good chemical and resistance features with the exception of the sample with 5% of metakaolin. A second parameter keep in consideration for establish the quality of the geopolymers is the appearance of white efflorescence consisting of trona ($Na_3(CO_3)(HCO_3)\cdot 2(H_2O)$) as determined by XRD analysis. In the series VM1 and GM1, efflorescence occurrence was observed on samples with metakaolin content lower than of 20%. Indeed, with the aim to investigate the formulations that have not this undesirable behaviour, others AAMs with different activators ratio and metakaolin content were produced which, afterwards, they passed the integrity test (VM5-20; VMT2-10; VM1-20LS; VMT1-20; VMT3-15; VMX-20; VMT4-25; VM4-20LS, see Table 3.2). Using the same approach described for the volcanic ash formulations, AAMs based on ghiara and metakaolin were produced to obtain a complete scenario on efflorescence occurrence. The experiment results demonstrate that the addition of moderate quantities of metakaolin (>10%) allowed the formation of AAMs with good resistance to the integrity test as suggested also by Robayo-salazar & Gutiérrez, 2018.

3.2.2 MACROSCOPIC OBSERVATIONS ON CARBONATATION PHENOMENA

In this context, the presence of white efflorescence consisting of trona (and/or thermonatrite) represents an undesirable salification process. With the aim to observe the mixtures that have given good results in terms of chemical stability and efflorescence, the experimental data of geopolymers are reported in Fig. 3.4 and Fig. 3.5. In particular, samples with the use of volcanic ash, 20% of metakaolin and NaOH amount lower than 20% (VM5-20) or higher than 60% (VM4-LS) failed the integrity test while the efflorescence is not present in AAMs with MK> 20% and NaOH<50%.

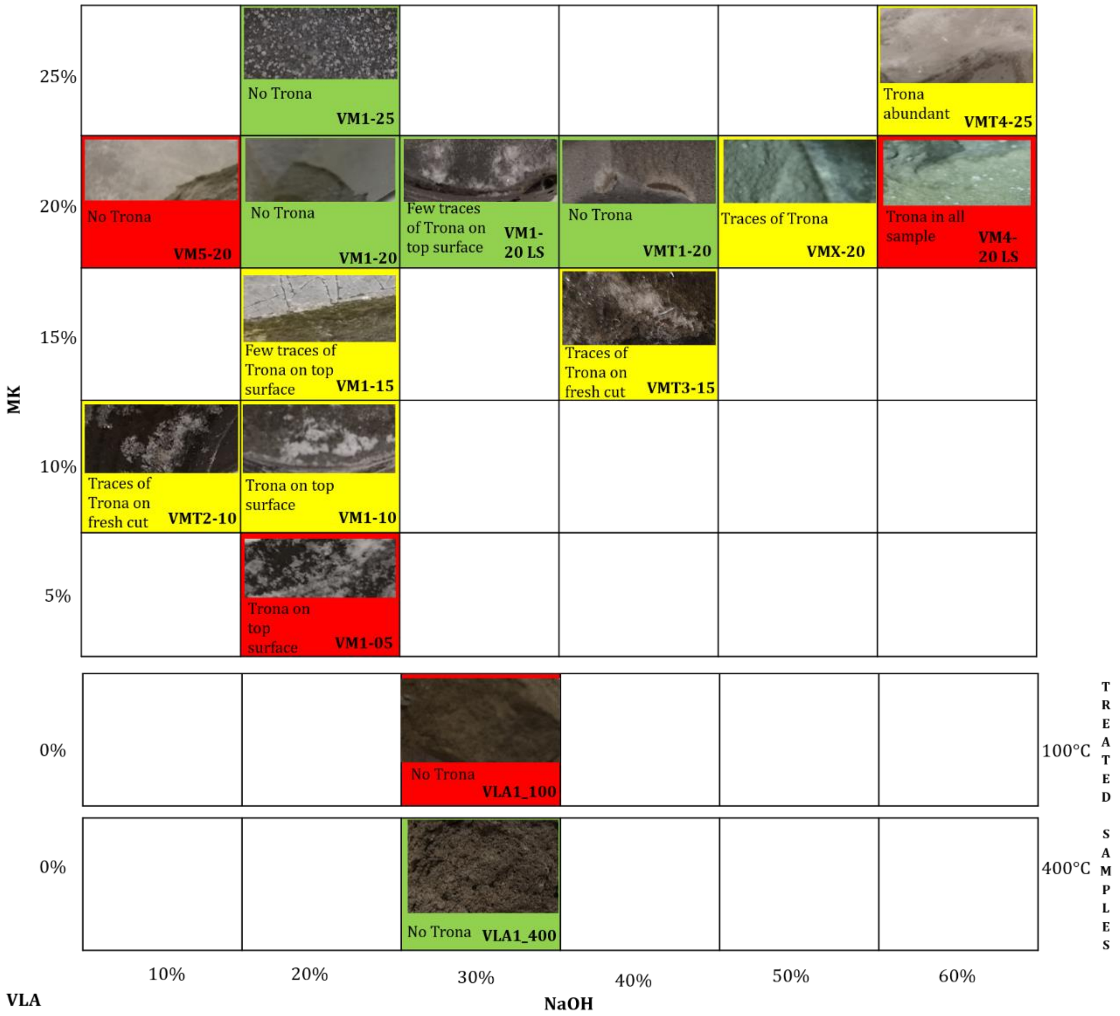

Fig. 3.4 - Carbonates crystallization micro-pictures (approximately each photo represents 1 cm^2 of sample) with a short description of AAMs based on volcanic ash and metakaolin with different percentage of NaOH (x-axis) and metakaolin (y-axis). Map results evidenced by different colours (green: positive and without carbonates crystallization; yellow: passed the integrity test but crystallization occurred; red failed test).

AAMs with ghiara and the addition of metakaolin content higher than 20% and NaOH lower than 10% successfully passed the test and efflorescence occurrence was not evidenced, such as sample with NaOH=20% and treated at 400°C (Fig. 3.5). Instead, despite the others treated samples and those ones with 10-15% of metakaolin and 20% NaOH have passed integrity test, carbonates crystallization occurred.

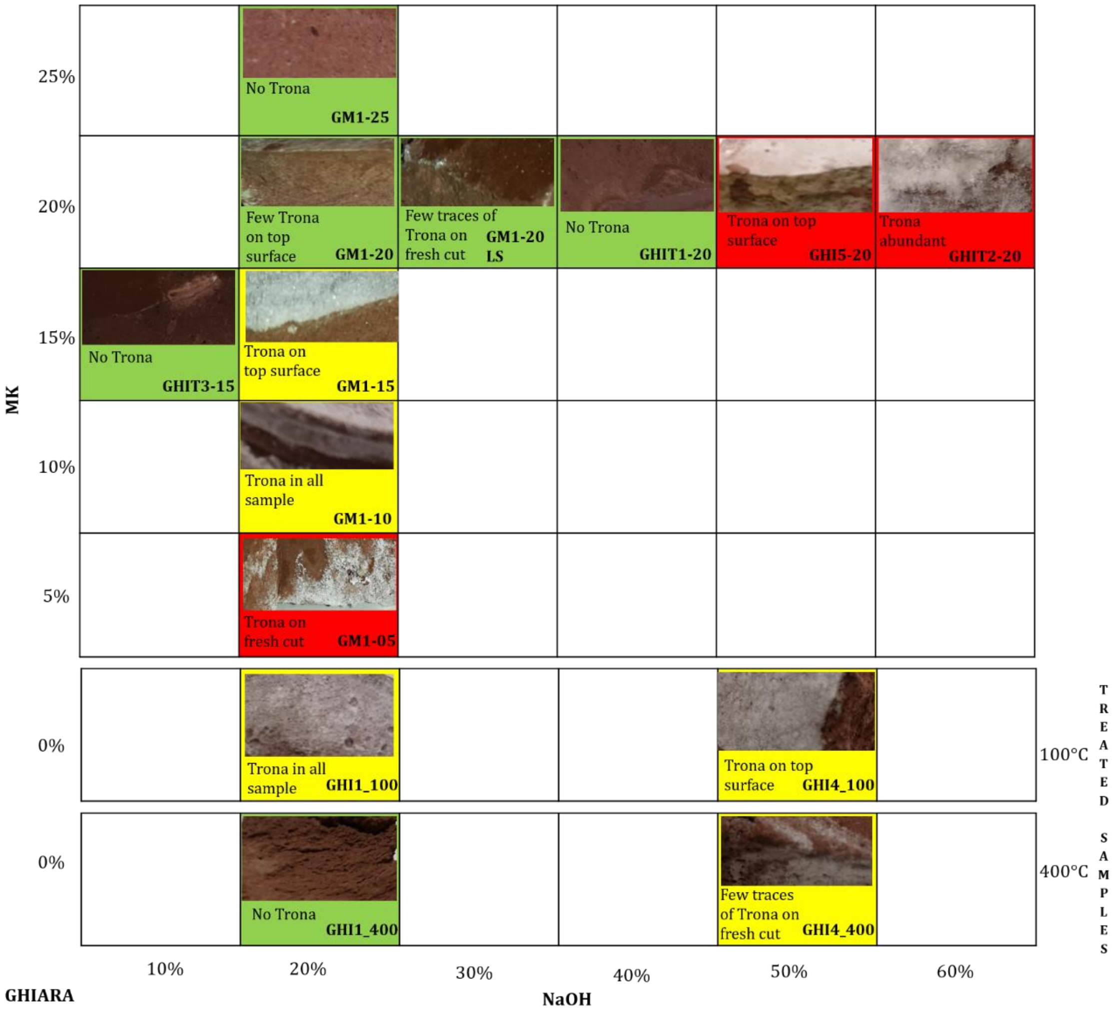

Fig. 3.5 - Carbonates crystallization micro-pictures (approximately each photo represents 1 cm^2 of sample) with a short description of AAMs based on ghiara and metakaolin with different percentage of NaOH (x-axis) and metakaolin (y-axis). Map results evidenced by different colours (green: positive and whiteout carbonates crystallization; yellow: passed the test but crystallization occurred; red failed test).

Finally, efflorescence observations evidenced interesting features: for both raw materials no evidence occurred with MK > 20% and 20% < NaOH < 50%. Moreover, for AAMs based on ghiara, no evidences of Na-carbonates hydrate with MK=15% and 10% < NaOH < 20% occurred. This undesirable behaviour is linked to an excess of Na$^+$

quantity (due to activators) within the pore network, which reacted with air of laboratory atmosphere after few days (Najafi et al., 2012; Lemougna et al., 2013).

3.3 THERMAL TREATMENTS ON VOLCANIC PRECURSORS

In the first part of the second year of my doctoral path, at laboratory of department of Engineering “Enzo Ferrari” of Modena and Reggio Emilia University, a new approach was tested, which have foreseen the thermal treatments on raw materials at 400°C for 4 hours before the mixing with alkaline solution. In these experiments, in addition to sodium hydroxide (8M) a sodium silicate with a lower molar ratio ($SiO_2/Na_2O = 1.6$) was used different from the others mentioned until now. In this scenario, the aim was to enhance the reactivity of volcanic precursor in alkaline environment and to reduce the cost of silicate. However, this approach didn’t produce the expect results: the consistency of fresh slurries was soft for long time as well as the samples produced without the treatments. The temperature used and/or the time of the treatments haven’t been enough to increase the reactivity of the process, as well as the polymerization power of silicate, maybe due to the few silica released. Therefore, this approach was set aside due to the high energy consumption of the thermal treatments, such as to not make it really eco-friendly.

3.4 MECHANOSYNTHESIS

Simultaneously to the approach aforementioned before, a new way of synthesis was performed at laboratory of department of Engineering “Enzo Ferrari” of Modena and Reggio Emilia University using porcelain jars and balls with the aim to favour the process mechanically on volcanic sources. Firstly, volcanic powder was mixed with the sodium hydroxide to allow the volcanic glass dissolution and so to release the silica in the system. Afterwards, the sodium silicate with molar ratio $SiO_2/Na_2O = 3$ was added in the jar for 10 minutes to complete the mechanical synthesis. Despite the heating emitted during the mechanical mixing and the further milling of the powder in finer fractions, the results obtained were very poor. Moreover, the cleaning of the slurry in the balls was very complicated, considering this approach unsuitable for mortar production in work conditions.

4. CHARACTERIZATION APPROACHES AND RESULTS

In this chapter, the characterization approaches and the corresponding results regarding the samples thermically treated and those of VM1 and GM1 series will be presented. In detail, the samples thermically treated have undergone petrographic observations through Optical microscope investigations, XRD, and FTIR analyses, while a deeply investigation, including also RAMAN, SEM, mechanical test and porosity analyses, for the samples belonging to the series with metakaolin. These latter were considered more interesting due to the potential applications as restoration materials in situ interventions.

4.1 METHODS DETAILS

Some of the geopolymers which passed the integrity test were characterized with different analytical techniques, whose details of each method are reported in the corresponding sub-paragraph, regardless some of them have been already explained in Chapter 2 for raw materials analysis.

4.1.1 OM: OPTICAL MICROSCOPE

Mineralogical and petrographical properties were identified under the polarizing microscope by thin sections observations at the Department of Biological, Geological and Environmental Sciences of Catania University.

4.1.2 XRD: X-RAY POWDER DIFFRACTION

The XRD analysis was carried out on powdered samples after seven days of aging using a Siemens D5000 diffractometer, whose details are reported in Chapter 2.4.1.

4.1.3 FTIR: FOURIER TRANSFORM INFRARED

Infrared analyses were performed using a Thermo Fisher Scientific 380 infrared spectrometer (Nicolet) of IRCER lab during my first phase of abroad period in Limoges on some samples with more than 28 days of aging, whose details are reported in Chapter 2.4.3.

4.1.4 RAMAN SPECTROSCOPY

Micro-Raman analysis were performed using a Jasco NRS-3100 apparatus of our department, equipped by a microscope with ×10, ×20, ×50 and ×100 objectives. An excitation source of 532 nm was used because, as well known, Raman spectroscopic analyses of disordered aluminosilicates, such as for example natural and artificial glasses, gives better results when performed with laser excitations in the green, blue and UV regions. In fact, with the 785 nm, no Raman bands attributable to the aluminosilicatic network (400-700 cm^{-1}: Si-O bending; ca. 1000 cm^{-1}: Si-O stretching) could be detected (Carter et al., 2012; Colomban & Prinsloo, 2009). Moreover, the green laser is powerful to detect Si-O bonds (less for Al-O bonds) typical of glass spectrum which could be similar to that one of geopolymers. For the measurements of geopolymers based on ghiara, six accumulation cycles of five minutes with no filter (OD open) and 50x (and/or 20x) objective was set, differently for those one based on volcanic ash, twelve accumulation cycles of five minutes with an optical density (OD) one. The analyses were carried out on sherds of V/GM1-10/20 and 20LS samples aged more than 28 days.

4.1.5 MECHANICAL PERFORMANCE: COMPRESSIVE TEST

Compressive strength was determined using an Instron 5567 Universal Testing Machine with 30 kN load limit and displacement of 3mm/min according to the standard UNI EN 826 at Engineering Department “Enzo Ferrari” of Modena and Reggio Emilia University (UNIMORE). In particular, four specimens for each formulation were prepared in cubic plastic moulds with a length of 2 cm (Fig. 4.1). All cubes were broken after 28 days of curing.

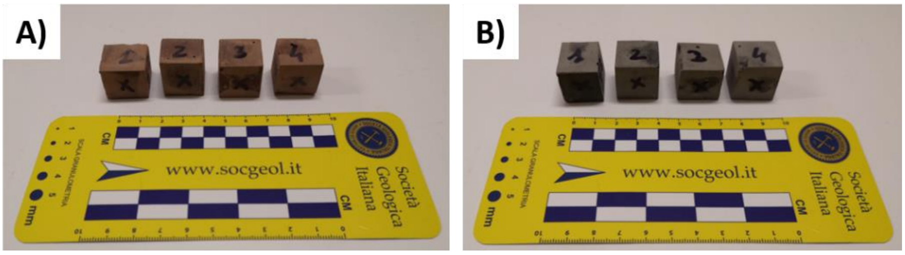

Fig. 4.1 - Representative photographs of cubic samples regarding the series GM1 (a) and VM1 (b) after polishing surfaces step.

4.1.6 SEM-EDX: SCANNING ELECTRON MICROSCOPE – ENERGY DISPERSIVE X-RAY

Morphological analysis was performed using a Tescan Vega LMU scanning electron microscope, equipped with a with EDAX energy dispersive spectrometer (EDS) of Biological, Geological and Environments Sciences Department (Catania University). Data were collected using a voltage of 20kV and a beam current of 0.2 nA. The measurements were performed on four thin sections of geopolymeric samples aged more than 28 days (VM1-10/20 and GM1-10/20, considered as representative of the VM1 and GM1 series) fixed on a metal support and covered with a thin layer of graphite with the aim to highlight the morphological and compositional features of microstructure whose characterize this type of material. Four images for each sample at low magnifications were taken to evaluate the main features of texture as whole porosity and general discontinuities, while different spot analyses were collected on small areas (high magnification) to estimate a semi quantitative chemical composition.

4.1.7 PERMEABLE POROSITY TEST FOR TOTAL ABSORPTION

To evaluate the effective permeable porosity of representative geopolymers belonging to series VM1 and GM1 (with 10, 20% wt. metakaolin and the “green” formulation), permeable porosity test for total absorption were performed. The test was conducted on small cubic samples dried in an oven at temperature of 100°C for 24h to ensure that a constant mass was achieved. The specimens were left at room temperature in a desiccator for two hours to allow the cooling and to obtain their initial weight (w_d). Afterwards, they were immersed in distilled water at room temperature and covered by 2 cm of water. The samples, once swabbed with a damp cloth, were weighed at various time intervals (starting to 1 minute up to few hours). The test was considered ended once no recorded significant variation of wet mass (<1% w_w) between two following measurements. Water absorption was then quantified using Eq. (1) to quantify the change of weight as percentage of the initial one.

$$Water\ absorption, \% = \frac{w_w - w_d}{w_d} x100 \qquad (1)$$

4.1.8 HG POROSIMETRY

The investigation at sub-micrometric dimensional scale was carried out by Hg intrusion porosimetry (MIP) on small sherds of following samples: *VM1-10, 20 and 20 LS* and the equivalents for ghiara once removed humidity in the oven at 100°C temperature. Moreover, specimens aged one year of the same formulations were analysed with the aim to compare them with the shards of cubic samples aged 5 months. Porosimetric analysis was carried out with a Thermoquest Pascal 240 macropore unit in order to explore a porosity range ~ 0.0074 µm < r < ~ 15 µm (r being the radius of the pores), and by a Thermoquest Pascal 140 porosimeter instrument in order to investigate a porosity range from ~ 3.8 µm < r < ~ 116 µm.

4.2 RESULTS ON GEOPOLYMERS THERMICALLY TREATED

In this paragraph, mineralogical, petrographic and infrared results regarding the thermically treated geopolymers respectively after 100° and 400°C (VLA1 100/400 and GHI4_100/400) are presented.

4.2.1 OM: PETROGRAPHIC ANALYSIS

Generally, optical microscope analyses aren’t used to perform for this kind of materials due to the amorphous structure following the alkaline activation. Indeed, only two references regarding flay ash based geopolymers were found in literature (Màdai et al., 2015; Yousefi Oderji et al., 2019). Fig. 4.2 shows the thin sections of VLA1 samples: particles with grain size below <75 µm confirming a good milling degree with spherical and/or elongated shapes and a complex amorphous matrix. The sample treated at 100°C evidenced a higher crystallinity and smaller holes than that one treated at 400°C. Regardless the difficulty to detect the mineralogical phases due to fine grain size, agglomerates of plagioclases and pyroxenes can be observed in Fig. 4.2a. Moreover, the holes of VLA_400°C have a size ranging 100-400 µm (Fig. 4.2b). Fig. 4.3 shows the thin sections of GHI4 samples: amorphous matrix with particles of grain size >100 µm and spherical shape. The sample treated at 100°C evidence a more homogeneous structure (Fig. 4.3a) than that one treated at 400°C, which seems to be affected by cracks (Fig. 4.3b).

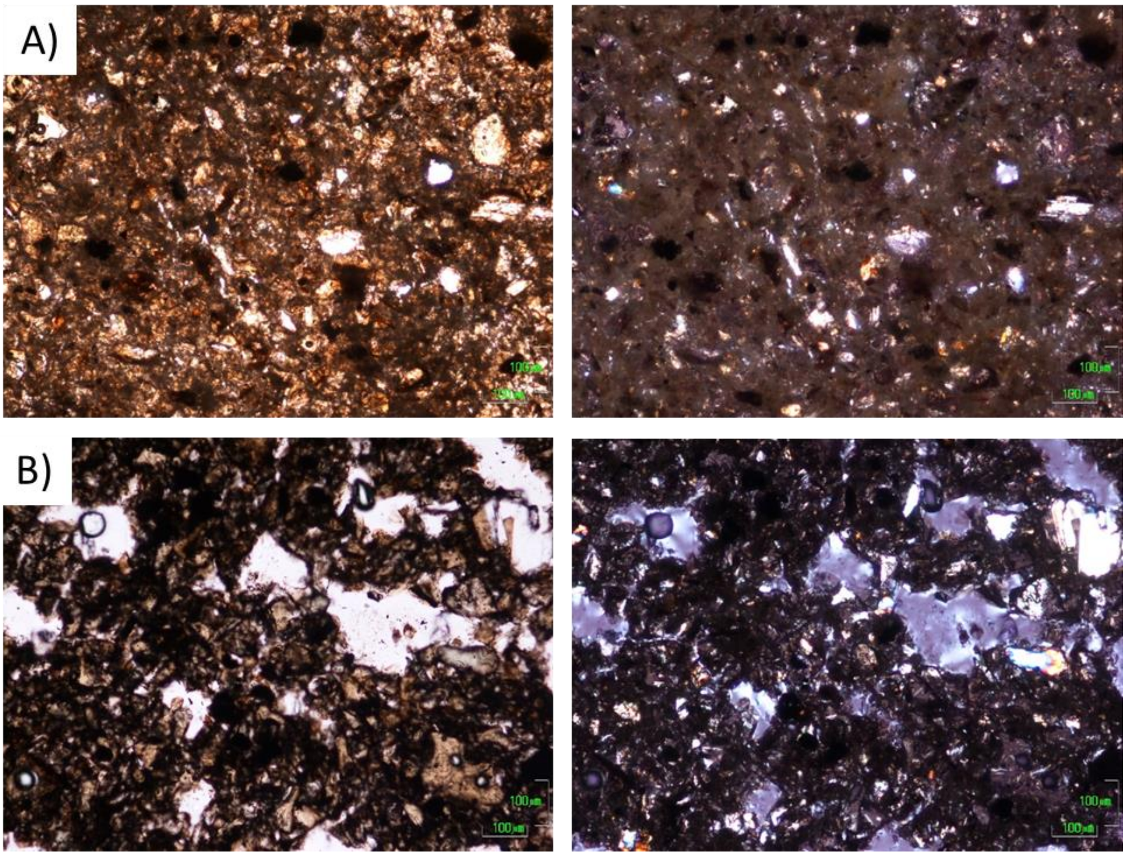

Fig. 4.2 – OM micrographs (left: parallel nicols; right: crossed nicols) of the following geopolymers with volcanic ash: A) geopolymer treated at 100 ° C (VLA1_100); B) geopolymer treated at 400 ° C (VLA1_400).

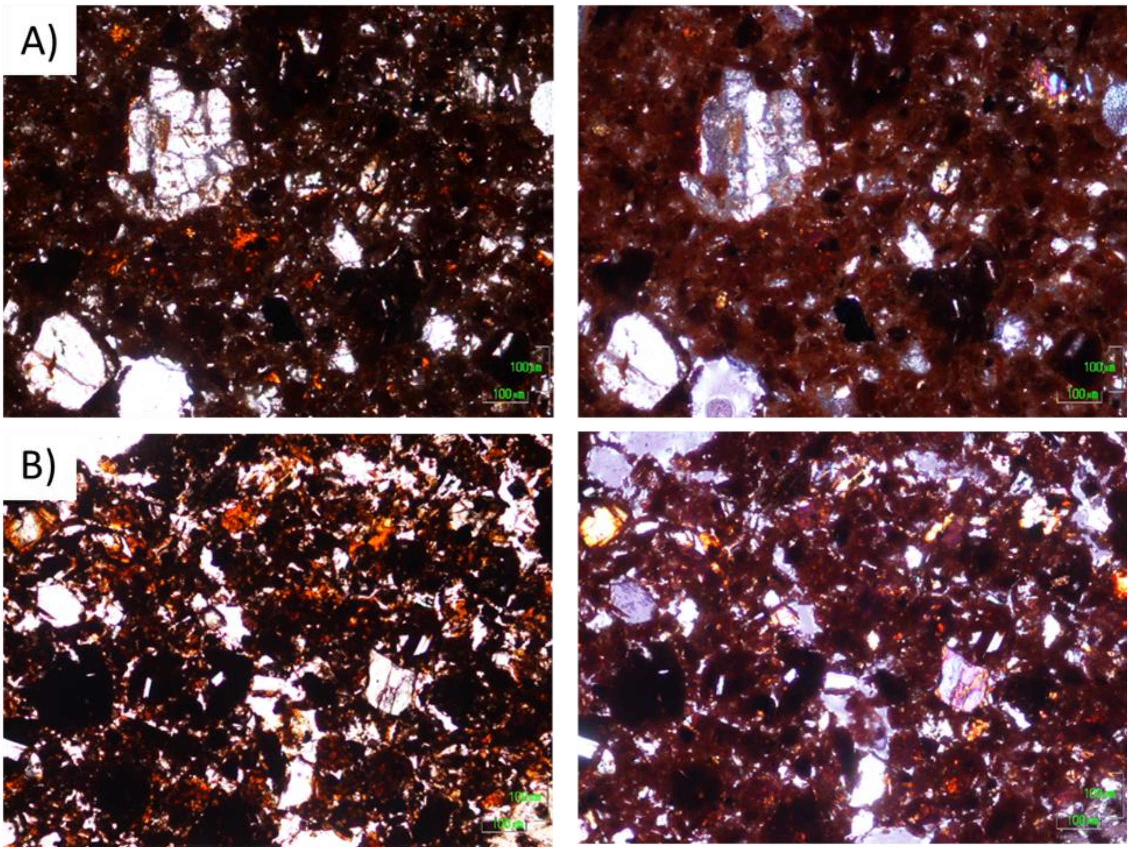

Fig. 4.3 – OM micrographs (left: parallel nicols; right: crossed nicols) of the following geopolymers with ghiara: A) geopolymer treated at 100 ° C (GHI4_100); B) geopolymer treated at 400 ° C (GHI4_400).

4.2.2 XRD ANALYSIS

Both volcanic raw materials and the produced geopolymers showed, as attested in the literature (Davidovits, 1991; Duxson, 2007; Alehyen et al., 2017; Riessen et al., 2017), high amorphous content as evidenced by the broad band in the 20-35 2θ range. The mineralogical phases typical of Mt. Etna volcanic ash (i.e. Ca-rich plagioclase, pyroxene, and olivine) and ghiara (i.e. Ca-rich plagioclase, anorthoclase, pyroxene, hematite, goethite ± calcite) are the prevalent ones in the raw materials as well as in geopolymers. In these latter, in some cases, zeolites (phillipsite and zeolite-P) are present, suggesting the formation of more ordered structure during the polymerization process (Criado et al., 2007). The presence of zeolites after thermal treatment can be related to the reorganization of geopolymeric gel formed after alkali activation induced by temperature. In VLA1 samples, the amorphous phase is the more abundant (> 80%) both after 100°C and 400°C curing. Moreover, in the 100°C sample, zeolite P and phillipsite are present while in the 400°C only zeolite P is observable (Fig. 4.4). On the other hand, mineralogical results concerning GHI4 samples, on average, they have lower amorphous phase abundance than corresponding volcanic ash geopolymers; ii) the amorphous percentage of the formulations treated at 400°C is lower than those treated at 100°C; iii) in all the thermally treated samples, small amount of zeolite were observed (Fig. 4.5). The quantitative values of the most representative phases are reported in Table 4.1, while the references/labels, used for the Rietveld method, are: anorthite (An), amcsd 0001287 (Angel et al., 1990); anorthoclase (Ano), code 9000855 (Harlow, 1982); augite (Aug), code 1000035 (Clark & Appleman, 1969); forsterite (Fo), amcsd 0000886 (Nord et al., 1982); hematite (Hem), amcsd 0002228 (Gualtieri & Venturelli, 1999); goethite (Gt), amcsd 0002226 (Gualtieri & Venturelli, 1999); magnetite (Mag), amcsd 0013508 (Greaves, 1983); phillipsite (Phi), amcsd 0012860 (Gualtieri, 2000); zeolite P (ZeoP), 8104214 (Gramlich & Meier, 1971); calcite (Cal), amcsd 0000989 (Markgraf & Reeder, 1985); amorphous (Amorp).

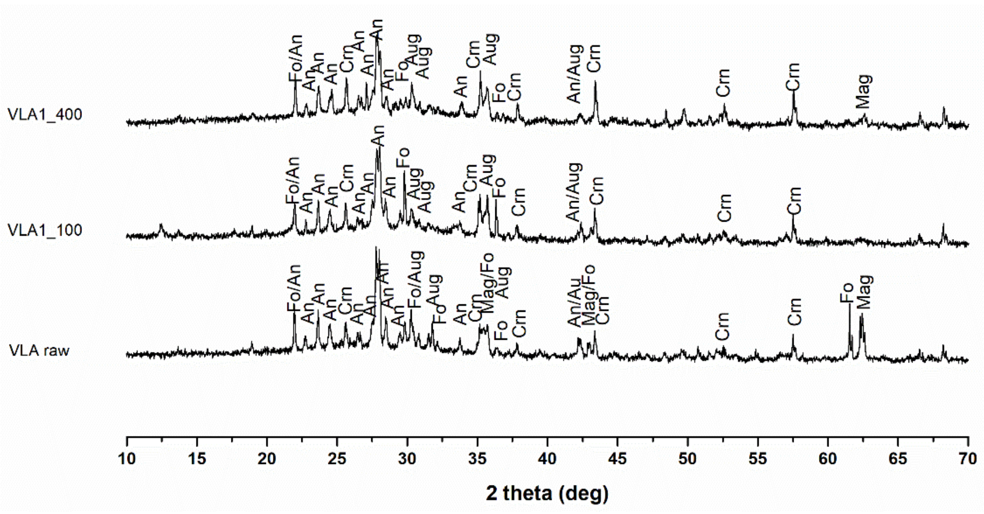

Fig. 4.4 – Representative pattern of volcanic ash for following typology: raw materials and AAMs treated at 100/400°C (An: anorthite; Aug: Augite; Fo: forsterite; Mag: magnetite; Crn: corundum).

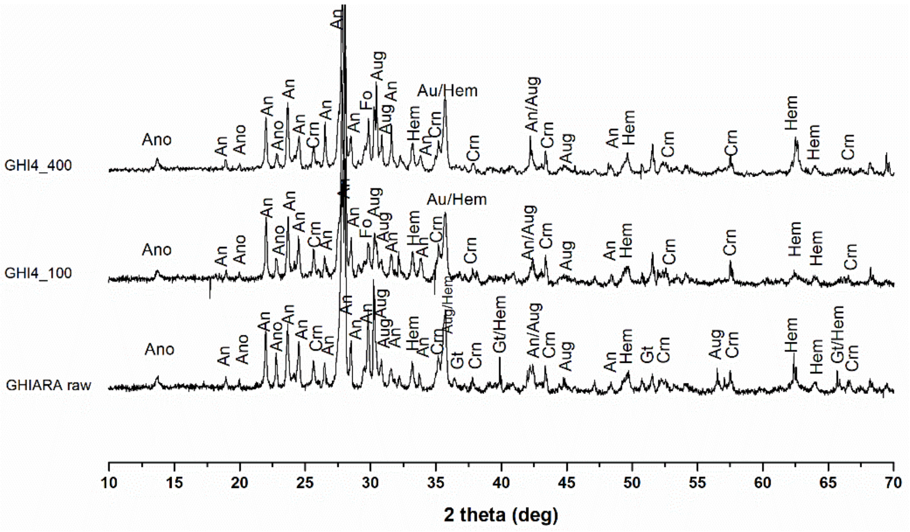

Fig. 4.5 – Representative pattern of ghiara for following typology: raw material and AAMs treated at 100/400°C (An: anorthite; Ano: anorthoclase; Aug: augite; Fo: forsterite; Hem: hematite; Gt: goethite Mag: magnetite; Crn: corundum).

Table 4.1 - Mineralogical results obtained by XRD analysis with Rietveld Method.

									Zeolite group			
	% Weight	**An**	**Anor**	**Aug**	**Fo**	**Mgh**	**Hem**	**Gt**	**Phl**	**ZeoP**	**Cal**	**Amorp**
Raw materials	*Volcanic ash*	*12.4*	–	*12.5*	*0.7*	–	–	–	–	–	–	*74.5*
	Ghiara	*23.3*	*11.8*	*9.1*	–	–	*1.9*	*0.1*	–	–	–	*53.8*
Thermal treated samples	*VLA1_100*	*8.7*	–	*3.8*	–	*0.2*	–	–	*0.6*	*0.3*	–	*86.5*
	VLA1_400	*14.1*	–	*2.4*	–	*0.5*	–	–	–	*1.6*	–	*81.5*
	GHI4_100	*30.7*	*4.1*	*3.9*	–	*0.8*	*1.7*	–	–	–	*0.7*	*58.2*
	GHI4_400	*28.5*	*5.8*	*11.2*	–	*0.6*	*2.0*	–	–	–	*0.3*	*51.6*

4.2.3 FTIR ANALYSIS (KBR METHOD)

FT-IR results of both series (VLA1 and GHI4) are comparable, and no main chemical bonds differences are detected, contrary to the corresponding samples treated at different temperatures which showed variations in water content attributions. Indeed, geopolymers based on volcanic ash evidenced some different peak positions: e.g. that one treated at 100°C two peaks respectively at 3600 and 3300 cm^{-1} corresponding to ν O-H or ν Si-OH in addition to the peaks at 1650 cm^{-1} regarding to δ H-O-H, instead of the unique one at 3470 cm^{-1} (ν O-H) and at 1730 cm^{-1} (O-H) recorded in the other sample treated at 400°C (Fig. 4.6a). Less evident are the differences among the geopolymers based on ghiara: both showed a clear contribution centred at 3460 cm^{-1} (ν O-H), although that one treated at 400°C evidenced a peak in the position 1730 cm^{-1} (O-H) (Fig. 4.6b) as well as in that one of volcanic ash. However, no differences are recorded in the aluminosilicate and carbonate area ranging at 1500-400 cm^{-1} as listed in Table 4.2. Finally, the curing temperatures of 100 and 400°C were chosen in order to evaluate the reactivity of volcanic residues as a function of temperature. Obviously, these curing conditions are not suitable for an in-situ application but helps to understand if these powders can react or not in strong conditions.

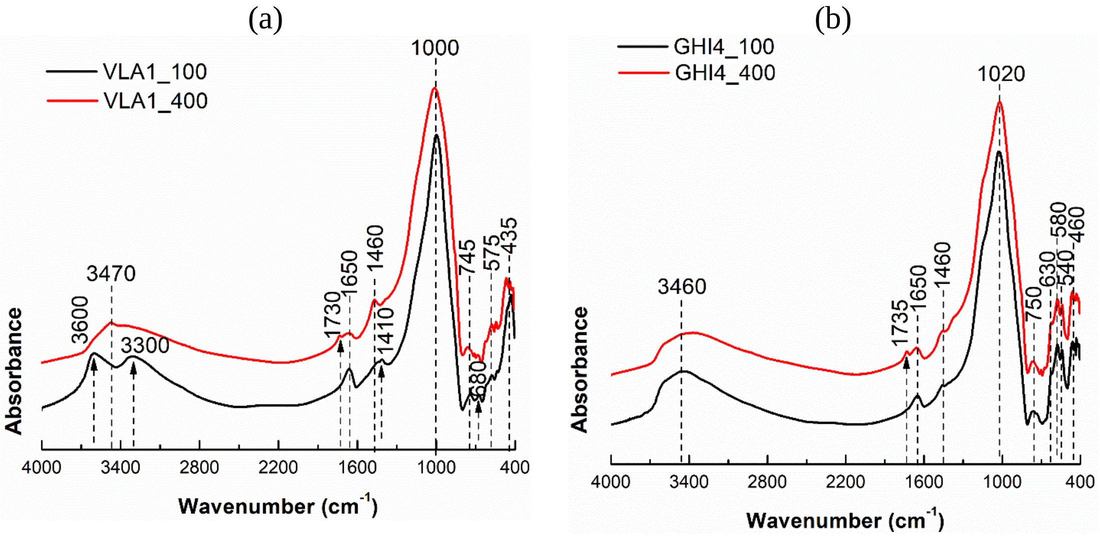

Fig. 4.6 – FT-IR spectra obtained by KBr method. a) AAMs based on volcanic ash thermically treated at 100° (black) and 400°C (red); b) AAMs based on ghiara thermically treated at 100° (black) and 400°C (red). The dashed lines indicate the main contributions. Spectra resolution 4 cm^{-1}.

Table 4.2 - Summary of main IR attributions in the range 1500-400 cm^{-1} *for geopolymers based on volcanic ash and ghiara thermically treated at 100°C and 400°C.*

	vla1_100	***vla1_400***	***ghi4_100***	***ghi4_400***	**Assignments**
Wavenumber range (1500-400 cm^{-1}*)*	1454	1463	1463	1457	νas CO_3^{2-} or Na_2CO_3
	1409	–	–	–	νas CO_3^{2-}
	–	–	1028	1021	ν Si-O
	1000	1005	–	–	νs Si-O-Si (Al) or ν Si-O
	741	756	764	766	ν Si-O or ν *Al^4-O-Si*
	676	681	670	–	δ Si-O-Si SiO4 or *Si-O-Al*
	–	624	624	624	νs Si-O-Si
	577	574	578	580	ν SiO4
	538	537	541	543	δ Si-O-Al or *ν Si-O*
	461	464	464	462	ρ Si-O-Si or *ν Si-O*
	435	435	–	–	ρ Si-O-Si or *ν Si-O*

4.3 RESULTS OF VM1 AND GM1 SERIES

In this paragraph, OM, XRD, FTIR, compressive strengths, SEM, porosity for total absorption and Hg porosimetry results regarding the series with the progressive addition of metakaolin (VM1 and GM1) are presented.

4.3.1 OM: PETROGRAPHIC ANALYSIS

Fig. 4.7 show the micrographs of optical microscope observations of some sample representative of VM1 series, including the formulation with low liquid/solid ratio (L/S). In detail, the samples VM1-15 and VM1-25 evidenced particles with a grain size < 75 µm and spherical or sharp-cornered shapes immersed in an amorphous matrix (Fig. 4.7a-b). However, the crystallinity degree seems to be higher in the sample with less metakaolin amount than VM1-25, where an amorphous gel prevails supposing a higher dissolution of the original mineralogical phases. The sample VM1-20 LS highlights the finest particles and a higher crystallinity among all the samples considered (Fig. 4.7c).

The individuation of relict minerals is complicated for all samples due to the fine sizes and inhomogeneous shapes. Moreover, all samples didn’t evidence macro porosity.

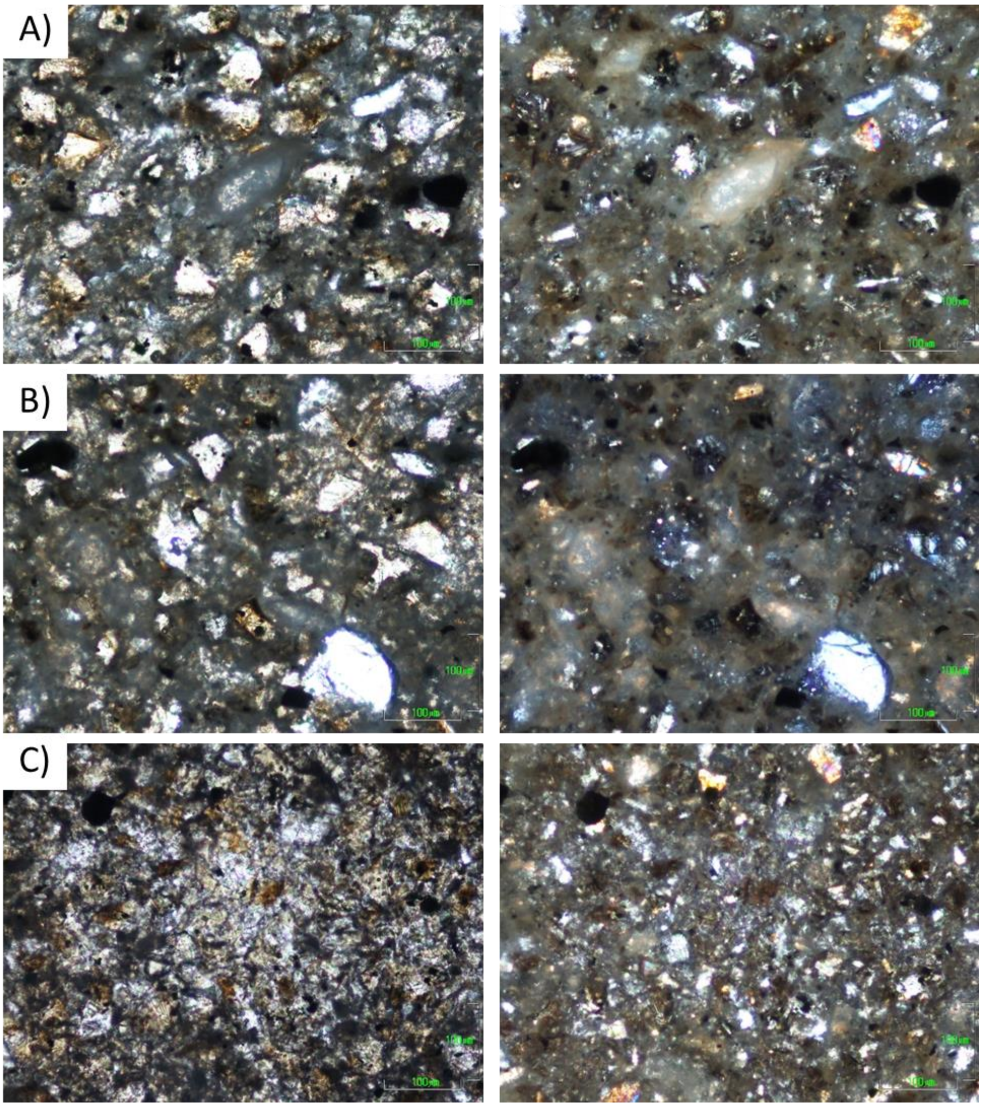

Fig. 4.7 – OM micrographs (left: parallel nicols; right: crossed nicols) of the following geopolymers with volcanic ash: A) geopol. volcanic ash and 15 wt. % of MK (VM1-15); B) geopol. volcanic ash and 25 wt. % of MK (VM1-25); C) geopol. volcanic ash and 20 wt. % of MK with low L/S ratio (VM1-20LS).

The equivalent samples based on ghiara are showed in Fig. 4.8. The sample GM1-15 evidences holes with different size reaching dimensions > 100 µm (Fig. 4.8a) differently for the microporous of other samples (Fig. 4.8b-c). Generally, the holes have spherical shape. The crystallinity degree appears higher in the GM1-15 than the others. Even for GM1 series, the mineralogical phases are difficult to detect. From comparison of two series, the VM1's samples evidence a major amorphous structure and a lower porosity than the GM1's ones.

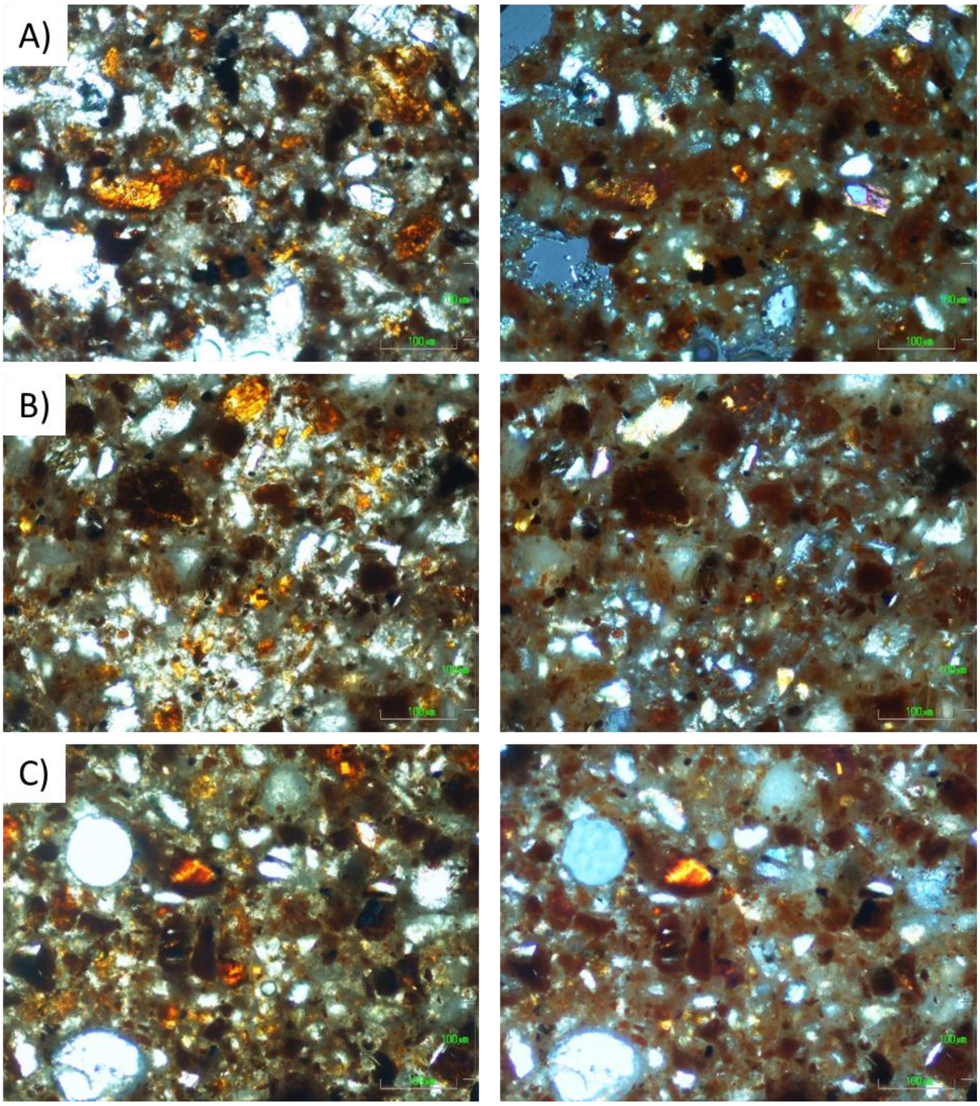

Fig. 4.8 – OM micrographs (left: parallel nicols; right: crossed nicols) of the following geopolymers with ghiara: A) geopol. ghiara and 15 wt. % of MK (GM1-15); B) geopol. ghiara and 25 wt. % of MK (GM1-25); C) geopol. ghiara and 20 wt. % of MK with low L/S ratio (GM1-20LS).

4.3.2 XRD ANALYSIS

X-ray powder diffraction analysis were performed on all samples of VM1 and GM1 series, whose diffrattometric patterns are showed in Fig. 4.9 and Fig. 4.10. However, quantitative analysis wasn't performed on "LS" formulations for the strong similarities with other patterns of the series. In addition to the original mineralogical phases found in raw materials (anorthite, anorthoclase and augite), gismondine phase, belonging to zeolite group, was observed in VM1 series (Fig. 4.9). Moreover, the amorphous content is constant in all the samples reaching as average values 75% about (Table 4.3). Contrary, GM1 series showed an amorphous content higher than 44% and phases belonging to zeolite group in small quantities (phillipsite, faujasite and zeolite P) in addition to the original ones of raw materials (Fig. 4.10) (Barone et al., 2020). Finally, comparing the augite amount of raw materials with those of geopolymers, a general decreasing of this value in geopolymers was recorded (Table 4.3), as indication of good reactivity due to the relatively easily capacity of this phase to dissolve in alkaline conditions (Lemougna et al., 2013; Nikolov et al., 2017). The references/labels of the mineralogical phases detected are: anorthite (An), amcsd 0001287 (Angel et al., 1990); anorthoclase (Ano), code 9000855 (Harlow, 1982); augite (Aug), code 1000035 (Clark & Appleman, 1969); forsterite (Fo), amcsd 0000886 (Nord et al., 1982); hematite (Hem), amcsd 0002228 (Gualtieri & Venturelli, 1999); goethite (Gt), amcsd 0002226 (Gualtieri & Venturelli, 1999); magnetite (Mag), amcsd 0013508 (Greaves, 1983); phillipsite (Phi), amcsd 0012860 (Gualtieri, 2000); faujasite (Fau), amcsd 0006772 (Porcher et al., 1999); zeolite P (ZeoP), 8104214 (Gramlich & Meier, 1971); gismondine (Gis), amcsd 0020103 (Wadoski-Romeijn & Armbruster, 2013); calcite (Cal), amcsd 0000989 (Markgraf & Reeder, 1985); anatase (Ant), amcsd 0011765 (WYCKOFF, 1963) amorphous (Amorp).

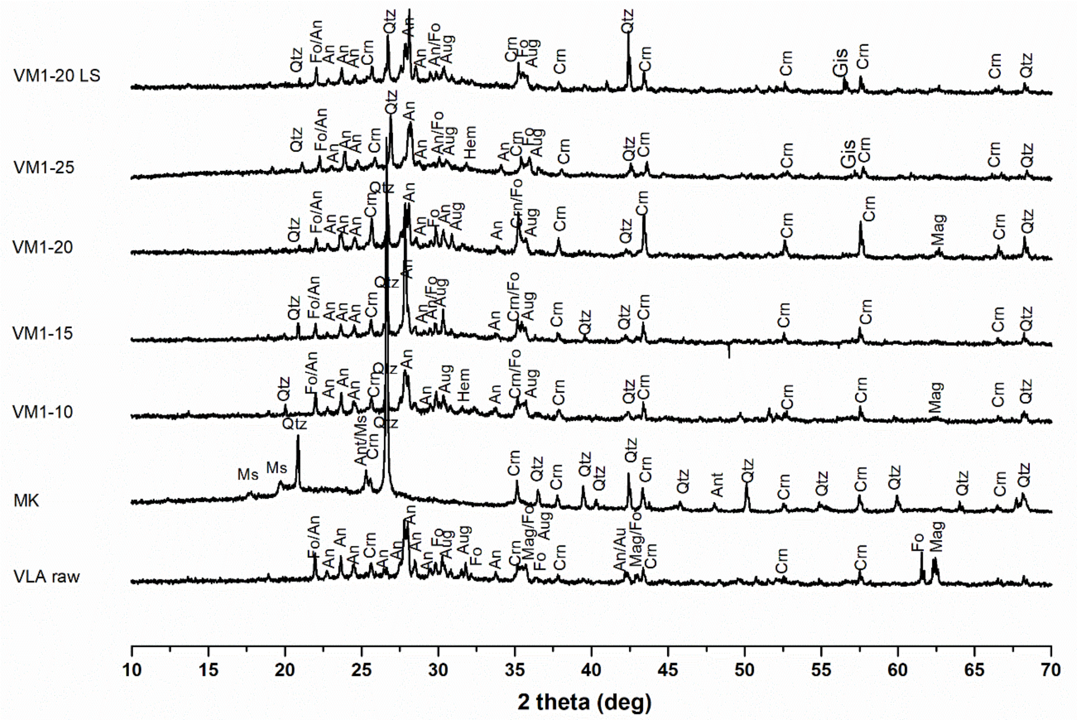

Fig. 4.9 – XRD pattern of VM1 series and precursors: volcanic ash (VLA raw) and metakaolin (MK). Legenda: An: anorthite; Aug: augite; Fo: forsterite; Hem: hematite; Mag: magnetite; Gis: gismondine; Qtz: quartz; Ms: muscovite; Ant: anatase; Crn: corundum.

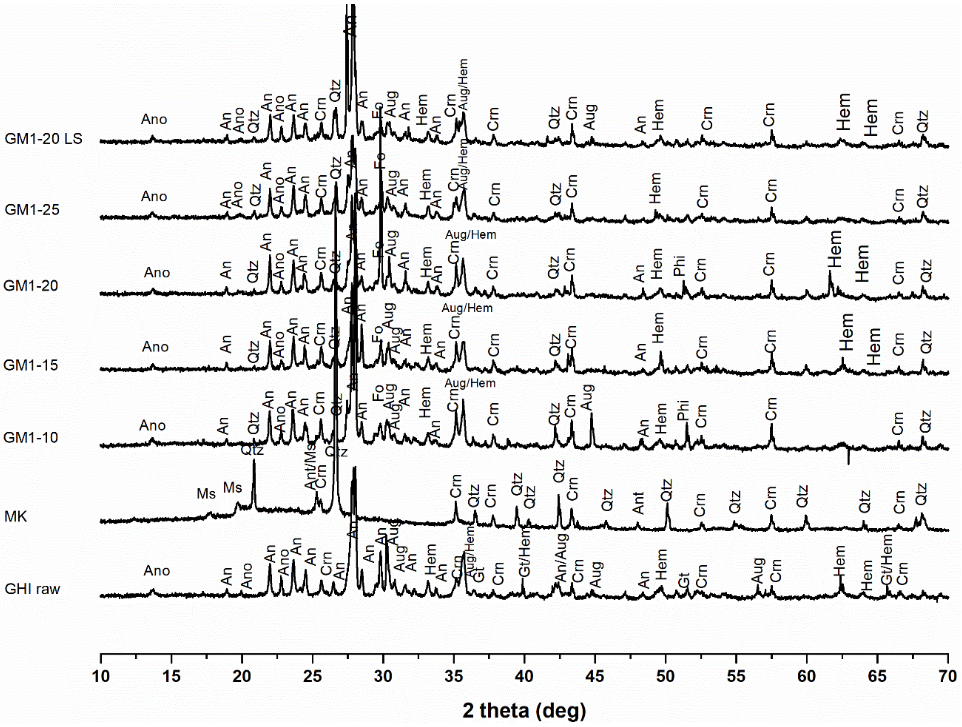

Fig. 4.10 – XRD pattern of GM1 series and precursors: ghiara (GHI raw) and metakaolin (MK). Legenda: An: anorthite; Ano: anorthoclase; Aug: augite; Fo: forsterite; Hem: hematite; Gt: goethite; Qtz: quartz; Ms: muscovite; Ant: anatase; Crn: corundum.

Table 4.3 - Mineralogical results obtained by XRD analysis with Rietveld Method.

									Zeolite group						
	% Weight	**An**	**Ano**	**Aug**	**Fo**	**Mag**	**Hem**	**Gt**	**Phi**	**Fau**	**ZeoP**	**Gis**	**Cal**	**Ant**	**Amorp**
Raw materials	*Volcanic ash*	*12.4*	–	*12.5*	*0.7*	–	–	–	–	–	–	–	–	–	*74.5*
	Ghiara	*23.3*	*11.8*	*9.1*	–	–	*1.9*	*0.1*	–	–	–	–	–	–	*53.8*
Samples with MK addition	*VM 1 -10*	*12.1*	*1.7*	*4.8*	–	–	–	–	–	–	–	*1.6*	–	*0.2*	*79.6*
	VM 1 -15	*15.5*	*8.4*	*4.5*	–	–	–	–	–	–	–	*1.5*	–	*0.2*	*69.9*
	VM 1 -20	*7.6*	*1.3*	*2.7*	–	–	–	–	–	–	–	*0.1*	–	*0.1*	*88.2*
	VM 1 -25	*21.2*	*3.9*	*5.8*	–	–	–	–	–	–	–	*0.4*	–	*0.1*	*68.7*
	GM 1 -10	*26.9*	*10.3*	*11.3*	*2.8*	*1.7*	*1.5*	–	*0.2*	*0.1*	*0.3*	–	*0.7*	–	*44.4*
	GM 1 -15	*14.5*	*12.7*	*8.0*	*2.2*	*0.7*	*1.8*	–	*0.5*	*0.1*	*0.2*	–	*0.5*	*0.3*	*58.6*
	GM 1 -20	*15.6*	*6.3*	*3.4*	*2.1*	*0.2*	*1.5*	–	*0.5*	*0.1*	*0.1*	–	*4.3*	–	*65.9*
	GM 1 -25	*15.9*	*8.3*	*7.4*	*2.2*	*0.5*	*0.3*	–	*0.3*	–	–	–	*0.7*	–	*64.4*

4.3.3 FTIR ANALYSIS (KBR METHOD)

The infrared results regarding the series VM1 and GM1 of both volcanic precursors no showed differences (Fig. 4.11a-b), resulting strongly comparable also with the green formulations labelled “LEO” (or LS) (Fig. 4.11c). Indeed, all spectra have recorded the same contributions: water (3460 and 1645 cm^{-1} corresponding to ν O-H and δ H-O-H respectively), carbonate (1470 cm^{-1} due to νas CO_3^{2}) and aluminosilicate (ranging at 1200-400 cm^{-1}) contents as listed in the Table 4.4. However, from the waterfall graph (Fig. 4.11b) which enclose all formulations except the green ones showed an interesting behaviour linked to the carbonate phases: to increasing the metakaolin decreases the intensity of carbonate band. This behaviour can be explained as a progressive development of a better and organized network thanks to complete metakaolin dissolution.

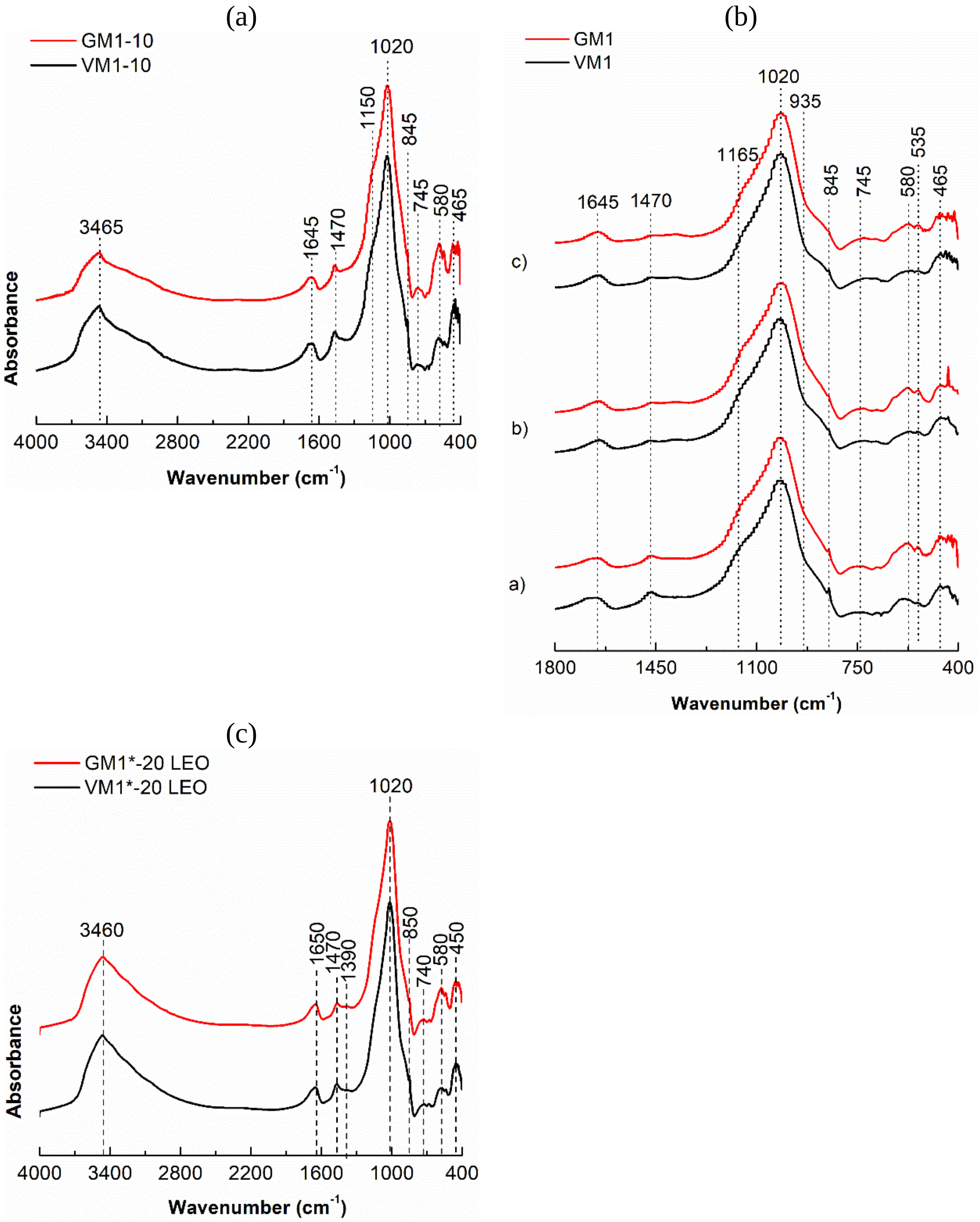

Fig. 4.11 – FT-IR spectra obtained by KBr method on samples belonging to VM1 and GM1 series. a) complete spectra of geopolymers with 10 wt % MK; b) spectra of geopolymers with 15 (a), 20 (b) and 25 (c) wt % of MK in the range 1800-400 cm^{-1}; c) complete spectra of geopolymers labelled "green formulations" with 20 wt % MK and lowest L/S ratio. The dashed lines indicate the main contributions. Spectra resolution 4 cm^{-1}.

Table 4.4 - Summary of IR attributions in the range 4000-400 cm^{-1} for geopolymers belonging to VM1 and GM1 series (expect green formulations).

	VM1-10	*VM1-15*	*VM1-20*	*VM1-25*	**Assignments:**
Wavenumber cm^{-1}	3471	3468	3465	3464	ν O-H
	1672	1669	1647	1654	δ H-O-H
	1469	1468	1471	1467	νas CO_3^{2-} or Na_2CO_3
	1157	1142	1155	1122	ν Al-O as Si (TO4)
	1023	1020	1023	1020	νs Si-O-Si (Al) or ν Si-O
	912	910	934	931	ν Si,Al-O- or ν SiO4
	853	851	849	851	ν Al-O
	764	750	732	728	ν Si-O or ν *Al^4-O-Si*
	588	593	568	590	ν SiO4
	462	465	464	461	ρ Si-O-Si or *ν Si-O*

	GM1-10	*GM1-15*	*GM1-20*	*GM1-25*	**Assignments:**
Wavenumber cm^{-1}	3469	3467	3461	3458	ν O-H
	1668	1662	1654	1651	δ H-O-H
	1469	1465	1463	1468	νas CO_3^{2-} or Na_2CO_3
	1137	1127	1145	1130	ν Al-O as Si (TO4)
	1021	1021	1015	1018	νs Si-O-Si (Al) or ν Si-O
	940	940	940	949	ν Si,Al-O- or ν SiO4
	851	851	855	851	ν Al-O
	760	746	734	729	ν Si-O or ν *Al^4-O-Si*
	580	582	578	577	ν SiO4
	543	543	541	542	δ Si-O-Al or *ν Si-O*
	468	466	458	469	ρ Si-O-Si or *ν Si-O*

4.3.4 RAMAN SPECTROSCOPY

Raman analysis were carried out on some sherds of samples belonging to VM1 and GM1 series with a x50 objective. In detail, the samples with 10 and 20% wt. of metakaolin addition, including the formulation with low silicate labelled "LS", were analysed. The green laser source was used for the reasons explained in the chapter of raw materials, as well as the same optical density (OD) and exposure time were used according the type of volcanic precursors: OD 0.3 and 30 minutes as total measurement time for ghiara material while OD 0.6 and long acquisition time (1 hour of total measurement time) for volcanic ash geopolymers. In each figure, the representative Raman spectra (or in some case single spectrum) are compared to the spectra of the main mineralogical phases found in XRD analysis and downloaded by rruff dataset (https://rruff.info/): anorthite, augite, forsterite and hematite. The comparison has allowed to identify the peaks recorded in the spectra of samples analysed. The spectra of the sample VM1-10 showed the typical spectrum of augite phases with the peaks located in the following positions: 325, 390, 665 and 1005 cm^{-1} (Fig. 4.12), while the peaks of the sample VM1-20 evidenced those one of anorthite phase (485, 505 and 680 cm^{-1}) (Fig. 4.13). The sample with low silicate (VM1-20 LS) evidenced anatase in the positions 395, 514 and 637 cm^{-1} and a contribution of trona at 1060 cm^{-1} demonstrating the effect of efflorescence occurrence after long time at air exposition and the old age of the sample (Fig. 4.14). The geopolymers of volcanic ash are not easy to analyses due to the fluorescence phenomena and the amorphous content of volcanic ash, but the analysis of these samples demonstrated the presence of anorthite, augite coming from volcanic ash contribution while anatase from metakaolin addition maybe not all reacted during the alkaline synthesis.

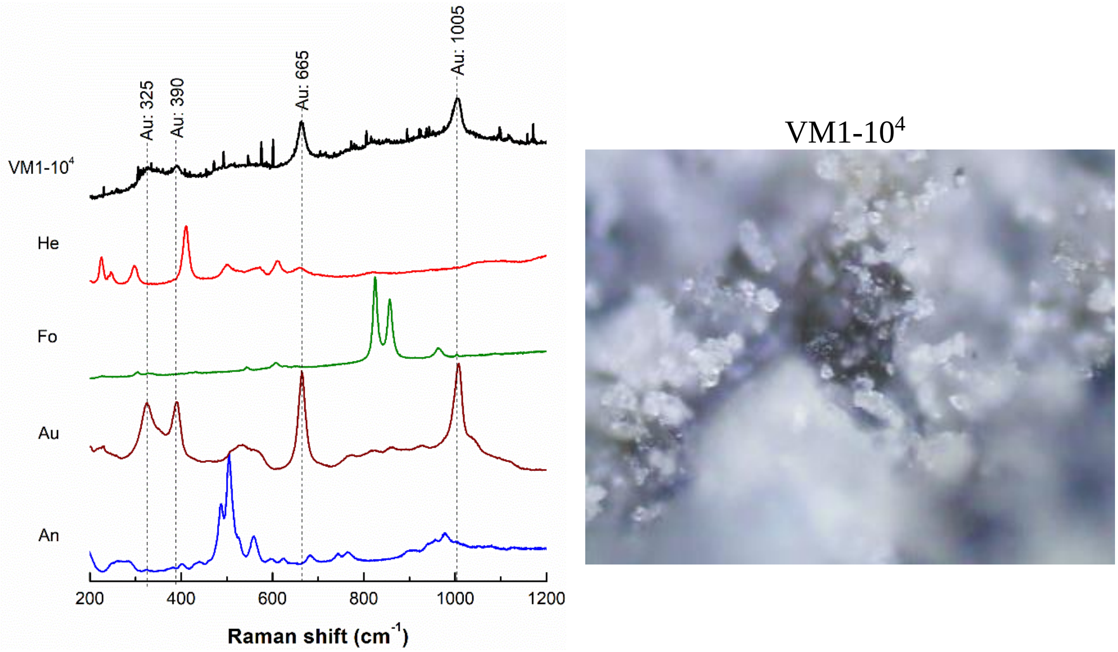

Fig. 4.12 - Overlapping of Raman spectra regarding the sample VM1-10 and some mineralogical phases downloaded by rruff database (An: anorthite, Au: augite, Fo: forsterite, He: hematite) and micrograph of spot analyses corresponding to the spectrum.

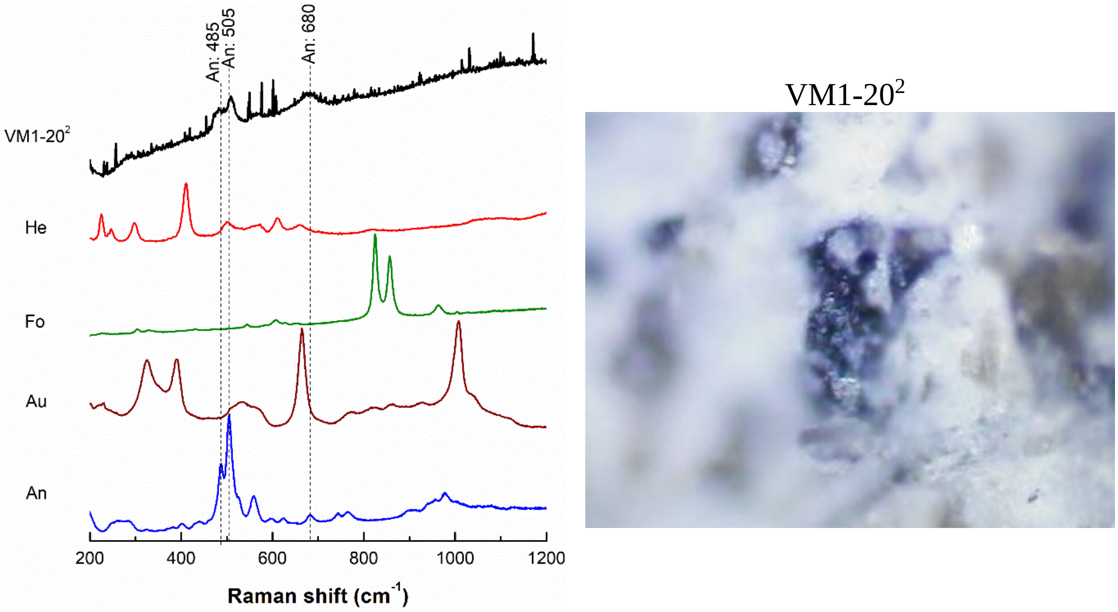

Fig. 4.13 - Overlapping of Raman spectra regarding the sample VM-20 and some mineralogical phases downloaded by rruff database (An: anorthite, Au: augite, Fo: forsterite, He: hematite) and micrograph of spot analyses corresponding to the spectrum.

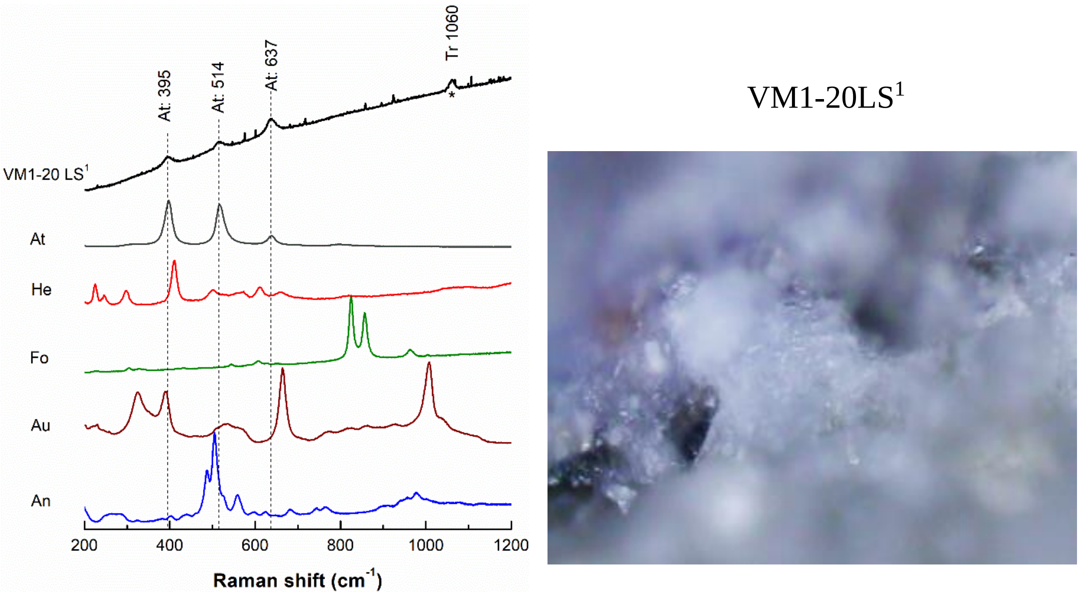

Fig. 4.14 - Overlapping of Raman spectra regarding the sample VM1-20LS and some mineralogical phases downloaded by rruff database (An: anorthite, Au: augite, Fo: forsterite, He: hematite; At: anatase) and micrograph of spot analyses corresponding to each spectrum. The peak indicated with "" corresponds to trona phase according to rruff catalogue (R050499).*

Differently, ghiara samples evidenced more complex spectra including more than one mineralogical phase. Indeed, GM1-10 sample showed peaks corresponding to hematite (228, 247, 295 and 410 cm^{-1}), anorthite (508 cm^{-1}) and augite (665 cm^{-1}) (Fig.

4.15). A spectrum of the sample GM1-20 evidenced hematite (225 and 295 cm^{-1}), pyroxene phases: augite (325, 390, 665 and 1005 cm^{-1}) with a possible contribution of diopside (355 cm^{-1}) due to more structured band in the range 300-400 cm^{-1}, while only contributions of anatase phase (395, 515 and 638 cm^{-1}) was recorded in the other spectrum (Fig. 4.16). Instead, in the spectra of the sample with low silicate (GM1-20LS) anatase (395, 515 and 638 cm^{-1}) and quartz (210, 265, 355 and 465 cm^{-1}) are detected, demonstrating the partial dissolution of metakaolin (Fig. 4.17). Finally, no evidences of geopolymeric gel in the spectra were observed regardless volcanic precursor used, but only detection of mineralogical phases maybe due to their predominance on gel of new formation.

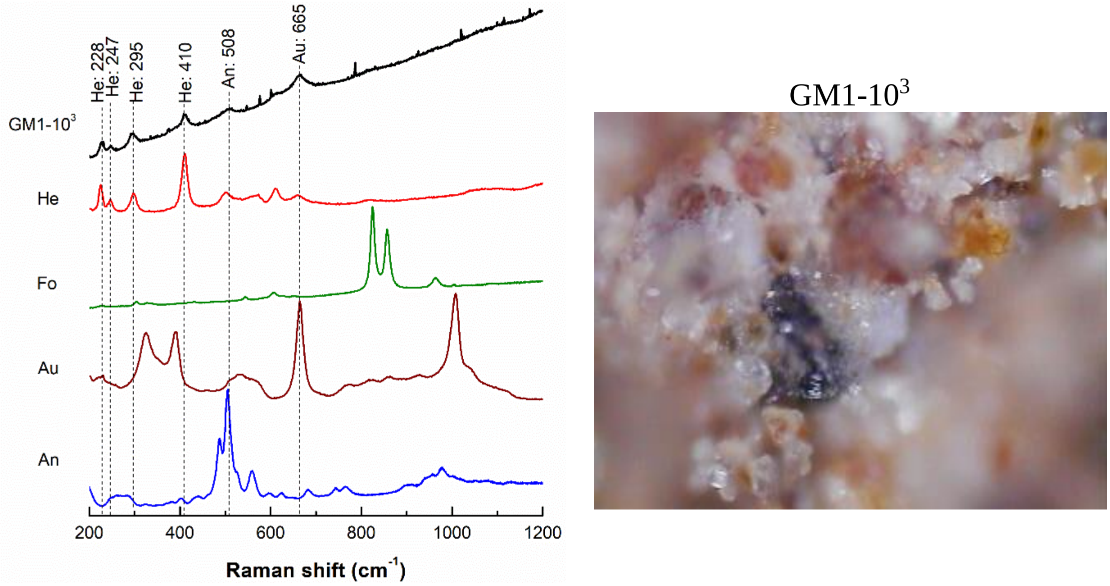

Fig. 4.15 - Overlapping of Raman spectrum regarding the sample GM1-10 and some mineralogical phases downloaded by rruff database (An: anorthite, Au: augite, Fo: forsterite, He: hematite) and micrograph of spot analyses corresponding to the spectrum.

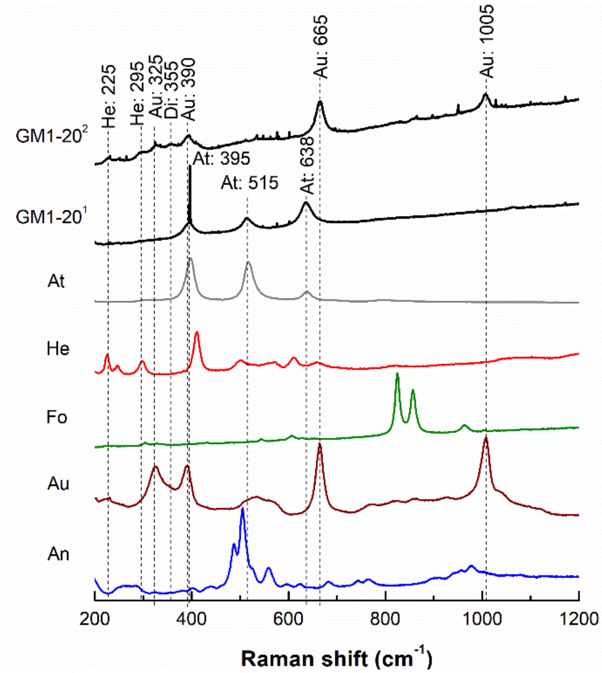

GM1-20^1 GM1-20^2

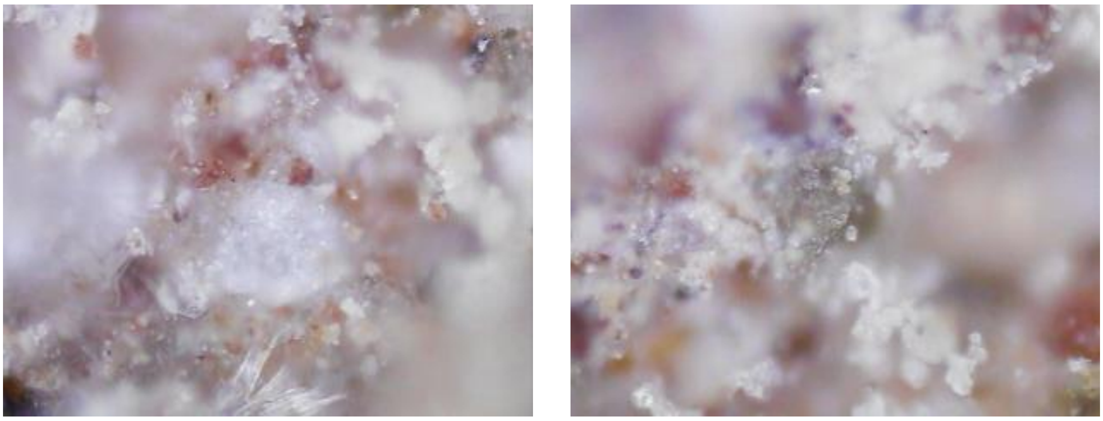

Fig. 4.16 - Overlapping of Raman spectra regarding the sample GM1-20 and some mineralogical phases downloaded by rruff database (An: anorthite, Au: augite, Fo: forsterite, He: hematite; At: anatase) and micrographs of spot analyses corresponding to each spectrum.

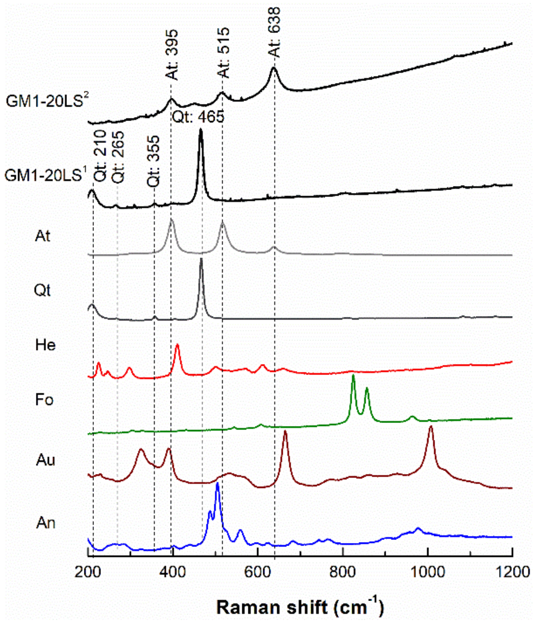

GM1-20LS^1 GM1-20LS^2

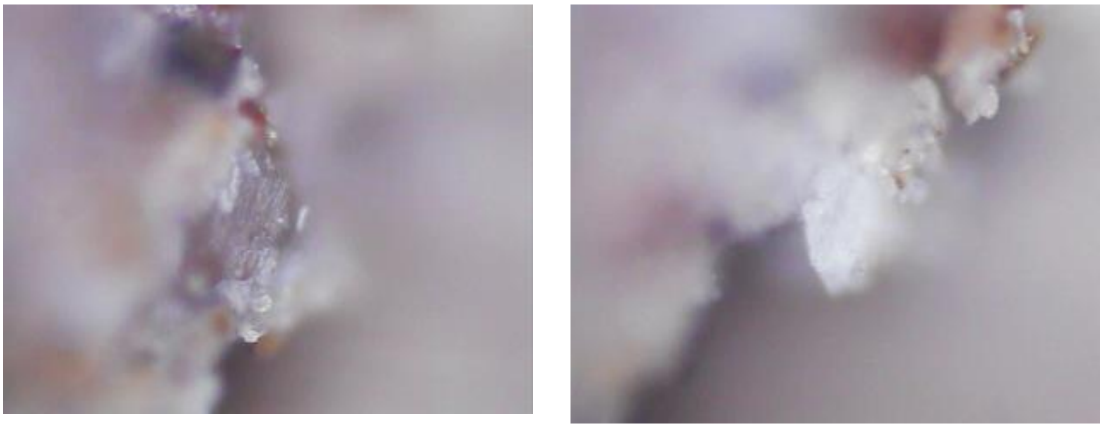

Fig. 4.17 - Overlapping of Raman spectra regarding the sample GM1-20LS and some mineralogical phases downloaded by rruff database (An: anorthite, Au: augite, Fo: forsterite, He: hematite; Qt: quartz; At: anatase) and micrographs of spot analyses corresponding to each spectrum.

4.3.5 SEM: MICROSTRUCTURAL ANALYSIS

All the SEM images obtained at low magnifications showed a microporous structure typical of these materials (Jean Noël Yankwa Djobo et al., 2017; Lemougna et al., 2018; Obonyo et al., 2014; Tchakoute et al., 2013; Yankwa Djobo et al., 2016) with variable pore size in the range of 50-200 μm and rounded shape (Fig. 4.18). These pores occurred during sample preparation as air entrapped during mixing was not able to get to the surface as a consequence of paste's high viscosity. The grains of volcanic ash appeared as irregular polyhedral particles with dimensions measured in the 20-100 μm range as well as reported by (Jean Noël Yankwa Djobo et al., 2017). Contemporary, other images were taken at high magnifications to evidence the finer microstructure and to collect the local chemical compositions in different spot analysis (Fig. 4.19a-d). Generally, the AAMs evidenced:

- A major micro porosity (pore diameter range 50-200 μm) was detected more abundant on samples with 10 wt% of metakaolin (VM1-10 and GM1-10) in comparison with the others (VM1-20 and GM1-20).
- All samples at high magnifications showed elongated and acicular crystals whose compositions appeared to be similar to that of the sodium carbonate laid down onto the amorphous matrix of geopolymeric gel (Garcia-Lodeiro et al., 2011) (for example point “b” in Fig. 4.19a).
- Other grains were detected with affinities in chemical compositions to volcanic glass (point “a” in Fig. 4.19a), or relict mineralogical phases not completely reacted during alkali activation (e.g. point “a” in Fig. 4.19b).
- Plies of metakaolin foils are not evidenced, indicating a good mixing process during fresh paste preparation.

Cracks and void are difficult to analyse and discuss due to fracturing operation during sample preparation. Nevertheless, the presence of irregular polyhedral grains of volcanic ash act as reinforcement for the alkali activated matrix, with crack bending or crack deflection toughening mechanism as indicated by the arrows in Fig. 4.19d. Finally, microstructure results showed a good mixing, confirmed by total absence of plies of metakaolin foils, despite the evidence of volcanic glass and mineralogical relicts. In order to obtain a chemical preview of morphological sketch, different elements maps were performed on VM1-10 sample, chosen as representative one (Fig. 4.20). The predominant chemical elements are Si, Al and Ca which represent the polyhedral grains (Fig. 4.20 a-c), while Na is mainly located around them where gel prevails (Fig. 4.20 f).

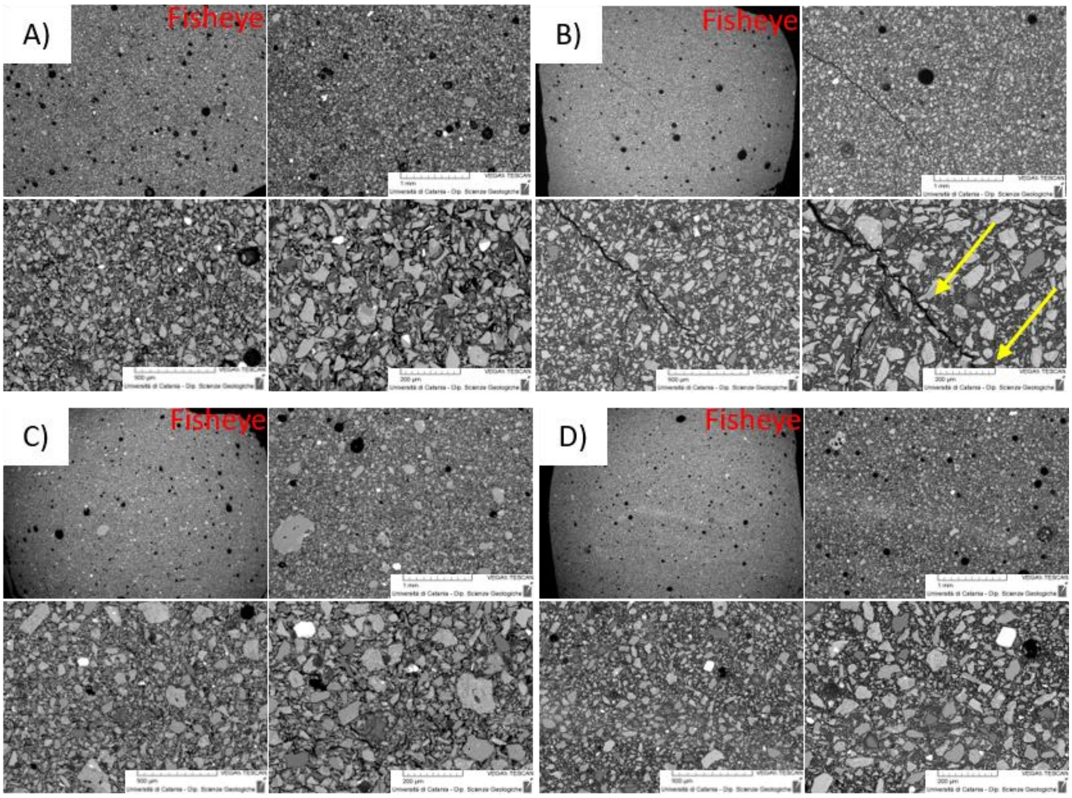

Fig. 4.18 (a-d) – SEM images at high magnifications. Legenda: a) sample VM1-10; b) sample VM1-20; c) sample GM1-10; d) sample GM1-20. Images acquired respectively in fisheye, 53x, 124x and 228x (magnifications). Crack deflection mechanism indicated by yellow arrows.

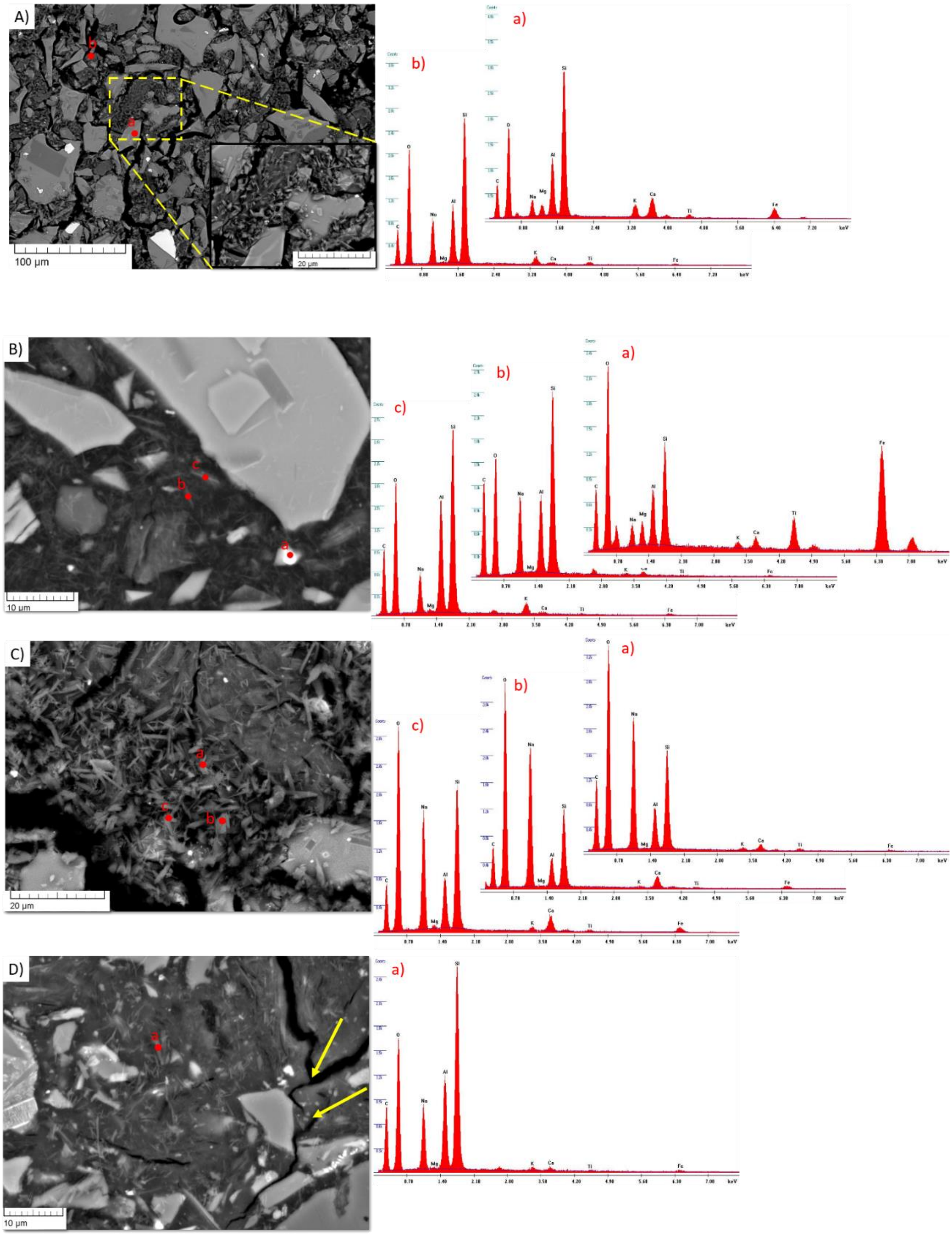

Fig. 4.19 (a-d) – SEM micro-images of thin sections with high magnifications with spot analysis expressed in red dots, EDS spectra of representative point analyses and tables with histograms where weight of the oxides (% wt.) are listed. Legenda: A) sample VM1-10 (magnifications 498x and 2.38 kx); B) sample VM1-20 (magnification 3.67 kx); C) sample GM1-10 (magnification 2.58 kx); D) sample GM1-20 (magnification 3.23 kx). Crack deflection mechanism indicated by yellow arrows.

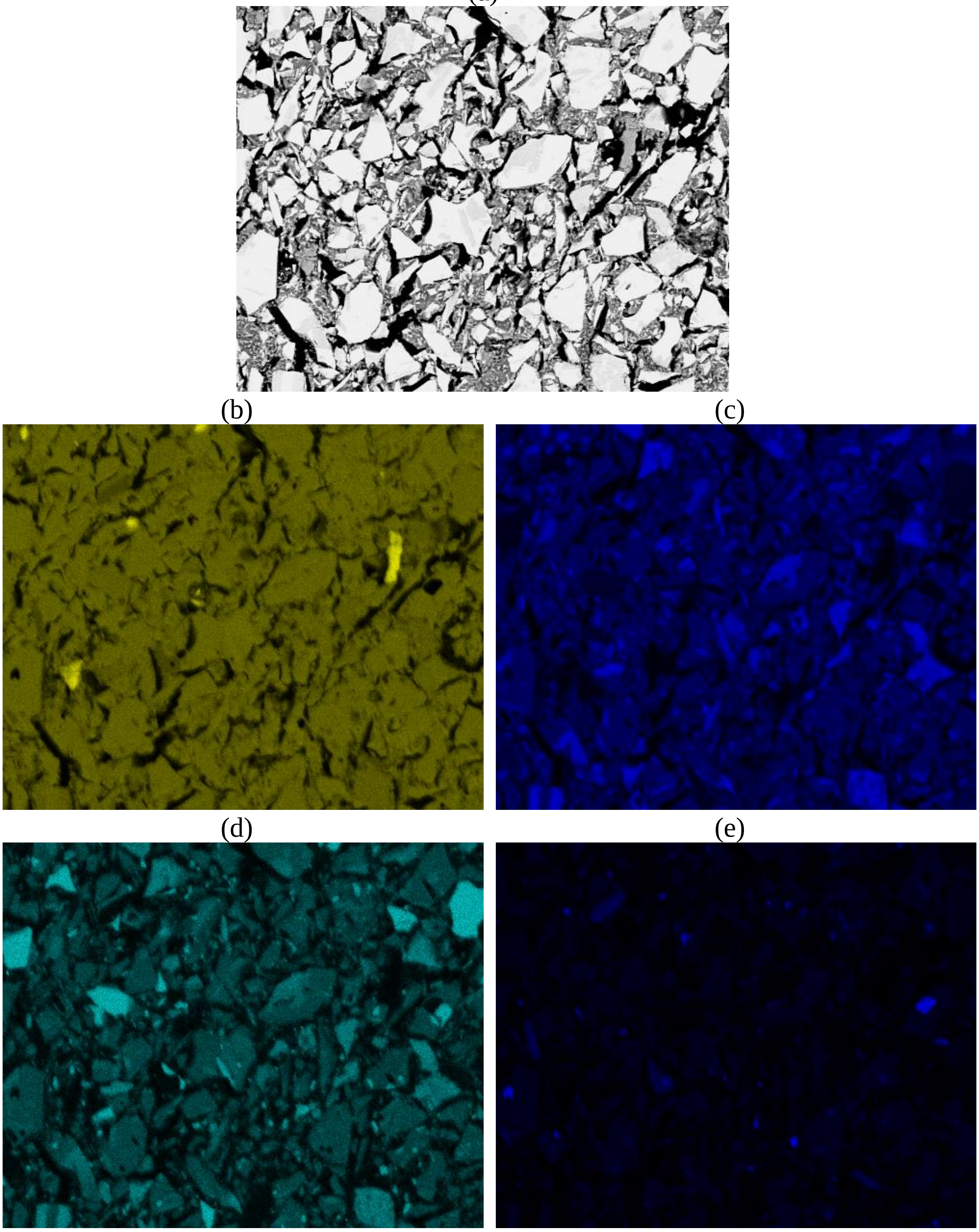
(a)

(b) (c)

(d) (e)

(f) (g)

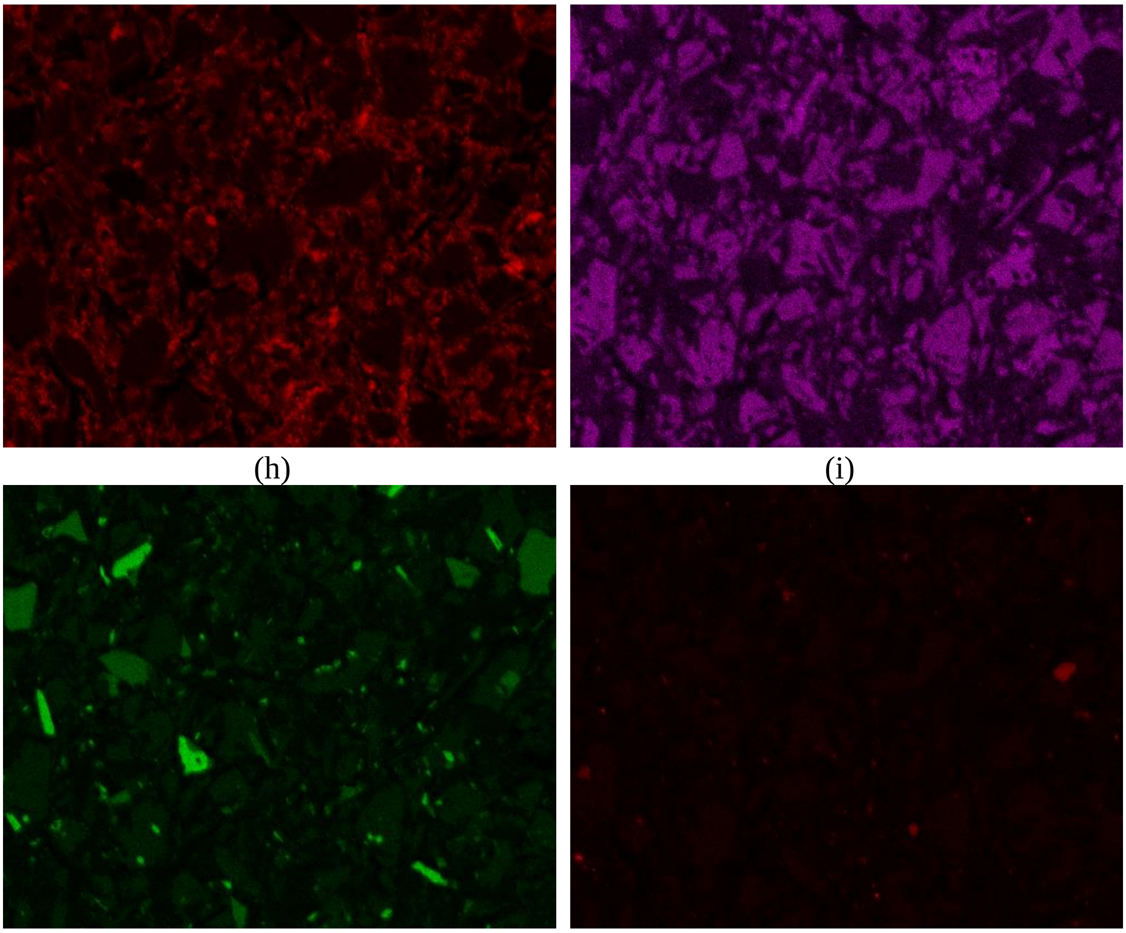
(h)
(i)

Fig. 4.20 (a-i) - Elements maps of VM1-10 sample: a) backscattered electron (BSE) map; b) SiK; c) AlK; d) Ca; e) FeK; f) NaK; g) KK; h) MgK; i) TiK.

4.3.6 MECHANICAL COMPRESSIVE STRENGTH

The samples of VM1 and GM1 series, including their "green" formulations (labelled with suffix LS), showed density ranging 1.7 - 2 g/cm^3 calculated after 24/36 h and the rectification step of the specimen's surfaces. The mechanical compressive values range from 10 to 38 MPa after 28 days of curing (Table 4.5). The values of both series showed a positive correlation with the progressive metakaolin addition in the mixture, validating a direct proportion between the two factors (Fig. 4.21). This behaviour is more evident in GM1 set than VM1 set. However, the results of green formulations of both series, where precursors and activators were mixed in the same ratios, confirmed the similarity of these volcanic precursors. Generally, literature data concerning the mechanical compressive test of alkali activated materials (AAMs) show "higher" values in compressive strength due to the bigger size of the specimens. Indeed, the small sizes of the samples used for the compressive test may have influenced the final strengths due to the high concentration of small defect, eventually produced by the air bubbles entrapped in the paste during the mixing. Therefore, assuming the distribution of these defects as constant in the large samples, much higher compressive strength during tests according to norm UNI EN 826 (Thermal insulating products for building applications - Determination of compression behavior) are supposed.

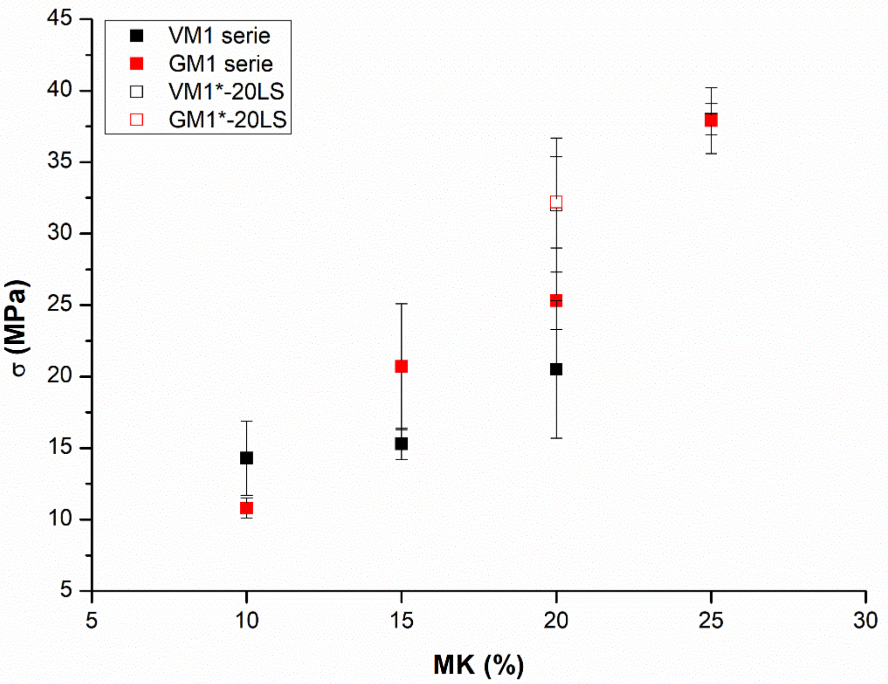

Fig. 4.21 – Correlation between compressive strengths and metakaolin (wt.%) (including standard deviation).

Table 4.5 – Summary table with the average values regarding the density after 24/36 h and mechanical strength after 28 curing days with its relative standard deviation (S.d.).

	After 28 curing days		
Labels	*AAMs ρ (g/cm^3)*	*σ (MPa)*	*S.d. (±)*
VM1-10	1.9	14.3	2.6
VM1-15	1.9	15.3	1.1
VM1-20	1.8	20.5	4.8
VM1-25	1.8	38.0	1.1
VM1*-20 LS	2.0	32.0	4.7
GM1-10	2.0	10.8	0.7
GM1-15	2.0	20.7	4.4
GM1-20	1.9	25.3	2.0
GM1-25	1.9	37.9	2.3
GM1*-20 LS	2.0	32.2	3.2

4.3.7 WATER ABSORPTION AND POROSITY

According to total absorption test results, the analysed samples reached the saturation very rapidly. Indeed, the water absorption range between 9-15 % for both volcanic precursors (Table 4.6). Moreover, the samples with only 10% wt. of metakaolin evidenced the lowest percentage. However, these results may have been influenced by efflorescence formation.

Table 4.6 - Results of permeable porosity test for total absorption (W_a) and average density of cubes prepared for mechanical compressive test.

Samples	**ρ (g/cm^3)**	**W_a%**
VM1-10	1.94	9
VM1-20	1.84	12
VM1*-20 LS	1.99	15
GM1-10	2.03	9
GM1-20	1.89	14
GM1*-20 LS	1.96	15

Hg porosimetry data showed a micro-porosity with an average accessible porosity of 27.31% and average pore diameter of 0.08µm for VM1 series while 26.06% and 0.05 µm for GM1 one (Table 4.7). Considering the amount of metakaolin added and the difference of alkaline solution in the "green" formulations, both series evidenced same features: the samples with 20% wt. of MK showed a higher volume in the pore sizes range 0.1-0.01µm than those with 10% wt., while the samples with lower liquid/solid ratio (*LS* samples) evidenced a similar pore volume distribution but a lower accessible porosity. All samples of both series were compared with the corresponding samples aged after one year (Fig. 4.22a-b). The average value of this latter highlighted a decrease of accessible porosity and an increase of pore volume in the range 0.1-0.01 µm while the pores in the range 100-1 µm decrease except for GM1-10 samples. Finally, the obtained results confirmed the micro porosity nature of these materials, highlighting a clear decreasing of pore size vs time, as well as reported by (Gunasekara et al., 2016). Indeed, the samples aged one year showed a cumulative pore volume higher in pore size range 0.1-0.01 µm contrary to the range 100-1 µm, than the younger ones, confirming the improving of durability properties with time due to on-going geopolymerization and gel production which fill voids in the gel matrix resulting in a more homogeneous and denser pore-structure with time. Generally, Ordinary Portland Cement (OPC) concrete has lower water absorption than geopolymer pastes, such as to define OPC in high permeable concrete (>5%) and low permeable concreate (<3%) (Gunasekara et al., 2016). However, considering the possibility to improve the microstructure of geopolymer concrete with the addition of graphene nanoplatelets (GNPs) to geopolymer binders (Albitar et al., 2017) and inversional proportionality between the water absorption and density of geopolymer paste, the obtained values match with those ones found by (Muthu Kumar & Ramamurthy, 2017), even though efflorescence phenomena could have influenced them.

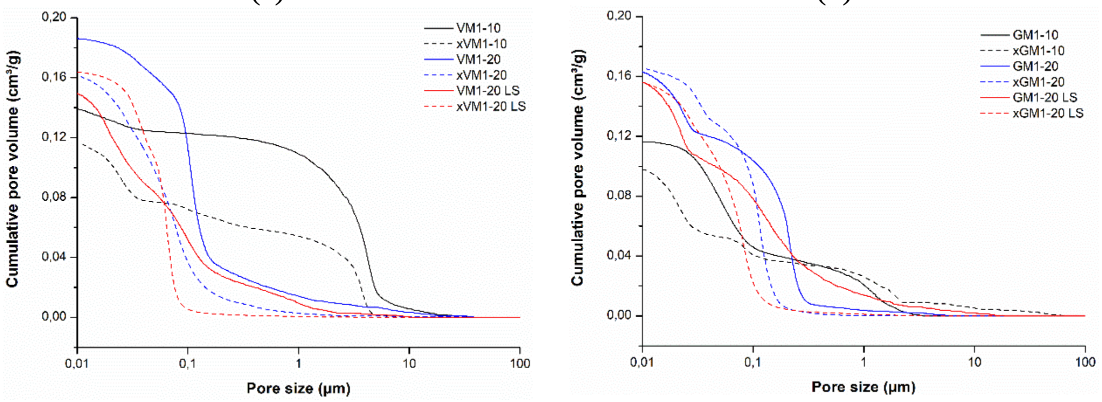
(a)
(b)

Fig. 4.22 (a-b) – Cumulative pore volume vs pore size graphs: a) representative samples of VM1 set and the corresponding aged one year (dashed lines); b) representative samples of GM1 set and the corresponding aged one year (dashed lines).

Table 4.7 – Density, porosity and pore information obtained by Hg porosimetry analysis. For each pore size ranges the total incremental volumes (%) were calculated. The prefix x indicates samples aged one year.

								∑ incremental volume (cm^3/g) in the following ranges:				
	Bulk density (g/cm^3):	**Accessible porosity (%):**	**Total pore volume (cm^3/g):**	**Total pore surface area (m^2/g):**	**Average pore diameter (µm):**	**Median pore diameter (µm):**	**Modal pore diameter (µm):**	**100-10 µm**	**10-1 µm**	**1-0.1 µm**	**0.1-0.01 µm**	**0.01-0.001 µm**
GM1-10	2.00	23.45	0.12	7.47	0.06	0.07	0.08	0.00	0.57	3.21	29.19	5.37
xGM1-10	1.66	16.77	0.10	11.77	0.03	0.06	0.01	0.06	0.70	1.16	14.49	5.28
GM1-20	1.78	29.49	0.17	13.29	0.05	0.16	0.23	0.00	0.04	18.08	46.51	9.06
xGM1-20	1.55	25.83	0.17	11.30	0.06	0.10	0.11	0.00	0.00	8.58	39.38	8.63
GM1*-20 LS	1.58	25.23	0.16	15.74	0.04	0.10	0.02	0.01	0.27	6.88	32.06	8.70
xGM1*-20 LS	1.74	27.31	0.16	14.39	0.04	0.06	0.07	0.00	0.01	1.91	107.03	9.24
VM1-10	1.76	24.88	0.14	4.71	0.12	3.13	3.98	0.08	12.24	6.41	18.53	7.58
xVM1-10	1.86	22.27	0.12	9.71	0.05	0.36	3.57	0.00	5.84	11.22	49.04	8.54
VM1-20	1.58	29.60	0.19	9.46	0.08	0.11	0.07	0.03	0.38	17.20	47.00	8.78
xVM1-20	1.73	28.06	0.16	14.94	0.04	0.06	0.06	0.00	0.03	4.22	85.04	8.91
VM1*-20 LS	1.80	27.46	0.15	16.80	0.04	0.06	0.02	0.00	0.16	4.19	41.69	8.48
xVM1*-20 LS	1.69	27.80	0.16	14.32	0.05	0.06	0.06	0.00	0.00	0.12	88.60	8.37
Tot. Average	1.73	25.68	0.15	11.99	0.06	0.36	0.69	0.02	1.69	6.93	49.88	8.08
Average AAMs ghiara	1.79	26.06	0.15	12.17	0.05	0.11	0.11	0.00	0.29	9.39	35.92	7.71
Average AAMs ghiara (x)	1.65	23.30	0.14	12.49	0.05	0.08	0.07	0.02	0.24	3.88	53.63	7.71
Average AAMs volcanic ash	1.71	27.31	0.16	10.32	0.08	1.10	1.36	0.04	4.26	9.26	35.74	8.28
Average AAMs volcanic ash (x)	1.76	26.04	0.15	12.99	0.05	0.16	1.23	0.00	1.96	5.18	74.22	8.61

4.4 CONCLUSIONS

The experimental results demonstrated the suitability of these materials for alkaline activation if cured at high temperatures or at room temperature with the addition of appropriated quantities of metakaolin. Furthermore, the NaOH and metakaolin amounts that restrict the appearance of efflorescence were identified. The choice of optimize the composition with the metakaolin instead of curing at high temperature is due to the need to apply as mortars in restoration application. Moreover, the chromatic aspects, essential parameter in Cultural Heritage field, between volcanic raw materials with the respective AAMs produced demonstrate a good compatibility, confirmed by the comparison with the colour classification ("Reichsausschuss für Lieferbedingungen" - RAL) which showed the following affinities: RAL 8019 for AAMs based on volcanic ash and RAL 8002 for AAMs based on ghiara (Fig. 4.23) (Barone et al., 2020).

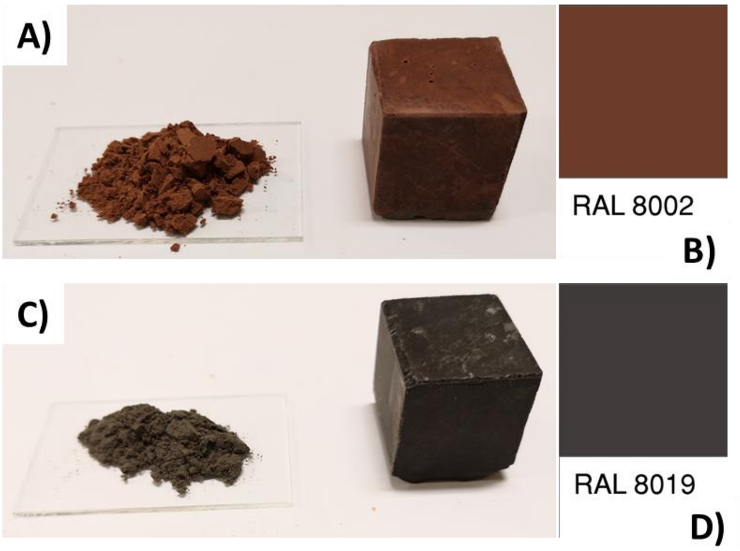

Fig. 4.23 – Chromatic comparison between the volcanic raw materials and the respective AAMs with the colour classification (RAL). Legenda: A) ghiara raw material and representative sample belonging to GM1 series; B) Colour card (RAL 8002) corresponding to signal brown; C) volcanic ash raw material and representative sample belonging to VM1 series; B) Colour card (RAL 8019) corresponding to grey brown.

5. I INSIGHT: COMPARISON BETWEEN TWO SAMPLES SET ACTIVATED BY NA AND K SOLUTIONS

In this chapter, the work carried out during my international period at the “Institut de recherche sur les céramiques” (IRCER) of Limoges (France) and followed by the supervisor Prof. Sylvie Rossignol will be explained. Briefly, volcanic raw materials were analysed and the performance of two different set of samples, activated respectively using a Na and K solutions and 10 and 20 wt.% of commercial metakaolin (used as additive component as already explained in previous chapters), were compared using different methods. Moreover, particular attention was taken on the study of polycondensation reaction, fingerprint of geopolymerization occurrence through *in situ FTIR*.

5.1 MATERIALS: PRECURSORS, ACTIVATORS AND GEOPOLYMERS

Volcanic ash deposits and volcanic paleo-soil, coming from Mt. Etna volcano (Italy), were chosen as aluminosilicate precursors for geopolymeric process, whose details are already explained in the Chapter 2. However, they have undergone some different steps of powder preparation: once sampled, the particles have been cleaned with water to remove organic elements and finest dust. Afterwards, they were dried at 110°C into the oven and dry milled (except the metakaolin because already milled) with porcelain jars and alumina balls after sediment quartering (Fig. 5.1a-c). In detail, volcanic ash was milled, once undergone a preliminary and manually sieving, starting from 500 µm (d90) for 1 hour, while ghiara starting from 120 µm (d90) for 45 min (Fig. 5.1d). The main aim is to obtain a grain size as closely as possible homogeneous among all the precursors with the low milling time to limit the operational cost. Granulometric measurements were performed for each material three times using laser particle sizer (Fig. 5.1e) and the average values were taken into account and listed in Fig. 5.2.

Fig. 5.1 – Milling and granulometric analysis of raw materials: a) sediment quartering; b) mechanical milling using porcelain jars; c) sieve to easily remove the alumina balls from the powder; d) final powder; e) laser particle sizer used to evaluate the granulometric curve of the volcanic precursors.

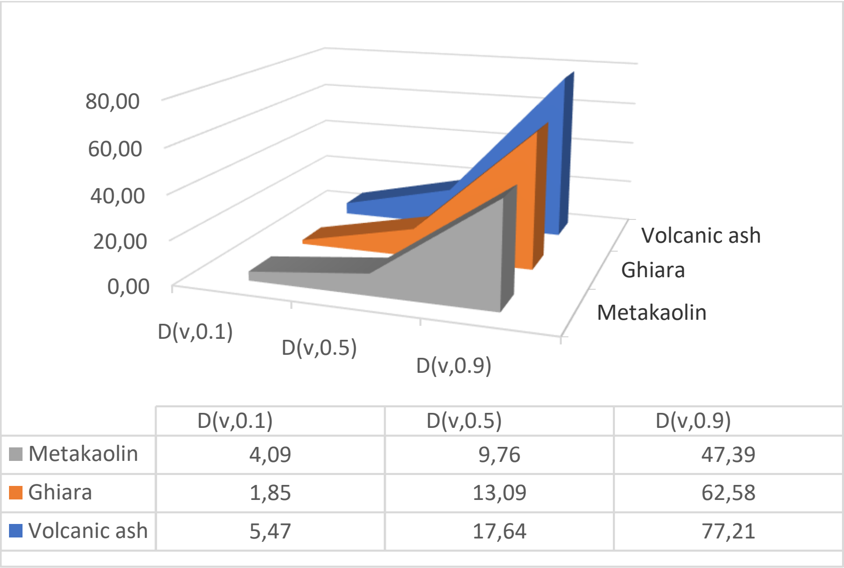

	D(v,0.1)	D(v,0.5)	D(v,0.9)
■ Metakaolin	4,09	9,76	47,39
🟧 Ghiara	1,85	13,09	62,58
🟦 Volcanic ash	5,47	17,64	77,21

Fig. 5.2 – Values of particle size distribution after dry milling.

For each volcanic raw materials, four alkaline activations were carried out using the addition of 10 and 20 % wt. (on the total weight of the powder) of metakaolin, known as ARGICAL™ M1000 (Gharzouni et al., 2014) (see for details Chapter 2.3), and two different alkaline activators based on Na or K alkaline cation. For the Na solution, combination of sodium hydroxide (8M) and sodium silicate, provided by Ingessil s.r.l.

with a molar ratio $SiO_2/Na_2O = 3$ was used, while a potassium silicate, commercially named Geosil 14515, provided by Wollner with 0.65 Si/K molar ratio (Gharzouni et al., 2015), were used for the K solution. Moreover, the density ρ (g/ml) of each solution was evaluated: Na solution 1.3, while K one 1.5. The same formulation protocol was used: preparation of solutions and following addition of the powders, once weighted in a precision balance; mixing with mechanical mixer for 5 minutes and, once filled the cylindrical plastic pots, vibrating to remove air bubbles. High viscosity was obtained for every formulation with a liquid / solid (L/S) ratio ~ 0.3 to reduce at minimum the use of alkaline solution and the setting time. Four samples for each volcanic precursor (indicating with the letter "V", the samples with volcanic ash, while with the "G", the samples with ghiara) were prepared: two activated by sodium solution (prefix Na-) and likewise the others by potassium (prefix K-) with the respectively of 10 and 20 % wt. of metakaolin (M-10 or M-20) used as additive to allow the reaction at room temperature, simulating so in situ applications. Therefore, the samples with volcanic ash activated by sodium solution were labeled with Na-VM-10 and Na-VM-20, while those with the potassium one, K-VM-10 and K-VM-20, as well as the samples with ghiara as listed in Table 5.1.

Table 5.1 – List of formulations, detailing labels, precursors and activating solutions.

Labels	***Volcanic powder***	***Metakaolin (% wt.)***	***Activating solution***
Na-VM-10	Volcanic ash	10	Sodium
Na-GM-10	Ghiara	10	Sodium
Na-VM-20	Volcanic ash	20	Sodium
Na-GM-20	Ghiara	20	Sodium
K-VM-10	Volcanic ash	10	Potassium
K-GM-10	Ghiara	10	Potassium
K-VM-20	Volcanic ash	20	Potassium
K-GM-20	Ghiara	20	Potassium

5.2 METHODS

All formulations developed in this case study were compared with the aim of highlighting the strengths and weaknesses in terms of polycondensation rate, structure and mechanical strengths. In detail, in this paragraph each method used will be explained. Two different FT-IR approaches were used using a Thermo Fisher Scientific 380 infrared spectrometer (Nicolet) (Fig. 5.3): i) punctual and continuous measurements on fresh alkaline pastes to observe the structural changes in time after the alkaline reaction; ii) measurements on consolidated samples after 21 days. For the first approach, a micro diamond cell was used on all fresh pastes for punctual analysis carried out at different time, starting from 0 to 30 hours, in addition to progressive analysis in time from 0 to 8 hours with collection every 10 min (Fig. 5.3f). In detail, once mixed the aluminosilicate sources with both alkaline solutions, a drop of each formulation was deposited onto diamond substrate of FTIR apparatus in the ATR mode to monitor the structural development of the synthesized mixtures. The main advantage of this technique is to observe two steps: solid mixture dissolution's and the geopolymerization process, thus highlighting the kinetic variations of samples activated respectively with both alkaline solutions. Contrary, KBr method was carried out as second approach, whose details are reported in Chapter 2.4.

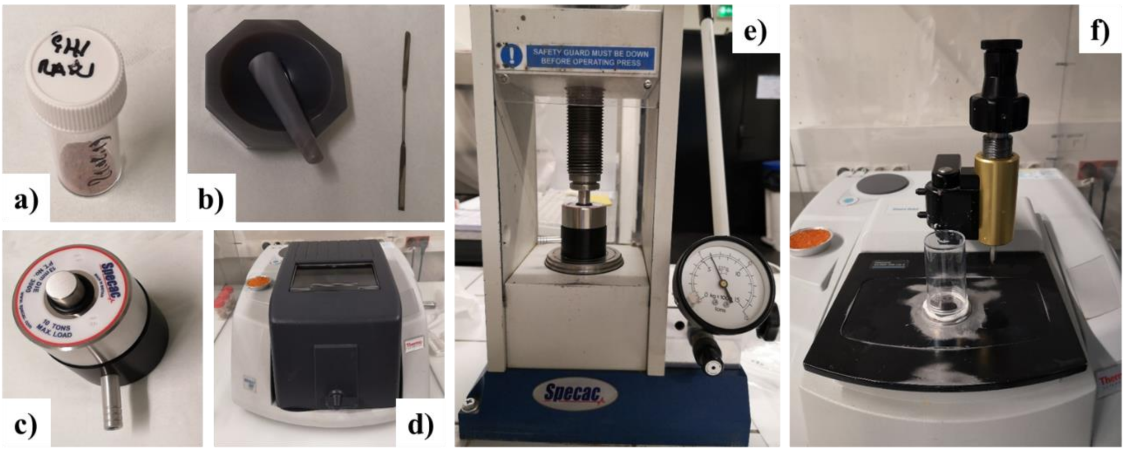

Fig. 5.3 – Photos of FT-IR equipment and sample preparation: a) little plastic pot with powder to be analysed; b) small agata mortar with alumina spatula for sample preparation; c) matrix "Specac" for pressure step; d) Thermo Fisher Scientific 380 infrared spectrometer (Nicolet) programmed for KBr measurements; e) press used to pellet preparation; f) analysis on fresh slurry of geopolymer in ATR mode.

X-ray diffraction (XRD) patterns were acquired using a Brucker-D8 Advance with a Bragg-Brentano geometry and a Cu Kα1α2 detector (Fig. 5.4). The analytical range is between 20 and 50 (2 θ) with a resolution of 0.02 (2 θ) and a dwell time of 1.5 s. Phase identification was performed with reference to a Joint Committee Powder Diffraction Standard (JCPDS). The patterns were processed using Eva software.

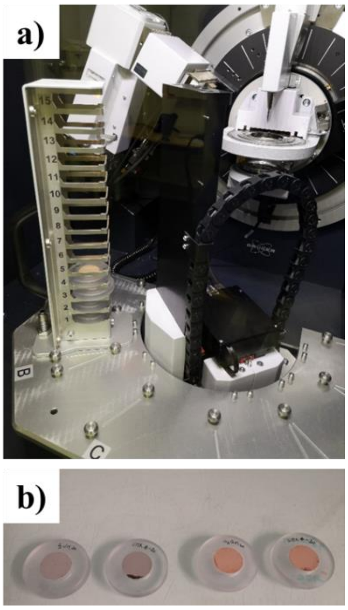

Fig. 5.4 – XRD analysis: a) XRD equipment of IRCER (Limoges University): Brucker-D8 Advance with a Bragg-Brentano geometry; b) geopolymer specimens in powder ready to be analysed.

Thermogravimetric analysis (TGA) analysis were performed on geopolymers with 20% wt. of MK addition, using an SDT-Q600 apparatus from Thermal Analyzer in an atmosphere of flowing dry air (100mL/min) (Fig. 5.5a-b). The signal was measured with Pt/Pt-10% Rh thermocouples. The geopolymers were heated at 500°C with a rate of 5°C/min using platinum crucibles (Fig. 5.5c-d).

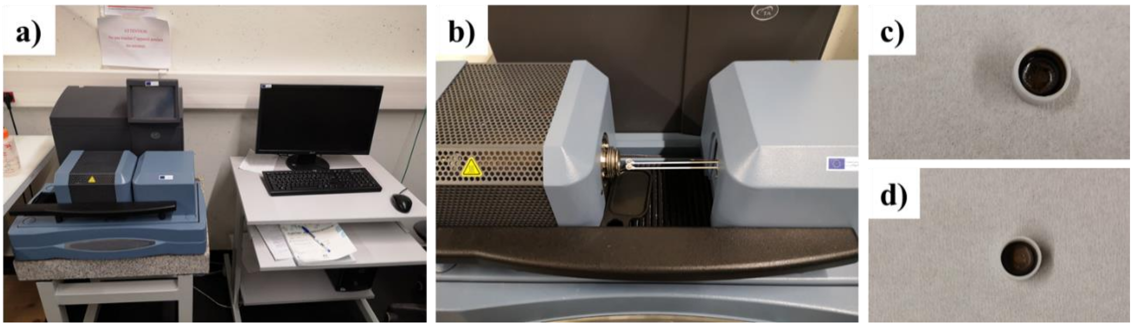

Fig. 5.5 – a) TGA equipment; b) detail of sample measuring; c) sample of geopolymer based on volcanic ash after TGA; d) sample of geopolymer based on ghiara after TGA.

Compressive test was performed on 5 samples of each formulations (Fig. 5.6a), using an Instron 5969 universal testing machine with a crosshead speed of 0.5 mm/min and a 50 kN sensor. The samples were cylindrical in shape with a diameter of 15 mm and a height of approximately 30 mm. Once hardened and before to broke them, respectively at 7 and 21 days, rectification on both basal surfaces were carried out to obtain homogenous and parallel surfaces (Fig. 5.6b-g).

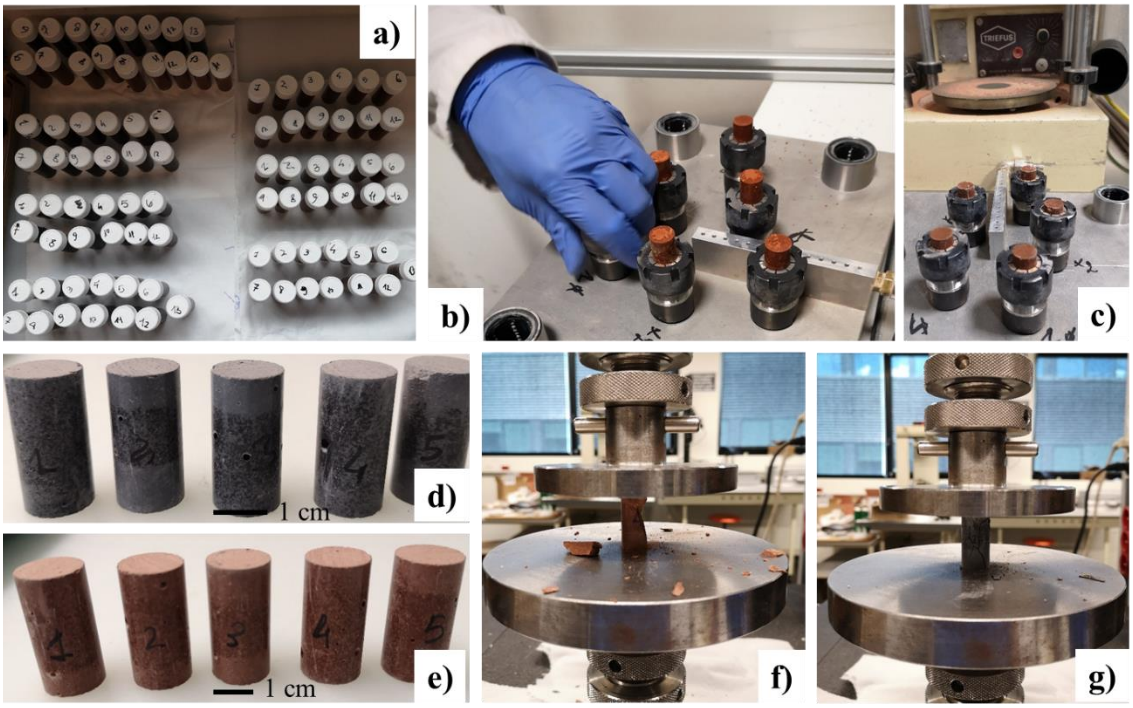

Fig. 5.6 – Photos of mechanical compressive test: a) panoramic of samples prepared and cured in plastic pots; b) filling of accommodations to polish both surfaces of samples; c) polishing phase through abrasion mechanism; d) volcanic ash samples after surfaces rectification; e) ghiara samples after surfaces rectification; f) breaking moment of ghiara sample after compressive test; g) breaking moment of volcanic ash sample after compressive test.

At the end of my abroad experience in France, I continued to analyse these samples at my department through measurements of Raman spectroscopy and Hg intrusion porosimetry (MIP), already described in Chapter 4. Moreover, morphological and EDX analysis were carried out using a Gemini Field Emission SEM (FE-SEM) Carl Zeiss SUPRA 25, equipped with an EDAX EDX detector of Physics and Astronomy Department (Catania University). Data were collected using a voltage of 20 kV and different magnification according the interest of spot analysis. The analysis surfaces were covered with a thin layer of gold to prevent charging of the specimen and to increase signal to noise ratio.

5.3 RESULTS

5.3.1 IN SITU ATR-FTIR SPECTROSCOPY ON FRESH SLURRIES

FTIR spectroscopy in ATR mode, also known as *in situ ATR-FTIR spectroscopy*, was used for the first time to monitor the kinetics of geopolymer gel formation on fresh slurries based on fly ash (Rees et al., 2007). Moreover, this method is applied to assess the effects of precursors and the activating solutions on structural evolution which reflects the reorganization of the network due to a geopolymerization reaction. The shift toward lower wavenumbers over time of Si-O-M is characteristic of polycondensation reaction occurrence (Autef et al., 2013). Once activated the aluminosilicate sources through alkaline solutions, the fresh pastes were monitored by in-situ FTIR spectroscopy to record the structural evolution. The final result reflects the trend reported in Fig. 5.7, which shows the overlapping of each acquisition and the shift toward low wavenumbers. The main peak position related to Si-O-M band is plotted in function of time in Fig. 5.8. Whatever the sample, a continuous and progressive shift of the Si-O-M band position in time toward lower wavenumbers was evidenced. This behaviour indicates the substitution of Si–O–Si by Si–O–Al bonds which reflects a polycondensation reaction (Gharzouni et al., 2016). Moreover, the slope of the curve is characteristic of the kinetics of this substitution (i.e. low slope indicates a slow kinetic) (Autef et al., 2013). Na/K-VM-10/20 showed the same behaviour regardless of the different quantity of metakaolin added in the mixture: in both cases, the trends of the samples, activated with Na solution, highlighted higher wavelengths then that ones with K solution (Fig. 5.8a-b). Analogously, Na/K-GM-10/20 showed the same trend. However, differently from Na/K-VM-10/20, the samples with 20% of M (metakaolin) showed a higher displacement among the two trends (Fig. 5.8d), while a different behaviour was recorded for the samples with 10% of M: initially, the trends showed the high displacement, but, which was recovered over time (Fig. 5.8c). For all the samples considered regardless the type of volcanic precursors used and the quantity of M added, the shift is almost the same reaching values ranging 12-18 cm^{-1}, as well as the slope of the curves expect for Na/K-GM-10 sample. Therefore, FT-IR analysis in situ on the slurries were useful to demonstrate the occurrences of polycondensation reactions. Moreover, the obtained shift values are characteristic of aluminosilicate network formation, although are lower than other formulations based on metakaolin (Gharzouni et al., 2014). However, to make sure of an exhaustive comprehension of the reaction rate, NMR analysis is necessary. To corroborate the trends just described and thus the polycondensation reaction occurrence, a counter-verification test was performed: the precursors were activated using only 40 wt.% of the standard potassium solution. The obtained trend showed an immediately increasing in wavelengths due to the drying in the time of the mixture and unsuitable contribution of alkaline solution able to trigger the alkaline reaction Fig. 5.9.

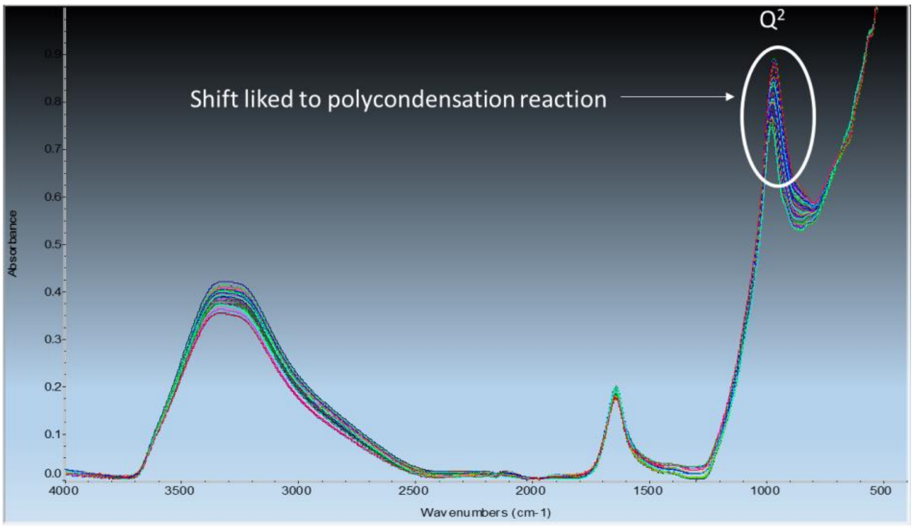

Fig. 5.7 – Demonstrative example of a polycondensation reaction occurrence through the progressive shift of in situ FTIR spectra over time (a spectrum represents the acquisition each 10 minutes).

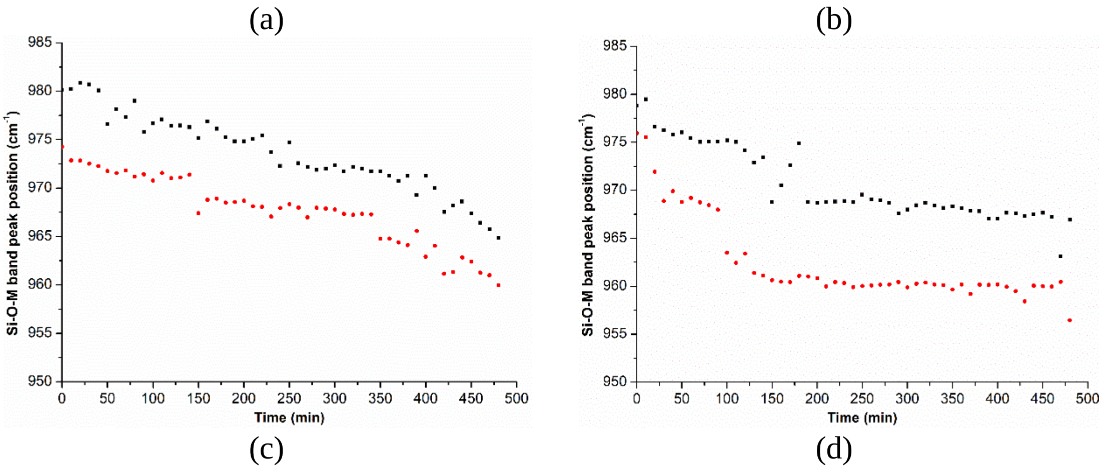

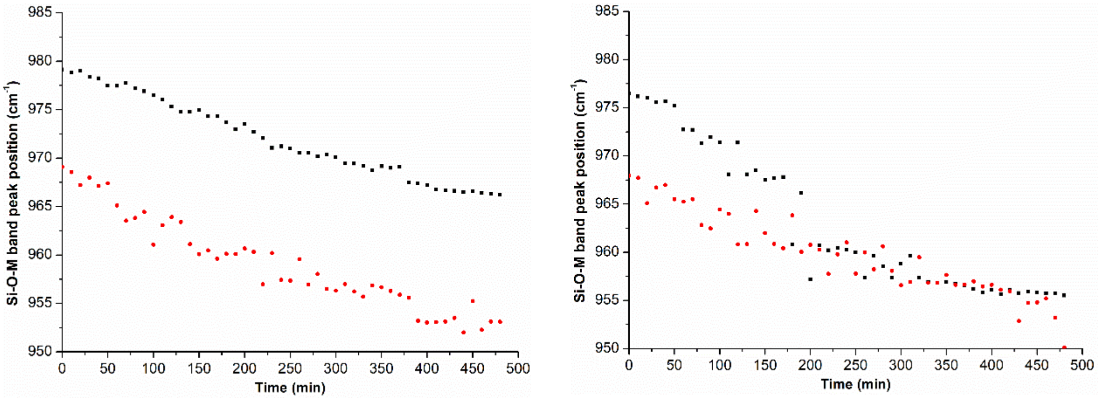

Fig. 5.8 – Trends of in situ FTIR regarding the progressive shift of Si-O-M positions in 8 hour (spectra resolution: 4 cm^{-1}). Legenda: (—) Na-VM/GM, (—) K-VM/GM; a) Na/K-VM-20; b) Na/K-VM-10; c) Na/K-GM-20; d) Na/K-GM-10.

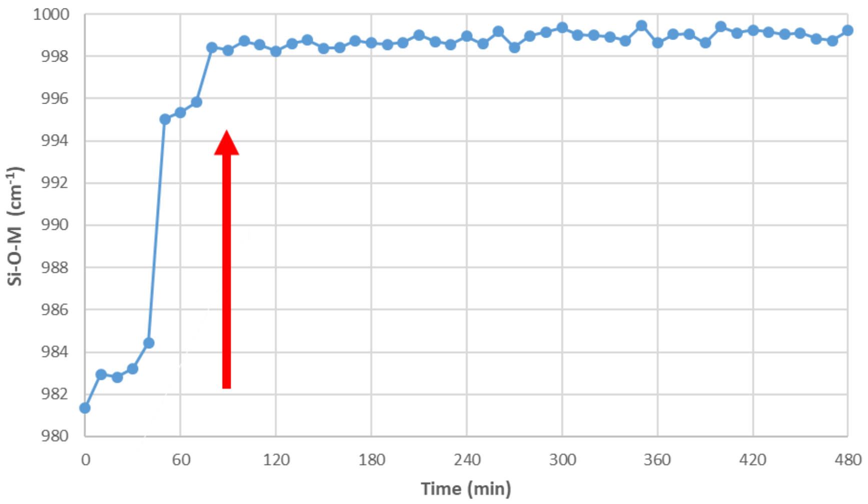

Fig. 5.9 – Demonstrative example of no polycondensation reaction.

Furthermore, with the aim to observe structural modification in a wider time window, punctual measurements were performed at different times, starting to 0 up to 30 hours on all fresh activated slurries. In Fig. 5.10, two representative FT-IR spectra, collected after 7 hours, are plotted, highlighting the differences between the two set of samples activated using Na and K solutions respectively. The comparison has evidenced a clear influence of K-silicate which contributed to the formation of a carbonate species, located at 1420/1380 cm^{-1} and ~880 cm^{-1} positions, contrary to the samples activated by Na solution. However, the contributions at ~880 cm^{-1} is more evident than the others and for this reason, it has plotted in the graph (Fig. 5.10). Therefore, free potassium cations could have been influenced the formation of carbonate phases (Rudolph et al., 2006).

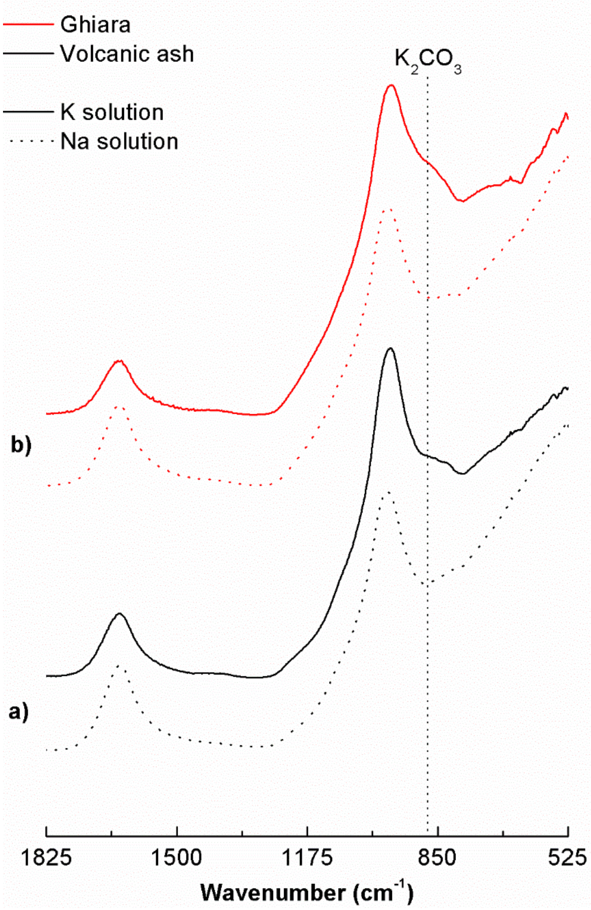

Fig. 5.10 – Comparison of effects caused by the activation with both alkaline solutions. A) Na/K-VM-20; B) Na/K-GM-20 (spectra resolution: 4 cm^{-1}).

Moreover, as already proposed above for the continuous infrared analysis (up to 8 hours), the evolution of each formulation was plotted up to 30 hours taking into account the position of Si-O-M band (Fig. 5.11). However, it must consider as a test not useful for the research due to the questionable trends caused by the difficulty of measurement approach in *sensu strictu* used. For every measurement different spot analysis of the slurry was taken to guarantee the cyclical measurement turnover of each formulation to limit the measurement-days and thus the availability of the equipment for the other researchers in the lab. Moreover, the need of preparing a "twin" slurry to allow the analysis at 17 and 18 hours in working time. Indeed, this latter more influenced negatively the results, highlighting the drops of trends at those times. Despite these difficulties, slight shifts were detected, ranging between 6-13 values, demonstrating the occurrence of polycondensation reactions, even if they are lower than those one detected in continuous analysis (12-18 cm^{-1}). However, the K-VM-20 sample showed a strange behaviour: similar values at starting and ending times. For this reason (and only for this sample), the lower value (related to 17 hours) was considered as ending point. This undesirable behaviour, as well as the anomalous difference of values between the measurements performed after 1 hours (17 and 18 hours) for the same sample have confirmed the intrinsic problems of this methodological approach. To sum-up these trends, the values were listed in the Table 5.2.

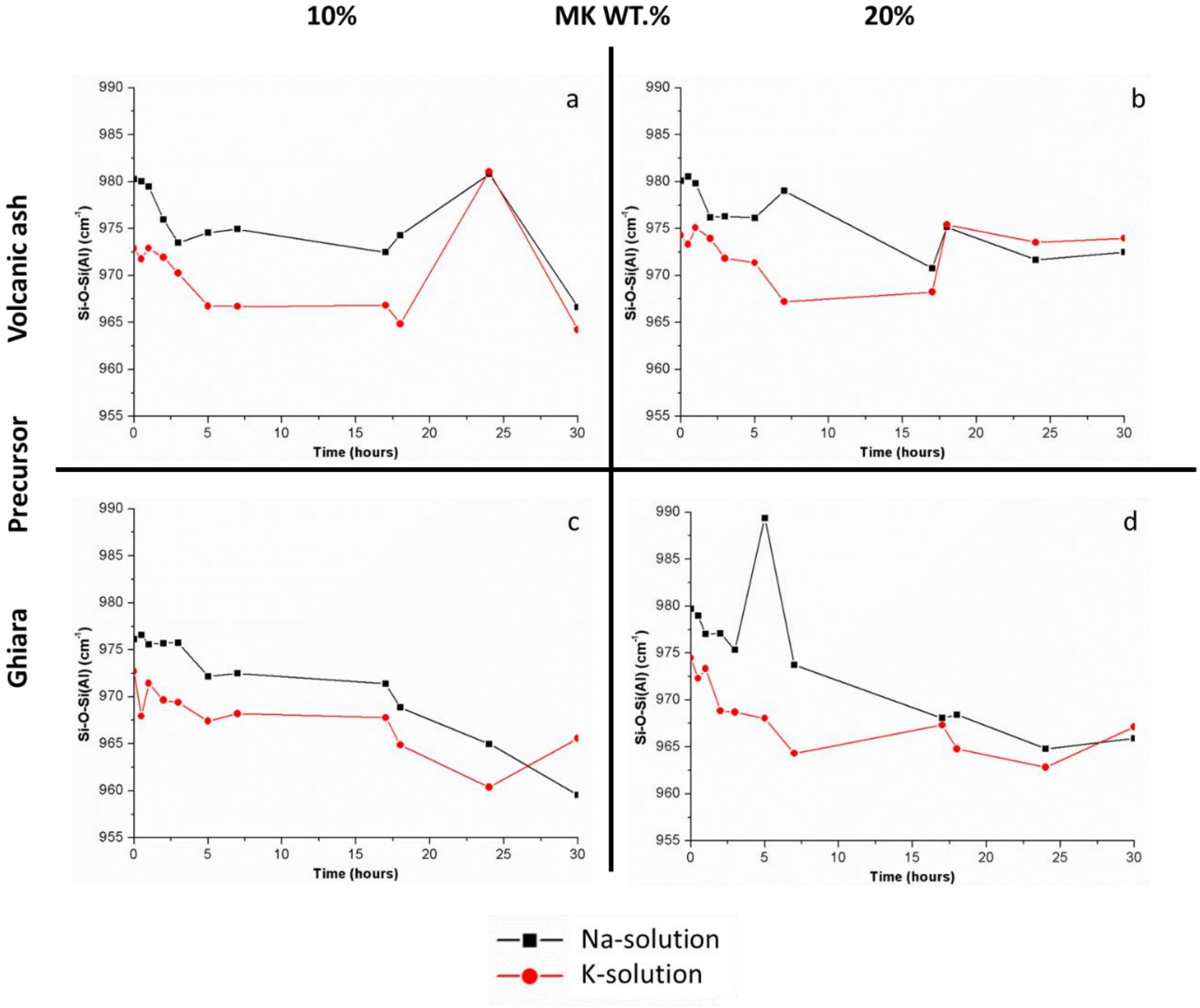

Fig. 5.11 – Trends of the progressive shift of Si-O-M positions over 30 hours obtained by in situ FT-IR analysis. Legenda: a) Na/K-VM-10; b) Na/K-VM-20; c) Na/K-GM-10; d) Na/K-GM-20.

To overcome the limit found with the approach just described, another analytical strategy was test. Considering the intensities of the positions at 1642 cm^{-1} and 920 cm^{-1} at different times: 0, 5, 18 and 30 hours, the corresponding ratios were calculated with the aim to define the progressive increase of this ratio in time, typical of alkaline activated materials (Gharzouni et al., 2014) (Table 5.3). The results showed two features: i) higher values in the samples activated by K solution than Na one; ii) higher values in VM-20 than VM-10, while opposite tendency for GM's samples. Therefore, according to these behaviours, regardless both series seem to be not comparable, seem that the potassium solution showed a higher alkaline degree triggering a more intense activation. However, also this test must consider itself as a proof because it has used a measurement approach not adequate to obtain results without errors.

Table 5.2 – Summary of all Si-O-M positions and values obtained by the differences between the starting and ending points (except for the sample K-VM-20 where the value of 17 hours was considered as ending point).

Na-VM-10		**K-VM-10**		**Na-VM-20**		**K-VM-20**		**Na-GM-10**		**K-GM-10**		**Na-GM-20**		**K-GM-20**	
Time (hours)	*Si-O-Si (Al) (cm^{-1})*	*Time (hours)*	*Si-O-Si (Al) (cm^{-1})*	*Time (hours)*	*Si-O-Si (Al) (cm^{-1})*	*Time (hours)*	*Si-O-Si (Al) (cm^{-1})*	*Time (hours)*	*Si-O-Si (Al) (cm^{-1})*	*Time (hours)*	*Si-O-Si (Al) (cm^{-1})*	*Time (hours)*	*Si-O-Si (Al) (cm^{-1})*	*Time (hours)*	*Si-O-Si (Al) (cm^{-1})*
0	980.27	0	972.89	0	980.12	0	974.28	0	976.11	0	972.73	0	979.72	0	974.49
0.5	980.04	0.5	971.77	0.5	980.52	0.5	973.34	0.5	976.56	0.5	967.96	0.5	979	0.5	972.32
1	979.5	1	972.91	1	979.83	1	975.09	1	975.55	1	971.44	1	977.02	1	973.34
2	975.97	2	971.95	2	976.19	2	973.94	2	975.71	2	969.65	2	977.1	2	968.83
3	973.51	3	970.26	3	976.31	3	971.83	3	975.73	3	969.4	3	975.33	3	968.69
5	974.56	5	966.75	5	976.14	5	971.35	5	972.19	5	967.41	5	989.37	5	968.05
7	974.95	7	966.71	7	979.01	7	967.21	7	972.49	7	968.2	7	973.74	7	964.31
17	972.49	17	966.84	17	970.79	17	*968.25*	17	971.38	17	967.78	17	968.08	17	967.34
18	974.29	18	964.84	18	975.16	18	975.39	18	968.86	18	964.86	18	968.45	18	964.78
24	980.8	24	981.08	24	971.68	24	973.54	24	964.98	24	960.37	24	964.8	24	962.84
30	966.62	30	964.22	30	972.49	30	973.99	30	959.54	30	965.56	30	965.9	30	967.13
Differences	***13.65***		***8.67***		***7.63***		*0.29* ***6.03***		***16.57***		***7.17***		***13.82***		***7.36***

Table 5.3 – Summary of all intensity ratios over time (t0, t5, t18 and t30 hours) considering the absorbance intensity of positions: 1642 and 920 cm^{-1}.

		Na-VM-10	***K-VM-10***	***Na-VM-20***	***K-VM-20***	***Na-GM-10***	***K-GM-10***	***Na-GM-20***	***K-GM-20***
Time	***Positions (cm^{-1})***	***Ratio***	***Ratio***	***Ratio***	***Ratio***	***Ratio***	***Ratio***	***Ratio***	***Ratio***
0	1642	2.22	3.26	2.06	3.21	2.36	3.57	2.28	3.65
	920								
5	1642	2.27	3.63	2.22	3.46	2.51	3.89	1.85	3.89
	920								
18	1642	2.26	3.58	2.54	3.12	2.52	3.96	3.28	4.83
	920								
30	1642	2.68	4.00	3.25	5.60	4.19	5.74	3.23	5.57
	920								

5.3.2 FTIR ON CONSOLIDATED SAMPLES AFTER 21 DAYS (KBR METHOD)

The structures of all consolidated samples were analysed also using FT-IR with KBr method. The results showed for both series (VM and GM) the same behaviour: no differences in terms of water content or silicate contributions. In the first case, vibrations of bound water molecules were recorded at 3445 and 1650 cm^{-1} assigned to the stretching (–OH) and bending (H–O–H) respectively (Jean Noël Yankwa Djobo et al., 2016; Tchadjié et al., 2016), while the silicate structure is characterized by the main peak located at 1015 cm^{-1} related to the vibration of SiO/Al–O bond of aluminosilicate framework reflecting the formation of the amorphous aluminosilicate gel in binary systems (Robayo-salazar et al., 2016) and by the ring vibrations of Si–O bonds of silicate network at 575 and 530 cm^{-1} (Jean Noël Yankwa Djobo et al., 2016; Tchadjié et al., 2016) (Fig. 5.12a). However, an evident difference in terms of intensity for the influence of carbonates, located at 1430 and 1385 cm^{-1} (Fig. 5.12b), corresponding to the stretching vibrations of O-C-O bonds in the carbonate group (CO_3^{2-}) due to the carbonation reaction between the carbon dioxide from the air and the geopolymer was recorded (Bernal et al., 2010; Cyr & Pouhet, 2016; Dupuy et al., 2020). The detected increases were caused by a larger carbonation due to high free ions amount. The contribution of carbonates is higher in the samples activated using potassium solution and in those one with 10 wt.% of M added revealing the presence of free alkali cation which can react with atmospheric CO_2 to form K_2CO_3 or Na_2CO_3 species (Gao et al., 2013), while the decreasing of intensity, recorded in samples with higher metakaolin amount can be explained by lower amount of alkali cation due to a better organization of geopolymer network. From FTIR data, it was evidenced that the formation of a reticulated network in sodium and potassium with the presence of some carbonate species in both series (Na/K-VM/GM), decreasing at increasing M content.

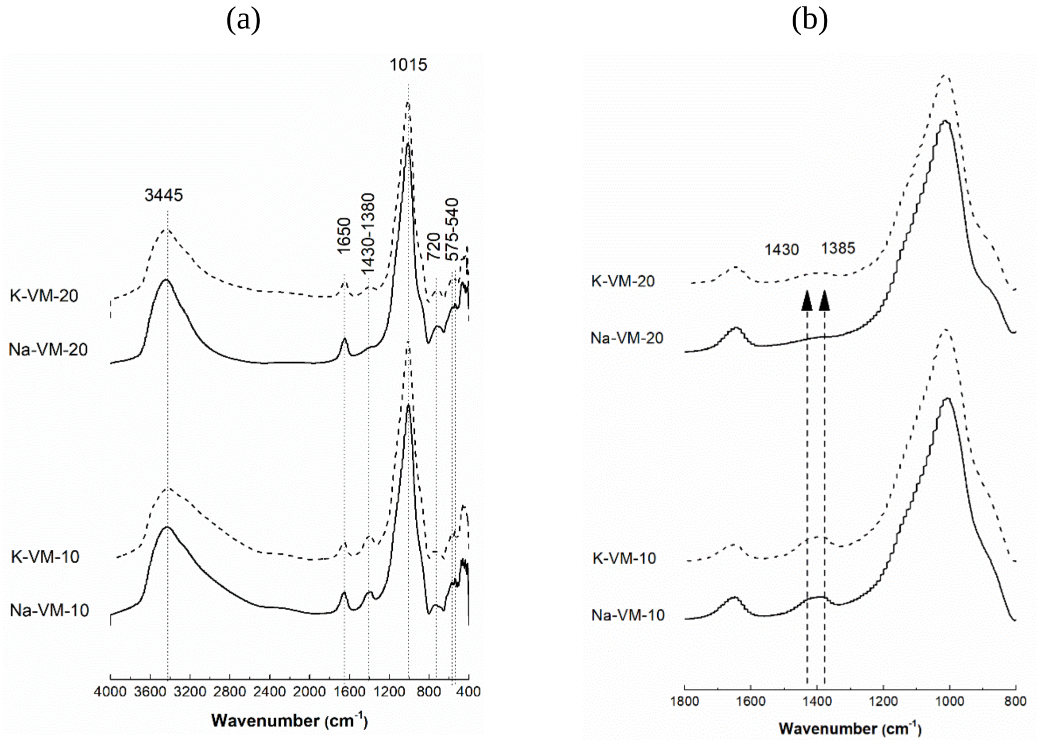

Fig. 5.12 (a-b) – a) FT-IR spectra obtained using KBr method collected in the range of 4000-400 cm-1 for (---) K-VM and (—) Na-VM; b) in the range of 1800-800 cm-1. The dashed arrows indicate the carbonate contributions.

5.3.3 XRD: MINERALOGICAL ANALYSIS

XRD analysis was also performed on the hardened materials (Fig. 5.13). All the samples showed anorthite, augite, forsterite, magnetite and hematite derived from original precursors (V and G) and quartz and anatase from metakaolin (M). However, in Na/K-VM-20 samples, anorthite and forsterite peaks showed lower intensity in comparison with raw material patterns, demonstrating a partial dissolution due to polycondensation reaction regardless of the alkaline solution used (Fig. 5.13) and revealing the low reactivity of volcanic materials in alkaline environment (Djobo et al., 2017). On the contrary in GM-20, a slight difference of intensity of anorthite peaks among Na and K samples were observed, highlighting a higher dissolution in K-GM-20 (Fig. 5.13) than in the Na-ones. Finally, these intensity modifications in comparison with volcanic raw materials can be associated to metakaolin contribution which induces the increase of the Si and Al species available, thereby favoring dissolution and network formation (Hajimohammadi et al., 2011; Ruiz-Santaquiteria et al., 2013).

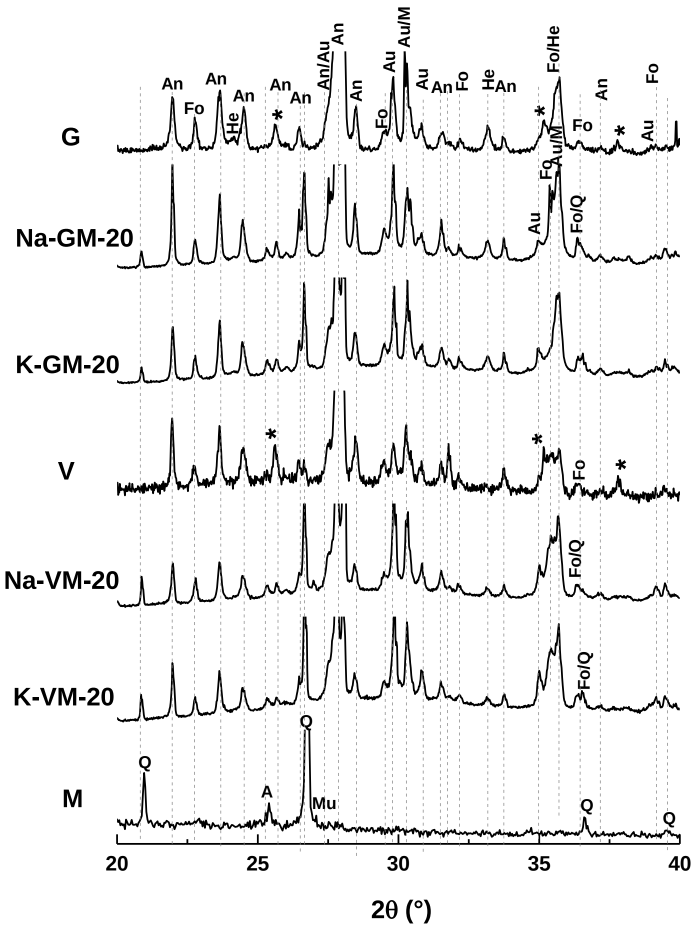

*Fig. 5.13 – XRD patterns of raw precursors and consolidated materials. Pdf files : Q : quartz (04-016-2085) ; An : anorthite (04-05-4988) ; Au : augite (04-017-4396) ; Fo : forsterite (04-017-0663) ; M : Magnetite (00-900-5814) Mu: muscovite (00-060-1516) ; He :hematite (00024-0072) ; A : anatase (00-021-1272), * corundum.*

5.3.4 THERMAL ANALYSIS

Thermal analysis was performed on all samples belonging to VM and GM series to compare the effect of the activating solutions on the thermal stability of the consolidated materials. Fig. 5.14 shows the thermal behavior of all samples, but only GM-10 samples, activated respectively by Na (Fig. 5.14a) and K (Fig. 5.14b) solutions, were amply described, because no main differences were found with the others. Regardless alkaline solution used, the major weight loss of 4.9 % is observed below 200 °C and reveals the water of the geopolymer samples (Gharzouni et al., 2015). Moreover, the remaining weight loss recorded at higher temperature (200-500°C) is minimal attesting below 1% related to the release of silicate or aluminate hydroxyl groups as in all materials

(Gharzouni et al., 2015). Furthermore, the heat flow profiles show a large endothermic peak from 25 to 125 °C, corresponding to water, which appears to be controlled by the alkaline solutions used. Indeed, the thermal curve of sample Na-GM-10 (Fig. 5.14a) shows a splitting of the large endothermic peak into two smaller ones (~ 30 and 70°C), slowly differently from sample K-GM-10, whose endothermic peak is centered around 50°C (Fig. 5.14b). The small difference is only due to the intensity of the both contribution corresponding to physical water's loss indicates that there are two type of evaporation process: one of the water molecules evaporating from the pores in the proximity of the particle surface (peak at 30°C), and one due to the evaporation of water entrapped pores (peak at about 70°C). Porosity in NaOH/Na silicate activated geopolymers seems to be finer than in the KOH/K silicate activated ones due to the difficulties of water to leave the pores. Further explanation in the paragraphs reporting porosity measurements (Table 5.6 and Fig. 5.17). All TGA results are reported in Table 5.4: generally, in the low temperature range (25-200°C), the samples activated by the potassium solution have evidenced a lower weight loss then those activated by sodium solution, except for Na-VM-20, which have showed a contrary tendency. Instead, GM-10 samples evidenced the same values irrespective of the alkaline solutions. These results correlated well with those obtained from FT-IR. The higher the reticulation degree, the lower amount of water is found in the geopolymeric network. In details, the weight loss recorded below 120-150°C is due to the water content located in the porosity of the samples where are entrapped few H_2O molecules produced during the polycondensation step of the geopolymerization reaction. Such progressive release of water molecules was observed with *in situ* FTIR analysis during the induration of the fresh pastes. No relation between water and amorphous network was observed with XRD analysis since no hydrated phases were detected. In addition, the TGA results did not show dihydroxylation phenomenon occurring generally from 300-800°C (temperature range for the study of residual polycondensation) (Duxson et al., 2007), demonstrating the stability of the aluminosilicate network and OH- groups already condensed.

(a)

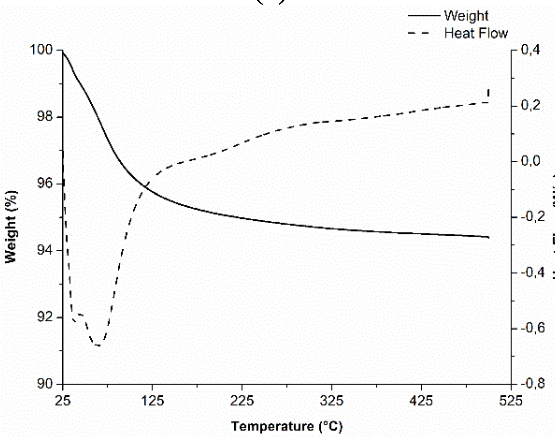
Weight
Heat Flow
Weight (%)
100
98
96
94
92
90
0,4
0,2
0,0
-0,2
-0,4
-0,6
-0,8
25
125
225
325
425
525
Temperature (°C)

(b)

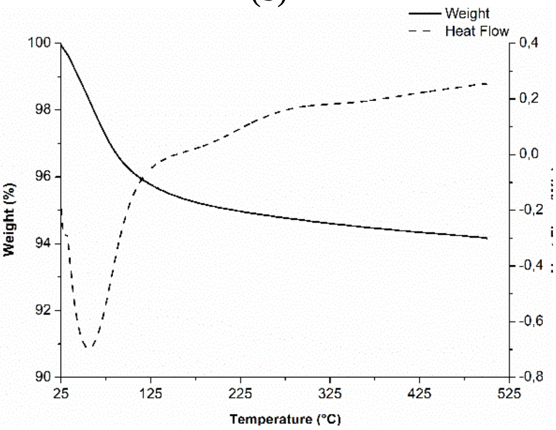
Weight
Heat Flow
Weight (%)
100
98
96
94
92
90
0,4
0,2
0,0
-0,2
-0,4
-0,6
-0,8
25
125
225
325
425
525
Temperature (°C)

(c)

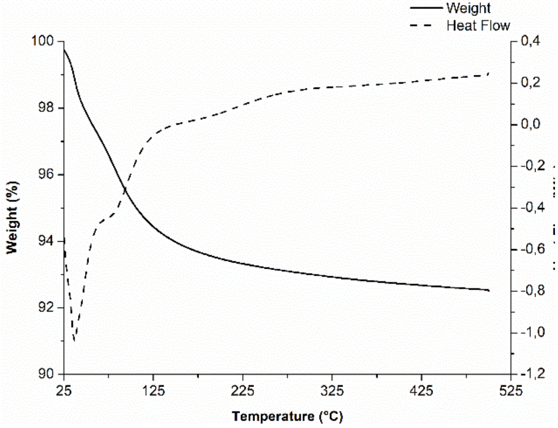
Weight
Heat Flow
Weight (%)
100
98
96
94
92
90
0,4
0,2
0,0
-0,2
-0,4
-0,6
-0,8
-1,0
-1,2
25
125
225
325
425
525
Temperature (°C)

(d)

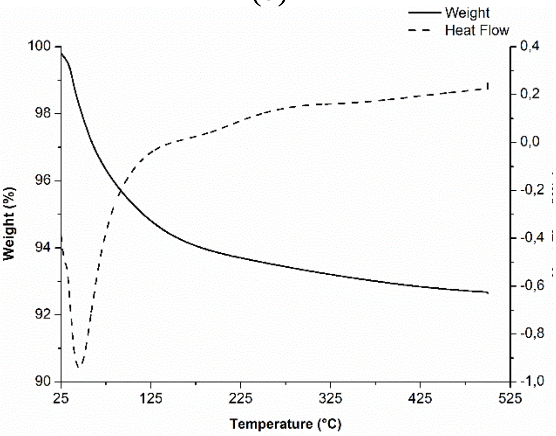
Weight
Heat Flow
Weight (%)
100
98
96
94
92
90
0,4
0,2
0,0
-0,2
-0,4
-0,6
-0,8
-1,0
25
125
225
325
425
525
Temperature (°C)

(e)

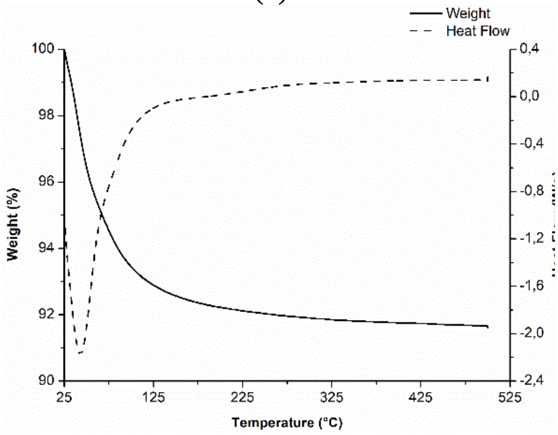
Weight
Heat Flow
Weight (%)
100
98
96
94
92
90
0,4
0,0
-0,4
-0,8
-1,2
-1,6
-2,0
-2,4
25
125
225
325
425
525
Temperature (°C)

(f)

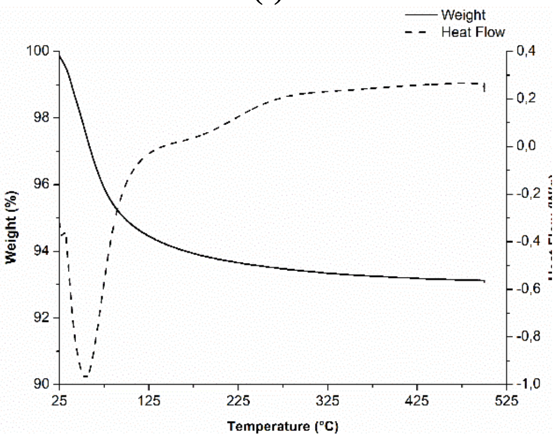
Weight
Heat Flow
Weight (%)
100
98
96
94
92
90
0,4
0,2
0,0
-0,2
-0,4
-0,6
-0,8
-1,0
25
125
225
325
425
525
Temperature (°C)

(g)

(h)

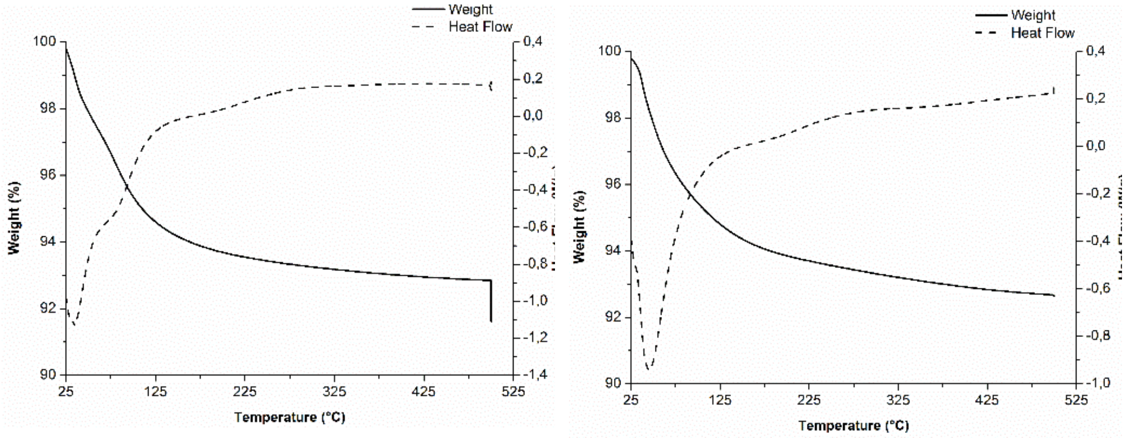

Fig. 5.14 - Thermal curves of weight loss (—) and (---) heat flow for (a) Na-GM-10, (b) K-GM-10, (c) Na-GM-20, (d) K-GM-20, (e) Na-VM-10, (f) K-VM-10, (g) Na-VM-20 and (h) K-VM-20.

Table 5.4 – Weight's loss values in the two temperature regions (25-200°C and 200-500°C) for all the AAMs considered.

	Ranges (T °C)	*Na-VM-10*	*K-VM-10*	*Na-VM-20*	*K-VM-20*	*Na-GM-10*	*K-GM-10*	*Na-GM-20*	*K-GM-20*
% Weight loss	***25-200***	7.78	6.22	6.31	7.13	4.91	4.91	6.52	6.14
	200-500	0.57	0.66	0.84	1.03	0.74	0.92	0.99	1.24
	Total	8.34	6.88	7.15	8.15	5.65	5.83	7.51	7.37

5.3.5 MECHANICAL PROPERTIES

The stress/strain (σ/ε) curves of all samples after 7 and 21 curing days were plotted in Fig. 5.15. In general, the metakaolin addition strongly influenced the final mechanical properties such as to observe a considerable increasing of strengths in both VM-20 and GM-20 samples. During mechanical test procedure, the geometrical determination of the apparent density was required, and its values after 7 and 21 curing days, as well as the compressive strength values given by the average of the best 4 values recorded per each formulation with a variability attesting around 5% were reported in Table 5.5. All samples showed apparent density values ranging between 2.1 – 2.2 g/cm^3 with K-activated samples reporting slightly higher one (Table 5.5). The sodium samples (Fig. 5.15A) evidenced the lowest strengths in comparison with the potassium ones. The higher value after 7 aging days of samples belonging to Na-VM formulation (Fig. 5.15Aa), was reached by Na-VM-20 (44 MPa), contrary to 17 MPa recorded for Na-VM-10. Analogously, the samples aged 21 days showed the same behavior: 50 and 18 MPa respectively for Na-VM-20 and Na-VM-10. Similar values were obtained by Na-GM formulation (Fig. 5.15Ab), whose values reached respectively 46 and 16 MPa after 7 days and 51 and 17 MPa after 21 days, respectively for Na-GM-20 and Na-GM-10. The compressive strengths values after 21 days find corresponding feedback in literature within the range of 23-60 MPa, depending on alumina available in the geopolymer matrix (Kouamo et al., 2012; Robayo-salazar et al., 2016; Tchakoute Kouamo et al., 2013). Differently, the potassium samples (Fig. 5.15B) showed the highest values. Indeed, K-VM samples recorded 23 and 69 MPa after 7 days and 29 and 71 MPa after 21 days, while K-GM samples achieved the highest values of all formulations with 26/78 MPa and 30/89 MPa respectively after 7 and 21 aging days (Fig. 5.15Bb). Therefore, the addition of metakaolin generates a dense composite/mortar where the volcanic ash or ghiara particles act as reactive aggregates. At short aging time (7 days) the strength is not yet developed, indicating the slow reactivity of the volcanic materials with respect to metakaolin that usually completes the reticulation in 7 days for a final strength around 30 MPa (Gharzouni et al., 2014). Additionally, even though all samples showed a brittle behavior, there are evidence of a plastic trend, visible as a relevant value of elongation before fracture, in both VM-10 and GM-10 series when activated with sodium (Fig. 5.15Aa, Ab). This is another indication that the geopolymers with these formulations are not yet completely rigid even after 21 days. Differently from Na activation, K-solution strongly increases elastic modulus and the final mechanical strength (Fig. 5.15Ba, Bb). When 20% wt. of M is added, the shape of the curves drastically changes and the elongation is strongly reduced. Finally, the mechanical compressive results evidenced some differences among the two activators used: the samples activated by potassium solution showed the higher values then those ones with the sodium, with an increase estimated about 50-60%; in addition to an increase of strength for the samples with 20% of M, reaching an increase of about 200%. The compressive strengths showed a slight variation, of about 15%, between the values obtained by the test at 7 and 21 days of curing. Moreover, taking into account the average density of each formulation’s set and the concentration of alumina in the matrix, progressive linear trends, more evident for the AAMs based on volcanic ash than those one with ghiara were highlighted in Fig. 5.16. Therefore, the direct proportionality among the concentration of alumina of the precursors and the final compressive resistance was demonstrated.

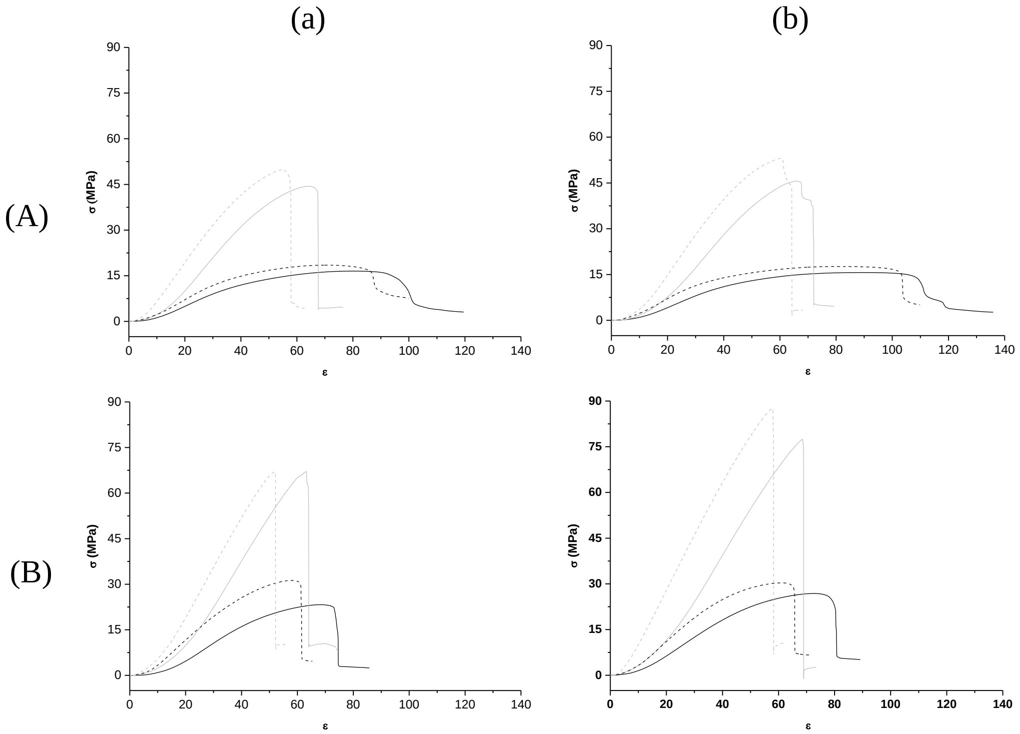

Fig. 5.15 – Average of compressive strength in function of time after (—)7 and (---) 21 days for samples based on (a) VM and (b) GM activated with (A) sodium and (B) potassium solution and with (—)10 and (—)20% of metakaolin.

Table 5.5 – Values of density and mechanical compressive strengths (MPa) of all samples after 7 and 21 of aging days.

Labels	***After 7 days***		***After 21 days***	
	AAMs ρ (g/cm^3)	***σ (MPa)***	***AAMs ρ (g/cm^3)***	***σ (MPa)***
Na-VM-10	2.16	17	2.15	18
Na-GM-10	2.15	16	2.14	17
Na-VM-20	2.13	44	2.12	50
Na-GM-20	2.13	46	2.12	51
K-VM-10	2.19	23	2.20	29
K-GM-10	2.21	26	2.21	30
K-VM-20	2.18	69	2.16	71
K-GM-20	2.16	78	2.16	89

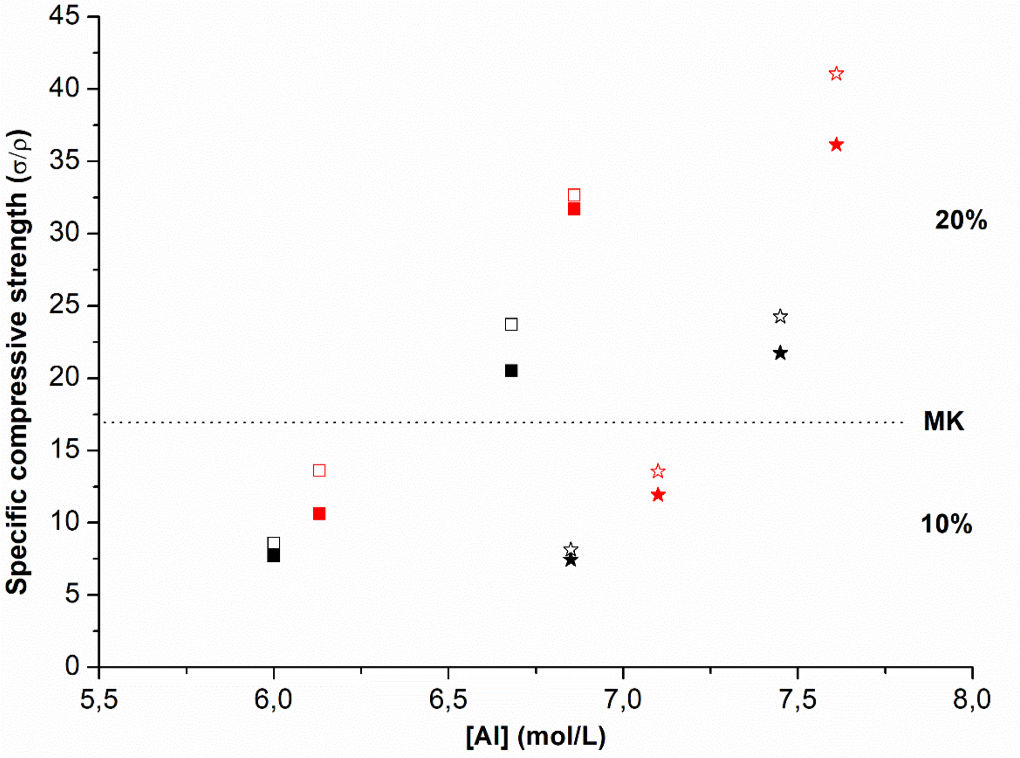

Fig. 5.16 – Value of specific mechanical compressive in function of Al concentration for (■)VM, (★) GM, (—) Na-samples, (—)K-samples, (■) after 7 days, (□) after 21 days.

5.3.6 POROSIMETRIC PROPERTIES

The comparison of cumulative pore volume trends for each sample taking into account the influence of metakaolin added in the mixture were showed in Fig. 5.17, while all porosimetric values obtained by Hg porosimetry analysis, including accessible porosity and cumulative pore volume values in the specific ranges considered were summarized in Table 5.6. In detail, Na-VM recorded a higher pore volume in the range 1-0.1 µm (2.61 cm^3/g) and 0.1-0.01 µm (59.26 cm^3/g), respectively in VM-10 and VM-20 samples (Fig. 5.17a) with quite equivalent accessible porosity (~ 25%) and bulk density (1.9 g/cm^3; Table 5.6). Instead, K-VM evidenced a higher cumulative pore volume in the large range 1-0.01 µm (18.06 cm^3/g) in VM-20, while the main pore volume for VM-10 was recorded in the smallest range 0.01-0.001 µm (6.36 cm^3/g) (Fig. 5.17a), demonstrating its low accessible porosity attesting around 15% contrary to a higher bulk density (2.1 g/cm^3) (Table 5.6). The Na-GM samples showed the same trends of Na-VM: higher cumulative pore volume in 1-0.1 µm range (12.58 cm^3/g) for GM-10, while 12.58

cm^3/g in the 0.1-0.01 range for GM-20 (Fig. 5.17b). Moreover, slight difference in terms of accessible porosity (±1) and bulk density (±0.1) were recorded (Table 5.6). K-GM showed a lower porosity (12%) and higher density (2.1 g/cm^3) in GM-10 than GM-20's features (Table 5.6), in addition to higher pore concentration in the bigger range 100-1 µm (0.22 cm^3/g) differently to 24.05 cm^3/g in 0.1-0.001 µm range (Fig. 5.17b). Therefore, the potassium- samples (K-VM and K-GM) evidenced, generally, higher density and lower accessible porosity with a general decreasing of bigger pore volume than those of sodium one, as also reported by (Gharzouni et al., 2016). The porosity values of Na-samples are in accordance to values found in literature (Barone et al., 2020) as well as the density (Lemougna et al., 2011). Moreover, the influence of metakaolin is better highlighted in potassium samples, which recorded a lower porosity in VM-10 and GM-10 than those with higher metakaolin. Finally, the Fig. 5.17c relates the porosity and the bulk density of each formulation. Two clusters are well-defined for sodium and potassium samples respectively.

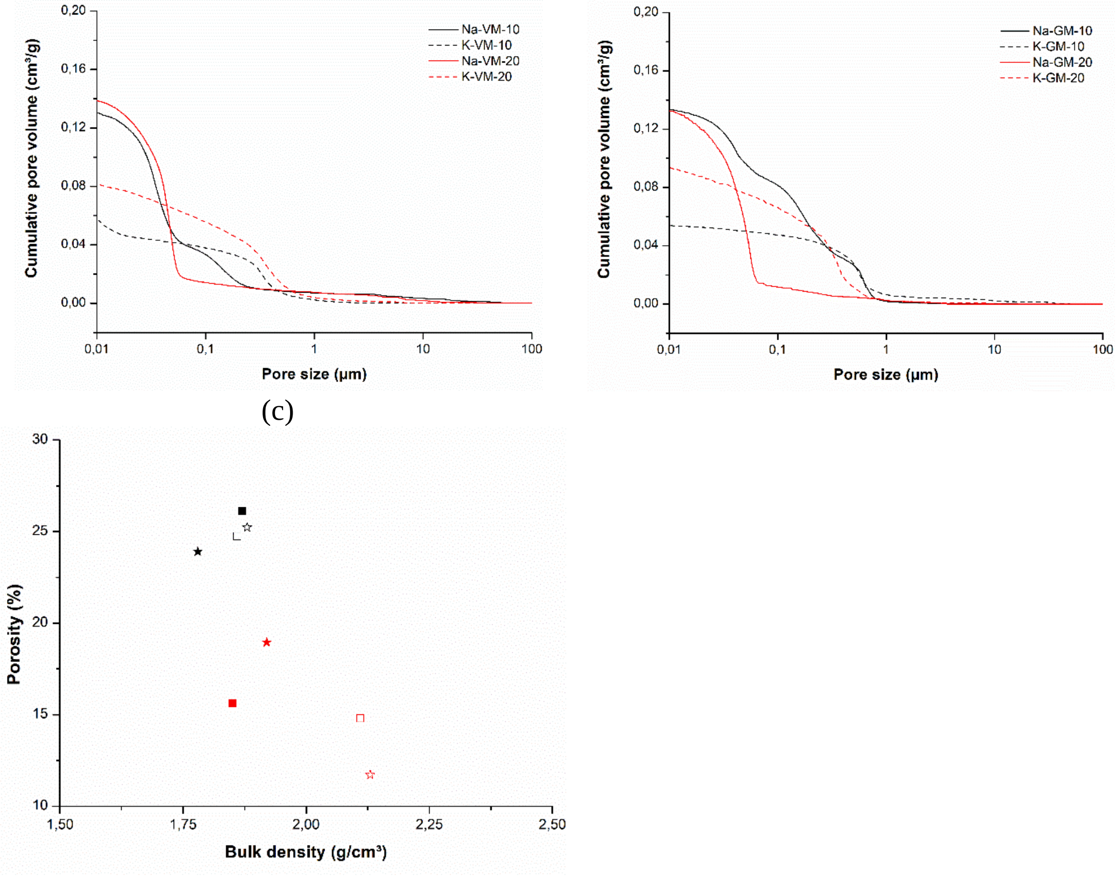
(a)

(b)

(c)

Fig. 5.17 (a-c) – Cumulative pore volume vs pore size graphs: a) Na/K-VM-10/20; b) Na/K-GM-10/20; (—) Na-solution, (---) K-solution, (—) 10% wt. M, (—) 20% wt. M; c) plot bulk density vs porosity: (■)VM, (★) GM, (—) Na-samples, (—) K-samples, (□) 10% wt. M, (■)20% wt. M.

Table 5.6 – Density, porosity and pore information obtained by Hg porosimetry analysis for each AAMs samples and summary results. For each pore size ranges the total incremental volumes were calculated.

					∑ incremental volume (cm^3/g) in the following ranges:				
	Bulk density (g/cm^3):	**Accessible porosity (%):**	**Total pore volume (cm^3/g):**	**Average pore diameter (µm):**	**100-10 µm**	**10-1 µm**	**1-0.1 µm**	**0.1-0.01 µm**	**0.01-0.001 µm**
K-GM-10	2.13	11.71	0.05	0.12	0.03	0.19	6.75	6.75	2.83
K-GM-20	1.92	18.95	0.10	0.05	0.00	0.03	8.48	17.41	6.64
K-VM-10	2.11	14.80	0.07	0.03	0.00	0.01	3.29	8.28	6.36
K-VM-20	1.85	15.62	0.08	0.06	0.00	0.04	5.65	12.41	4.73
Na-GM-10	1.88	25.23	0.13	0.07	0.00	0.01	12.58	31.09	6.56
Na-GM-20	1.78	23.91	0.13	0.04	0.00	0.01	0.18	28.45	6.82
Na-VM-10	1.86	24.75	0.13	0.04	0.04	0.17	2.61	45.19	7.53
Na-VM-20	1.87	26.12	0.14	0.04	0.02	0.19	0.48	59.26	7.11
K-solution	2.00	15.27	0.08	0.07	0.01	0.07	6.04	11.21	5.14
Na-solution	1.85	25.00	0.14	0.04	0.02	0.10	3.96	41.00	7.00
Volcanic ash	1.92	20.32	0.11	0.04	0.01	0.10	3.01	31.29	6.43
Ghiara	1.93	19.95	0.11	0.07	0.01	0.06	7.00	20.93	5.71
10% wt. MK	1.85	21.15	0.11	0.05	0.00	0.07	3.70	29.38	6.32
20% wt. MK	1.99	19.12	0.10	0.06	0.02	0.10	6.31	22.83	5.82

5.3.7 PHYSICAL PROPERTIES CORRELATIONS

To obtain an overview on physical properties measured with different methods (apparent density, weight loss, compressive strength and accessible porosity) and to compare the behaviour of the two alkaline solutions used (not focusing on M content), a matrix scatter plot with the boxplot of variables set in the diagonal to enclose all values measured for easily sum-up was proposed (Fig. 5.18). Indeed, considering the diagrams IIc and IIIb of Fig. 5.18, a direct correlation between the weight loss [200-500 °C] and the compressive stress values after 7 days can be observed. The potassium samples with higher M content show higher weight loss differently to sodium samples with lower M amount. Moreover, there is a relation between apparent density and weight loss for all the samples, the lower the density, the higher the weight loss (Fig. 5.18, see the box Ic and IIIa), in addition to a clear distribution of Na and K-samples represented by two parallel trends. Finally, an inverse correlation between apparent density, geometrically determined, and accessible porosity, as measured by the Hg-intrusion porosimetry (Fig. 5.18, see the box IVa and Id) was found indicating the validity of our measurements and a clear polymerization degree, more evident for Na-samples.

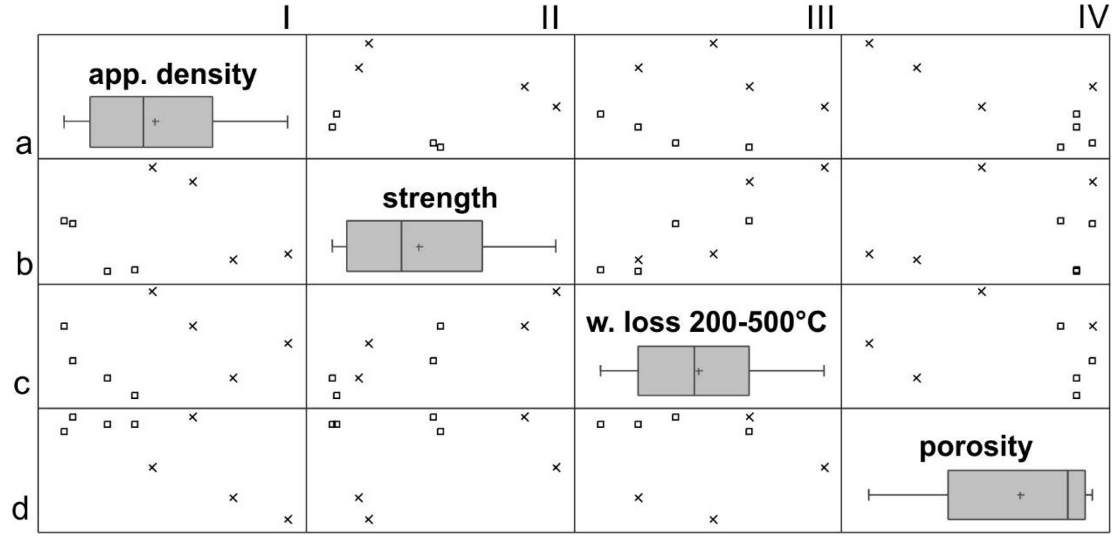

Fig. 5.18 - Matrix scatter plot of density, mechanical strengths after 7 days, weight loss in the range 200-500°C and accessible porosity; (□) Na and (x) K solutions; Sequences: I-IV for columns; a-d for rows. The boxplots of each variable are reported in the matrix are formed by scatter plots of the variable defined by the intersection with the diagonal.

5.3.8 RAMAN SPECTROSCOPY

Raman analysis were carried out on sherds of all samples belonging to Na-series with a x50 objective. Ten measurements were performed for each sample in order to analyse different sample's areas and so to obtain as much as possible a complete characterization. Indeed, in each figure, only three Raman spectra are considered representative of all measurements and they are indicated with superscript. The spectra were compared with those one of the main mineralogical phases found in XRD analysis and downloaded by rruff dataset (https://rruff.info/): anorthite, augite, forsterite and hematite. Indeed, thanks to the overlapping of all representative spectra, different peaks have been observed. The results of Na-VM-10 sample have evidenced many contributions related to different mineralogical phases: augite (230, 325, 388, 660 and 1000 cm^{-1}), hematite (298 and 410 cm^{-1}), anorthite (487 cm^{-1}) and forsterite (825 and 855 cm^{-1}) combined to a slight fluorescence (Fig. 5.19). Contrary, for Na-VM-20, only one spectrum was selected as representative due to the similarities with the others. However, this spectrum is mainly articulated by the peaks linked to augite (325, 390, 528, 665 and 1005 cm^{-1}) and anorthite (485 and 510 cm^{-1}), regardless fluorescence phenomena recorded in background (Fig. 5.20). In general, samples based on ghiara have showed major contribution than those one based on volcanic ash. In detail, Na-GM-10 sample is characterized by four spectra, which presented the same mineralogical phases contributions: anorthite, augite, forsterite and hematite. However, the spectra NaGM10^3 could have a contribution of diopside (Fig. 5.21). Analogously, Na-GM-20 is characterized by the same phases (Fig. 5.22).

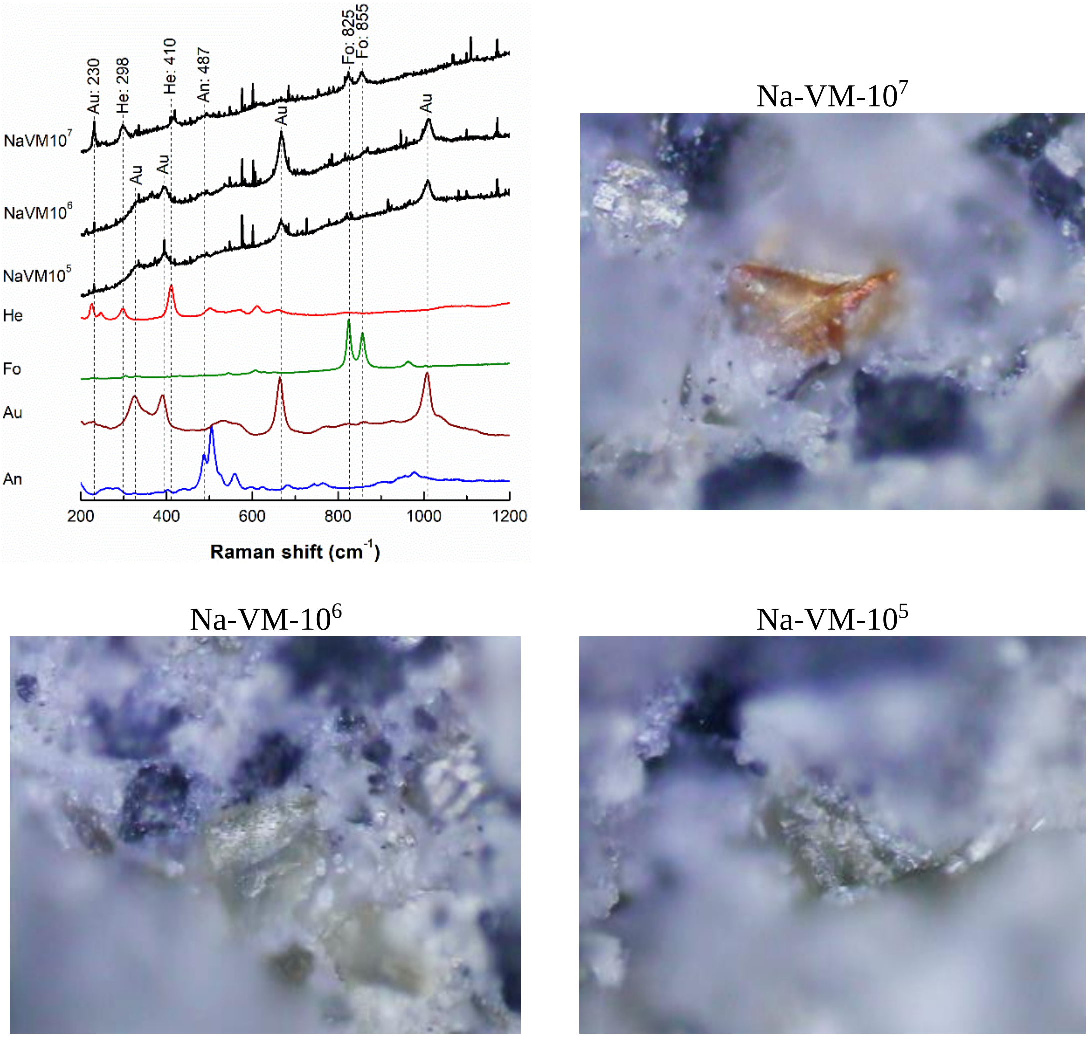

Na-VM-10^7

Na-VM-10^6

Na-VM-10^5

Fig. 5.19 - Overlapping of Raman spectra regarding the sample Na-VM-10 and some mineralogical phases downloaded by rruff database (An: anorthite, Au: augite, Fo: forsterite, He: hematite) and micrographs of spot analyses corresponding to each spectrum.

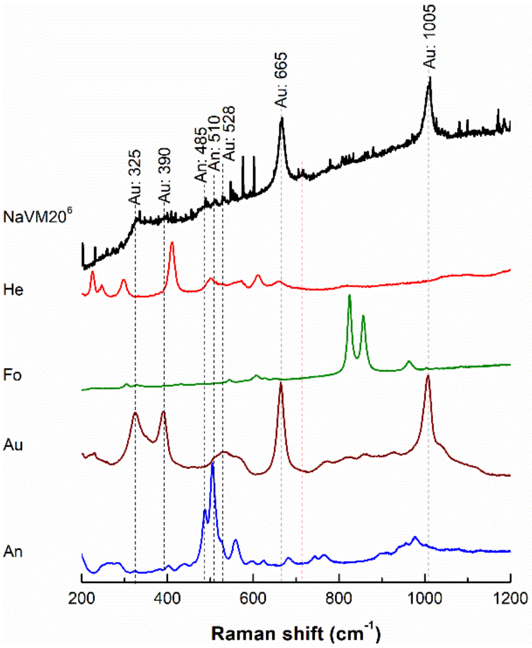

Na-VM-20^6

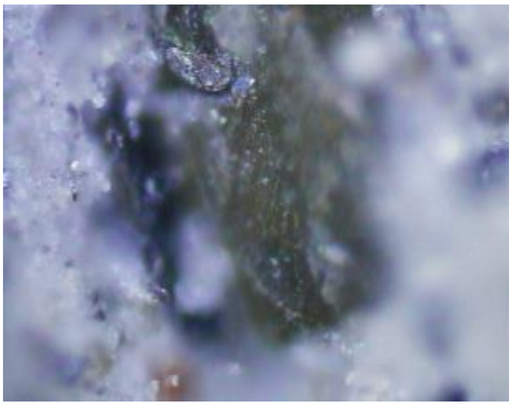

Fig. 5.20 - Overlapping of Raman spectra regarding the sample Na-VM-20 and some mineralogical phases downloaded by rruff database (An: anorthite, Au: augite, Fo: forsterite, He: hematite) and micrograph of spot analysis corresponding to the spectrum.

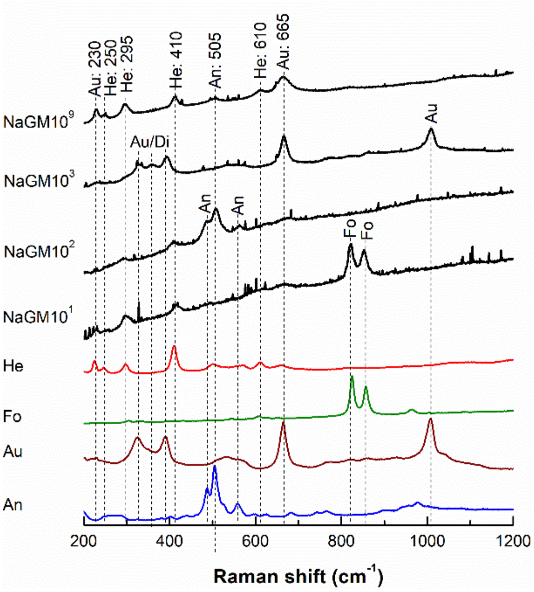

Na-GM-10^9

Na-GM-10^3

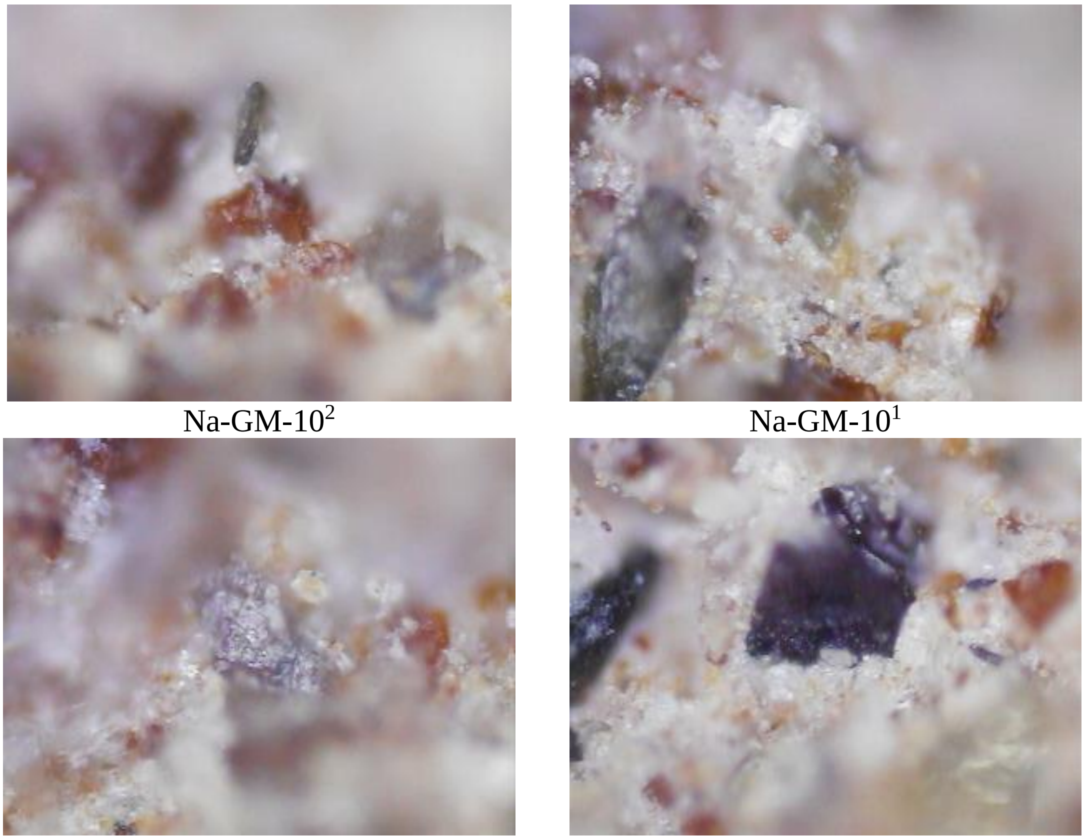

Na-GM-10^2 Na-GM-10^1

Fig. 5.21 - Overlapping of Raman spectra regarding the sample Na-GM-10 and some mineralogical phases downloaded by rruff database (An: anorthite, Au: augite, Fo: forsterite, He: hematite) and micrographs of spot analyses corresponding to each spectrum.

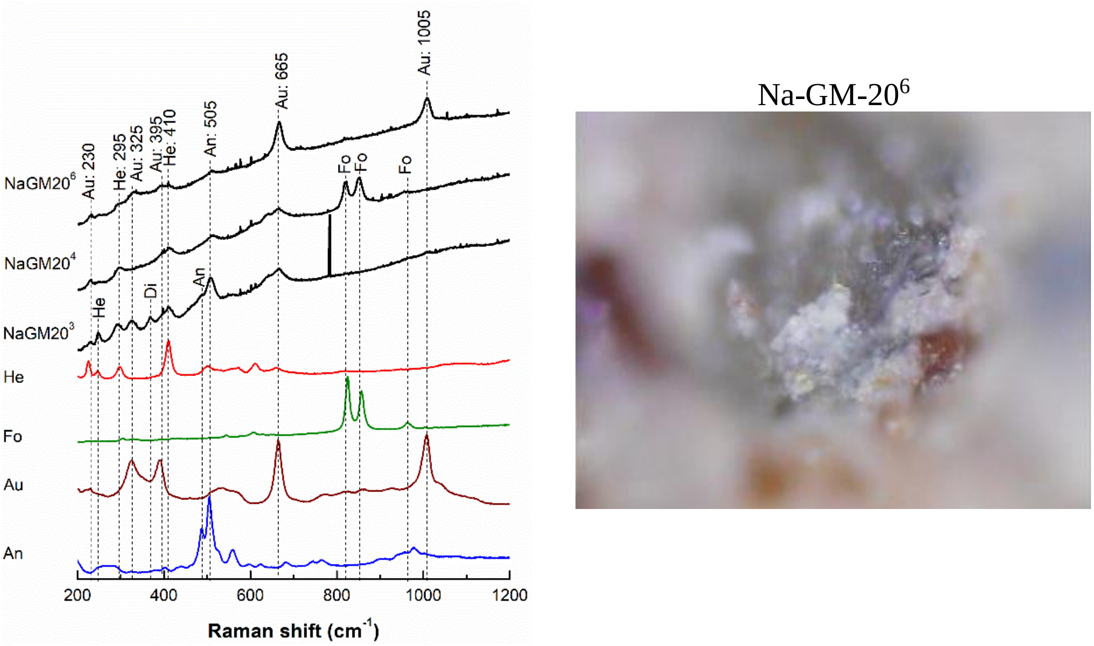

Na-GM-20^6

Na-GM-20^4 Na-GM-20^3

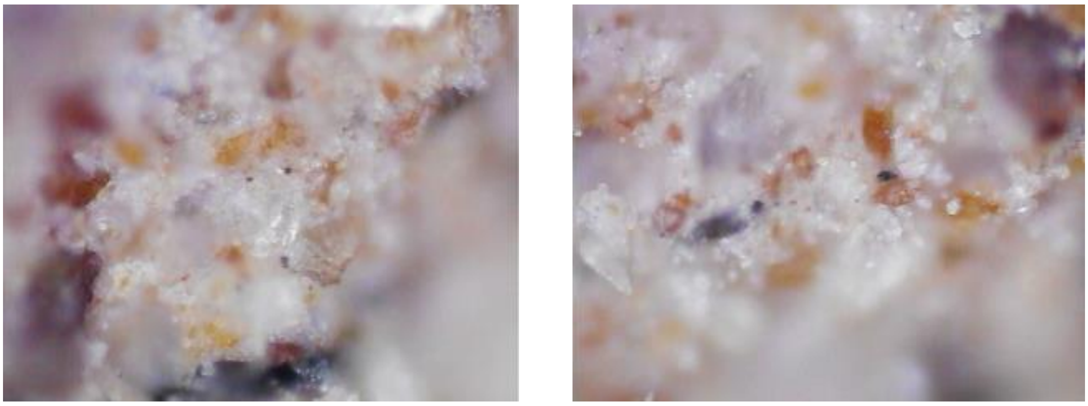

Fig. 5.22 - Overlapping of Raman spectra regarding the sample Na-GM-20 and some mineralogical phases downloaded by rruff database (An: anorthite, Au: augite, Fo: forsterite, He: hematite) and micrographs of spot analyses corresponding to each spectrum.

The potassium series developed during the abroad period were rapidly investigated by Raman spectroscopy regardless there are not intentions to optimize them. Therefore, sherds of each sample were analysed with the same measurement setting of Na-series, though some measurements of ghiara samples were carried out using a x20 objective to investigate a wider area (20x objective wasn’t possible to apply to volcanic ash samples due to the high fluorescence). The results of K-VM-10 sample showed the only contribution of augite (230, 390, 665 and 1005 cm^{-1}) (Fig. 5.23). Contrary, the sample K-VM-20, evidenced in addition to augite, hematite (295 and 410 cm^{-1}), anorthite (503 cm^{-1}) and forsterite (605 cm^{-1}) (Fig. 5.24). Instead, the samples based on ghiara evidenced: augite (230 and 665 cm^{-1}), hematite (299 and 413 cm^{-1}), anorthite (503 cm^{-1}) and magnetite (468 cm^{-1}) in K-GM-10 (Fig. 5.25); while double possibility for pyroxene phases: diopside/augite, hematite and plagioclase in K-GM-20 (Fig. 5.26). To summarise, no evidences of geopolymeric gel in the spectra were observed regardless alkaline activation solution used, but only detection of crystalline phases coming from the precursors used as found in the samples belonging to VM1 and GM1 series presented in paragraph 4.3.4.

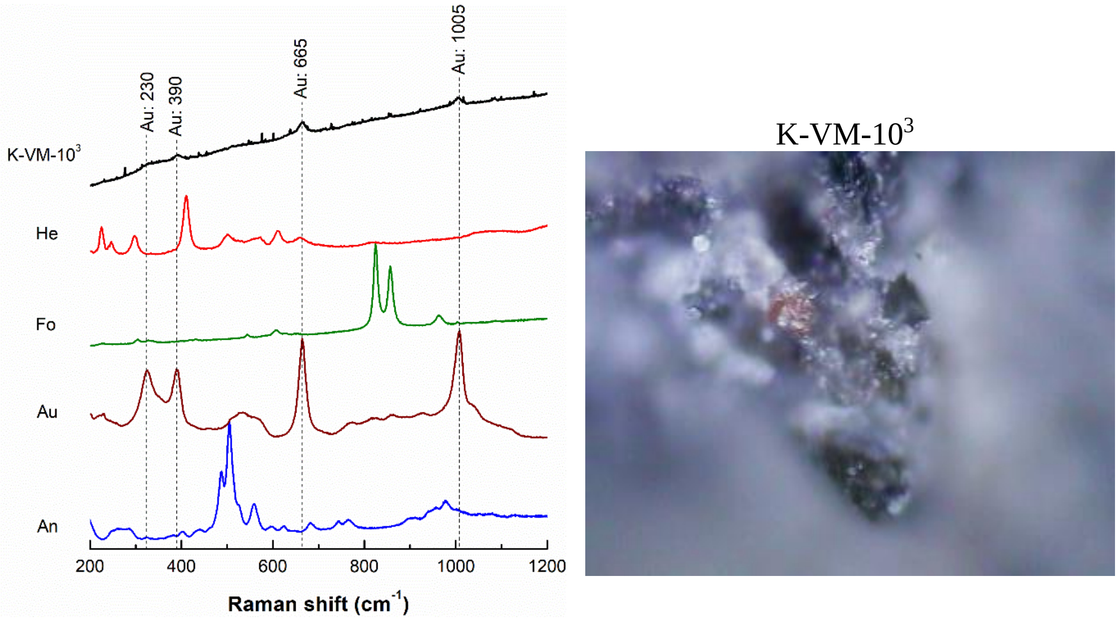

Fig. 5.23 - Overlapping of Raman spectra regarding the sample K-VM-10 and some mineralogical phases downloaded by rruff database (An: anorthite, Au: augite, Fo: forsterite, He: hematite) and micrograph of spot analyses corresponding to the spectrum.

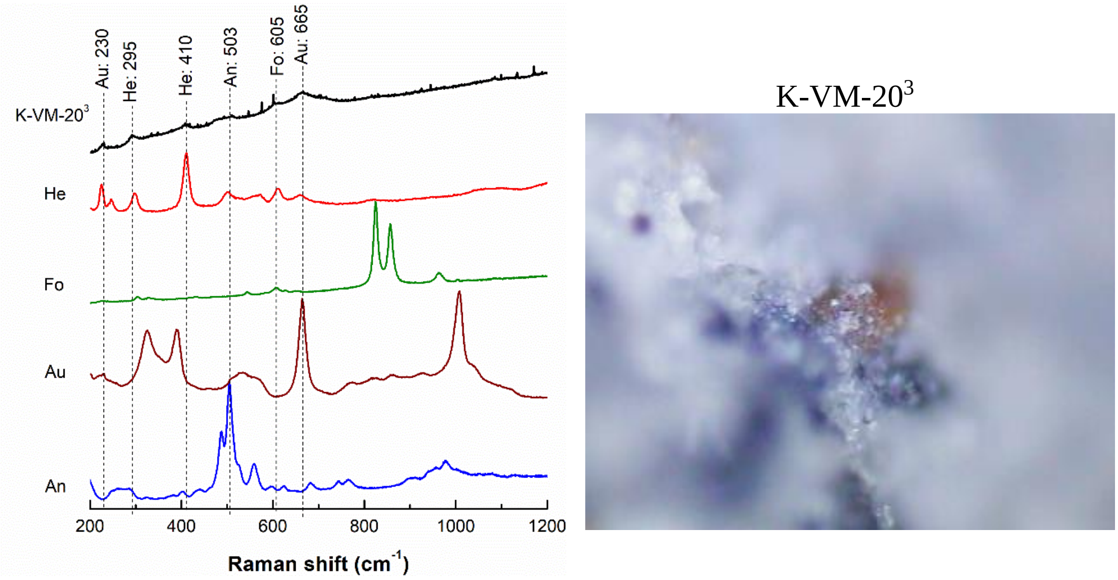

Fig. 5.24 - Overlapping of Raman spectra regarding the sample K-VM-20 and some mineralogical phases downloaded by rruff database (An: anorthite, Au: augite, Fo: forsterite, He: hematite) and micrograph of spot analyses corresponding to the spectrum.

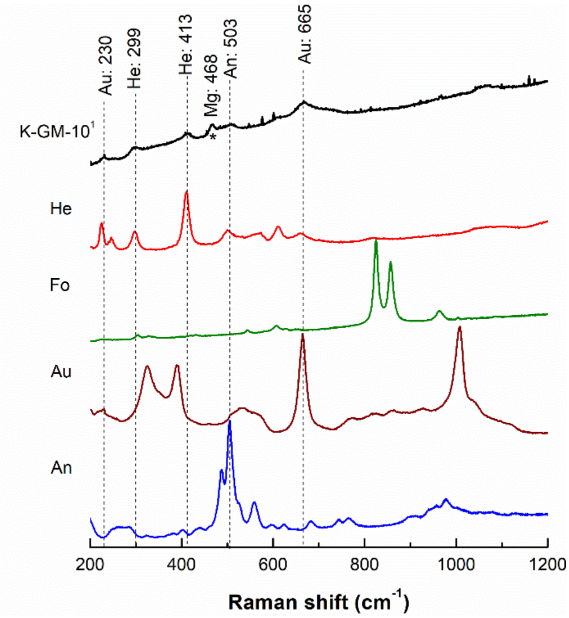


K-GM-10^1

Fig. 5.25 - Overlapping of Raman spectra regarding the sample K-GM-10 and some mineralogical phases downloaded by rruff database (An: anorthite, Au: augite, Fo: forsterite, He: hematite) and micrograph of spot analyses corresponding to the spectrum performed using a 20x objective. The peak indicates with "" corresponding to magnetite phase according to rruff catalogue (R061111).*

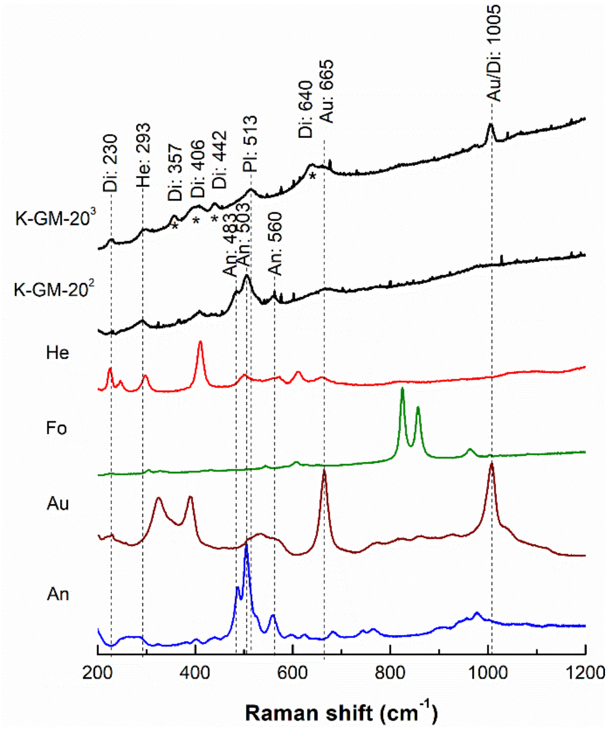

K-GM-20^2 K-GM-20^3

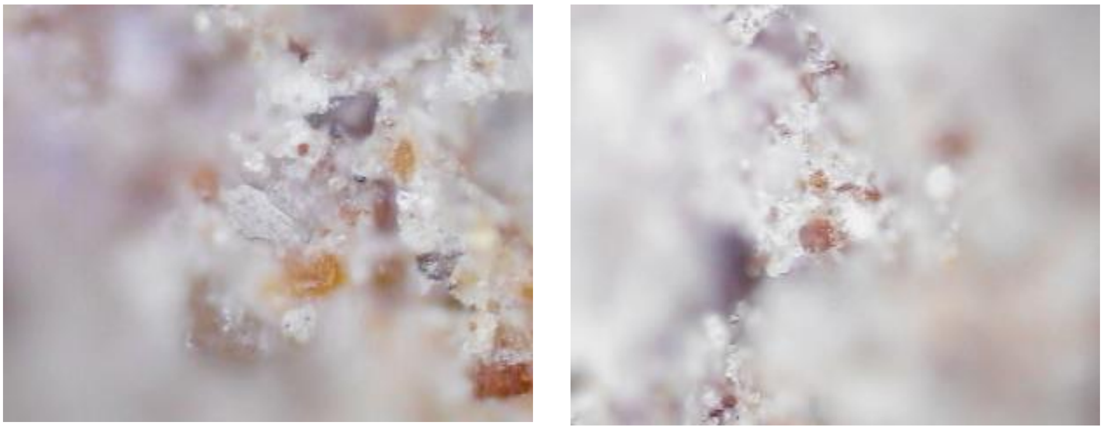

Fig. 5.26 - Overlapping of Raman spectra regarding the sample K-GM-20 and some mineralogical phases downloaded by rruff database (An: anorthite, Au: augite, Fo: forsterite, He: hematite) and micrographs of spot analyses corresponding to each spectrum. The peaks indicated with "" correspond to diopside (R040028), while Pl (plagioclase) indicates bytownite (R070598) phases according to rruff catalogue.*

5.3.9 SEM-EDX ANALYSIS

Morphological and EDX analysis ware carried out on sherds of Na-samples. The microstructure of each specimen was investigated using three different magnifications. Fig. 5.27 shows the morphology of Na-VM-10 sample, which is characterized mainly by elongated particles of 10 µm order. These latter border grains of different size and shape and whose chemistry is made mainly of Na, Si and Al elements, with Fe and Ca as secondary ones. This structure is comparable to those one found in VM1 and GM1 series (Paragraph 4.3.5). Contrary, the microstructures recorded in Na-VM-20 evidence a micro porosity with pores of < 75 µm size and spherical shape. Moreover, it presents a very compact amorphous matrix chemically characterized by Na, Si and Al elements, where some spherical grains of 100 µm are immersed whose origin can be linked to metakaolin clumps formed during the mixing phase (Fig. 5.28). Analogously, Na-GM-10 sample evidences a compact matrix with grains of 10-20-micron order and bigger volcanic original grains partially or non-reacted, chemically made of Ca-Al-Si elements. Moreover, at higher magnification, very fine elongated particles (< 2 µm) can be observed, whose chemistry is characterized by Na, Si and Al (± calcium and iron) elements (Fig. 5.29). Fig. 5.30 shows the equivalent with 20% wt. of M with a very similar and dense morphology. Finally, to summarise, all the samples, except Na-VM-10, evidence a comparable morphology characterized by a dense and microporous matrix in accordance to structures found by (Djobo et al., 2016). Moreover, the very fine gel particles show a N-A-S-H (sodium aluminosilicate hydrate) chemistry with ± calcium and iron (García-lodeiro et al., 2015).

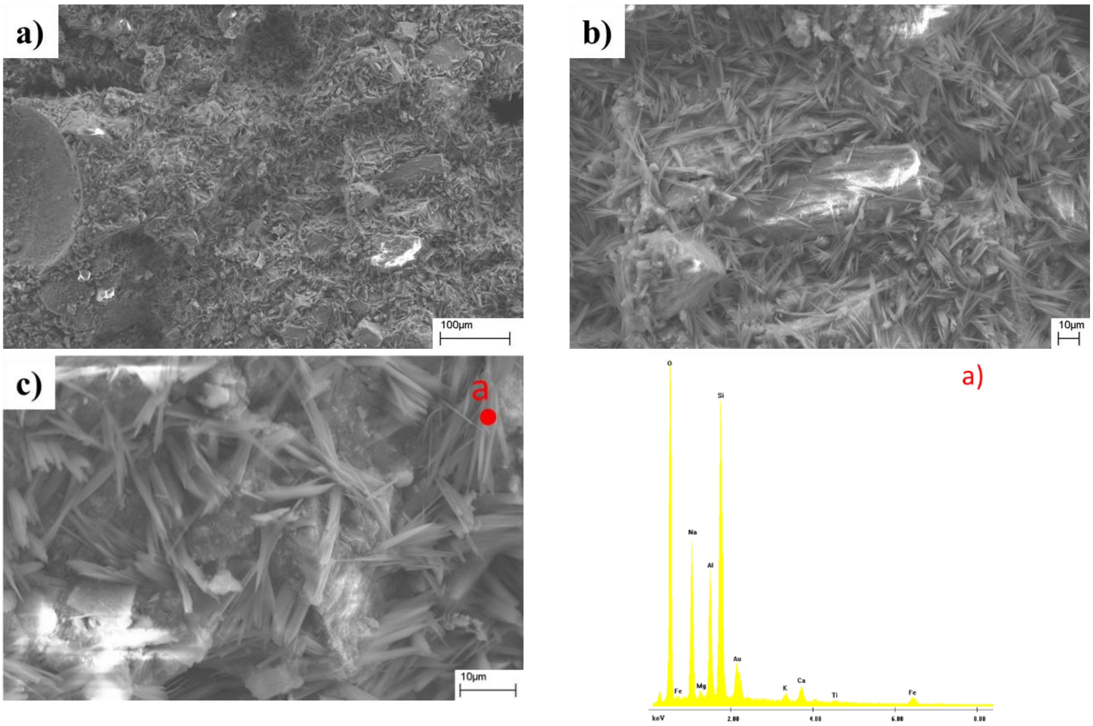

Fig. 5.27 – SEM micrographs of Na-VM-10 sample: a) Mag. 500x; b) Mag. 1.5Kx; c) Mag. 4 Kx and EDX analysis whose spot analysis is indicated in red dot (a).

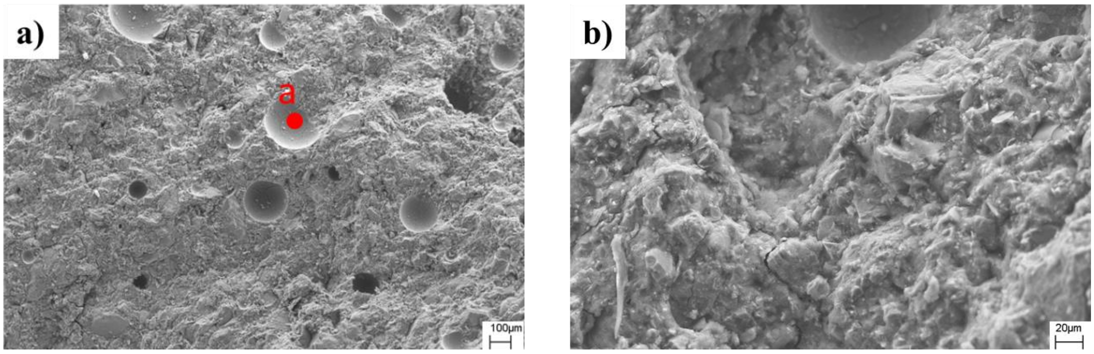

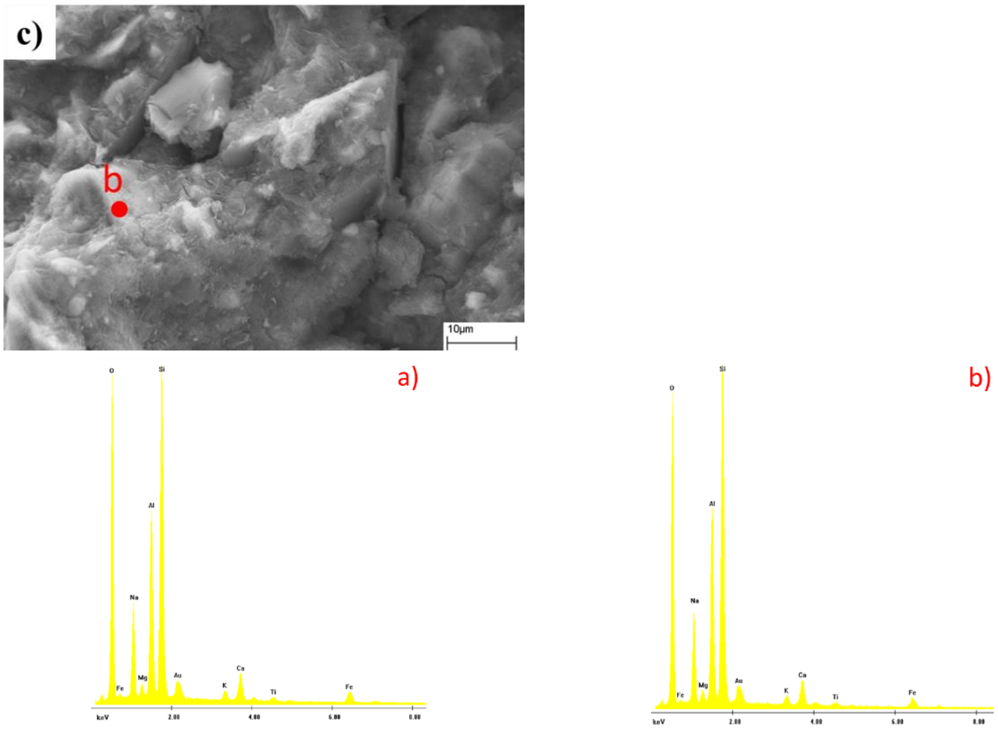

Fig. 5.28 – SEM micrographs of Na-VM-20 sample: a) Mag. 500x; b) Mag. 1.5Kx; c) Mag. 4 Kx and EDX analysis whose spot analysis are indicated in red dots (a and b).

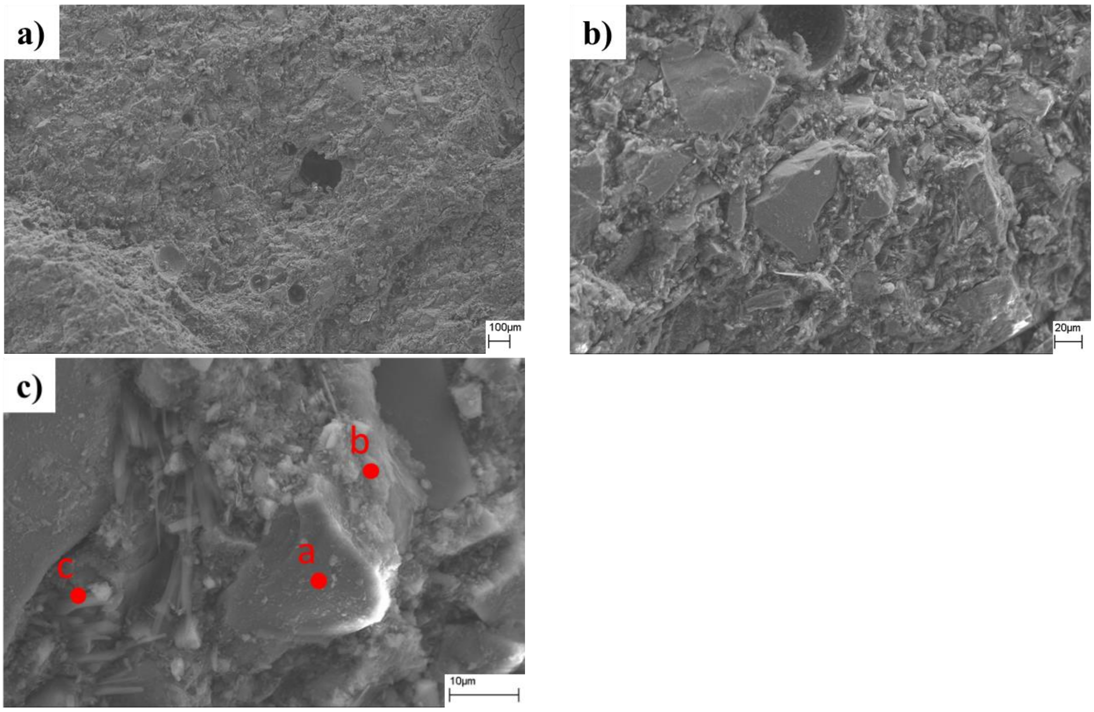

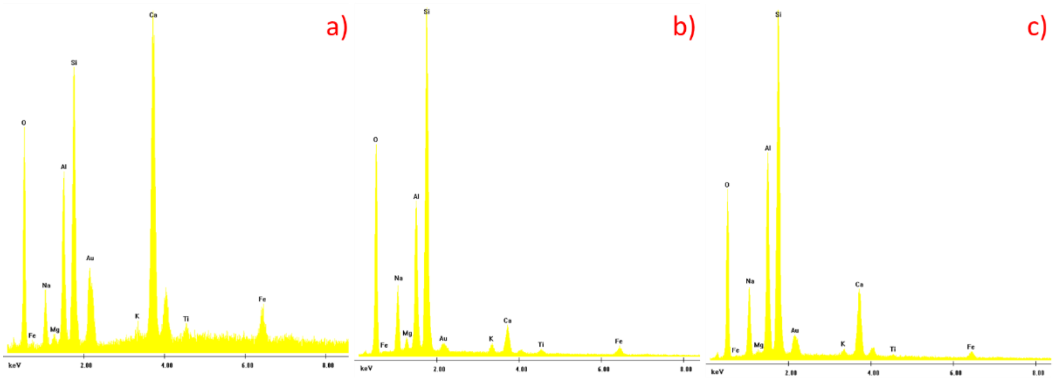

Fig. 5.29 – SEM micrographs of Na-GM-10 sample: Mag. 150x; b) Mag. 1Kx; c) Mag. 5 Kx., and EDX analysis whose spot analysis are indicated in red dots (a-c).

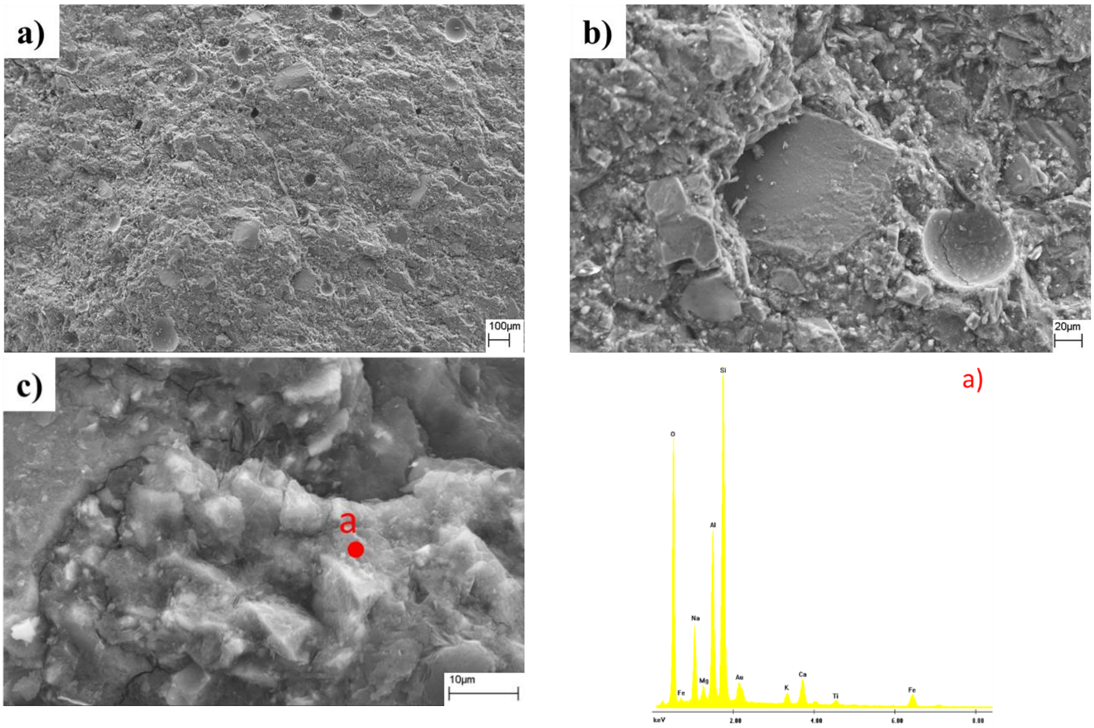

Fig. 5.30 – SEM micrographs of Na-GM-20 sample: Mag. 150x; b) Mag. 1Kx; c) Mag. 5 Kx., and EDX analysis whose spot analysis is indicated in red dot (a).

Analogously to Na-samples, the potassium ones were analysed with the same approach with the aim to observe morphological features at different magnifications as well as the chemical compositions of the matrix. In detail, K-VM-10 sample showed a homogenous and compact structure, characterized by spherical pores whose main dimension is below 100 µm. Moreover, the structure is made of sharp-cornered and/or elongated particles, whose chemical compositions reflect the chemistry’s system of reactants involved in the process, so Si, Al, Ca, Fe, Mg elements as well as K one, which overcomes the Na, as expected, due to the use of the potassium activating solution (Fig. 5.31). The same considerations can be done for K-VM-20 samples, although a more stable system can be assumed due to the high values of Si, Al and K recorded in the spot analysis “a” demonstrating a good mixing with the potassium silicate and the higher addition of metakaolin which produced a K-A-S-H gel (Fig. 5.32). The Fig. 5.33 and Fig. 5.34 showed the morphologies of samples based on ghiara. Their structures are very homogeneous and compact and presented a micro-porosity with spherical pores, while the chemistries are comparable. Moreover, the chemistry of K-GM-20 showed the same behaviour of the corresponding sample based on volcanic ash (see spot analysis “b” of Fig. 5.34).

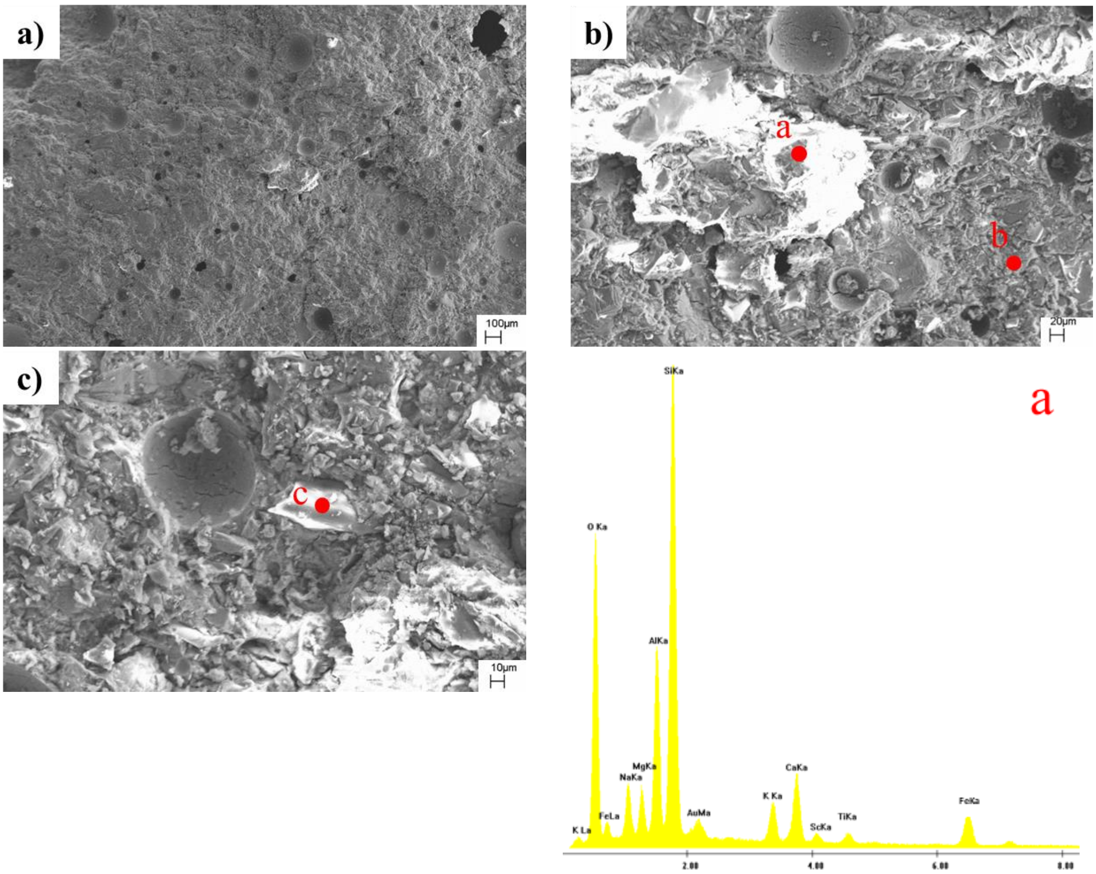

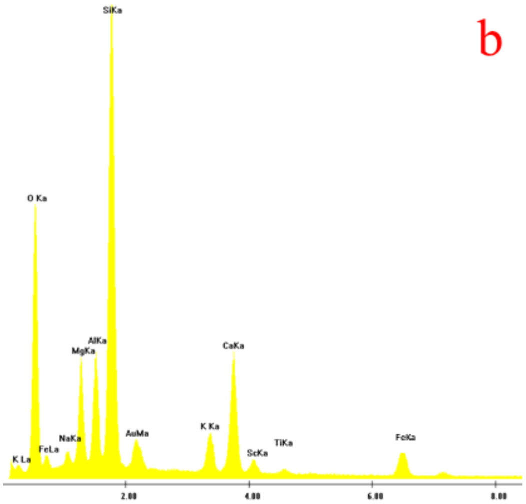

Fig. 5.31 – SEM micrographs of K-VM-10 sample: Mag. 150x; b) Mag. 500x; c) Mag. 1Kx and EDX analysis whose spot analysis are indicated in red dots (a-c).

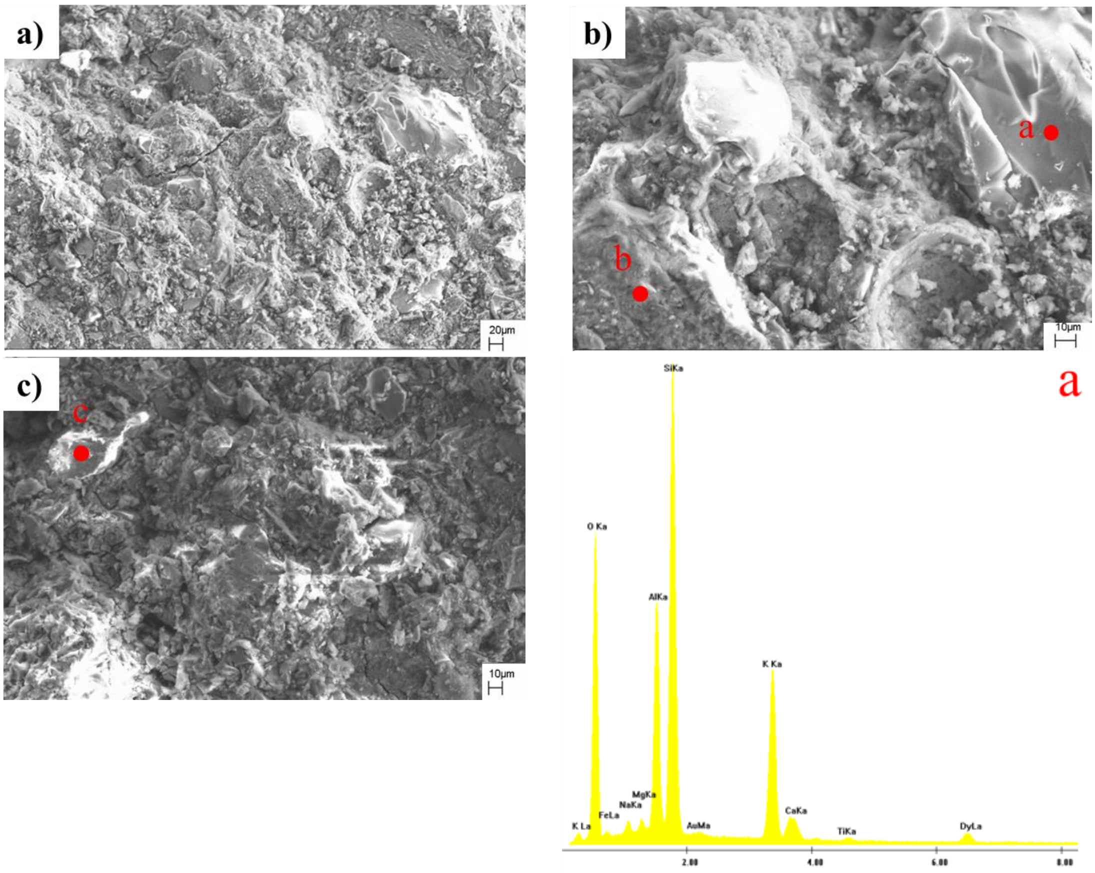

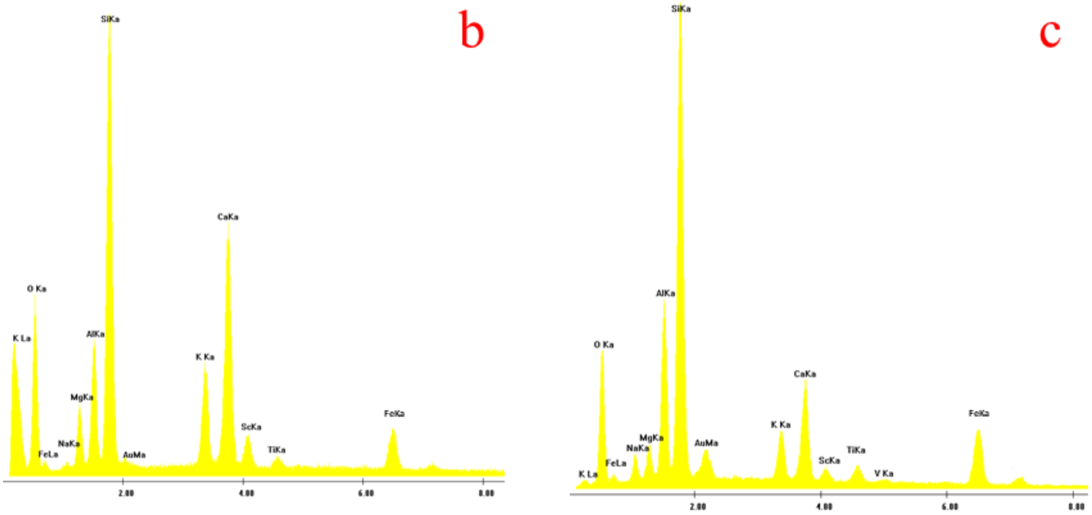

Fig. 5.32 – SEM micrographs of K-VM-20 sample: Mag. 500x; b) Mag. 1.5Kx; c) Mag. 1Kx and EDX analysis whose spot analysis are indicated in red dots (a-c).

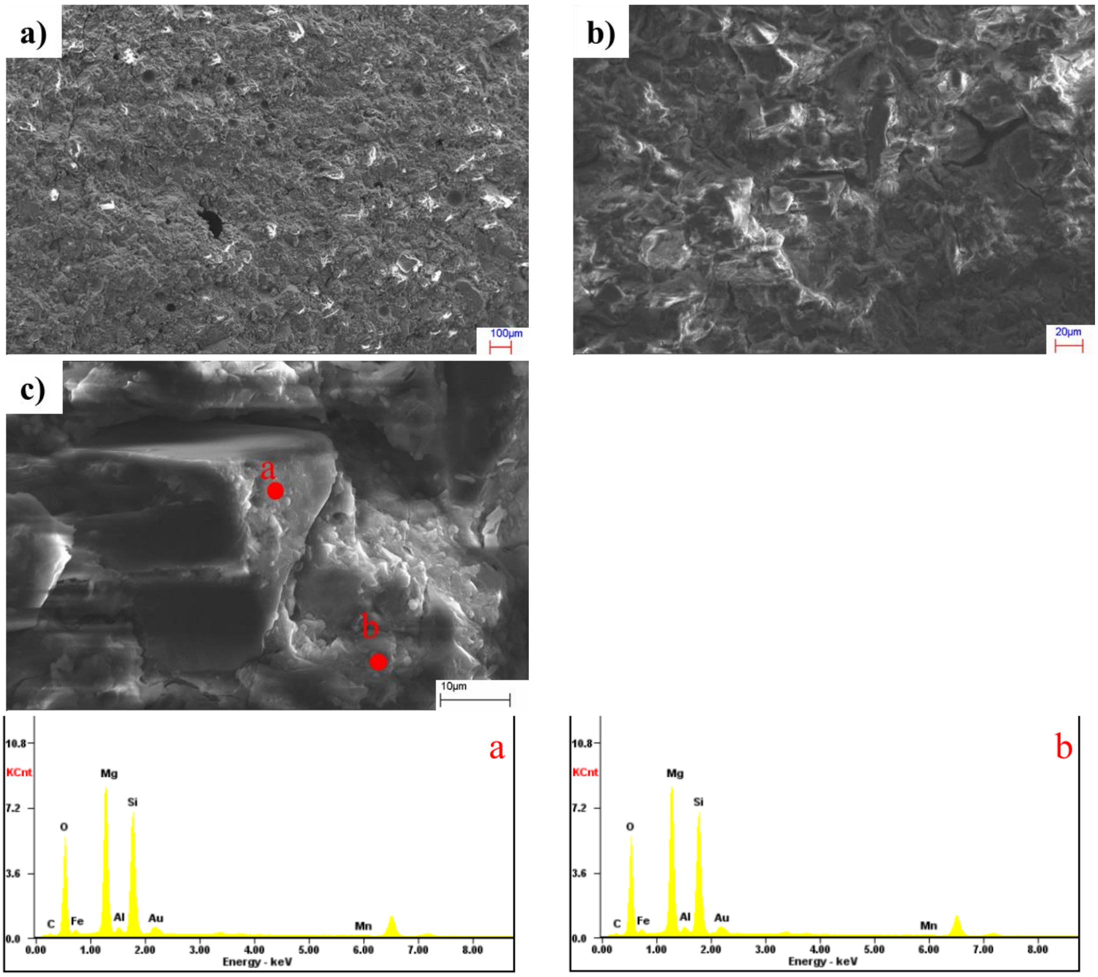

Fig. 5.33 – SEM micrographs of K-GM-10 sample: Mag. 150x; b) Mag. 1Kx; c) Mag. 5Kx and EDX analysis whose spot analysis are indicated in red dots (a and b).

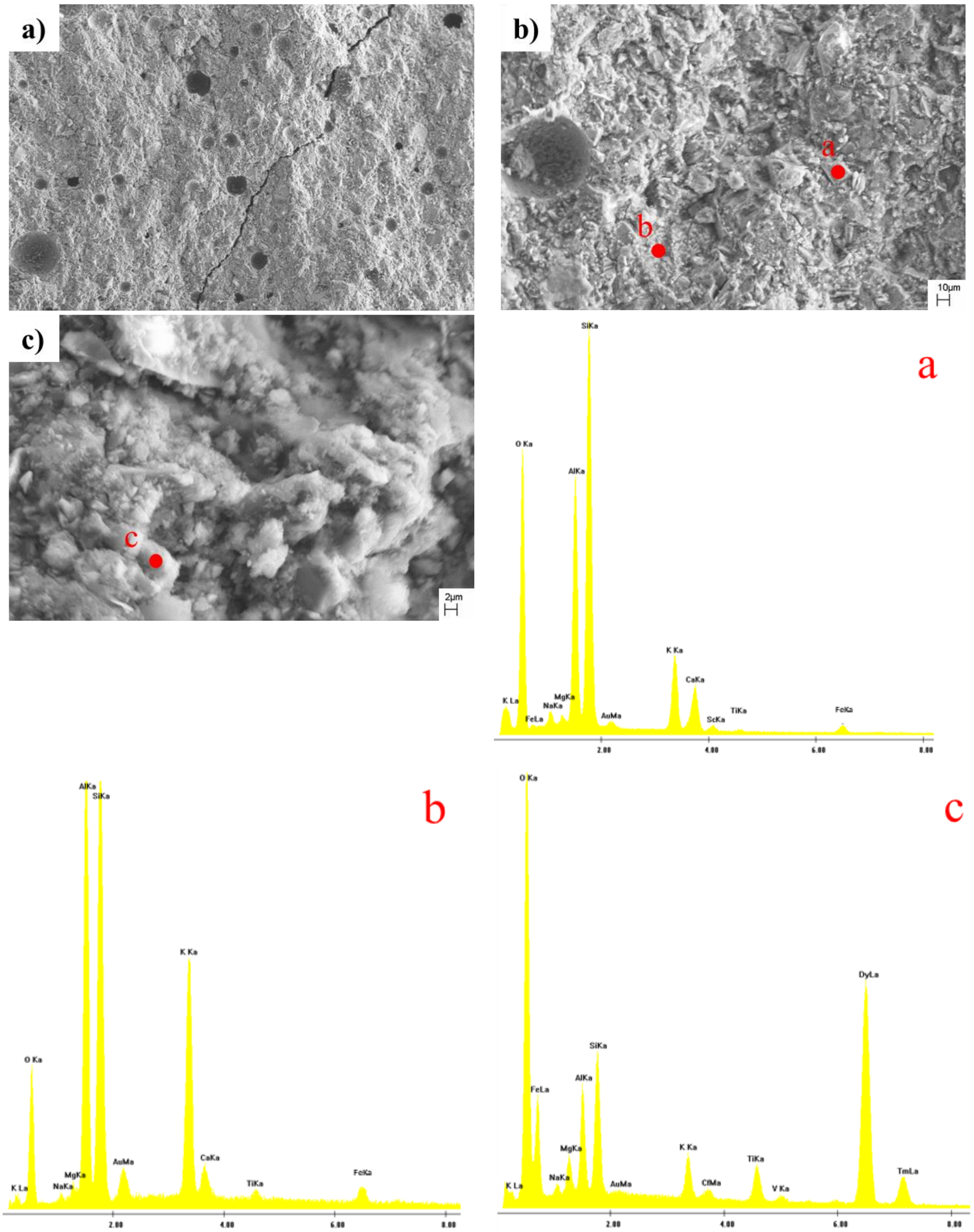

Fig. 5.34 – SEM micrographs of K-GM-20 sample: Mag. 150x; b) Mag. 1Kx; c) Mag. 5Kx and EDX analysis whose spot analysis are indicated in red dots (a-c).

5.4 CONCLUSIONS

The multiparametric approach used in this case study have given interesting results. Firstly, the polycondensation reaction, fingerprint of alkaline activated materials, was confirmed by in situ FTIR analysis, through the observations of continuous and progressive shift of the Si-O-M band position in time toward lower wavenumbers. The additive function of metakaolin demonstrated a better reticulation, favouring the partial dissolution of volcanic precursor’s mineralogical phases, inducing the increase of the Si and Al species available and a stable structure (decreasing of carbonate species at increasing of metakaolin content), as well as an improvement of mechanical compressive strengths. The comparison of alkaline solutions evidenced higher mechanical strengths for potassium one despite of higher density combined to a lower porosity differently to sodium samples. All these results (except RAMAN ones and SEM-EDX of K-samples) were published in Finocchiaro et al., 2020. This case study has represented an important opportunity for my personal and educational grow, as well as a development of my knowledge on these materials.

6. II INSIGHT: NEURAL NETWORK APPROACH AND COMPARISON WITH CONVENTIONAL APPROACH (MLR)

The second case study was born in collaboration with the Department of Engineering “Enzo Ferrari” of Modena and Reggio Emilia University and it focus on neural network approach to predict the chemical stability of two set of geopolymers, one of them already discussed in Chapter 4.3 (VM1 and GM1 series). In general, the final physical properties of alkali activated materials (AAMs) are strongly influenced by different variables, such as SiO_2/Al_2O_3, Na/Al and solid/liquid ratios (Duxson et al., 2007; Xu & Van Deventer, 2000), especially when for aluminosilicate sources, natural waste materials (i.e. pyroclastic deposits) characterized by an intrinsic heterogeneity are used. In the last two decades, the interest towards previsional modeling methods has strongly increased, and among all methods, artificial neural networks (ANNs) are very appreciated for engineering applications, although in geopolymer field is still few explored. Generally, ANNs have been focused on mechanical behaviour (Bondar 2014; Ling et al. 2019; Nazari 2013; Sadat et al. 2018; Sadat et al., 2018) and abrasion resistance predictions (Lau et al., 2019) of geopolymer materials. However, none ANNs have been applied to geopolymers based on volcanic particles until now. Therefore, in this chapter, ANNs were tested for the first time to AAMs based on pyroclastic deposits, evaluating chemico-physical properties: weight loss after leaching test in water, ionic conductivity and pH of the leachate and compressive strength. In this scenario, this previsional approach can be useful to provide an optimization of mix design for AAMs based on volcanic particles with great durability features. Simultaneously, traditional multiple linear regressions (MLR) were implemented to compare the correlation found with ANNs, aiming to highlight the strength points of previsional approaches used.

6.1 MATERIALS AND SAMPLE PREPARATION

The dataset is made of four series of geopolymers (two for each volcanic precursor): two already explained in Chapter 4.3 (VM1 and GM1 series) of which the labels will be different in this chapter, while the others were prepared for this test. In detail, eighteen binary mixtures made of volcanic ash (indicated with “V”) or ghiara paleo-soil (G) with small and progressive increases (10-25% wt. on the solid total weight) of metakaolin (MK), commercialized as ARGICAL™ M1000 (provided by IMERYS, France) (Medri et al., 2010) and two different sodium activating solutions were considered. These latter are differentiated by the type and the quantity of sodium silicate used: i) a combination of sodium hydroxide (8M) and sodium silicate, provided by Ingessil s.r.l., Italy, with a molar ratio SiO_2/Na_2O = 3; ii) a different sodium silicate (code: 373908), provided by Carlo Erba, Italy, with a molar ratio SiO_2/Na_2O = 2, maintaining constant the quantity of sodium hydroxide (8M). Therefore, the samples considered for the ANNs and MLR implementation are labelled as following: VM/GM_3-10/25 and VM/GM_2-10/25, indicating with the subscript the type of silicate according the SiO_2/Na_2O molar ratio. Moreover, for VM/GM_2 series, a formulation with lower silicate amount, labelled VM/GM_2-20LS, was considered. All the formulations with corresponding labels are reported in Table 6.1. The same preparation steps were adopted for all series to make them comparable.

Table 6.1 – Labels and formulation details (in % wt.) of the experimentally prepared AAMs.

Sample	**V or G (%)**	**MK (%)**	**NaOH (8M) (%)**	**Na_2SiO_3 (SiO_2/Na_2O = 3) (%)**	**Na_2SiO_3 (SiO_2/Na_2O = 2) (%)**	**H_2O (%)**
VM_3-10	68.18	7.58	2.24	5.45	0.00	16.56
VM_3-15	64.39	11.36	2.24	5.45	0.00	16.56
VM_3-20	60.61	15.15	2.24	5.45	0.00	16.56
VM_3-25	56.82	18.94	2.24	5.45	0.00	16.56
VM_2-10	59.21	6.58	1.94	0.00	12.89	19.37
VM_2-15	55.92	9.87	1.94	0.00	12.89	19.37
VM_2-20	52.63	13.16	1.94	0.00	12.89	19.37
VM_2-25	49.34	16.45	1.94	0.00	12.89	19.37
VM_2-20LS	57.14	14.29	2.11	0.00	9.80	16.66
GM_2-10	62.50	6.94	2.05	0.00	10.89	17.62
GM_2-15	59.03	10.42	2.05	0.00	10.89	17.62
GM_2-20	55.56	13.89	2.05	0.00	10.89	17.62
GM_2-25	52.08	17.36	2.05	0.00	10.89	17.62
GM_2-20LS	57.14	14.29	2.11	0.00	9.80	16.66
GM_3-10	68.18	7.58	2.24	5.45	0.00	16.56
GM_3-15	64.39	11.36	2.24	5.45	0.00	16.56
GM_3-20	60.61	15.15	2.24	5.45	0.00	16.56
GM_3-25	56.82	18.94	2.24	5.45	0.00	16.56

6.2 EXPERIMENTAL METHODS

The eighteen samples of both series were characterized with the aim to assess the chemical stability in aqueous environment evaluating the consolidation performance after alkaline activation. Therefore, the pH and the ionic conductivity test were performed on the solutions following the immersion of samples, after 28 room temperature curing days, at 25°C in de-ionized water. The ionic conductivity measures the solution's electrical conductivity which is influenced by the motion of all the free ionic charges released in the solutions and thus, strongly depending on the total dissolved solids. To perform pH tests, a Laboratory PH sensor Hamilton type Liq-glass SL was used, whose measurements were performed using an OAKTON Eutech Instruments Ph5/6 and Ion 6. Electrical conductivity was measured with OAKTON Eutech Instruments CON 6/TDS 6. Therefore, solid shreds of samples were immersed in distilled water with a solid/liquid ratio of 1/10 in stirring conditions for 24 hours in a beaker. Measurements were determined for different times 0, 5, 15, 30, 60, 120, 720, 1440 min, evaluating the values changes over the 24h as results of amount of dissolved solid (Barone et al., 2020). At the same time, the weight loss after water treatments in stirring condition were evaluated, comparing the initial (w_i) and the final (w_f) weights, whose values are expressed in percentage according the following equation:

$$weight\ loss\ (\%) = \frac{w_i - w_f}{w_i} x100$$

Compressive strength was determined using an Instron 5567 Universal Testing Machine with 30 kN load limit and displacement of 3mm/min according to the standard UNI EN 826 on four cubic samples (2x2x2 cm^3) of each formulation cured at 28 days.

6.3 ANALYSIS APPROACHES: ANN AND MLR

6.3.1 ANN PRINCIPLES

ANNs are computational modeling tools used in complex problem solving tasks organized with dense architectures, highly interconnected by simple computing elements (called artificial neurons or nodes) capable to perform parallel computations for data processing (Daniel, 2013; Haykin, 1994). ANNs find analogies with those of human brain network. In detail, they are arranged based on a hierarchical structure with three main layers: input layer, hidden layer (one or more) and output layer, linked through weighted connections (i.e. values) (Basheer & Hajmeer, 2000; Pala et al., 2007; Shi et al., 2010). Each node calculates the effect of inputs and weights through the sum function, which calculates the net input linked to a neuron (Nazari, 2013). The weighted sums of the input components $(net)_j$ are calculated using the following equation:

$$(net)_j = \sum_{i=1}^{n} W_{ij} x_i + b \tag{1}$$

where $(net)_j$ is the weighted sum of the *j*th neuron for the input received from the preceding layer with n neurons, W_{ij} is the weight between the *j*th neuron in the previous layer, x_i is the output of the *i*th neuron in the previous layer (Liu et al., 2002), *b* is a fix value, known as *bias*, and ∑ represents the sum function.

Activation function is a function that processes the net input obtained from sum function and determines the neuron output. In general, for multilayer feed-forward models as the activation function, sigmoid activation function is used. The output of the *j*th neuron $(out)_j$ is computed with a sigmoid activation function using the following equation (Günaydin & Doğan, 2004):

$$O_j = f(net)_j = \frac{1}{1 + e^{-\alpha (net)_j}} \tag{2}$$

where α is constant used to control the slope of the semi linear region. The sigmoid non-linearity activates in every layer except in the input layer (Günaydin & Doğan, 2004). The sigmoid activation function represented by Eq. (2) gives outputs in (0, 1). If it desired, the outputs of this function can be adjusted to (-1, 1) interval. As the sigmoid processor represents a continuous function, it is particularly used in non-linear descriptions. Because its derivatives can be determined easily with regard to the parameters within $(net)_j$ variable (Liu et al., 2002). However, these connections need to be trained to induce the input variables to the awaited results in agreement with the experimental ones through continuous iterations (Özcan et al., 2009; Yaprak et al., 2013), computed for example using a feed forward-backpropagation Neural Network aimed to minimize the total error or mean error of target computed by the neural network (Dou et al., 2015).

6.3.2 ANN DESIGN

Four ANNs for each physical parameter (weight loss, conductivity, pH and compressive strengths), measured during the laboratory experiments with the same measuring setting, were implemented using the design reported in Table 6.2. AAN model has 6 neurons in the input layer, ten neurons in one hidden layer and one neuron as output layer as schematically plotted in Fig. 6.1. The mix design of each formulation was used as input data, considering the volcanic precursor, metakaolin, sodium hydroxide, water, sodium silicate type and amounts (Table 6.3). In detail, the ANNs were created according the type of volcanic precursor (i.e. V-ANNs and G-ANNs). Moreover, these latter were used as training series for the opposite one with the aim to observe affinities among these pyroclastic materials (i.e. V-ANNs were used to predict GM samples and vice versa). The neurons of neighbouring layers are completely interconnected by weights. The software used was NNpred, a freeware MS-Excel implementation developed by Angshuman Saha (Saha, 2011) and extensively used across many field and academia. A feedforward-backpropagation Neural Network with a sigmoid activation function was used. Momentum rate and learning rate values did not optimise but the default values were used for model training. NNpred is set by the developer to perform only 500 training cycles, but it was forced to carry out 5000 epochs with the aim to obtain a better fitting, thus, to reach the least training error. This latter can be reached after epoch nr. 5000 or lower depend on the setting and/or dataset and generally, already after few tens of epochs the training error decreases of much.

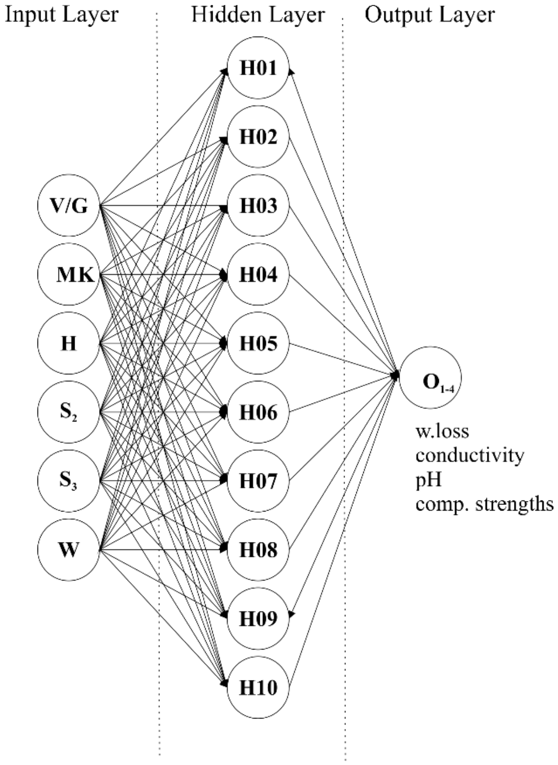

Fig. 6.1 – ANN model used: neuron (circle) and weight (arrow). Input layer: volcanic ash/ghiara (V/G); metakaolin (MK); sodium hydroxide (H); sodium silicate with SiO2/Na2O = 2 (S2); sodium silicate with SiO2/Na2O = 3 (S3); water (W). Hidden layer (H01-10); Output layer (O1-4): weight loss, conductivity, pH and compressive strengths.

Table 6.2 – Parameters used in ANNs.

Network Architecture	
Number of inputs	6
Number of hidden layers	1
Hidden layer size	10
Number of outputs	1
Learning parameter (range 0-1)	0.4
Momentum (range 0-1)	0
Number of training cycles	5000
Training Mode	Sequential

Table 6.3 – Summary with input data (% wt. reactants) and output data (experimental results). These latter include the results of chemical stability test (weight loss, ionic conductivity and pH) and compressive strengths after 28 curing days. The errors of each equipment are: 0.01g referred to balance sensitivity for weight loss; ±1% full scale accuracy for ionic conductivity; ±0.1 pH;

standard deviation was calculated for compressive strength. The double line divides the samples according to V/G-ANNs. The results of VM/GM$_2$ are reported from (Barone et al., 2020).

							Output data			
	Input data						**O_1**	**O_2**	**O_3**	**O_4**
Sample	**V or G (%)**	**MK (%)**	**NaOH (8M) (%)**	**Na_2SiO_3 (SiO_2/Na_2O = 3) (%)**	**Na_2SiO_3 (SiO_2/Na_2O = 2) (%)**	**Tot. H_2O (%)**	**weight loss (%)**	**Conductivity (mS/m)**	**pH**	**Comp. Strength (MPa)**
VM$_3$-10	68.18	7.58	2.24	5.45	0.00	16.56	1.76	312	9.3	24.77
VM$_3$-15	64.39	11.36	2.24	5.45	0.00	16.56	5.18	372	9.5	37.79
VM$_3$-20	60.61	15.15	2.24	5.45	0.00	16.56	0.87	245	8.6	32.58
VM$_3$-25	56.82	18.94	2.24	5.45	0.00	16.56	0.91	261	8.5	39.59
VM$_2$-10	59.21	6.58	1.94	0.00	12.89	19.37	5.95	574.1	12.2	14.27
VM$_2$-15	55.92	9.87	1.94	0.00	12.89	19.37	4.68	574	12.2	15.32
VM$_2$-20	52.63	13.16	1.94	0.00	12.89	19.37	4.15	504	12.0	23.3
VM$_2$-25	49.34	16.45	1.94	0.00	12.89	19.37	3.23	261.1	12.0	38.03
VM$_2$-20LS	57.14	14.29	2.11	0.00	9.80	16.66	3.94	261.2	11.8	34.21
GM$_2$-10	62.50	6.94	2.05	0.00	10.89	17.62	5.56	598	12.0	10.84
GM$_2$-15	59.03	10.42	2.05	0.00	10.89	17.62	4.38	648	12.2	15.09
GM$_2$-20	55.56	13.89	2.05	0.00	10.89	17.62	2.92	569	12.1	25.27
GM$_2$-25	52.08	17.36	2.05	0.00	10.89	17.62	1.76	454	12.1	37.9
GM$_2$-20LS	57.14	14.29	2.11	0.00	9.80	16.66	2.33	536	12.1	32.21
GM$_3$-10	68.18	7.58	2.24	5.45	0.00	16.56	1.84	331	9.0	16.87
GM$_3$-15	64.39	11.36	2.24	5.45	0.00	16.56	0.93	337	9.1	21.93
GM$_3$-20	60.61	15.15	2.24	5.45	0.00	16.56	0.87	265	9.2	27.65
GM$_3$-25	56.82	18.94	2.24	5.45	0.00	16.56	0.58	173	8.8	40.54

6.3.3 MLR PRINCIPLES

Through the regression analysis, the dependent variables (y) are evaluated considering the variations of independent variables (x), with the aim to determine which one has a significant impact. According to the relationship between the dataset, a straight-line regression is the commonly used. In statistics, a linear regression is defined by the following mathematical equation:

$$Y_i = \beta_0 + \beta_1 X_1 + \cdots + \beta_n X_n + \varepsilon$$

Where:

Y_i = dependent variable

X_m = explanatory variables

β_0 = y-intercept (constant term)

β_m = slope coefficient of m-th explanatory variable

ε = the model’s error term (also known as the residuals) which is the difference between the value of dependent value and the expected one (Argyrous, 2011).

6.3.4 MLR DESIGN

Two set of multiple linear regressions (MLR) were implemented, labelled V-MLR and G-MLR respectively for volcanic ash and ghiara precursors. The independent variables were chosen among the type of reactants involved in each formulation considering significant influences on dependent ones (i.e. weight loss, conductivity, pH and compressive strengths). In this scenario, all reactants used for alkaline activation were considered except the sodium hydroxide and the sodium silicate with molar ratio equal to three (S_3) which resulted insignificant on dependent variables due to: i) the constant amount of NaOH used in all formulations; ii) the constant amount of S_3 in VM_3 and GM_3 series contrary to the other series (Table 6.3).

MLRs were performed using Excel tool “Data Analysis → regression” based on the *least square method*, with the goal to obtain the smallest possible squares sum and draw a line closest to the data. The interpretation of MLR was carried out considering the determination coefficient R squared (range value 0-1), indicator of the goodness of the adaptation, the R squared adjusted coefficient takes into account the independent variables number in the model with the aim to obtain both values much close each other and finally, the significance (F) of variance analysis to statistically quantify the reliability of the obtained results. Generally, this latter should be less than 0.05 (5%) to demonstrate the goodness of the model used.

6.4 EXPERIMENTAL RESULTS

The results of pH and ionic solution conductivity measurements showed interesting information about chemical stability. However, no attention is given to VM_2-15 sample due to the contrasting values in comparison to the others, maybe due to instrumental error or preparation one. In this scenario, we consider it marginally. Both pH and ionic conductivity measures are related to the number of ions released in water by the solid geopolymer. The conductivity results showed a general progressive increase with the time due to the release of ions into the water (Table 6.4). Moreover, the values were strongly influenced by metakaolin content: at the increase of the percentage of this latter, the ions released in water decrease confirming greater chemical stability of formulations and a greater degree of geopolymerization due to the optimization of Si/Al ratio. In detail, VM/GM$_2$ series evidenced a higher release of ions of 400-600 µS order than VM/GM$_3$ series due to the higher liquid/solid ratio (Fig. 6.2). However, VM$_2$-25 and VM$_2$-20LS highlighted values very close to those one of VM/GM$_3$ series of 200-300 mS/m order (Fig. 6.2). In general, the values of ionic conductivity are just one order of magnitude higher than that typical drinking water, typically in the range of 5–50 mS/m. Other values that can be used as reference are high quality de-ionized water has a conductivity of about 5.5 μS/m at 25 °C, while sea water around 5 S/m (or 5,000,000 μS/m). The pH values remain fairly constant during the 24h of test, confirming the chemical stability of the material showing a steady value already after 15 minutes and an average value slightly below 10 for VM/GM$_3$ series and 12 for VM/GM$_2$ series (see Table 6.5). Furthermore, the weight loss recorded the same behaviour recorded by conductivity test in all the series (not considering the VM$_2$-15 sample): decreasing of values at increasing of metakaolin amount, confirming the important role of this latter in alkaline process. In detail, the values have been recorded <2% in VM/GM$_3$ series and 2-6% in VM/GM$_2$ ones (Fig. 6.3).

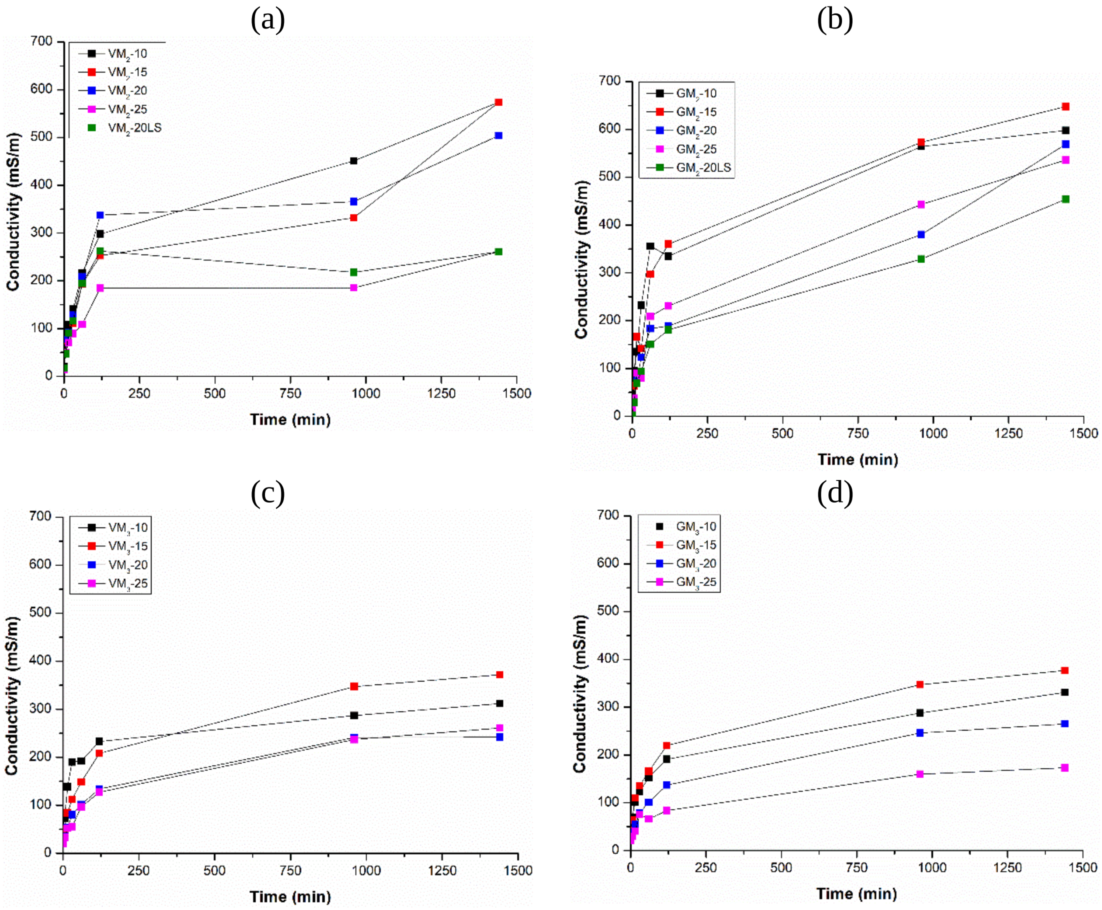

Fig. 6.2 - Conductivity trends over time for each series: a) VM$_2$; b) GM2; c) VM$_3$; d) GM$_3$.

Table 6.4 - Conductivity results over time (t0-t24) for each series.

	Time (min)							
Samples	**0**	**5**	**15**	**30**	**60**	**120**	**960**	**1440**
VM$_2$-10	20	72.4	107.6	141.2	216.4	298	451	574.1
VM$_2$-15	17.7	75.3	92.1	111	193.2	253	332.1	574
VM$_2$-20	16.2	77.7	92.5	128.1	208	337.4	366	504
VM$_2$-25	17.5	47.1	90.2	116.2	194.3	262.1	218	261.1
VM$_2$-20LS	13.5	50.4	70.7	89.5	109.2	185.1	185.4	261.2
GM$_2$-10	43.1	96	135.2	232	356	335	564	598
GM$_2$-15	16.7	63.8	166.5	142.1	297	360	573	648
GM$_2$-20	4.7	32.9	74.5	123.4	183.5	189	380	569
GM$_2$-25	2.5	28.9	69	94.1	150.6	181	329	454
GM$_2$-20LS	13	38	90.4	80.3	209	231	443	536
VM$_3$-10	52.3	71.9	138.1	189.9	192.4	233	287	312
VM$_3$-15	39.8	50.2	83.8	112.4	148.3	208.06	347	372
VM$_3$-20	20.9	35.1	53.8	80.3	101.9	134.1	241	242
VM$_3$-25	20.2	33.2	52.2	55.3	96.61	127.3	237	261
GM$_3$-10	56.7	69.8	102.1	123.5	152.7	191.2	288	331

GM_3-15	42.2	63.8	110.4	135.3	165.8	220	347	377
GM_3-20	20.61	39.3	54.6	79.5	100.7	136.9	246	265
GM_3-25	21.8	29.2	40.3	75.8	66	83.7	159.9	173.4

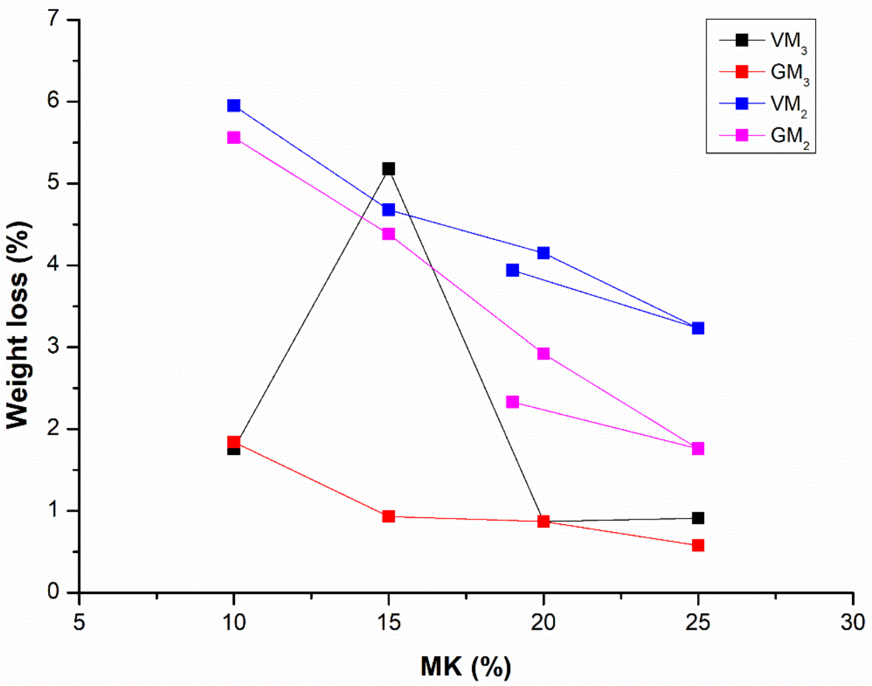

Fig. 6.3 - Trends of weight loss Vs metakaolin amount. The samples "LS" are set as 19% wt. MK.

Finally, the compressive strengths evidenced the contrary effect: increase at increasing of metakaolin amount (except for VM_3-15). In general, the samples of VM/GM_3 series showed higher strengths than those of VM/GM_2 series. Moreover, these differences are higher in the samples with lower metakaolin and gradually tends to zero in the samples with greater additive component. Moreover, the samples VM/GM_2-20LS show compressive strengths ranging among those with 20 and 25% wt. MK (Fig. 6.4). Therefore, according to these results summarized in Table 6.5, a better reticulation was reached in the samples with higher metakaolin amount, demonstrating the positive influence as additive component to obtain binders at room temperature as in situ interventions. By comparing the series activated with alkaline solution with SiO_2/Na_2O = 3 and with SiO_2/Na_2O = 2, it appears evident the improvement of all the properties for ratio = 3. This is an important finding because it means such ratio strongly influences the reticulation as well as the leaching of ionic species in water, while the effect on compressive strength is not so evident. In particular, all the chemical properties such as weight loss, pH and conductivity decrease for ratio 3, indicating the formation of a more stable matrix, with a correlated increase of mechanical properties. A study of such trend with statistical model will allow a deeper understanding and quantification of the role of the alkaline solution and the aluminosilicate precursor.

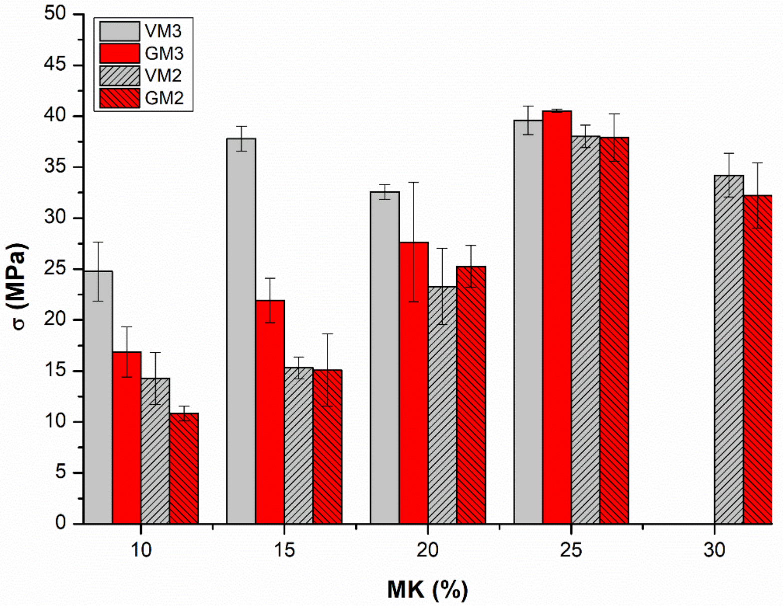

Fig. 6.4 - Histograms of compressive strengths of all series. The samples "LS" are set as 30% wt. MK.

Table 6.5 - Summary results of all experimental test after 28 curing days: weight loss, conductivity, pH and compressive strengths.

	Chemical stability			**Compressive strengths**	
Sample	**Weight loss (%)**	**Conductivity (mS/m)**	**pH**	**Average (MPa)**	**St. deviation**
VM$_3$-10	1.76	312	9.3	24.77	2.89
VM$_3$-15	5.18	372	9.53	37.79	1.21
VM$_3$-20	0.87	245	8.58	32.58	0.73
VM$_3$-25	0.91	261	8.54	39.59	1.39
GM$_3$-10	1.84	331	8.98	16.87	2.46
GM$_3$-15	0.93	337	9.14	21.93	2.18
GM$_3$-20	0.87	265	9.21	27.65	5.85
GM$_3$-25	0.58	173	8.81	40.54	0.16
VM$_2$-10	5.95	574.1	12.2	14.27	2.55
VM$_2$-15	4.68	574	12.16	15.32	1.07
VM$_2$-20	4.15	504	11.96	23.3	3.74
VM$_2$-25	3.23	261.2	11.96	38.03	1.1
VM$_2$-20LS	3.94	261.1	11.8	34.21	2.17
GM$_2$-10	5.56	598	12.01	10.84	0.74

GM_2-15	4.38	648	12.15	15.09	3.56
GM_2-20	2.92	569	12.06	25.27	2.04
GM_2-25	1.76	454	12.13	37.9	2.32
GM_2-20LS	2.33	536	12.13	32.21	3.22

6.5 ANNS RESULTS

6.5.1 V-ANNS

The V-ANNs trained with the input data of VM samples shows an excellent capacity to predict the experimental data. Fig. 6.5 plots the correlations between the experimental (x axis) and calculated (y axis) data for each physical property by VM input data. Indeed, the high determination coefficients (R^2) of each trendline confirms the good fitting. Moreover, the correlation coefficients of each physical property are almost equal to one (Table 6.6). Differently, the previsions on calculated data of GM samples driven by VM training data show, in general, a discrete predicting capacity (Fig. 6.6) with a correlation coefficient ranging around 0.53-0.98. In particular. the pH is the best predicted variable (Fig. 6.6c), while the conductivity the worst among all the material properties considered (Fig. 6.6b). Concerning the chemical stability results, in the prediction of ionic conductivity (Fig. 6.5b) and pH (Fig. 6.5c), the V-ANNs tends to linearize the results for the V-AAMs series, leaving the VM_3-15 values out of trendline as expected. The G-ANNs plots using VM-training overestimate the ionic conductivity for the GM_3 series while underestimate the GM_2 series (Fig. 6.6b). This means that the alkaline solution with SiO_2/Na_2O molar ratio of 3 had a much stronger reticulation effect, i.e. lower conductivity values, on ghiara-based AAMs with respect to volcanic ash, that appeared almost insensitive to such molar ratio. Similar considerations can be deduced for the weight loss plot (Fig. 6.6a), where GM_3 series have values overestimated. Also, in this case the alkali activator had a more efficient role of consolidating the geopolymeric matrix in the ghiara-based materials with respect to the volcanic ash. The comparison of such ANNs results provide an interesting support to the interpretation of the role of the two different alkaline solutions used as activators for the production of alkali activated materials. In particular, the ghiara-based formulation reacted much better in the SiO_2/Na_2O molar ratio = 3 conditions, while in the volcanic ash-base materials the reactivity is mainly due to the metakaolin fraction and proceed with the linearity expected from the % amount of MK in the mixture whatever the alkaline solution is used.

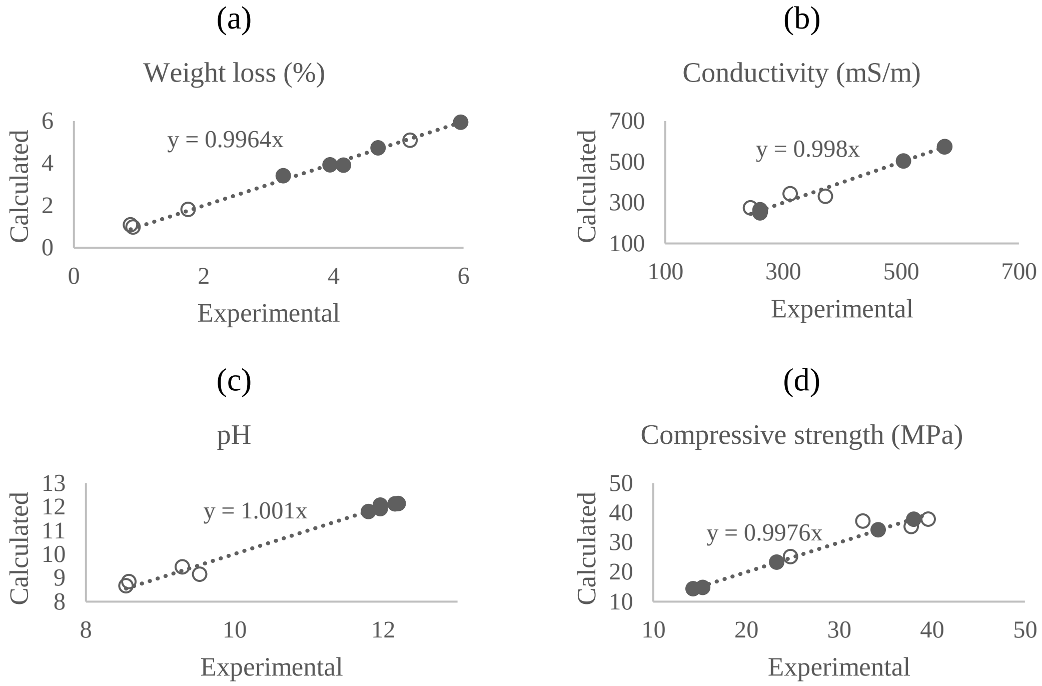

Fig. 6.5 (a-d) – V-ANNs plots for each ANN created: a) weight loss; b) conductivity; c) pH; d) average compressive strengths. In x axis experimental results, while in y axis calculated one. The dashed line indicates the trendline passing for the origin. Legends: ● VM$_2$ series ○ VM$_3$ series.

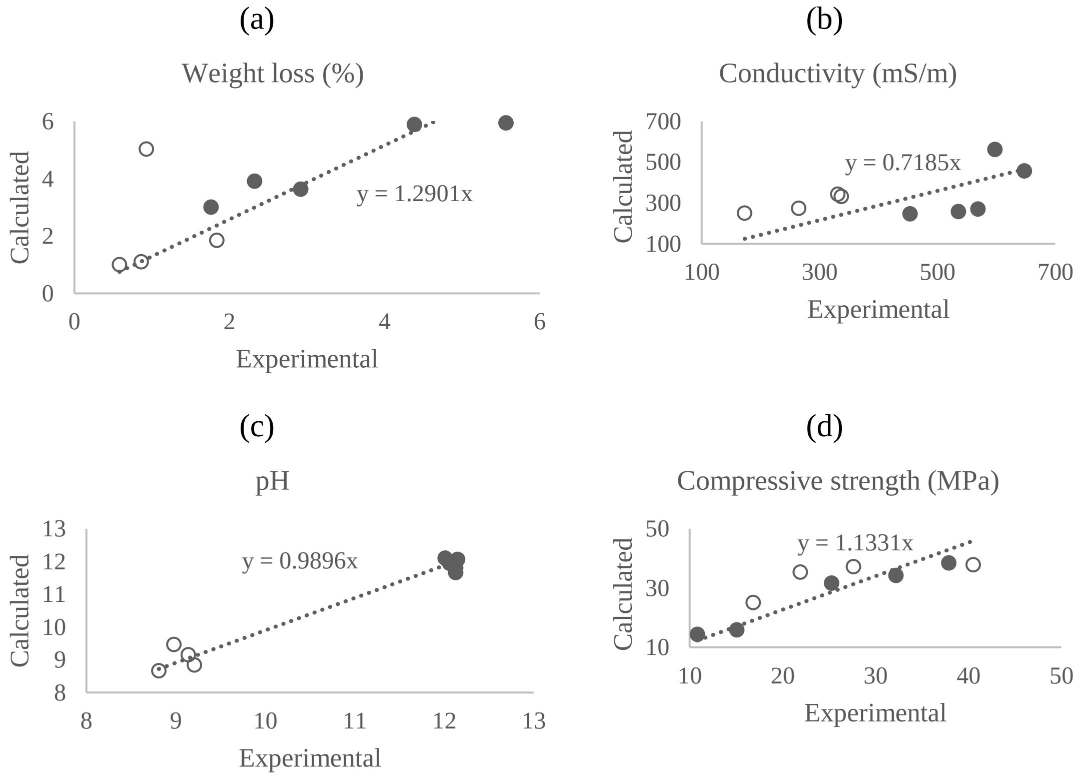

Fig. 6.6 (a-d) – G-ANNs plots using VM-training: a) weight loss; b) conductivity; c) pH; d) average compressive strengths. In x axis experimental results, while in y axis calculated one. The dashed line indicates the trendline passing for the origin. Legends: ● GM$_2$ series ○ GM$_3$ series.

Table 6.6 – Correlation between experimental and calculated data using V-training.

	Experimental data				**Calculated data**			
Sample	**weight loss (%)**	**Conductivity (mS/m)**	**pH**	**Comp. Strength (MPa)**	**weight loss (%)**	**Conductivity (mS/m)**	**pH**	**Comp. Strength (MPa)**
VM$_3$-10	1.76	312	9.3	24.77	1.80	342.3	9.5	25.09
VM$_3$-15	5.18	372	9.5	37.79	5.08	330.8	9.1	35.31
VM$_3$-20	0.87	245	8.6	32.58	1.09	273.6	8.8	37.15
VM$_3$-25	0.91	261	8.5	39.59	0.97	249.1	8.7	37.79
VM$_2$-10	5.95	574.1	12.2	14.27	5.95	573.9	12.1	14.34
VM$_2$-15	4.68	574	12.2	15.32	4.73	572.3	12.1	14.86
VM$_2$-20	4.15	504	12.0	23.3	3.91	504.3	12.1	23.38
VM$_2$-25	3.23	261.1	12.0	38.03	3.41	264.6	11.9	37.80
VM$_2$-20LS	3.94	261.2	11.8	34.21	3.92	258.1	11.8	34.25
				Corr. Coef.	0.998	0.988	0.994	0.980
GM$_3$-10	1.84	331	9.0	16.87	1.85	342.3	9.5	25.09
GM$_3$-15	0.93	337	9.1	21.93	5.03	330.8	9.1	35.31
GM$_3$-20	0.87	265	9.2	27.65	1.10	273.6	8.8	37.15
GM$_3$-25	0.58	173	8.8	40.54	1.00	249.1	8.7	37.79
GM$_2$-10	5.56	598	12.0	10.84	5.95	562.4	12.1	14.39
GM$_2$-15	4.38	648	12.2	15.09	5.89	457.7	12.1	15.92
GM$_2$-20	2.92	569	12.1	25.27	3.64	270.6	12.0	31.65
GM$_2$-25	1.76	454	12.1	37.9	3.01	247.6	11.7	38.47
GM$_2$-20LS	2.33	536	12.1	32.21	3.92	258.1	11.8	34.25
				Corr. Coef.	0.766	0.538	0.985	0.867

6.5.2 G-ANNS

Analogously to the V-ANNs, the input data of GM series were used to train the G-ANNs. The obtained data, following the mathematical iterations of neural networks, evidence great capacity to predict the experimental results, as confirmed by the high correlation coefficients (i.e. about one) (Table 6.7). The correlations between the experimental (x axis) and calculated (y axis) data were plotted in Fig. 6.7, whose determination coefficients (R^2) of each trendlines demonstrated the good fitting. Moreover, the previsions on calculated data of VM samples, driven by GM training data, evidence an excellent predicting capacity (Fig. 6.8) with a correlation coefficient ranging around 0.71-0.98, whose highest value is linked to the pH (Fig. 6.8c) following by the compressive strengths (Fig. 6.8d). Also, in this case, when considering the chemical aspects of the stabilization of the solid structure derived from the alkali activation process, the V-ANNs plots using GM-training indicate the sensitivity of the ghiara-based formulation upon the activating alkaline solution used. In plots reported in Fig. 6.8a-b, the ANNs are not predicting the linearity typical of the volcanic ash-base materials for the VM$_2$ series, that were clearly overestimated by the prediction. These results suggest the strategy for optimizing the mix design using S$_3$ Na-silicate.

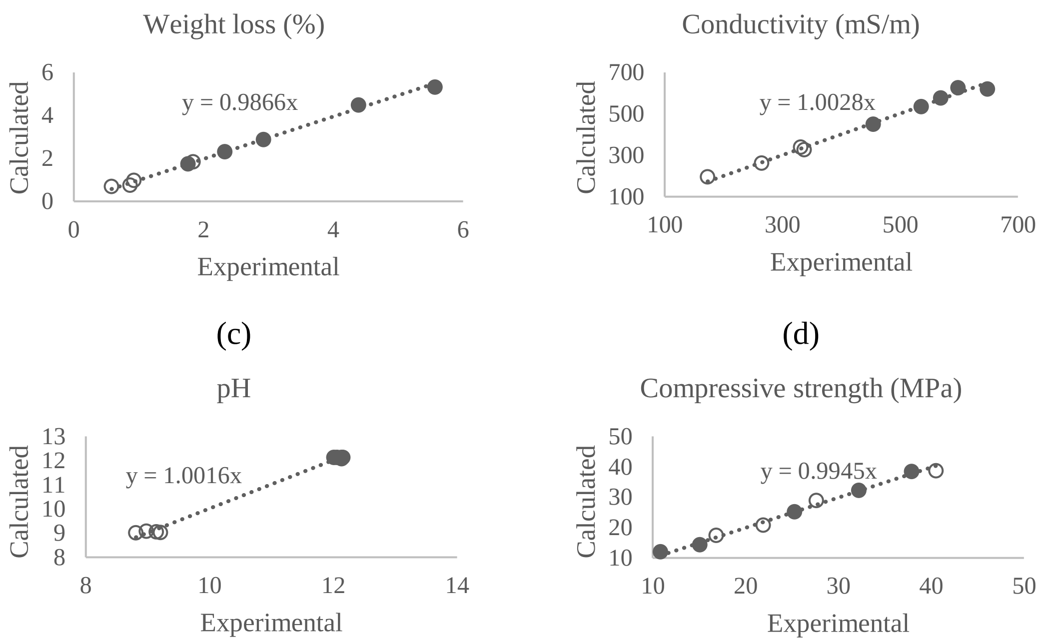
(a) (b) (c) (d)

Fig. 6.7 (a-d) – G-ANNs plots for each ANN created: a) weight loss; b) conductivity; c) pH; d) average compressive strengths. In x axis experimental results, while in y axis calculated one. The dashed line indicates the trendline passing for the origin. Legends: ● GM$_2$ series ○ GM$_3$ series.

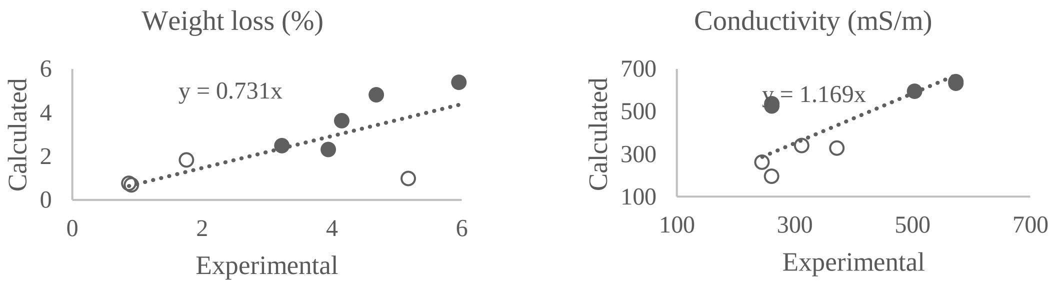
(a) (b)

(c) (d)

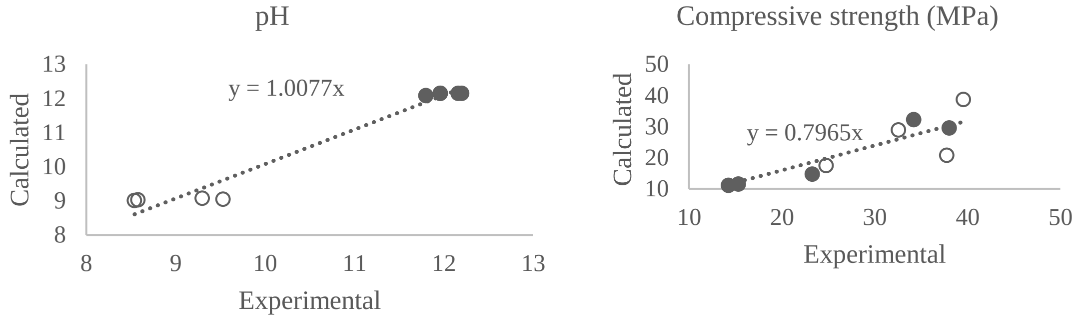

Fig. 6.8 (a-d) – V-ANNs plots using GM-training: a) weight loss; b) conductivity; c) pH; d) average compressive strengths. In x axis experimental results, while in y axis calculated one. The dashed line indicates the trendline passing for the origin. Legends: ● VM$_2$ series ○ VM$_3$ series.

Table 6.7 – Correlation between experimental and calculated data using G-training.

	Experimental data				**Calculated data**			
Sample	**weight loss (%)**	**Conductivity (mS/m)**	**pH**	**Comp. Strength (MPa)**	**weight loss (%)**	**Conductivity (mS/m)**	**pH**	**Comp. Strength (MPa)**
GM$_3$-10	1.84	331	9.0	16.87	1.83	339.1	9.1	17.40
GM$_3$-15	0.93	337	9.1	21.93	0.98	327.0	9.0	20.77
GM$_3$-20	0.87	265	9.2	27.65	0.75	261.4	9.0	28.82
GM$_3$-25	0.58	173	8.8	40.54	0.68	195.1	9.0	38.62
GM$_2$-10	5.56	598	12.0	10.84	5.33	626.7	12.1	12.11
GM$_2$-15	4.38	648	12.2	15.09	4.49	620.5	12.1	14.34
GM$_2$-20	2.92	569	12.1	25.27	2.89	577.6	12.1	25.27
GM$_2$-25	1.76	454	12.1	37.9	1.75	451.2	12.1	38.47
GM$_2$-20LS	2.33	536	12.1	32.21	2.32	536.3	12.1	32.23
				Corr. Coef.	0.998	0.995	0.997	0.995
VM$_3$-10	1.76	312	9.3	24.77	1.83	339.1	9.1	17.40
VM$_3$-15	5.18	372	9.5	37.79	0.98	327.0	9.0	20.77
VM$_3$-20	0.87	245	8.6	32.58	0.75	261.4	9.0	28.82
VM$_3$-25	0.91	261	8.5	39.59	0.68	195.1	9.0	38.62
VM$_2$-10	5.95	574.1	12.2	14.27	5.39	640.6	12.1	11.13
VM$_2$-15	4.68	574	12.2	15.32	4.83	633.9	12.1	11.55
VM$_2$-20	4.15	504	12.0	23.3	3.64	596.3	12.1	14.70
VM$_2$-25	3.23	261.1	12.0	38.03	2.49	526.9	12.1	29.48
VM$_2$-20LS	3.94	261.2	11.8	34.21	2.32	536.3	12.1	32.23
				Corr. Coef.	0.715	0.713	0.982	0.873

6.6 MLR RESULTS

6.6.1 V-MLR

With the aim to compare the ANN results with those of other more conventional statistical methods, Multiple Linear Regression approach was carried out on the same sample sets. The results of each physical property and the corresponding trendlines considering, set passing for the origin of Cartesian graph to avoid the negative intercepts obtained by least square iterations, were plotted in Fig. 6.9, while the original (R^2) and adjusted determination coefficient, as well as the significance of variance analysis, are showed in Table 6.8 (see Table 6.9 for details on experimental and calculated results). The MLR of the weight loss showed a better fitting for the VM_2 series (Fig. 6.9a), although R^2 and R^2 adjusted are the lowest among all V-MLR, as well as confirmed by the highest significance (F) value (31%) (Table 6). The MLR of conductivity (Fig. 6.9b) and compressive strengths (Fig. 6.9d) showed a comparable behaviour, from which no series prevails and whose values suggest a poor correlation. Contrary, the MLR of pH evidences an excellent correlation (Fig. 6.9c), as highlighted by the significance (F) and the high determination coefficient close to one (Table 6.8). From the figures it appears evident the higher correlation for VM_2 with respect to VM_3, probably because the activation with S_3 solution is not considered as reported in MLR design paragraph. Further, the lower correlation is for chemical properties (weight loss and conductivity) strictly related to reticulation degree in terms of amount of release ions. The pH values within the same series are less influenced due to the alkaline environment for all the compositions.

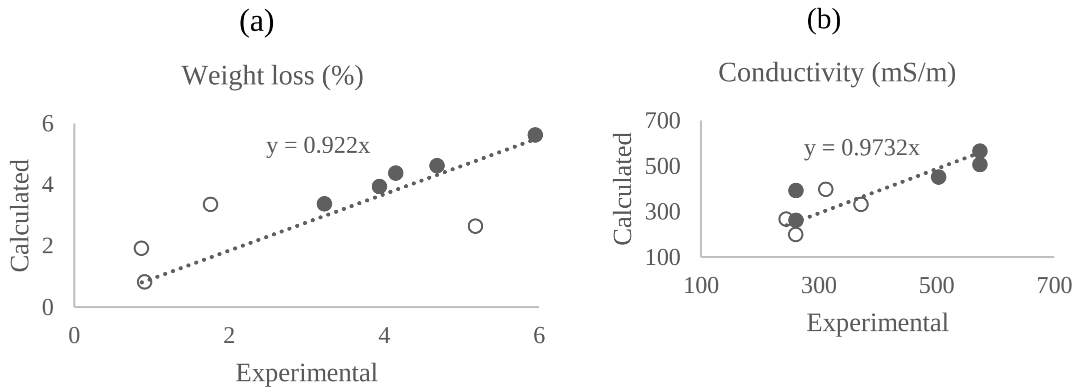
(a)
(b)

(c)

(d)

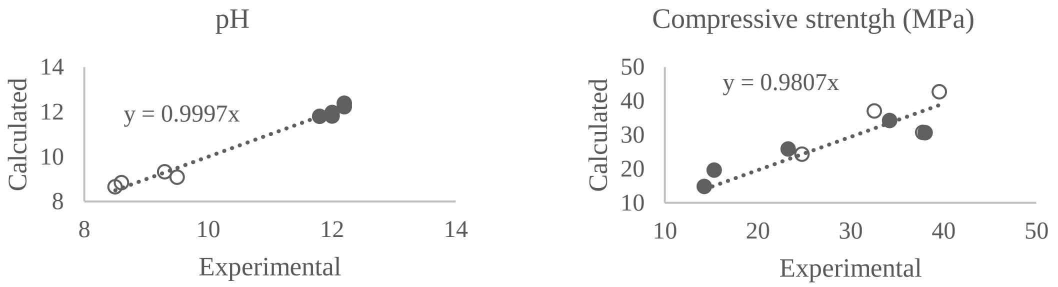

Fig. 6.9 (a-d) – V-MLR plots for each MLR created: a) weight loss; b) conductivity; c) pH; d) average compressive strengths. In x axis experimental results, while in y axis calculated one. The dashed line indicates the trendline passing for the origin. Legends: ● VM$_2$ series ○ VM$_3$ series.

6.6.2 G-MLR

All G-MLR evidenced excellent correlations for each physical property, whose graphs are plotted in Fig. 6.10 while the coefficients in Table 6.8 (see Table 6.9 for details on experimental and calculated results). Regardless the values higher than 90%, some thin distinctions can be done. The MLR of weight loss showed the lowest R^2 and the highest significance coefficient (Fig. 6.10a), while those one of conductivity (Fig. 6.10b) and compressive strengths (Fig. 6.10d) are comparable and that one of pH the highest determination coefficient (Fig. 6.10c; Table 6.8). Both GM$_2$ and GM$_3$ series highlighted the same behaviour and a great fitting, from which cannot be suppose none better network.

(a) (b)

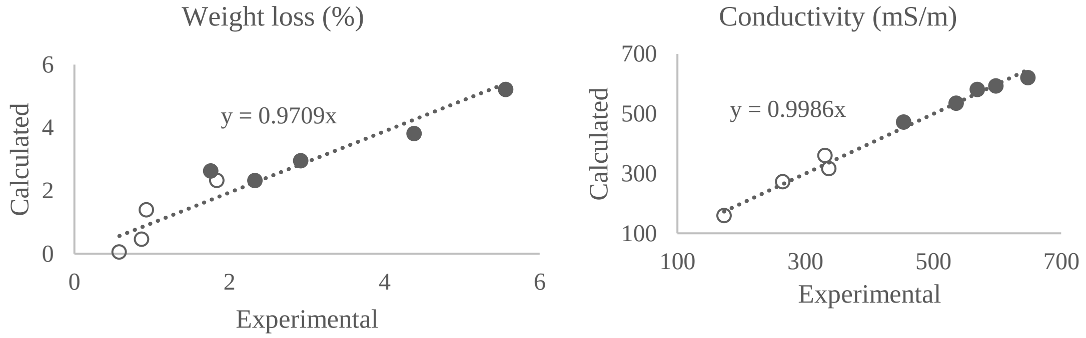

(c) (d)

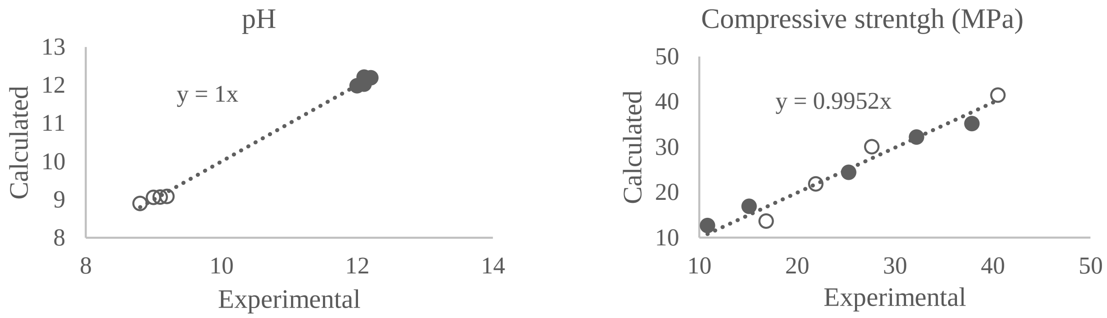

Fig. 6.10 (a-d) – G-MLR plots for each MLR created: a) weight loss; b) conductivity; c) pH; d) average compressive strengths. In x axis experimental results, while in y axis calculated one. The dashed line indicates the trendline passing for the origin. Legends: ● GM_2 series ○ GM_3 series.

Table 6.8 – MLR correlations of VM and GM samples for each physical property.

	Weight loss (%)		**Conductivity (mS/m)**		**pH**		**Compressive strength (MPa)**	
	VM	*GM*	*VM*	*GM*	*VM*	*GM*	*VM*	*GM*
R^2	0.625	0.907	0.756	0.988	0.985	0.998	0.791	0.962
R^2 adjusted	0.250	0.814	0.513	0.975	0.970	0.996	0.582	0.925
Significance (F)	0.31616	0.02425	0.14905	0.00046	0.00068	0.00001	0.11257	0.00415

Table 6.9 – Experimental and calculated results for each physical property. MLR formula was applied to calculate the data.

	Weight loss (%)	**Weight loss calc. (%)**	**Conductivity (mS/m)**	**Conductivity (mS/m) calc.**	**pH**	**pH calc.**	**Comp. strengths (MPa)**	**Comp. strengths (MPa) calc.**
VM_3-10	1.76	3.35	312.0	396.1	9.3	9.3	24.77	24.33
VM_3-15	5.18	2.63	372.0	330.7	9.5	9.1	37.79	30.68
VM_3-20	0.87	1.91	245.0	265.2	8.6	8.8	32.58	37.04
VM_3-25	0.91	0.82	261.0	198.0	8.5	8.7	39.59	42.68
VM_2-10	5.95	5.63	574.1	564.4	12.2	12.4	14.27	14.81
VM_2-15	4.68	4.63	574.0	505.9	12.2	12.2	15.32	19.61
VM_2-20	4.15	4.38	504.0	450.7	12.0	12.0	23.30	25.85
VM_2-25	3.23	3.38	261.1	392.2	12.0	11.8	38.03	30.65
VM_2-20LS	3.94	3.94	261.2	261.2	11.8	11.8	34.21	34.21
GM_3-10	1.84	2.33	331.0	359.6	9.0	9.1	16.87	13.65
GM_3-15	0.93	1.39	337.0	315.6	9.1	9.1	21.93	21.84
GM_3-20	0.87	0.45	265.0	271.7	9.2	9.1	27.65	30.03
GM_3-25	0.58	0.05	173.0	159.1	8.8	8.9	40.54	41.47
GM_2-10	5.56	5.21	598.0	593.3	12.0	12.0	10.84	12.64

GM_2-15	4.38	3.82	648.0	621.7	12.2	12.2	15.09	16.89
GM_2-20	2.92	2.96	569.0	581.4	12.1	12.2	25.27	24.40
GM_2-25	1.76	2.64	454.0	472.5	12.1	12.0	37.90	35.16
GM_2-20LS	2.33	2.33	536.0	536.0	12.1	12.1	32.21	32.21

6.7 CONCLUSION

Artificial Neural Network (ANN) was successfully applied to predict the chemical stability of volcanic alkali activated materials. Nine input data per each chemical-physical property was used to train each ANN. The training series of a specific volcanic precursors were tested also for the other one: excellent correlation among experimental and calculated data for the corresponding training series was found. Medium previsional capability for cross-correlations with the opposite volcanic series. This behaviour can be due to the need of a further round of experimental data aimed to increase the prediction capacity. As it is known, the ANNs have a good ability to extrapolate the result of samples that are outside the training range of the network, but this must be verified, and it will be subject to further study. Concerning the chemical stability results, from the AAN results appear evident that the alkaline solution with SiO_2/Na_2O molar ratio of 3 had a much stronger reticulation effect on GM samples with respect to volcanic ash, that appeared almost insensitive to such molar ratio. For these VM samples the reactivity is mainly due to the metakaolin fraction and proceed with the linearity expected from the % amount of MK in the mixture whatever the alkaline solution is used. In this context, the comparison of such ANNs results provides an interesting support to the interpretation of the role of the two different alkaline solutions used as activators. The comparison of the ANN results with more conventional Multiple Linear Regression (MLR) testify the high prediction performance of the first method. Indeed, no suppositions on better network or on the best alkaline activation solution can be done according to MLR results due to the insensitive S_3 which was excluded by MLR iteration for the null and void influence. However, G-MLR evidenced an excellent correlation contrary to V-MLR. However, only thanks to the combination of both methods was possible to reach these conclusions. Finally, the compressive strength values of similar precursors and few knowns in literature (in comparison to metakaolin and fly ash), such as volcanic deposits, are almost insensitive to the chemical network variations, differently from the results of weight loss, conductivity and pH that are strongly influenced by the degree of reticulation of the aluminosilicate matrix and in turn by Si/Al ratio of precursor mixtures. This study, as few others, on the chemical stability of AAMs provide a great contribution in the direction of durability and in-life mechanical performance of these class of materials and it was published in (Finocchiaro et al., 2020b).

7. APPLICATIONS: TILES, QUICK-SETTING BINDERS AND MORTARS

This chapter is aimed to describe, according to the developments and circumstances occurred during my educational path, some applications of geopolymers based on pyroclastic deposits, usable, potentially, in building and conservation fields. In the first case, some tiles were produced in *precasting* way using geopolymeric mortars, whose binders are the formulations of VM1 and GM1 series (described in Chapter 3.2). Secondly, some test to simulate quick-setting cement were performed, using respectively volcanic precursor, alkaline activating solution and small quantity of PROMPT cement provided by VICAT company. Finally, geopolymeric mortars were prepared using the binders found (Na-VM/GM-10/20) and already characterized in Chapter 5, in addition to volcanic aggregates sorted in two grain size ranges, considering the wide need to restore and conserve the historical buildings of Catania architecture with innovative recipes of mortars maintaining unaltered the aesthetic, chromatic and durability features of original substrates. Moreover, these latter were analysed in terms of microstructure to observe the connection between binders and aggregates using scanning electron microscope (SEM) technique.

7.1 TILES: SYNTHESIS APPROACH

Once prepared the moulds with epoxy resin with the dimensions of a standard tile (10x10x1cm), two mortars using one formulation for each volcanic precursor were produced to fill the mould. In detail, for this test, the VM1 and GM1 formulations with 20% wt. of metakaolin (VM1/GM1-20) were chosen as binders and the 30% wt. of aggregated with 500 µm-1 mm size was added to the total weight of the binders to limit the retraction and enhance the strengths. Moreover, small quantities of water were added to improve the mixing among binders and aggregates. All formulation details were reported in Table 7.1, whose values are considered on all reactants of binders, aggregates and water amounts. The curing time of tiles was of 24h at room temperature, once removed by the mould, they showed a good aspect without retraction. The Fig. 7.1 showed the tiles produced during this experiment.

Table 7.1 – Formulation details of geopolymeric mortars of testes for tiles production. The values were calculated considering the total weight among binders, aggregates and water.

Binder labels	**V or G (%)**	**MK (%)**	**NaOH (8M) (%)**	**Na2SiO3 (SiO2/Na2O = 2) (%)**	**Aggregates 500µm-1 mm (%)**	**H_2O (%)**
VM1-20	38,2	9,5	5,7	19,1	21,8	5,7
GM1-20	41,0	10,2	6,1	16,4	22,1	4,1

Fig. 7.1 – Tiles just removed from the mould.

7.1.1 TESTS ON TILES

On both tiles different tests were carried out by a local ceramic society “LBC società coperativa artigiana” specialized in artisan tiles production with the aim to evaluate the performance and to compare them with the traditional ones. Thermal-shock test, frost and thaw test following thermal treatments for firing at high temperature before and after the glazing were performed. The tiles produced in our laboratory showed excellent properties supporting all the physical shocks undergone, resulting thus suitable for this kind of application.

7.2 QUICK-SETTING GEOPOLYMERIC BINDERS: SYNTHESIS APPROACH

During my second experience at the laboratory of department of Engineering “Enzo Ferrari” of Modena and Reggio Emilia University, occurred in the first part of the second year of my doctoral path, a new material was tested in combination with a volcanic precursor in an alkaline environment. This latter is commercialized by VICAT company, cement expertise, and commercially known as Prompt due to the high speed of hardening. This cement is totally natural, without any addition of chemical additives, thanks to the chemical and mineralogical composition of limestone deposit exploited in the Chartreuse massif (France). Moreover, the cement production positively contributes to the reduction of CO_2 emissions thanks to its low temperature cooking (500-1200°C), making it an eco-friendly cement. It is very appreciated in restoration and conservation field thanks to minimum quantities of lime releases during hydration, which make it a guaranteed and certified cement with good durability. The test of this prompt cement has foreseen its combination with the volcanic precursors in alkaline solution. In detail, solid mixtures with different weight ratios (volcanic precursor/prompt = 90-60/40-10 with interval of 10) were prepared and then mixed with a sodium silicate, known "Rocasil" and produced by Ingessil company, whose SiO_2/Na_2O molar ratio is around 1.55, with the aim to quantify approximately the curing time of the mixtures. To compare the formulations, the quantity of Rocasil was maintained constant, changing only the ratio of volcanic precursor/prompt (Fig. 7.2). This experiment was performed only using ghiara source, considering comparable with volcanic ash and enough to quantify the curing time influenced by prompt amount. All formulation details are reported in the following Table 7.2, as well as the obtained curing time. A strongly dependence among prompt and curing time is very clear, increasing the prompt amount in the mixture, the curing time decreases. However, also the minimum use of prompt strongly accelerates the reaction. Therefore, this material can be used as reaction accelerator when a rapid hardening is required.

Table 7.2 - Details of ratio sources and curing time estimation.

Samples	**G (%)**	**Prompt (%)**	**Curing time (h)**
G_{p10}	90	10	~ 3h
G_{p20}	80	20	~ 2.5h
G_{p30}	70	30	~ 2h
G_{p40}	60	40	~ 1.5h

Fig. 7.2 - Samples prepared to estimate the curing time at increasing prompt amount.

7.3 GEOPOLYMERIC MORTARS: SYNTHESIS APPROACH

For each precursors six mortars were produced using on one hand the best binders already found and characterized (Na-VM-10/20 and Na-GM-10/20) and on the other hand two range of grain size for aggregates (500µm – 1mm and 1 – 2 mm). Regarding the binders, metakaolin content represents the variable and its contribution strongly influence on binder’s workability. The aggregates used depend on the nature of binder (e.g. ghiara aggregates for ghiara binders or pyroclastic particles for volcanic ash binders). Two approaches were carried out as following: i) test of maximum quantity of aggregates which can be added taking into account the workability of the original binder, so without water addition (ID1); ii) addition of 30% wt. of aggregates in each binder and small water addition where requested to reach a good workability (ID2-5) (Table 7.3). For both approaches the same method was used as following summarized: preparation and weight of reactants; pressing of precursors with a pestle to remove metakaolin clumps; mixing of reactants with mechanical mixer; gradually addition of aggregates; ± small quantity of water to allow an adequate workability; and vibration for 1 minute to remove air bubbles entrapped in the mixture. The details of both approaches were summarized in (Table 7.3). During the synthesis step, two main features were observed: i) the mortars with addition of bigger aggregates (1-2 mm) requested more water than the others with small ones due to the considerable volume increasing; ii) the workability cannot be considered standard but it depend on the final application of the material. Fig. 7.3 shows the photographs of all samples prepared with aggregates of both grain size.

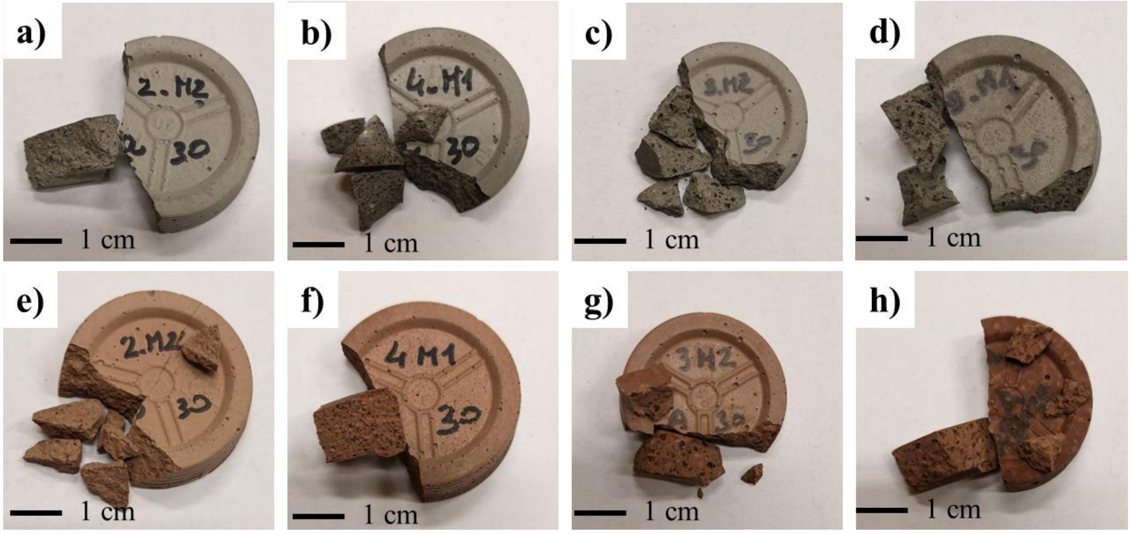

Fig. 7.3 – Photographs of geopolymeric mortars prepared with 30 % wt. aggregates of two grain size ranges: (a-b-e-f) 500µm-1mm; (c-d-g-h) 1-2 mm. Legenda: a) 2_VM2_a30; b) 4_VM1_a30; c) 3_VM2_A30; d) 5_VM1_A30; e) 2_GM2_a30; f) 4_GM1_a30; g) 3_GM2_A30; h) 5_GM1_A30.

Table 7.3 - Formulation details of geopolymeric mortars express in wt %. Mortars with ID 1 represent test with maximum possible (in terms of workability) aggregate contents for each binder without water addition, differently for the other ID mortars which indicate test with a fixed aggregate content (30 wt %) and small water additions to allow the mixing.

			Precursors (%)		***Activators (%)***		***Aggregates 500µm-1 mm***		***Aggregates 1- 2 mm***	
ID mortars	***ID binders***	***Labels***	**Volcanic powder**	**Metakaolin**	**NaOH (8M)**	**Na_2SiO_3**	***H_2O (ml)***	***wt %***	***H_2O (ml)***	***wt %***
1_M1_a29	Na-VM-10	*VM-10-a29*	53	6	7	12	0	23	/	
1_M2_a7	Na-VM-20	*VM-20-a7*	56	14	8	14	0	7		
2_M2_a30	Na-VM-20	*VM-20-a30*	43	11	6	11	0.5	30		
4_M1_a30	Na-VM-10	*VM-10-a30*	48	5	6	11	0.25	30		
1_M1_a51	Na-GM-10	*GM-10-a51*	45	5	6	10	0	34		
1_M2_a25	Na-GM-20	*GM-20-a25*	48	12	7	12	0	21		
2_M2_a30	Na-GM-20	*GM-20-a30*	43	11	6	11	1	30		
4_M1_a30	Na-GM-10	*GM-10-a30*	48	5	6	11	0	30		
1_M1_A22	Na-VM-10	*VM-10-A22*	56	6	7	12	/		0	18
1_M2_A8	Na-VM-20	*VM-20-A8*	56	14	8	14			0	8
3_M2_A30	Na-VM-20	*VM-20-A30*	43	11	6	11			0.75	30
5_M1_A30	Na-VM-10	*VM-10-A30*	48	5	6	11			0.75	30
1_M1_A27	Na-GM-10	*GM-10-A27*	53	6	7	12			0	22
1_M2_A17	Na-GM-20	*GM-20-A17*	52	13	8	13			0	15
3_M2_A30	Na-GM-20	*GM-20-A30*	43	11	6	11			1.25	30
5_M1_A30	Na-GM-10	*GM-10-A30*	48	5	6	11			0.25	30

7.4 CHARACTERIZATION METHODS

Considering the innumerable variables in each mortar formulations, only the samples with fixed percentage (30% wt.) of aggregates, independently of their size, were analysed in order to observe the microstructures using SEM method and comparing them with those of binders, highlighting so their differences and/or affinities, as well as the differences among the two categories of aggregates.

A Gemini Field Emission SEM (FE-SEM) Carl Zeiss SUPRA 25, belonging to Physics and Astronomy Department (Catania University), was used to perform morphological analysis at different magnification. In this scenario, the morphology of mortars with different aggregates of different grain size were compared with the corresponding binders, as well as the influence of volcanic precursors and the amount of metakaolin used as additive were evaluated.

7.5 RESULTS

SEM images were performed taking into account the magnification used for the binders and not considering the grain size of aggregates used. Otherwise, for this latter case, we have could make them in fisheye. Therefore, the contact between binder and aggregates is not so evident or immediate to observe in all the proposed images. The images collected for VM-10-a30 sample showed interesting circular structures made of prismatic, elongated and sharp-cornered particles with a size below 50 µm, assimilable to a probable metakaolin clump (Fig. 7.4). The corresponding sample with bigger aggregates (VM-10-A30) didn’t evidence particular structure and the size and shapes of the particles are comparable with those of the previous one (Fig. 7.5). Generally, both samples recorded a compact structure but the contact between binders and aggregates wasn’t easy to detect. The images of VM-20-a30 showed, in addition to sharp-cornered particles, also circular ones as well as we can assume a good mixing with the aggregate due to the observable contact on the left of Fig. 7.6a, characterized by an area with concentrated pores with the same size immersed in an amorphous matrix. Analogously, pieces of aggregate with circular pores (see the right sector of Fig. 7.7a) and particular morphologies (elongated particles with a width of 20 µm made of layers piles and interconnected tubes) can be observed in VM-20-A30 (Fig. 7.7).

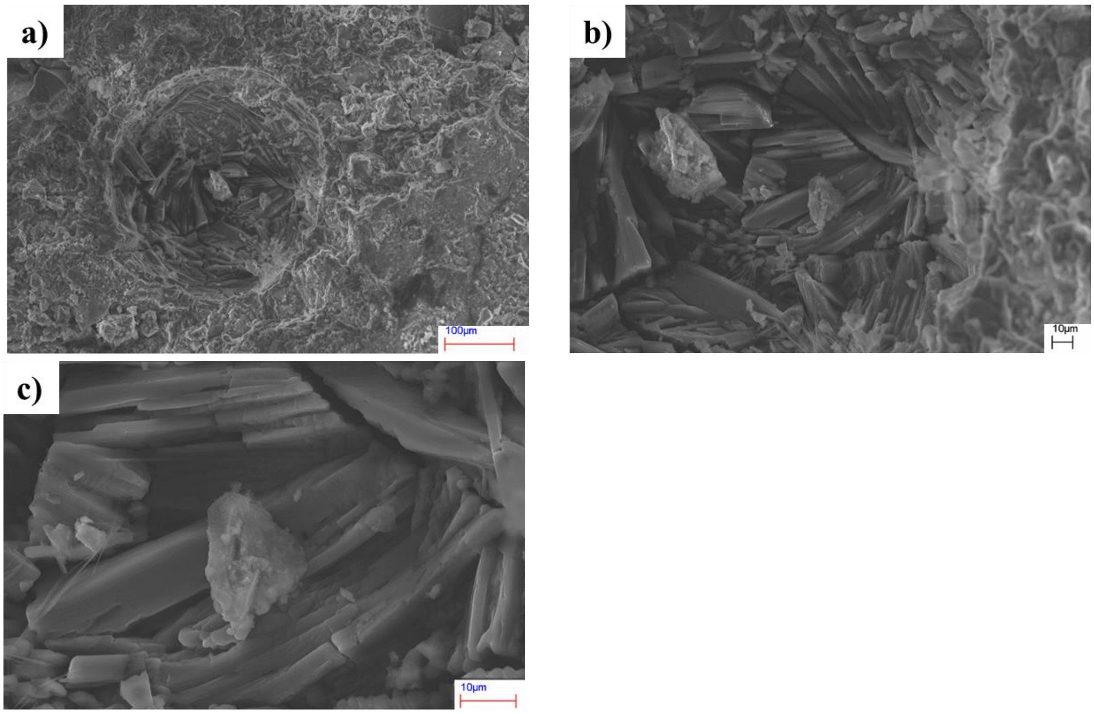

Fig. 7.4 – SEM photographs of VM-10-a30 sample: a) Mag. 500x; b) Mag. 1,5Kx; c) Mag. 4Kx.

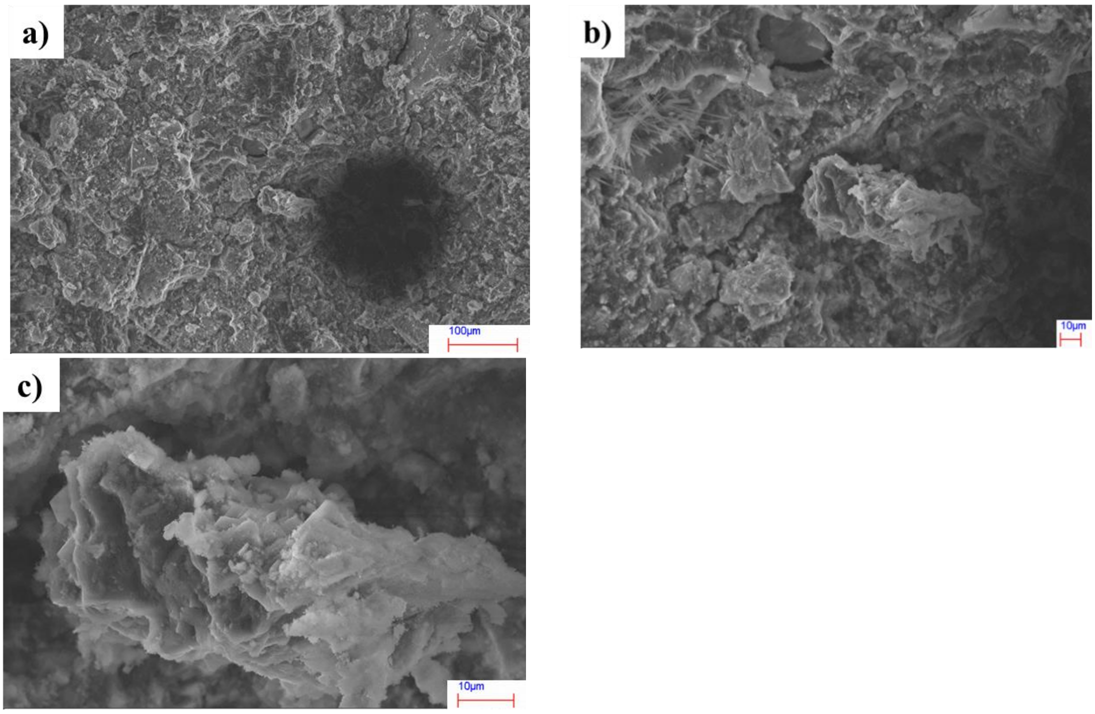

Fig. 7.5 – SEM photographs of VM-10-A30 sample: a) Mag. 500x; b) Mag. 1,5Kx; c) Mag. 4Kx.

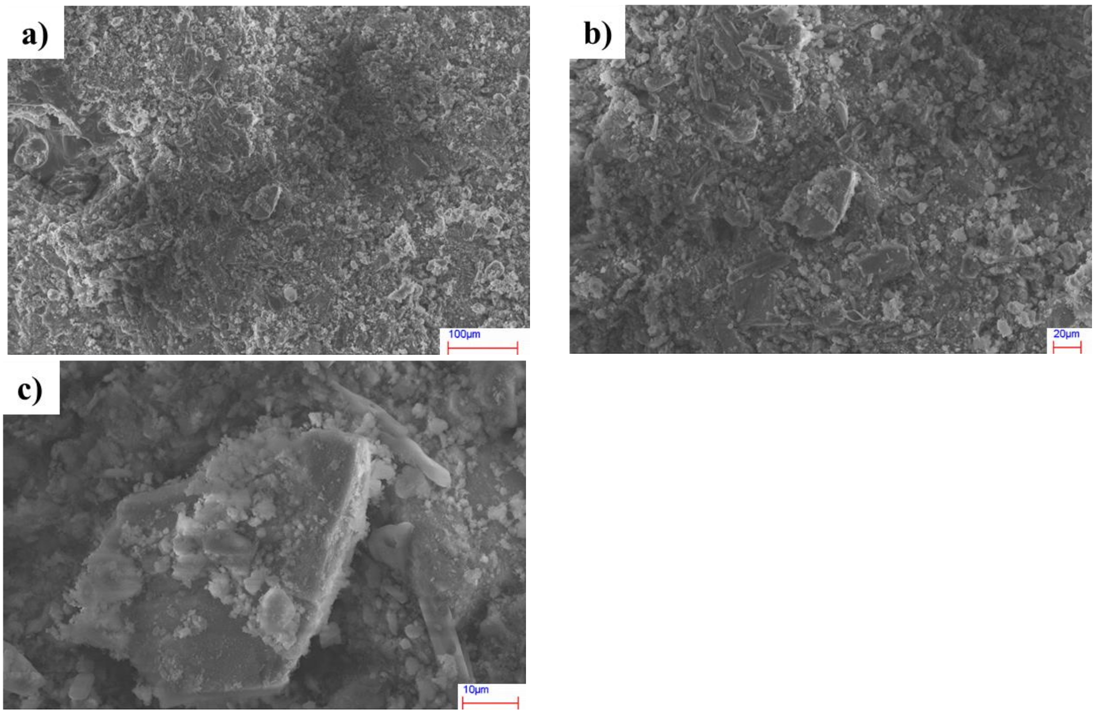

Fig. 7.6 – SEM photographs of VM-20-a30 sample: a) Mag. 500x; b) Mag. 1Kx; c) Mag. 4Kx.

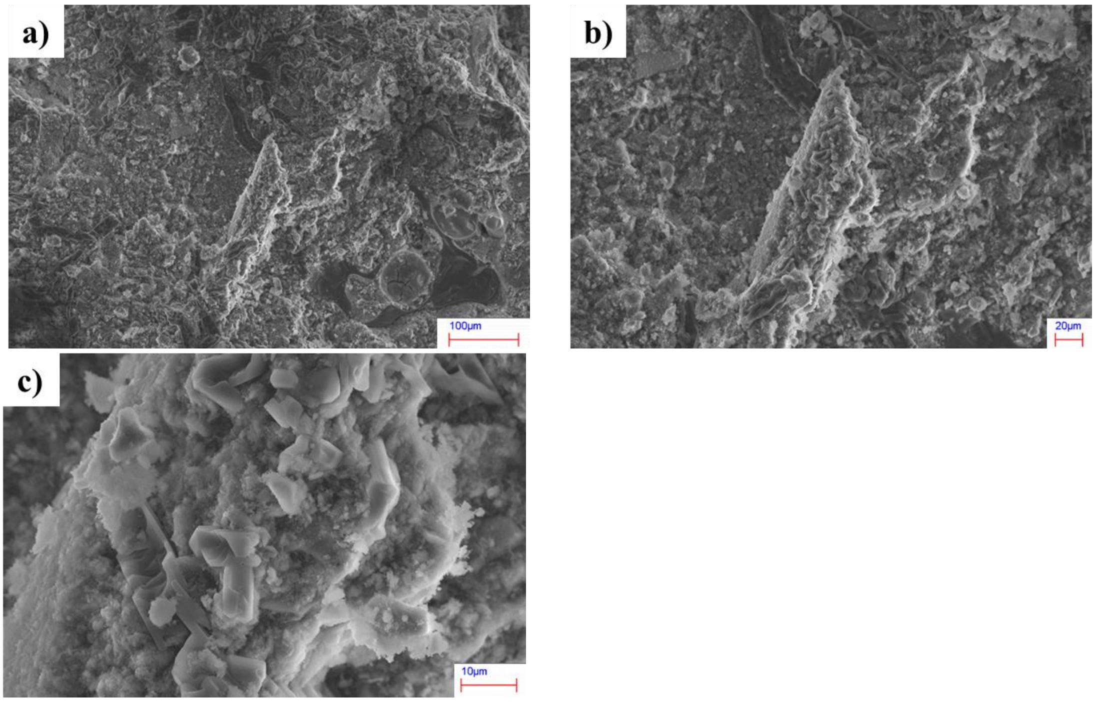

Fig. 7.7 – SEM photographs of VM-20-A30 sample: a) Mag. 500x; b) Mag. 1Kx; c) Mag. 4Kx.

Differently to the samples based on volcanic ash, the contact among binders and aggregates is better recognisable in those of ghiara due to the presence of defined areas with high concentration of circular pores immersed in an amorphous matrix. Moreover, the pore sizes of aggregates is strongly influenced by the dimensions of aggregates itself:

the aggregates with 1-2 mm size contain pores of 100 µm or more (Fig. 7.9 and Fig. 7.11), while those with 500 µm -1 mm size, pores with size below 50 µm (Fig. 7.8 and Fig. 7.10). No particular morphologies, already widely described, were recorded in the samples, except for GM-10-A30 sample which is characterized by a compact structure with piles of fine layers (about 10 µm). Generally, the aggregates adhere well with the binders, but also some cracks can be observable surrounded the borders of aggregates as recorded in Fig. 7.10. However, this brittle behaviour is due to the mechanical performance of the binders. Indeed, the samples with 20 % wt. of metakaolin evidenced a brittle behaviour and a consequently higher performance than those with minor metakaolin (see 5.3.5 paragraph).

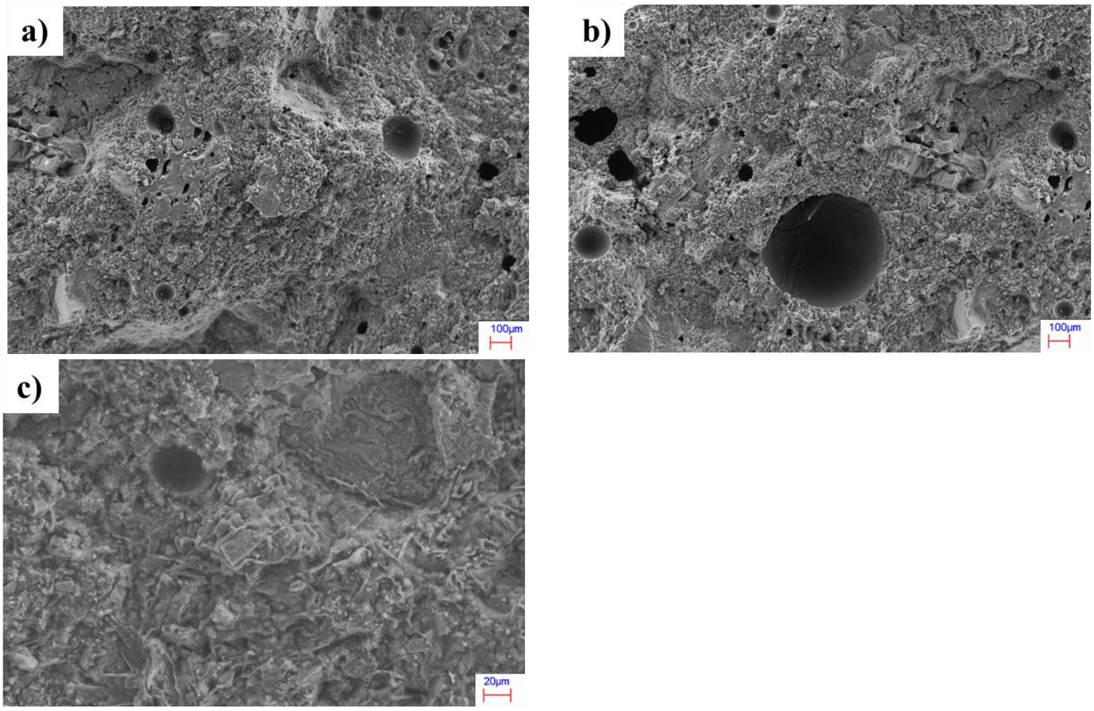

Fig. 7.8 – SEM photographs of GM-10-a30 sample: a) Mag. 150x; b) Mag. 150x; c) Mag. 1Kx.

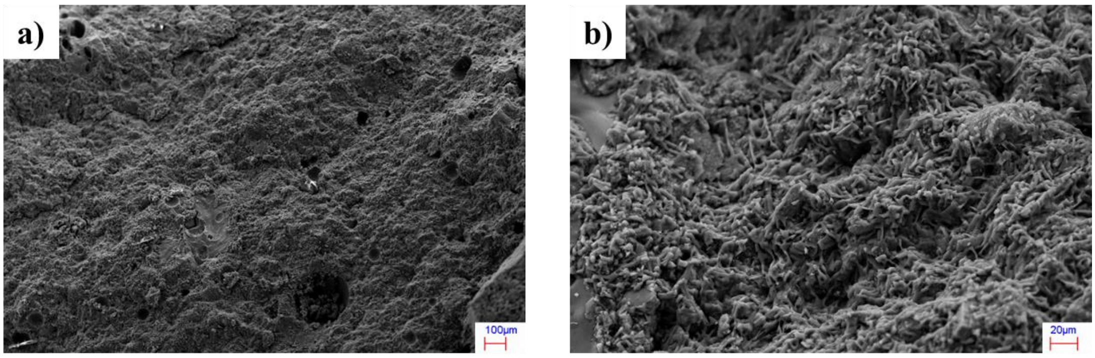

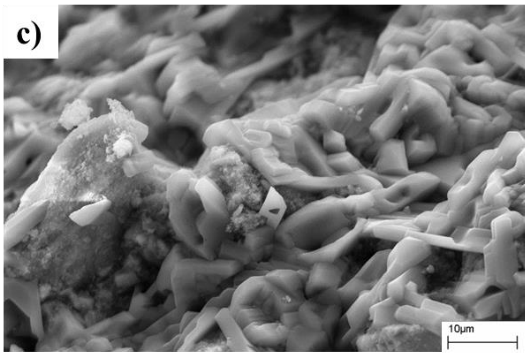

Fig. 7.9 – SEM photographs of GM-10-A30 sample: a) Mag. 150x; b) Mag. 1Kx; c) Mag. 5Kx.

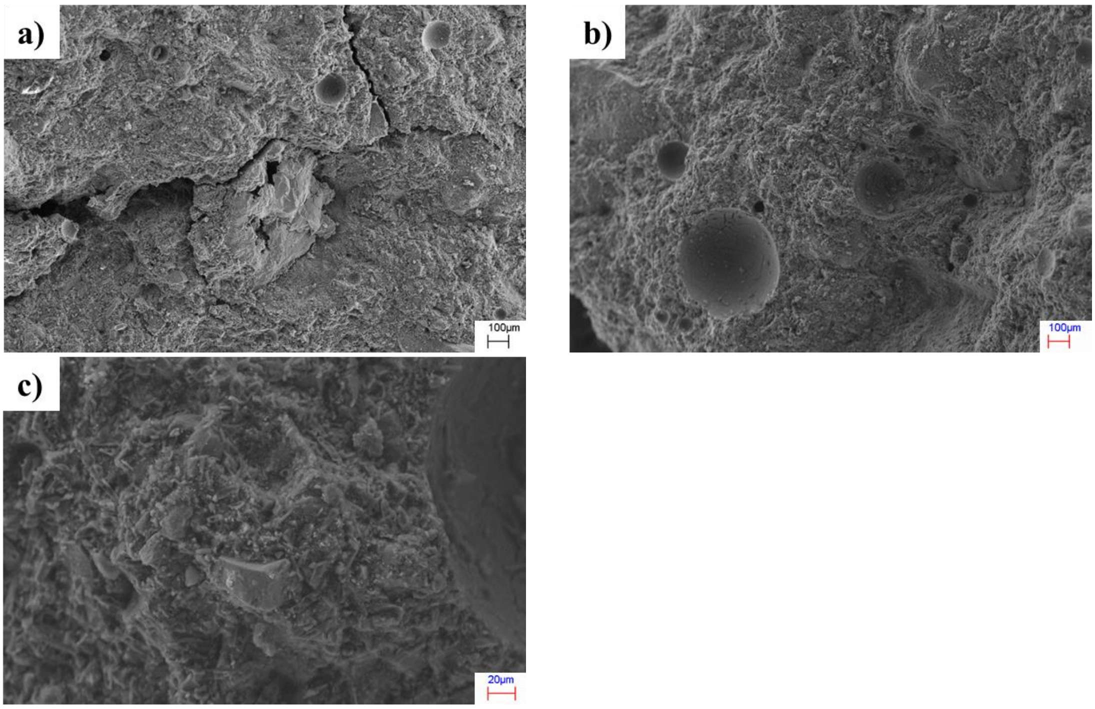

Fig. 7.10 – SEM photographs of GM-20-a30 sample: a) Mag. 150x; b) Mag. 150x; c) Mag. 1Kx.

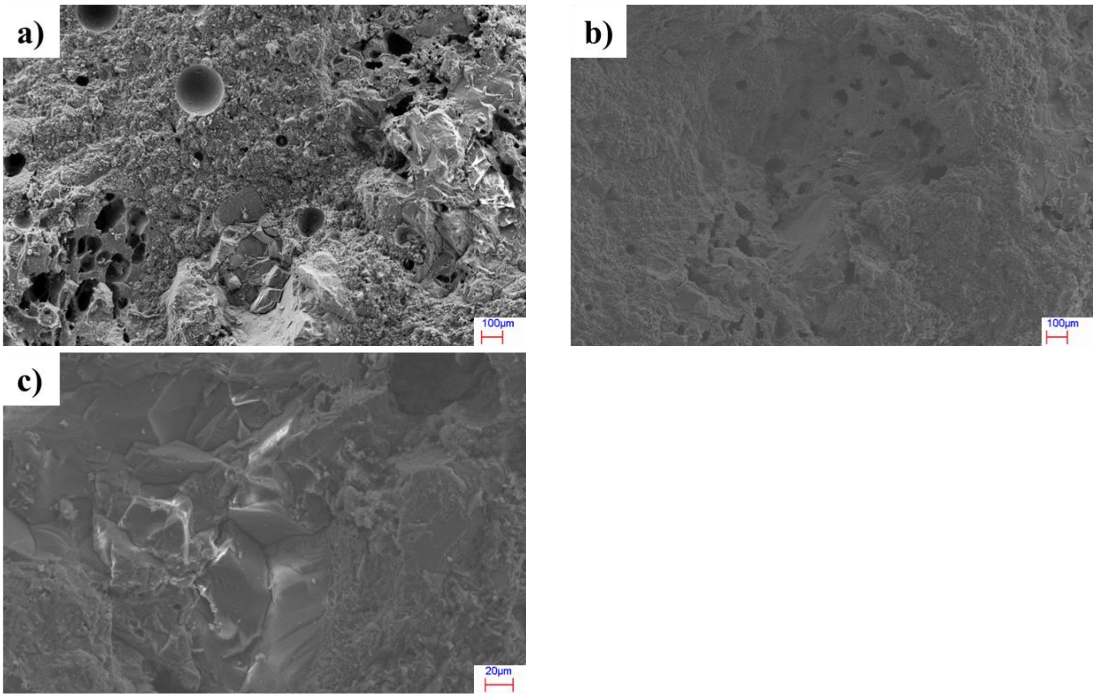

Fig. 7.11 – SEM photographs of GM-20-A30 sample: a) Mag. 150x; b) Mag. 150x; c) Mag. 1Kx.

7.6 CONCLUSION

Alkali activated materials are innovative materials extremely versatile. According to the test performed using these materials, we have demonstrated their potentiality. The production in precasting way should be the simplest and fasted in an industrial view. However, they gave a good feedback also as prompt binders to apply in extreme circumstances where the short curing time is mandatory (i.e. extreme climate conditions). Moreover, the mortars showed chromatic affinities with the historical ones which characterizes the Catania old town, imaging thus to restore them with restoration interventions, once performed other test as those to evaluate the porosity, durability and the invasivity at the substrate. Generally, the morphologies evidenced pores in the micron range. In comparison to the binders, their porosity has increased due to the intrinsic one of aggregates added, which is also influenced by their size. The aggregates resulted well adhered to the binders whose structure was maintained unaltered and compact. However, the workability is an important parameter to be consider according to the final destination of the mortars.

8. CONCLUSIONS AND FINAL REMARKS

This PhD thesis has foreseen to valorise two volcanic materials, which continue to influence (or have influenced in the previous centuries) in different way the Cultural and Social Heritage of Catania town. On one hand, the volcanic ash deposits widespread in Mt. Etna area and considered until now natural waste materials following explosive eruptions according to the current regulations, and on the other hand, the ghiara paleo-soils, widely used in the architecture of Catania old town, were used through the alkaline activation process with the aim to find an eco-friendly alternative to the traditional building materials, favouring the circular economy. Indeed, alkali activated materials (AAMs) represent a new class of materials, whose interest is increasing exponentially over time thanks to their high-tech performance in combination to low emission and good money for value. The results on volcanic raw materials have confirmed the suitability of using them as precursors for the alkaline synthesis thanks to their chemical and mineralogical compositions, made of a high aluminosilicate content and amorphous structure. Therefore, the main aim of my thesis to find a way to valorise these pyroclastic deposits was achieved. In detail, the initial task to use only the volcanic deposits to produces geopolymers was abandoned very rapidly due to the need to perform thermal treatments with consequent increase of energy consumption and emissions, as well as the impossibility to produce binders and/or mortars to apply in restoration interventions. Therefore, binary mixtures with small additions of metakaolin amounts were produced at room temperature, simulating, in this way, in situ interventions, with good mechanical and physical performance. The characterization of these materials was performed by a multidisciplinary approach. XRD results showed an amorphous composition (also confirmed by SEM-EDX analysis which evidenced N-A-S-H *sodium aluminosilicate hydrate* gel) combined with the mineralogical phases of volcanic precursors, as well as small quantity of phases belonging to zeolite group (e.g. VM1 and GM1 series), testifying a partial network organization. The combination of the spectroscopic techniques used (i.e. Raman and FTIR) has allowed to observe aluminosilicate structures with a more or less contribution of carbonates which decreases at increasing metakaolin content in the mixture (i.e. Na/K-V/GM-10/20) or due to the much time at air exposure generating efflorescence phenomena (i.e. VM1 and GM1 series). Furthermore, in situ FTIR analysis were useful to highlight the polycondensation reactions immediately after the mixing with the alkaline solutions (i.e. Na/K-V/GM-10/20). According to the obtained results, I can affirm that geopolymers based on volcanic deposits need a low liquid/solid ratio to avoid efflorescence phenomena (nonetheless it is very common in alkaline system) and to obtain higher compressive strengths, differently to metakaolin which require higher liquid demand to favour the workability. Moreover, the metakaolin used as additive component demonstrates the positive influence on mechanical performance as well as a better network organization. The compressive strengths showed also after one-week high value (i.e. 17 MPa for Na-V/GM-10 while 45 MPa for Na-V/GM-20) with an increase of 15% after 21 curing days. At this purpose, mortars with aggregates of the same nature of volcanic precursor and the binders with lower liquid/ solid ratio (i.e. Na-V/GM-10/20) were produced with the aim to simulate the historical mortars of Catania architecture. Microscopically, these materials are microporous with average pore of 0.04 µm mainly concentrated in the range of 0.1-0.01 µm. However, these size increase in mortar system due to the intrinsic porosity of aggregates used.

Finally, the feasibility studies performed in this thesis on the use of volcanic deposits in alkaline activation have allowed publishing three papers in international journals (Barone et al., 2020; Finocchiaro et al., 2020; Finocchiaro et al., 2020b). Moreover, they have encouraged us to hypothesize these materials in the future market of building materials with high performance as an eco-friendly alternative to the traditional ones. However, the industrial scale up plan to produce these materials is not easy to imagine due to the corrosive solutions involved in the process, which can be partially solved with the implementation of one-parts geopolymer (i.e. mixing of solid reactants with water) (Luukkonen et al., 2018). Therefore, the future outlooks of this thesis are different and can be drawn as following:

- Durability characterization thought acid or sulphates attacks and frost and thaw test.
- Firing test to evaluate the maximum temperature resistance.
- Implementation of one-parts geopolymer based on pyroclastic deposits.

9. BIBLIOGRAPHY

ACI Committee. (2001). *Use of Raw or Processed Natural Pozzolans in Concrete*.

Akman, M. S., Mazlum, F., & Esenli, F. (1992). Comparative Study of Natural Pozzolans Used in Blended Cement Production. *Special Publication*, *132*, 471–494. https://doi.org/10.14359/1994

Albitar, M., Mohamed Ali, M. S., Visintin, P., & Drechsler, M. (2017). Durability evaluation of geopolymer and conventional concretes. *Construction and Building Materials*, *136*, 374–385. https://doi.org/10.1016/j.conbuildmat.2017.01.056

Alehyen, S., Achouri, M. E. L., & Taibi, M. (2017). Characterization, microstructure and properties of fly ash-based geopolymer. *Journal of Materials and Environmental Science*, *8*(5), 1783–1796.

Allahverdi, A., Najafi Kani, E., & Yazdanipour, M. (2011). EFFECTS OF BLAST-FURNACE SLAG ON NATURAL POZZOLAN-BASED GEOPOLYMER CEMENT. In *Ceramics-Silikáty* (Vol. 55).

Allard, P., Carbonnelle, J., Dajlevic, D., Bronec, J. Le, Morel, P., Robe, M. C., … Zettwoog, P. (1991). Eruptive and diffuse emissions of CO2 from Mount Etna. *Nature*, *351*(6325), 387–391. https://doi.org/10.1038/351387a0

Alraddadi, S. (2020). Surface and thermal properties of fine black and white volcanic ash. *Materials Today: Proceedings*. https://doi.org/10.1016/j.matpr.2020.02.429

Andreozzi, L. (2003). *La lava, l'uomo e l'architettura*. Enna - Italy: Il Lunario.

Angel, R. J., Carpenter, M. A., & Finger, L. W. (1990). Structural variation associated with compositional variation and order-disorder behaviour in anorthite-rich feldspars. *American Mineralogist*, *75*(1–2), 150–162.

Argyrous, G. (2011). *Statistics for research: With a guide to SPSS* (III). Sage Publications.

Autef, A., Prud'Homme, E., Joussein, E., Gasgnier, G., Pronier, S., & Rossignol, S. (2013). Evidence of a gel in geopolymer compounds from pure metakaolin. *Journal of Sol-Gel Science and Technology*, *67*(3), 534–544. https://doi.org/10.1007/s10971-013-3111-9

Azzaro, R., Bonforte, A., Branca, S., & Guglielmino, F. (2013). Geometry and kinematics of the fault systems controlling the unstable flank of Etna volcano (Sicily). *Journal of Volcanology and Geothermal Research*, *251*, 5–15. https://doi.org/10.1016/j.jvolgeores.2012.10.001

Azzaro, Raffaele, Branca, S., Gwinner, K., & Coltelli, M. (2012). The volcano-tectonic map of Etna volcano, 1:100.000 scale: An integrated approach based on a morphotectonic analysis from high-resolution DEM constrained by geologic, active faulting and seismotectonic data. *Italian Journal of Geosciences*, *131*(1), 153–170. https://doi.org/10.3301/IJG.2011.29

Bakharev, T. (2005a). Durability of geopolymer materials in sodium and magnesium sulfate solutions. *Cement and Concrete Research*, *35*(6), 1233–1246. https://doi.org/10.1016/j.cemconres.2004.09.002

Bakharev, T. (2005b). Resistance of geopolymer materials to acid attack. *Cement and Concrete Research*, *35*(4), 658–670. https://doi.org/10.1016/j.cemconres.2004.06.005

Balczár, I., Korim, T., Kovács, A., & Makó, E. (2016). Mechanochemical and thermal activation of kaolin for manufacturing geopolymer mortars – Comparative study. *Ceramics International*, *42*(14), 15367–15375. https://doi.org/10.1016/j.ceramint.2016.06.182

Barbosa, V. F. F., & MacKenzie, K. J. D. (2003). Synthesis and thermal behaviour of potassium sialate geopolymers. *Materials Letters*, *57*(9–10), 1477–1482. https://doi.org/10.1016/S0167-577X(02)01009-1

Barbosa, V. F. F., MacKenzie, K. J. D., & Thaumaturgo, C. (2000). Synthesis and characterisation of materials based on inorganic polymers of alumina and silica: Sodium polysialate polymers. *International Journal of Inorganic Materials*, *2*(4), 309–317. https://doi.org/10.1016/S1466-6049(00)00041-6

Bardelli, F., Giuli, G., Di Benedetto, F., Costagliola, P., Montegrossi, G., Rimondi, V., … Mazzoleni, P. (2020). Spectroscopic study of volcanic ashes. *Journal of Hazardous Materials*, *400*, 123213. https://doi.org/10.1016/j.jhazmat.2020.123213

Barone, G., & Mazzoleni, P. (2012). Le lave. *Lexicon. Storie e Architettura in Sicilia*, *14–15*, 69.

Barone, G., Mazzoleni, P., Corsaro, R. A., Costagliola, P., Di Benedetto, F., Ciliberto, E., … Spinella, C. (2016a). Nanoscale surface modification of Mt. Etna volcanic ashes. *Geochimica et Cosmochimica Acta*, *174*. https://doi.org/10.1016/j.gca.2015.11.011

Barone, Germana, Finocchiaro, C., Lancellotti, I., Leonelli, C., Mazzoleni, P., Sgarlata, C., & Stroscio, A. (2020). Potentiality of the Use of Pyroclastic Volcanic Residues in the Production of Alkali Activated Material. *Waste and Biomass Valorization*. https://doi.org/10.1007/s12649-020-01004-6

Basheer, I. A., & Hajmeer, M. (2000). Artificial neural networks: Fundamentals, computing, design, and application. *Journal of Microbiological Methods*, *43*(1), 3–31. https://doi.org/10.1016/S0167-7012(00)00201-3

Battiato, G. (1988). Le malte del centro storico di Catania. *Documenti Dell'Istituto Dipartimentale Di Architettura e Urbanistica Dell'Università Di Catania, 16*, 85–107.

Behncket, B. (2001). Volcanism in the Southern Apennines and Sicily. In *Anatomy of an Orogen: the Apennines and Adjacent Mediterranean Basins* (pp. 105–120). https://doi.org/10.1007/978-94-015-9829-3_9

Belfiore, C. M., Fichera, G. V., La Russa, M. F., Pezzino, A., Ruffolo, S. A., Galli, G., & Barca, D. (2015). A Multidisciplinary Approach for the Archaeometric Study of Pozzolanic Aggregate in Roman Mortars: The Case of Villa dei Quintili (Rome, Italy). *Archaeometry*, *57*(2), 269–296. https://doi.org/10.1111/arcm.12085

Belfiore, Cristina M, La, M. F., & Viccaro, M. (2010). *Technological study of '" ghiara "' mortars from the historical city centre of Catania (Eastern Sicily , Italy) and petro-chemical characterisation of raw materials*. 995–1003. https://doi.org/10.1007/s12665-009-0418-5

Bernal, S. A., de Gutierrez, R. M., Provis, J. L., & Rose, V. (2010). Effect of silicate modulus and metakaolin incorporation on the carbonation of alkali silicate-activated slags. *Cement and Concrete Research*, *40*(6), 898–907. https://doi.org/10.1016/j.cemconres.2010.02.003

Bonaccorso, A., Calvari, S., & Boschi, E. (2016). Hazard mitigation and crisis management during major flank eruptions at Etna volcano: Reporting on real experience. *Geological Society Special Publication*, *426*(1), 447–461. https://doi.org/10.1144/SP426.4

Bondar, D. (2014). Use of a neural network to predict strength and optimum compositions of natural alumina-silica-based geopolymers. *Journal of Materials in Civil Engineering*, *26*(3), 499–503. https://doi.org/10.1061/(ASCE)MT.1943-5533.0000829

Bondar, D., Lynsdale, C. J., Milestone, N. B., Hassani, N., & Ramezanianpour, A. A. (2011a). Cement & Concrete Composites Effect of type , form , and dosage of activators on strength of alkali-activated natural pozzolans. *Cement and Concrete Composites*, *33*(2), 251–260. https://doi.org/10.1016/j.cemconcomp.2010.10.021

Bondar, D., Lynsdale, C. J., Milestone, N. B., Hassani, N., & Ramezanianpour, A. A. (2011b). Effect of heat treatment on reactivity-strength of alkali-activated natural pozzolans. *Construction and Building Materials*, *25*(10), 4065–4071. https://doi.org/10.1016/j.conbuildmat.2011.04.044

Bonforte, A., Guglielmino, F., Coltelli, M., Ferretti, A., & Puglisi, G. (2011). Structural assessment of mount Etna volcano from permanent scatterers analysis. *Geochemistry, Geophysics, Geosystems*, *12*(2). https://doi.org/10.1029/2010GC003213

Borgia, A., Ferrari, L., & Pasquarè, G. (1992). Importance of gravitational spreading in the tectonic and volcanic evolution of Mount Etna. *Nature, 357*(6375), 231–235. https://doi.org/10.1038/357231a0

Bousquet, J. C., & Lanzafame, G. (2004). The tectonics and geodynamics of Mt. Etna: Synthesis and interpretation of geological and geophysical data. In *Geophysical Monograph Series* (Vol. 143, pp. 29–47). https://doi.org/10.1029/143GM03

Branca, S., Coltelli, M., De Beni, E., & Wijbrans, J. (2008). Geological evolution of Mount Etna volcano (Italy) from earliest products until the first central volcanism (between 500 and 100 ka ago) inferred from geochronological and stratigraphic data. *International Journal of Earth Sciences*, *97*(1), 135–152. https://doi.org/10.1007/s00531-006-0152-0

Branca, S., Coltelli, M., Groppelli, G., & Lentini, F. (2011). Geological map of Etna volcano, 1:50,000 scale. *Italian Journal of Geosciences*, *130*(3), 265–291. https://doi.org/10.3301/IJG.2011.15

Branca, S., De Beni, E., & Proietti, C. (2013). The large and destructive 1669 AD eruption at Etna volcano: reconstruction of the lava flow field evolution and effusion rate trend. *Bulletin of Volcanology*, *75*(2), 694. https://doi.org/10.1007/s00445-013-0694-5

Burduhos Nergis, D. D., Abdullah, M. M. A. B., Vizureanu, P., & Mohd Tahir, M. F. (2018). Geopolymers and Their Uses: Review. *IOP Conference Series: Materials*

Science and Engineering, *374*(1). https://doi.org/10.1088/1757-899X/374/1/012019

Cabadas-Báez, H. V., Solís-Castillo, B., Solleiro-Rebolledo, E., Sedov, S., Leonard, D., Teranishi-Castillo, K., … Korneychik, O. (2017). Reworked volcaniclastic deposits from the Usumacinta river, Mexico: A serendipitous source of volcanic glass in Maya ceramics. *Geoarchaeology*, *32*(3), 382–399. https://doi.org/10.1002/gea.21610

Carter, A. ., Kelloway, S. ., Kononenko, N., & Torrence, R. (2012). Raman Spectroscopic Studies of Obsidian. In G. M. E. Howell & P. Vandenabeele (Eds.), *Analytical Archaeometry* (pp. 323–349). Royal Society of Chemistry.

Chen, Y. H. (2013). Thermal properties of nanocrystalline goethite, magnetite, and maghemite. *Journal of Alloys and Compounds*, *553*, 194–198. https://doi.org/10.1016/j.jallcom.2012.11.102

Cheng, T. W., Lee, M. L., Ko, M. S., Ueng, T. H., & Yang, S. F. (2012). The heavy metal adsorption characteristics on metakaolin-based geopolymer. *Applied Clay Science*, *56*, 90–96. https://doi.org/10.1016/j.clay.2011.11.027

Clark J. R., Appleman D. E., P. J. (1969). Crystal-chemical cheracterization on clinopyroxenes based on eight new structure refinements. *Mineral. Soc. Amer. Spec. Pap.2*, *50*, 31–50.

Clausi, M., Magnani, L. L., Occhipinti, R., Riccardi, M. P., Zema, M., & Tarantino, S. C. (2016). Interaction of metakaolin-based geopolymers with natural and artificial stones and implications on their use in cultural heritage. *International Journal of Conservation Science*, *7*(Specialissue2), 871–884.

Clausi, M., Riccardi, M. P., Tedeschi, C., & Milano, P. (2016). *Metakaolin as a precursor of materials for applications in Cultural Heritage : Geopolymer- based mortars with ornamental stone aggregates*. (September). https://doi.org/10.1016/j.clay.2016.08.009

Clocchiatti, R., Schiano, P., Ottolini, L., & Bottazzi, P. (1998). Earlier alkaline and transitional magmatic pulsation of Mt Etna volcano. *Earth and Planetary Science Letters*, *163*(1–4), 399–407. https://doi.org/10.1016/S0012-821X(98)00170-8

Colomban, P., & Prinsloo, L. C. (2009). Optical spectroscopy of silicates and glasses. In *Spectroscopic Properties of Inorganic and Organometallic Compounds* (pp. 128–149). https://doi.org/10.1039/b715005a

Contrafatto, L. (2017). Recycled Etna volcanic ash for cement , mortar and concrete manufacturing. *Construction and Building Materials*, *151*, 704–713. https://doi.org/10.1016/j.conbuildmat.2017.06.125

Corsaro, R. A., & Métrich, N. (2016). Chemical heterogeneity of Mt. Etna magmas in the last 15 ka. Inferences on their mantle sources. *Lithos*, *252–253*, 123–134. https://doi.org/10.1016/J.LITHOS.2016.02.006

Criado, M., Fernández-Jiménez, A., de la Torre, A. G., Aranda, M. A. G., & Palomo, A. (2007). An XRD study of the effect of the SiO2/Na2O ratio on the alkali activation of fly ash. *Cement and Concrete Research*, *37*(5), 671–679. https://doi.org/10.1016/j.cemconres.2007.01.013

Cristofolini, R., Ghisetti, F., Scarpa, R., & Vezzani, L. (1985). Character of the stress field in the Calabrian Arc and Southern Apennines (Italy) as deduced by geological, seismological and volcanological information. *Tectonophysics*, *117*(1–2), 39–58. https://doi.org/10.1016/0040-1951(85)90235-5

Cyr, M., & Pouhet, R. (2016). Carbonation in the pore solution of metakaolin-based geopolymer. *Cement and Concrete Research*, *88,* 227–235. https://doi.org/10.1016/j.cemconres.2016.05.008

Daniel, G. (2013). *Principles Of Artificial Neural Networks (3rd Edition)* (W. Scientific, Ed.).

Davidovits, J. (1982). *U.S. Patent No. 4,349,386*.

Davidovits, J. (1991). Geopolymers - Inorganic polymeric new materials. *Journal of Thermal Analysis*, *37*(8), 1633–1656. https://doi.org/10.1007/BF01912193

Davidovits, J. (1994). *Directory Kantor Akuntan Publik dan Akuntan Publik*. 491.

Djobo, J N Y, Tchadjié, L. N., Tchakoute, H. K., Kenne, B. B. D., Elimbi, A., & Njopwouo, D. (2014). Journal of Asian Ceramic Societies Synthesis of geopolymer composites from a mixture of volcanic scoria and metakaolin. *Integrative Medicine Research*, *2*(4), 387–398. https://doi.org/10.1016/j.jascer.2014.08.003

Djobo, Jean Noël Yankwa, Elimbi, A., Tchakouté, H. K., & Kumar, S. (2016). Reactivity of volcanic ash in alkaline medium, microstructural and strength characteristics of resulting geopolymers under different synthesis conditions. *Journal of Materials Science*, *51*(22), 10301–10317. https://doi.org/10.1007/s10853-016-0257-1

Djobo, Jean Noël Yankwa, Elimbi, A., Tchakouté, H. K., & Kumar, S. (2017). Volcanic ash-based geopolymer cements/concretes: the current state of the art and perspectives. *Environmental Science and Pollution Research*, *24*(5), 4433–4446. https://doi.org/10.1007/s11356-016-8230-8

Djon Li Ndjock, B. I., Elimbi, A., & Cyr, M. (2017). Rational utilization of volcanic ashes based on factors affecting their alkaline activation. *Journal of Non-Crystalline Solids*, *463,* 31–39. https://doi.org/10.1016/j.jnoncrysol.2017.02.024

Dou, J., Yamagishi, H., Pourghasemi, H. R., Yunus, A. P., Song, X., Xu, Y., & Zhu, Z. (2015). An integrated artificial neural network model for the landslide susceptibility assessment of Osado Island, Japan. *Natural Hazards*, *78*(3), 1749–1776. https://doi.org/10.1007/s11069-015-1799-2

Dupuy, C., Gharzouni, A., Sobrados, I., Tessier-Doyen, N., Texier-Mandoki, N., Bourbon, X., & Rossignol, S. (2020). Formulation of an alkali-activated grout based on Callovo-Oxfordian argillite for an application in geological radioactive waste disposal. *Construction and Building Materials*, *232,* 117170. https://doi.org/10.1016/j.conbuildmat.2019.117170

Durant, A. J., Bonadonna, C., & Horwell, C. J. (2010). Atmospheric and environmental impacts of volcanic particulates. *Elements*, *6*(4), 235–240. https://doi.org/10.2113/gselements.6.4.235

Duxson, P., Fernández-Jiménez, A., Provis, J. L., Lukey, G. C., Palomo, A., & Van Deventer, J. S. J. (2007). Geopolymer technology: The current state of the art. *Journal of Materials Science*, *42*(9), 2917–2933. https://doi.org/10.1007/s10853-006-0637-z

Duxson, Peter, Lukey, G. C., & Van Deventer, J. S. J. (2007). Physical evolution of Na-geopolymer derived from metakaolin up to 1000 °c. *Journal of Materials Science*, *42*(9), 3044–3054. https://doi.org/10.1007/s10853-006-0535-4

Duxson, Peter, Provis, J. L., Lukey, G. C., & van Deventer, J. S. J. (2007). The role of inorganic polymer technology in the development of "green concrete." *Cement and Concrete Research*, *37*(12), 1590–1597. https://doi.org/10.1016/j.cemconres.2007.08.018

Faria, D. L. A. De. (1997). *Raman Microspectroscopy of Some Iron Oxides and Oxyhydroxides*. *28*(July), 873–878.

Fernández-Jiménez, A., Palomo, A., Sobrados, I., & Sanz, J. (2006). The role played by the reactive alumina content in the alkaline activation of fly ashes. *Microporous and Mesoporous Materials*, *91*(1–3), 111–119. https://doi.org/10.1016/j.micromeso.2005.11.015

Fernández-Jiménez, Ana, Pastor, J. Y., Martín, A., & Palomo, A. (2010). High-temperature resistance in alkali-activated cement. *Journal of the American Ceramic Society*, *93*(10), 3411–3417. https://doi.org/10.1111/j.1551-2916.2010.03887.x

Finocchiaro, C., Barone, G., Mazzoleni, P., Leonelli, C., Gharzouni, A., & Rossignol, S. (2020). FT-IR study of early stages of alkali activated materials based on pyroclastic deposits (Mt. Etna, Sicily, Italy) using two different alkaline solutions. *Construction and Building Materials*, *262*. https://doi.org/10.1016/j.conbuildmat.2020.120095

Finocchiaro, C., Barone, G., Mazzoleni, P., Sgarlata, C., Lancellotti, I., Leonelli, C., & Romagnoli, M. (2020). Artificial Neural Networks test for the prediction of chemical stability of pyroclastic deposits based AAMs and comparison with conventional mathematical approach (MLR). *Journal of Materials Science*. https://doi.org/DOI: 10.1007/s10853-020-05250-w

Forum, M. S. (2016). *Mechanical Properties of Volcanic Ash Based Geopolymer Concrete*. (March). https://doi.org/10.4028/www.scientific.net/MSF.857.377

Fubini, B., & Fenoglio, I. (2007). Toxic potential of mineral dusts. *Elements*, *3*(6), 407–414. https://doi.org/10.2113/GSELEMENTS.3.6.407

Gao, X. X., Michaud, P., Joussein, E., & Rossignol, S. (2013). Behavior of metakaolin-based potassium geopolymers in acidic solutions. *Journal of Non-Crystalline Solids*, *380*, 95–102. https://doi.org/10.1016/j.jnoncrysol.2013.09.002

García-lodeiro, I., Palomo, A., & Fernández-jiménez, A. (2015). *An overview of the chemistry of alkali- activated cement-based binders*. (December). https://doi.org/10.1533/9781782422884.1.19

Garcia-Lodeiro, I., Palomo, A., Fernández-Jiménez, A., & MacPhee, D. E. (2011). Compatibility studies between N-A-S-H and C-A-S-H gels. Study in the ternary diagram Na2O-CaO-Al2O3-SiO 2-H2O. *Cement and Concrete Research*, *41*(9), 923–931. https://doi.org/10.1016/j.cemconres.2011.05.006

Geraldes, C. F. M., Lima, A. M., Delgado-Rodrigues, J., Mimoso, J. M., & Pereira, S. R. M. (2016). Geopolymers as potential repair material in tiles conservation. *Applied Physics A: Materials Science and Processing*, *122*(3), 1–10. https://doi.org/10.1007/s00339-016-9709-3

Gharzouni, A., Joussein, E., Samet, B., Baklouti, S., Pronier, S., Sobrados, I., … Rossignol, S. (2014). The effect of an activation solution with siliceous species on the chemical reactivity and mechanical properties of geopolymers. *Journal of Sol-Gel Science and Technology, 73*(1), 250–259. https://doi.org/10.1007/s10971-014-3524-0

Gharzouni, A., Joussein, E., Samet, B., Baklouti, S., & Rossignol, S. (2015). Effect of the reactivity of alkaline solution and metakaolin on geopolymer formation. *Journal of Non-Crystalline Solids, 410,* 127–134. https://doi.org/10.1016/j.jnoncrysol.2014.12.021

Gharzouni, A., Samet, B., Baklouti, S., Joussein, E., & Rossignol, S. (2016). Addition of low reactive clay into metakaolin-based geopolymer formulation: Synthesis, existence domains and properties. *Powder Technology*, *288*, 212–220. https://doi.org/10.1016/j.powtec.2015.11.012

Gharzouni, A., Sobrados, I., Joussein, E., Baklouti, S., & Rossignol, S. (2016). Predictive tools to control the structure and the properties of metakaolin based geopolymer materials. *Colloids and Surfaces A: Physicochemical and Engineering Aspects*, *511*, 212–221. https://doi.org/10.1016/j.colsurfa.2016.09.089

Gillot, P. Y., Kieffer, G., & Romano, R. (1994). The evolution of Mount Etna in the light of potassium-argon dating. *Acta Vulcanologica*, *5*, 81–87.

Giudice, E. Lo, & Rasà, R. (1992). Very shallow earthquakes and brittle deformation in active volcanic areas: The Eatnean region as an example. *Tectonophysics*, *202*(2–4), 257–268. https://doi.org/10.1016/0040-1951(92)90111-I

Glukhovsky, V. D. (1959). Soil silicates. *Gostroiizdat Publish. Kiev, USSR.*

Gordon, M., Bell, J., & Kriven, W. M. (2006). Thermal conversion and microstructural evaluation of geopolymers or “Alkali Bonded Ceramics” (ABCs). *Ceramic Transactions*, *175*, 215–224. https://doi.org/10.1002/9781118407844.ch19

Gramlich, V., & Meier, W. M. (1971). The crystal structure of hydrated NaA: A detailed refinement of a pseudosymmetric zeolite structure. *Zeitschrift Fur Kristallographie - New Crystal Structures*, *133*(133), 134–149. https://doi.org/10.1524/zkri.1971.133.133.134

Greaves, C. (1983). A powder neutron diffraction investigation of vacancy ordering and covalence in γ-Fe2O3. *Journal of Solid State Chemistry*, *49*(3), 325–333. https://doi.org/10.1016/S0022-4596(83)80010-3

Gualtieri, A.F., & Zanni, M. (1998). Quantitative Determination of Crystalline and Amorphous Phase in Traditional Ceramics by Combined Rietveld-RIR Method. *Materials Science Forum*, *278–281*, 834–839. https://doi.org/10.4028/www.scientific.net/MSF.278-281.834

Gualtieri, Alessandro F. (2000). Accuracy of XRPD QPA using the combined Rietveld-RIR method. *Journal of Applied Crystallography*, *33*(2), 267–278. https://doi.org/10.1107/S002188989901643X

Gualtieri, Alessandro F., & Venturelli, P. (1999). In situ study of the goethite-hematite phase transformation by real time synchrotron powder diffraction. *American Mineralogist*, *84*(5–6), 895–904. https://doi.org/10.2138/am-1999-5-624

Gunasekara, C., Law, D. W., & Setunge, S. (2016). Long term permeation properties of different fly ash geopolymer concretes. *Construction and Building Materials*, *124*, 352–362. https://doi.org/10.1016/j.conbuildmat.2016.07.121

Günaydin, H. M., & Doğan, S. Z. (2004). A neural network approach for early cost estimation of structural systems of buildings. *International Journal of Project Management*, *22*(7), 595–602. https://doi.org/10.1016/j.ijproman.2004.04.002

Habert, G., D'Espinose De Lacaillerie, J. B., & Roussel, N. (2011). An environmental evaluation of geopolymer based concrete production: Reviewing current research trends. *Journal of Cleaner Production*, *19*(11), 1229–1238. https://doi.org/10.1016/j.jclepro.2011.03.012

Hajimohammadi, A., Provis, J. L., & Van Deventer, J. S. J. (2011). The effect of silica availability on the mechanism of geopolymerisation. *Cement and Concrete Research*, *41*(3), 210–216. https://doi.org/10.1016/j.cemconres.2011.02.001

Hanzlíček, T., Steinerová, M., Straka, P., Perná, I., Siegl, P., & Švarcová, T. (2009). Reinforcement of the terracotta sculpture by geopolymer composite. *Materials and Design*, *30*(8), 3229–3234. https://doi.org/10.1016/j.matdes.2008.12.015

Harlow, G. E. (1982). The anorthoclase structures: the effects of temperature and composition. *American Mineralogist*, *67*(9–10), 975–996.

Hawa, A., Tonnayopas, D., Prachasaree, W., & Taneerananon, P. (2013). Development and Performance Evaluation of Very High Early Strength Geopolymer for Rapid Road Repair. *Advances in Materials Science and Engineering*, *Volume 201*(Article ID 764180), 9. https://doi.org/DOI: 10.1155/2013/764180

Hayes, J. L., Wilson, T. M., & Magill, C. (2015, October 1). Tephra fall clean-up in urban environments. *Journal of Volcanology and Geothermal Research*, Vol. 304, pp. 359–377. https://doi.org/10.1016/j.jvolgeores.2015.09.014

Haykin, S. (1994). *Neural Networks: A Comprehensive Foundation*. Prentice Hall.

Horwell, C. J., & Baxter, P. J. (2006). The respiratory health hazards of volcanic ash: A review for volcanic risk mitigation. *Bulletin of Volcanology*, *69*(1), 1–24. https://doi.org/10.1007/s00445-006-0052-y

Infrastrutture, M. delle. (2008). *Norme Tecniche per le Costruzioni* (p. D.M. 14 Gennaio 2008). p. D.M. 14 Gennaio 2008.

ISCARSAH. (2003). Principles for the Analysis, Conservation and Structural Restoration of Architectural Heritage. *International Council on Monuments and Sites*, 3–6.

Izzo, F., Arizzi, A., Cappelletti, P., Cultrone, G., De Bonis, A., Germinario, C., … Langella, A. (2016). The art of building in the Roman period (89 B.C. - 79 A.D.): Mortars, plasters and mosaic floors from ancient Stabiae (Naples, Italy). *Construction and Building Materials*, *117*, 129–143. https://doi.org/10.1016/j.conbuildmat.2016.04.101

Kamalloo, A., Ganjkhanlou, Y., Aboutalebi, S. H., & Nouranian, H. (2010). Modeling of compressive strength of Metakaolin based geopolymers by the use of artificial neural network. *IJE Transactions A: Basics*, *23*(2), 145–152.

Kamseu, E., Leonelli, C., & Perera, D. S. (2009). *Investigation of Volcanic Ash Based*

Geopolymers as Potential Building Materials. (September).

Kani, E. N., & Allahverdi, A. (2009). Effect of chemical composition on basic engineering properties of inorganic polymeric binder based on natural pozzolan. *Ceramics - Silikaty*, *53*(3), 195–204.

Khan, M. I., Azizli, K., Sufian, S., Siyal, A. A., & Man, Z. (2014). *Sodium Silicate Free Geopolymer As Coating Material: Adhesion To Steel*. (May), b016. https://doi.org/10.3390/ecm-1-b016

Komnitsas, K., & Zaharaki, D. (2007). Geopolymerisation: A review and prospects for the minerals industry. *Minerals Engineering*, *20*(14), 1261–1277. https://doi.org/10.1016/j.mineng.2007.07.011

Kong, D. L. Y., Sanjayan, J. G., & Sagoe-Crentsil, K. (2007). Comparative performance of geopolymers made with metakaolin and fly ash after exposure to elevated temperatures. *Cement and Concrete Research*, *37*(12), 1583–1589. https://doi.org/10.1016/j.cemconres.2007.08.021

Kouamo, H. T., Elimbi, A., Mbey, J. A., Sabouang, C. J. N., & Njopwouo, D. (2012). The effect of adding alumina-oxide to metakaolin and volcanic ash on geopolymer products : A comparative study. *Construction and Building Materials*, *35*, 960–969. https://doi.org/10.1016/j.conbuildmat.2012.04.023

Kouamo Tchakoute, H., Elimbi, A., Diffo Kenne, B. B., Mbey, J. A., & Njopwouo, D. (2013). Synthesis of geopolymers from volcanic ash via the alkaline fusion method: Effect of Al 2O 3/Na 2O molar ratio of soda-volcanic ash. *Ceramics International*, *39*(1), 269–276. https://doi.org/10.1016/j.ceramint.2012.06.021

Krivenko, P. V. (1994). Alkaline cements. *1st International Conference on Alkaline Cements and Concretes*, 1, 11–129.

Kühl, H. (1908). *U.S. Patent No. 900,939*.

Lancellotti, I., Catauro, M., Ponzoni, C., Bollino, F., & Leonelli, C. (2013). Journal of Solid State Chemistry Inorganic polymers from alkali activation of metakaolin : Effect of setting and curing on structure. *Journal of Solid State Chemistry*, *200*, 341–348. https://doi.org/10.1016/j.jssc.2013.02.003

Lancellotti, I., Ponzoni, C., Barbieri, L., & Leonelli, C. (2013). Alkali activation processes for incinerator residues management. *Waste Management*, *33*(8), 1740–1749. https://doi.org/10.1016/j.wasman.2013.04.013

Lau, C. K., Lee, H., Vimonsatit, V., Huen, W. Y., & Chindaprasirt, P. (2019). Abrasion resistance behaviour of fly ash based geopolymer using nanoindentation and artificial neural network. *Construction and Building Materials*, *212*, 635–644. https://doi.org/10.1016/j.conbuildmat.2019.04.021

Lemougna, P. N., Chinje Melo, U. F., Delplancke, M. P., & Rahier, H. (2014). Influence of the chemical and mineralogical composition on the reactivity of volcanic ashes during alkali activation. *Ceramics International*, *40*(1 PART A), 811–820. https://doi.org/10.1016/j.ceramint.2013.06.072

Lemougna, P. N., Mackenzie, K. J. D., Jameson, G. N. L., & Chinje, H. R. U. F. (2013). *The role of iron in the formation of inorganic polymers ¨ ssbauer spectroscopy (geopolymers) from volcanic ash : a 57 Fe Mo study*. 5280–5286.

https://doi.org/10.1007/s10853-013-7319-4

Lemougna, P. N., MacKenzie, K. J. D., Jameson, G. N. L., Rahier, H., & Chinje Melo, U. F. (2013). The role of iron in the formation of inorganic polymers (geopolymers) from volcanic ash: A 57Fe Mössbauer spectroscopy study. *Journal of Materials Science*, *48*(15), 5280–5286. https://doi.org/10.1007/s10853-013-7319-4

Lemougna, P. N., Mackenzie, K. J. D., & Melo, U. F. C. (2011). *Synthesis and thermal properties of inorganic polymers (geopolymers) for structural and refractory applications from volcanic ash*. *37*, 3011–3018. https://doi.org/10.1016/j.ceramint.2011.05.002

Lemougna, P. N., Wang, K. tuo, Tang, Q., Nzeukou, A. N., Billong, N., Melo, U. C., & Cui, X. min. (2018). Review on the use of volcanic ashes for engineering applications. *Resources, Conservation and Recycling*, *137*(May), 177–190. https://doi.org/10.1016/j.resconrec.2018.05.031

Leonelli, C., Kamseu, E., Boccaccini, D. N., Melo, U. C., Rizzuti, A., Billong, N., & Misselli, P. (2007). Volcanic ash as alternative raw materials for traditional vitrified ceramic products. *Advances in Applied Ceramics*, *106*(3), 135–141. https://doi.org/10.1179/174367607X159329

Leonelli, Cristina, Kamseu, E., & Emilia, R. (2010). *Pubblicato su Ceramica Informazione, Luglio-Agosto 489 2010, 305-310*. 305–310.

Ling, Y., Wang, K., Wang, X., & Li, W. (2019). Prediction of engineering properties of fly ash-based geopolymer using artificial neural networks. *Neural Computing and Applications*, *3*. https://doi.org/10.1007/s00521-019-04662-3

Liu, S. W., Huang, J. H., Sung, J. C., & Lee, C. C. (2002). Detection of cracks using neural networks and computational mechanics. *Computer Methods in Applied Mechanics and Engineering*, *191*(25–26), 2831–2845. https://doi.org/10.1016/S0045-7825(02)00221-9

Luukkonen, T., Abdollahnejad, Z., Yliniemi, J., Kinnunen, P., & Illikainen, M. (2018). One-part alkali-activated materials: A review. *Cement and Concrete Research*, *103*(October 2017), 21–34. https://doi.org/10.1016/j.cemconres.2017.10.001

Mackenzie, K. J. D. (2016). *What are these things called geopolymers ? A physico-chemical perspective Copyright © 2003 , The American Ceramic Society Geopolymers and Geopolymer Matrix Composites Advances in Ceramic Matrix Composites IX*. (June).

Màdai, F., Kristàly, F., & Mucsi, G. (2015). MICROSTRUCTURE , MINERALOGY AND PHYSICAL PROPERTIES OF GROUND FLY ASH BASED GEOPOLYMERS. *Ceramics – Silikáty*, *59*(1), 70–79.

Markgraf, S. A., & Reeder, R. J. (1985). High-temperature structure refinements of calcite and magnesite. *American Mineralogist*, *70*, 590–600.

Mazzoleni, P. (2007). The use of volcanic stone in architecture: example of Etnean region. *Acta Vulcanologica*, *18*, 141–144.

Mc Guire, W. J., Moss, J. L., Saunders, S. J., & Stewart, I. S. (1996). Dyke induced rifting and edifice instability at Mount Etna. In *Gravestock, P.J., Mc Guire, W.J. (Eds.), Etna: Fifteen Years On.* (pp. 20–24). Cheltenham and Gloucester Special

Publication.

Medri, V., Fabbri, S., Dedecek, J., Sobalik, Z., Tvaruzkova, Z., & Vaccari, A. (2010). Role of the morphology and the dehydroxylation of metakaolins on geopolymerization. *Applied Clay Science*, *50*(4), 538–545. https://doi.org/10.1016/j.clay.2010.10.010

Memon, F. A., Nuruddin, M. F., Khan, S., Shafiq, N., & Ayub, T. (2013). Effect of Sodium Hydroxide Concentration on Fresh Properties and Compressive Strength of Self-Compacting Geopolymer Concrete. *Journal of Engineering Science and Technology*, *8*(1), 44–56.

Mielenz, R., Witte, L., & Glantz, O. (1950). Effect of Calcination on Natural Pozzolans. *Symposium on Use of Pozzolanic Materials in Mortars and Concretes, ASTM Speci*(99), 43–92.

Monaco, C., Tapponnier, P., Tortorici, L., & Gillot, P. Y. (1997). Late Quaternary slip rates on the Acireale-Piedimonte normal faults and tectonic origin of Mt. Etna (Sicily). *Earth and Planetary Science Letters*, *147*(1–4), 125–139.

Morra, V., De Bonis, A., Grifa, C., Langella, A., Cavassa, L., & Piovesan, R. (2013). Minero-petrographic study of cooking ware and pompeian red ware (Rosso Pompeiano) from Cuma (Southern Italy). *Archaeometry*, *55*(5), 852–879. https://doi.org/10.1111/j.1475-4754.2012.00710.x

Muthu Kumar, E., & Ramamurthy, K. (2017). Influence of production on the strength, density and water absorption of aerated geopolymer paste and mortar using Class F fly ash. *Construction and Building Materials*, *156*, 1137–1149. https://doi.org/10.1016/j.conbuildmat.2017.08.153

Najafi, E., Allahverdi, A., & Provis, J. L. (2012). Cement & Concrete Composites Efflorescence control in geopolymer binders based on natural pozzolan. *Cement and Concrete Composites*, *34*(1), 25–33. https://doi.org/10.1016/j.cemconcomp.2011.07.007

Nazari, A. (2013). Artificial neural networks application to predict the compressive damage of lightweight geopolymer. *Neural Computing and Applications*, *23*(2), 507–518. https://doi.org/10.1007/s00521-012-0945-y

Neri, M., Acocella, V., & Behncke, B. (2004). The role of the Pernicana Fault System in the spreading of Mt. Etna (Italy) during the 2002-2003 eruption. *Bulletin of Volcanology*, *66*(5), 417–430. https://doi.org/10.1007/s00445-003-0322-x

Nikolov, A., Rostovsky, I., & Nugteren, H. (2017). Geopolymer materials based on natural zeolite. *Case Studies in Construction Materials*, *6*, 198–205. https://doi.org/10.1016/j.cscm.2017.03.001

Nord, A. G., Annersten, H., & Filippidis, A. (1982). The cation distribution in synthetic Mg-Fe-Ni olivines. *American Mineralogist*, *67*(11–12), 1206–1211.

Obonyo, E. A., Kamseu, E., Lemougna, P. N., Tchamba, A. B., Melo, U. C., & Leonelli, C. (2014). A sustainable approach for the geopolymerization of natural iron-rich aluminosilicate materials. *Sustainability (Switzerland)*, *6*(9), 5535–5553. https://doi.org/10.3390/su6095535

Özcan, F., Atiş, C. D., Karahan, O., Uncuoğlu, E., & Tanyildizi, H. (2009). Comparison of artificial neural network and fuzzy logic models for prediction of long-term compressive strength of silica fume concrete. *Advances in Engineering Software, 40*(9), 856–863. https://doi.org/10.1016/j.advengsoft.2009.01.005

Pala, M., Özbay, E., Öztaş, A., & Yuce, M. I. (2007). Appraisal of long-term effects of fly ash and silica fume on compressive strength of concrete by neural networks. *Construction and Building Materials, 21*(2), 384–394. https://doi.org/10.1016/j.conbuildmat.2005.08.009

Palomo, A., Blanco-Varela, M. T., Granizo, M. L., Puertas, F., Vazquez, T., & Grutzeck, M. W. (1999). Chemical stability of cementitious materials based on metakaolin. *Cement and Concrete Research, 29*(7), 997–1004. https://doi.org/10.1016/S0008-8846(99)00074-5

Palomo, A., Krivenko, P., Garcia-Lodeiro, I., Kavalerova, E., Maltseva, O., & Fernández-Jiménez, A. (2014). A review on alkaline activation: New analytical perspectives. *Materiales de Construccion*, *64*(315). https://doi.org/10.3989/mc.2014.00314

Panagiotopoulou, C., Kontori, E., Perraki, T., & Kakali, G. (2007). Dissolution of aluminosilicate minerals and by-products in alkaline media. *Journal of Materials Science*, *42*(9), 2967–2973. https://doi.org/10.1007/s10853-006-0531-8

Piatanesi, A., & Tinti, S. (1998). *A revision of the 1693 eastern Sicily earthquake and tsunami*. *103*(97), 2749–2758.

Porcher, F., Souhassou, M., Dusausoy, Y., & Lecomte, C. (1999). The crystal structure of a low-silica dehydrated NaX zeolite. *European Journal of Mineralogy*, *11*(2), 333–343. https://doi.org/10.1127/ejm/11/2/0333

Prentice, J. E. (1990). *Geology of Construction Materials*. Springer Netherlands.

Provis, J. L., & Bernal, S. A. (2014). Geopolymers and Related Alkali-Activated Materials. *Annual Review of Materials Research*, *44*(1), 299–327. https://doi.org/10.1146/annurev-matsci-070813-113515

Provis, J. L., Lukey, G. C., & Van Deventer, J. S. J. (2005). Do geopolymers actually contain nanocrystalline zeolites? a reexamination of existing results. *Chemistry of Materials*, *17*(12), 3075–3085. https://doi.org/10.1021/cm050230i

Purdon, A. O. (1940). The action of alkalis on blast-furnace slag. *Journal of the Society of Chemical Industry, 59*(9), 191–202.

Pyle, D. M., Ricketts, G. D., Margari, V., van Andel, T. H., Sinitsyn, A. A., Praslov, N. D., & Lisitsyn, S. (2006). Wide dispersal and deposition of distal tephra during the Pleistocene “Campanian Ignimbrite/Y5” eruption, Italy. *Quaternary Science Reviews*, *25*(21–22), 2713–2728. https://doi.org/10.1016/j.quascirev.2006.06.008

Rasà, R., Azzaro, R., & Leonardi, O. (1996). Aseismic creep on faults and flank instability at Mount Etna volcano, Sicily. *Geological Society Special Publication*, *110*(1), 179–192. https://doi.org/10.1144/GSL.SP.1996.110.01.14

Rees, C. A., Provis, J. L., Lukey, G. C., & Van Deventer, J. S. J. (2007a). Attenuated total reflectance fourier transform infrared analysis of fly ash geopolymer gel aging. *Langmuir*, *23*(15), 8170–8179. https://doi.org/10.1021/la700713g

Rees, C. A., Provis, J. L., Lukey, G. C., & Van Deventer, J. S. J. (2007b). In situ ATR-

FTIR study of the early stages of fly ash geopolymer gel formation. *Langmuir*, *23*(17), 9076–9082. https://doi.org/10.1021/la701185g

Rickard, W. D. A., Vickers, L., & van Riessen, A. (2013). Performance of fibre reinforced, low density metakaolin geopolymers under simulated fire conditions. *Applied Clay Science*, *73*(1), 71–77. https://doi.org/10.1016/j.clay.2012.10.006

Robayo-salazar, Rafael Andres, & Gutiérrez, R. M. De. (2018). Natural volcanic pozzolans as an available raw material for alkali-activated materials in the foreseeable future : A review. *Construction and Building Materials*, *189*, 109–118. https://doi.org/10.1016/j.conbuildmat.2018.08.174

Robayo-salazar, Rafael Andrés, Mejía, R., Gutiérrez, D., & Puertas, F. (2016). Effect of metakaolin on natural volcanic pozzolan-based geopolymer cement. *Applied Clay Science*, *132–133*, 491–497. https://doi.org/10.1016/j.clay.2016.07.020

Romano, R. (1982). Succession of the volcanic activity in the Etnean area. *Memorie Della Società Geologica Italiana*, *23*, 27–48.

Romisuhani, A., Albakri, M. M., Kamarudin, H., & Andrei, S. V. (2017). The influence of sintering method on kaolin-based geopolymer ceramics with addition of ultra high molecular weight polyethylene as binder. *IOP Conference Series: Materials Science and Engineering*, *267*(1). https://doi.org/10.1088/1757-899X/267/1/012013

Rudolph, W. W., Fischer, D., & Irmer, G. (2006). Vibrational spectroscopic studies and density functional theory calculations of speciation in the CO2-water system. *Applied Spectroscopy*, *60*(2), 130–144. https://doi.org/10.1366/000370206776023421

Ruiz-Santaquiteria, C., Fernández-Jiménez, A., Skibsted, J., & Palomo, A. (2013). Clay reactivity: Production of alkali activated cements. *Applied Clay Science*, *73*(1), 11–16. https://doi.org/10.1016/j.clay.2012.10.012

Rust, D., & Neri, M. (1996). The boundaries of large-scale collapse on the flanks of Mount Etna, Sicily. *Geological Society Special Publication*, *110*, 193–208. https://doi.org/10.1144/GSL.SP.1996.110.01.15

Sadat, M. R., Bringuier, S., Muralidharan, K., Frantziskonis, G., & Zhang, L. (2018). Atomic-scale dynamics and mechanical response of geopolymer binder under nanoindentation. *Computational Materials Science*, *142*, 227–236. https://doi.org/10.1016/j.commatsci.2017.10.026

Sadat, M. R., Muralidharan, K., & Zhang, L. (2018). Reactive molecular dynamics simulation of the mechanical behavior of sodium aluminosilicate geopolymer and calcium silicate hydrate composites. *Computational Materials Science*, *150*, 500–509. https://doi.org/10.1016/j.commatsci.2018.04.041

Saha, A. (2011). Data Mining in Excel. Retrieved from https://www.sites.google.com/site/sayhello2angshu/dminexcel

Schmid, R. (1981). Descriptive nomenclature and classification of pyroclastic deposits and fragments - Recommendations of the IUGS Subcommission on the Systematics of Igneous Rocks. *Geologische Rundschau*, *70*(2), 794–799. https://doi.org/10.1007/BF01822152

Sciuto Patti, C. (1896). *Sui materiali da costruzioni più usati in Catania*. Catania:

Tipografia Editrice dell’Etna.

Scribano, V., Viccaro, M., Cristofolini, R., & Ottolini, L. (2009). Metasomatic events recorded in ultramafic xenoliths from the Hyblean area (Southeastern Sicily, Italy). *Mineralogy and Petrology*, *95*(3–4), 235–250. https://doi.org/10.1007/s00710-008-0031-4

Scrivener, K. L., John, V. M., & Gartner, E. M. (2018). Eco-efficient cements: Potential economically viable solutions for a low-CO2 cement-based materials industry. *Cement and Concrete Research*, *114*, 2–26. https://doi.org/10.1016/j.cemconres.2018.03.015

Shi, C., & Fernández-Jiménez, A. (2006). Stabilization/solidification of hazardous and radioactive wastes with alkali-activated cements. *Journal of Hazardous Materials*, *137*(3), 1656–1663. https://doi.org/10.1016/j.jhazmat.2006.05.008

Shi, H., Gao, Y., & Wang, X. (2010). Optimization of injection molding process parameters using integrated artificial neural network model and expected improvement function method. *International Journal of Advanced Manufacturing Technology*, *48*(9–12), 955–962. https://doi.org/10.1007/s00170-009-2346-7

Siddique, R., & Klaus, J. (2009, March). Influence of metakaolin on the properties of mortar and concrete: A review. *Applied Clay Science*, Vol. 43, pp. 392–400. https://doi.org/10.1016/j.clay.2008.11.007

Snellings, R., Elsen, J., & Mertens, G. (2012). Supplementary Cementitious Materials Supplementary Cementitious Materials. *Reviews in Mineralogy & Geochemistry*, *74*(December 2013), 211–278. https://doi.org/10.2138/rmg.2012.74.6

Solaro, G., Acocella, V., Pepe, S., Ruch, J., Neri, M., & Sansosti, E. (2010). Anatomy of an unstable volcano from InSAR: Multiple processes affecting flank instability at Mt. Etna, 1994-2008. *Journal of Geophysical Research: Solid Earth*, *115*(10), 1994–2008. https://doi.org/10.1029/2009JB000820

Sparks, R. S. J. (1978). The dynamics of bubble formation and growth in magmas: A review and analysis. *Journal of Volcanology and Geothermal Research*, *3*(1–2), 1–37. https://doi.org/10.1016/0377-0273(78)90002-1

Speight, J. G. (2002). Chemical and Process Design. In McGraw-Hill (Ed.), *Handbook* (pp. 530–539).

Spence, R. J. S., Kelman, I., Baxter, P. J., Zuccaro, G., & Petrazzuoli, S. (2005). Residential building and occupant vulnerability to tephra fall. *Natural Hazards and Earth System Science*, *5*(4), 477–494. https://doi.org/10.5194/nhess-5-477-2005

Stewart, C., Johnston, D. M., Leonard, G. S., Horwell, C. J., Thordarson, T., & Cronin, S. J. (2006). Contamination of water supplies by volcanic ashfall: A literature review and simple impact modelling. *Journal of Volcanology and Geothermal Research*, *158*(3–4), 296–306. https://doi.org/10.1016/j.jvolgeores.2006.07.002

Strydom, C. a., & Swanepoel, J. C. (2002). Utilisation of fly ash in a geopolymeric material. *Applied Geochemistry*, *17*(8), 1143–1148.

Tchadjié, L. N., Djobo, J. N. Y., Ranjbar, N., Tchakouté, H. K., Kenne, B. B. D., Elimbi, A., & Njopwouo, D. (2016). Potential of using granite waste as raw material for geopolymer synthesis. *Ceramics International*, *42*(2), 3046–3055.

https://doi.org/10.1016/j.ceramint.2015.10.091

Tchakoute, H. K., Elimbi, A., Yanne, E., & Djangang, C. N. (2013). Utilization of volcanic ashes for the production of geopolymers cured at ambient temperature. *Cement and Concrete Composites*, *38*(March), 75–81. https://doi.org/10.1016/j.cemconcomp.2013.03.010

Tchakouté, H. K., Kong, S., Djobo, J. N. Y., Tchadjié, L. N., & Njopwouo, D. (2015). A comparative study of two methods to produce geopolymer composites from volcanic scoria and the role of structural water contained in the volcanic scoria on its reactivity. *Ceramics International*, *41*(10), 12568–12577. https://doi.org/10.1016/j.ceramint.2015.06.073

Tchakoute Kouamo, H., Mbey, J. A., Elimbi, A., Kenne Diffo, B. B., & Njopwouo, D. (2013). Synthesis of volcanic ash-based geopolymer mortars by fusion method: Effects of adding metakaolin to fused volcanic ash. *Ceramics International*, *39*(2), 1613–1621. https://doi.org/10.1016/j.ceramint.2012.08.003

Toby, B. H., & Von Dreele, R. B. (2013). GSAS-II: the genesis of a modern open-source all purpose crystallography software package. *Journal of Applied Crystallography*, *46*(2), 544–549. https://doi.org/10.1107/S0021889813003531

Van Riessen, A., Rickard, W. D. A., Williams, R. P., & Van Riessen, G. A. (2017). Methods for geopolymer formulation development and microstructural analysis. *Journal of Ceramic Science and Technology*, *8*(3), 421–431. https://doi.org/10.4416/JCST2017-00065

Wadoski-Romeijn, E., & Armbruster, T. (2013). Topotactic transformation and dehydration of the zeolite gismondine to a novel Ca feldspar structure. *American Mineralogist*, *98*(11–12), 1988–1997. https://doi.org/10.2138/am.2013.4495

Walker, R., & Pavía, S. (2011). Physical properties and reactivity of pozzolans, and their influence on the properties of lime-pozzolan pastes. *Materials and Structures/Materiaux et Constructions*, *44*(6), 1139–1150. https://doi.org/10.1617/s11527-010-9689-2

WYCKOFF, R. W. G. (1963). THE STRUCTURE OF CRYSTALS. *Crystal Structure*, *1*, 239–444.

Xu, H., & Van Deventer, J. S. J. (2000). The geopolymerisation of alumino-silicate minerals. *International Journal of Mineral Processing*, *59*(3), 247–266. https://doi.org/10.1016/S0301-7516(99)00074-5

Yankwa Djobo, J. N., Elimbi, A., Tchakouté, H. K., & Kumar, S. (2016). Mechanical activation of volcanic ash for geopolymer synthesis: Effect on reaction kinetics, gel characteristics, physical and mechanical properties. *RSC Advances*, *6*(45), 39106–39117. https://doi.org/10.1039/c6ra03667h

Yaprak, H., Karaci, A., & Demir, I. (2013). Prediction of the effect of varying cure conditions and w/c ratio on the compressive strength of concrete using artificial neural networks. *Neural Computing and Applications*, *22*(1), 133–141. https://doi.org/10.1007/s00521-011-0671-x

Yousefi Oderji, S., Chen, B., Ahmad, M. R., & Shah, S. F. A. (2019). Fresh and hardened properties of one-part fly ash-based geopolymer binders cured at room temperature:

Effect of slag and alkali activators. *Journal of Cleaner Production*, *225*, 1–10. https://doi.org/10.1016/j.jclepro.2019.03.290

Zhang, Z., Yao, X., & Zhu, H. (2010a). Potential application of geopolymers as protection coatings for marine concrete I. Basic properties. *Applied Clay Science*, *49*(1–2), 1–6. https://doi.org/10.1016/j.clay.2010.01.014

Zhang, Z., Yao, X., & Zhu, H. (2010b). Potential application of geopolymers as protection coatings for marine concrete II. microstructure and anticorrosion mechanism. *Applied Clay Science*, *49*(1–2), 7–12. https://doi.org/10.1016/j.clay.2010.04.024